Fermilab FERMILAB-THESIS-1999-32

Multidimensional Resonance Analysis of $\Lambda_c^+ \to pK^-\pi^+$

by

George F. Fox

Bachelor of Science
Duke University, 1986

Masters of Science
University of South Carolina, 1996

Submitted in Partial Fulfillment of the Requirements

for the Degree of Doctor of Philosophy in the

Department of Physics and Astronomy

University of South Carolina

1999

Major Professor

Committee Member

Committee Member

Chairman, Examining Committee

Committee Member

Dean of The Graduate School

Acknowledgements

Although I may use the subject "I" in a number of sentences throughout this dissertation, I could not have done it without help. So I wish to thank the many people who made this dissertation possible.

Especially, Gussie, my wife and confidant, who supported me in every way while I stayed in school. She gave me time to work, a shoulder on which to cry, an ear to hear my venting, and the love without which I would be no one. I couldn't have done it without her. Besides, she would kick my butt if I didn't finish quickly enough.

Aleric, my son, who stayed as good as a son could be so that I didn't get too stressed out, and who seemed to enjoy my physics stories.

Tiamat, my daughter, who added an extra incentive to finish and more joy to the house.

Milind Purohit, my advisor, who opened up the possibility of my doing a Ph.D., and who gave me plenty of time to concentrate on my work and the understanding I needed as I balanced home and work. I have never heard anyone describe an advisor to make me think Milind wasn't the best.

The E791 Collaboration, my colleagues, whose members welcomed me and pushed me to dig a little deeper. Please, see appendix A for the list of their distinguished names.

Lucien Cremaldi (chairman), Jean Slaughter, Ray Stefanski, Austin Napier, and Milind Purohit, my E791 Committee, who read my work more than any human should be forced to read. They pushed and frustrated me, but the work is better for their suggestions. Also thanks to Jeff Appel, who wasn't officially a member of my collaboration committee but was a valuable part of the phone meetings.

Jeff Wilson (chairman), Frank Avignone, Fred Myhrer, Tom Owens, and Milind Purohit, my USC Committee, who pushed me out the door in the end. Jeff Wilson read my rough drafts and made me feel like I could do it. Frank Avignone helped me tremendously when I first arrived in graduate school. He also was a big part in convincing me to go on for the Ph.D. Fred Myhrer guided me in my Masters and agreed to help me on my Doctorate. Tom Owens, Geophysicist, subjected himself to high energy physics and, in turn, forced me to attempt to write my dissertation at a more understandable level.

Cheryl Stocker, Brenda Craft, Lynn Waters who helped me tremendously with setting appointments and filling out paper work. Graduate school would have so much more confusing without their help.

Sriram, Chitra, Kimberly, Laura, and countless others who, through their friendship supported my family and made life in Columbia that much better.

My former students who made me feel like a worthwhile teacher and who gave me the courage to keep going. I especially want to thank those who pursued a physics major in college: Joe Rice, who graduated with a double major of physics and english, and Anna Clower, Kristen Frederick,

Allan Powell, and Ryan White, who have started the major, and I hope, will finish it. I, also want to mention Michael Popp. Michael, it's all you.

And all the students and parents who drove me back to school.

E791 gratefully acknowledges the staffs of Fermilab and of all the participating institutions. This research was supported by the Brazilian Conselho Nacional de Desenvolvimento Científico e Technológio, the Mexican Consejo Nacional de Ciencia y Tecnologica, the Israeli Academy of Sciences and Humanities, the U.S. Department of Energy, the U.S.-Israeli Binational Science Foundation and the U.S. National Science Foundation. Fermilab is operated by the Universities Research Association, Inc., under contract with the United States Department of Energy.

Abstract

The $\Lambda_c^+ \rightarrow pK^-\pi^+$ decay is the first baryon decay which opens itself up to a Dalitz plot type analysis. However, unlike the previous Dalitz analyses on charm mesons, the baryon analysis involves particles with non-zero spin, and thus we are no longer dealing with a simple two dimensional problem, but a five dimensional problem. Using conventional and Neural Network techniques, we have optimized the significance of our Λ_c signal. Then we modeled our background and acceptance in five dimensions and used the Helicity Formalism outlined by Jacob and Wick [Jac 59] to model the signal density. Ultimately, we used MINUIT to optimize the 34 coefficients needed to describe the decay.

Preface

0.1 Personal Note

As I look back over the past 20 years, I am forced to reflect upon the journey I have taken to get my doctorate. When I was in high school, I could picture myself eventually getting my Ph.D., but by the time I graduated from college, I couldn't picture it anymore because I was burned out from being a student. Years of bad work habits had taken their toll on me, and now I thought I was ready for the "real world". So I struck out to conquer the world of teaching. Boy, was I unprepared.

As a high school teacher, I saw myself mastering the art, and eventually moving my way up to running a school. (Is that really "up"?) Ah, the best laid plans of mice and men. Although teaching was not as rewarding as I thought it should have been, I look back upon those days (being several years removed) and have very fond memories. I have no regrets being a teacher and for me, it was the best thing I could have done. I learned more than I taught.

Teaching served me best by preparing me for being a student (again?) because it gave me several lessons for my move to the other side of the desk. I developed an eagerness to learn. Until graduate school, I'm not sure that I ever really pursued an academic topic for any length of time just because I wanted to learn. But I found that the more I taught and delved into a topic, the more fascinating it became, especially in physics. Knowledge begat a thirst for more. It is said that the Sirens in **The Odyssey** lured men to their deaths by singing all of the knowledge of the world. More and more, I saw myself falling hypnotic under their spell.

Teaching also provided me with a role model. I saw a wide range of students' abilities and motivations. Besides learning to appreciate students for who they were and not the grades they made, I learned the characteristics that I felt I should have. In essence, I learned what a student should be.

Lastly, teaching gave a frame of reference. Teaching has many highs and lows, and very little in the middle - at least for me. As I worked on my dissertation, and hit low moments, I could always say to myself, "At least I don't have to grade." or "At least, I don't have to deal with parents". Yes, the highs of my dissertation work don't match the highs of the teaching, but they do come more frequently.

Overall, this whole journey toward the Ph.D. has been a roller coaster ride of frustrations and excitement, but what an intellectual journey it has been. And now that it is done (or near done), I'm very proud of my work and am glad to be here.

0.2 The Sections of the Dissertation

Chapter	Comments
1	Justification the benefit of the research.
2	Talk about the theory of charmed baryon decay and how it is different from the other decays.
3	Basics of Neural Networks, and why they offer a better way of analyzing data.
4	Explanation of the detector and the components, how they work, and how we get the information that we know.
5	Description of reconstruction, filtering, stripping, and substripping phases of data selection.
6	Discussion the final criteria for event selection culminating in the data sample that I analyzed.
7	The signal density that I fit using MINUIT.
8	The acceptance and background models that I used.
9	The results I got for my fit.
10	Systematic errors associated with my analysis.
11	Conclusions of the research.

Table 0.1: Overview of the chapters.

Appendix	Comments
A	The list of the members of the E791 Collaboration.
B	The parameters used to describe each Release 7 event.
C	The criteria for the stream A and stream B strips.
D	The criteria for the KSU substrip.
E	Exploration of the D's that were cut from the data set.
F	The advantages of constraining the fit.
G	A test of the fitting procedure.
H	A χ^2 comparison of the acceptance and the data vs. the modeled fit.
I	The results of the fits with simple assumptions.
J	A χ^2 comparison of the acceptance and the model that was tweaked to match the two dimensional scatter plots.
K	Detail about the mysterious spin $\frac{1}{2}-$ particle
L	The numbers used in calculating the numbers used to calculate the systematic errors from the Čerenkov counters.
M	Partial exploration of other topics.

Table 0.2: Overview of the appendices.

If You Want to Know More

For information on the following topics, please look at literature indicated.

Topic	Bibliographic Reference
Breit-Wigner	[Ast 88, Cor 75, Fra 94, Koc 80, Nag 76, Pil 79, Wat 63]
Detector (E791)	[Ait 98, Ama 93, App 86, Bar 87, Bra 96, E791, Les 96, Per 95]
Detector (General)	[Cha 84, Cus 84, Fer 91, Hei 96, PDG 98, Pei 92, Sau 92]
Dalitz Analyses	[Ait 97, Anj 93, Kal 64]
E791	[Ait 98, Ama 93, Bar 87, Bra 96, E791, Kwa 95, Pur 96, Tri 93, Yos 96]
Experiments	[App 92, PDG 98]
Helicity	[Bjo 89, Hab 94, Jac 59, Per 87, Per 74, Pil 67, Pur 96]
Λ_c	[Anj 90, App 92, Bas 81, Boz 93, Kor 91, Kwa 95, PDG 98, Pur 96]
Latex	[Bue 90, Lam 94, Shu 94]
Mathematics	[Fro 79, Jam 81, PDG 98, Row 66]
Neural Networks	[Alc 93, Bea 91, Bis 95, Pet 93, Smi 93]
Theory	[App 92, Dha 96, Dun 98, Fre 68, Gla 91, Iva 98, Kor 94, Kor 91, PDG 98, Per 87, Per 74, Pil 67, Upp 94]

Table 0.3: Sources for specific topics.

0.3 Basics for the Non-physicist

This section is for the novice to physics. If you are a physicist, then skipping this section will not affect the continuity of the rest of the paper. If you are unfamiliar with the terms, please see the Glossary on page 220. Also note that $\Lambda_c^+ \to p^+K^-\pi^+$ refers to the decay mentioned but also to its charge-conjugate decay, $\Lambda_c^- \to p^-K^+\pi^-$ where "+" and "-" refers to the charge of the particle.

In essence, this dissertation explores the short and happy life a parent particle: Λ_c, read as "Lambda c", and its three daughters: p (proton), K (kaon), and π (pion). This transformation is written as $\Lambda_c^+ \to p^+K^-\pi^+$. As the parent decays (falls apart and re-forms) into its children it can take several paths. In some cases the parent decays straight into the three children (a nonresonant decay), and sometimes it decays into two particles, one of which is unstable (called a resonance) which in turn decays into two particles. This can be written, in the case of a $\overline{K}^{*0}$ resonance, as $\Lambda_c^+ \to \overline{K}^{*0}(\to K^-\pi^+)p^+$. Regardless of the path, we start with one particle and end up with three.

To analyze the data, we will take the p,K, and π and work backwards to determine information about the Λ_c. If the K and π came from a $\overline{K}^{*0}$ then the reconstructed mass of $K\pi$ should be near the mass of a $\overline{K}^{*0}$, and this will be seen as a darker ban in the two dimensional projections. See figure 9.2 on page 72. The dark ban in "actual 2 v. 1" is $\sim$0.803 $(\mathrm{GeV/c^2})^2 = m_{K\pi}^2$ which translates to $m_{K\pi} = 0.896$ GeV/c^2 which is the mass of the $\overline{K}^{*0}$.

When we are done, we will have determined which resonances are present and how often they occur.

In order to create Λ_c's, one needs enough energy (the Λ_c, in one sense, is a little bigger than two protons), but since it is not a very common particle, one needs so much energy that some of the energy will become Λ_c's. To create this energy, high energy physicists have designed two basic kinds of experiments. One is to slam common particles (like protons and electrons) into other particles coming right at them - a colliding beam experiment; and the other is to slam a particle into a fixed target - a fixed target experiment. E791 is the latter kind, in which pions were slammed into a platinum and carbon target, which is, in essence, a whole lot of nucleons (protons and neutrons).

After the pions hit the nucleon, there is so much energy in the collision, that it starts to coalesce and form particles. Some of these particles are Λ_c's which then continue on their path into the detector.

Detectors are various machines designed to detect certain characteristics of a charged particle. Note that the particle needs to be charged to be detected directly. Neutral particles are detected when they decay into charged particles or when they interact with another particle and charged particles emerge. Some detectors are designed to determine the path the particle takes (e.g. a bubble chamber), some are designed to determine the mass or energy of the particle (e.g. calorimeter), and some are designed just to count the number of a particular kind of particle (e.g. a Geiger counter). It is also interesting to note that detectors need to be quite large to detect particles that are too small to be seen by the naked eye. For example, the E791 detector (see figure 4.2 on page 27 for a schematic drawing of the detector) is about 23 meters (75 feet) long.

Since every experiment is short of money, these detectors can not be placed everywhere. So they are placed where physicists can get the most information for the least amount of money. Also, since so many particles fly by at once, there is a whole lot of information which is collected and sorted later.

From all this information, some educated guess work is needed to eliminate background (that which is useless to the analysis at hand). For example, one of the detectors (the Čerenkov detector) determines the probability that a particle is a proton, kaon, or pion. We identify the possible kaon by its charge, then look at its Čerenkov probability. If the probability that the suspected kaon is actually a kaon is $\sim$0.01, then most likely that particle was misidentified. We would throw that event out.

Another issue is how long the Λ_c will survive before decaying. This, however, is not as simple as one might think. How long it lives depends on the reference frame of the observer. Without going into too much detail about relativity (see [Fre 68] for a good introduction), suffice it to say that the particle lives longer in the lab frame (i.e. from our point of view) than it does from its own reference frame, also known as its rest frame (from its point of view). In its own rest frame, the Λ_c lives, on average, 0.206 ps (= 0.206×10^{-12} s = 0.000000000000206 seconds), and therefore it will travel $\sim$62 microns (0.0025 inches) before decaying. In the lab frame, assuming the Λ_c is traveling at 0.999c (0.999 times the speed o f light), this translates to living for 4.5 ps and traveling 1.4 mm. The bottom line is that the Λ_c will most likely not be detected but its daughters will be.

When reconstructing, we wanted to find as many Λ_c's as possible. So we found all particles which seem to have decayed into three particles. We then made an educated guess as to which might be a p, K, or π, assuming the oppositely charged particle is a kaon and of the remaining two particles, assuming the one with the greater Čerenkov probability of being a proton actually is the proton. Thus, the remaining particle is assumed to be a π. Then using each particle's momentum, we calculated what their parent's mass must have been. From this, we had a lot of possibilities as can be seen in the upper left hand figure on page 43. After a series of cuts, we managed to whittle this huge number of events into a set of events which obviously contained a Λ_c as can be seen in figure 6.5 on page 46.

The rest of this paper, is my exploration of the experimental data and what it means.

Contents

List of Tables

List of Figures

Chapter 1

Introduction

Since the discovery of charm particles in 1974, a great deal of study has been made of them, especially concerning charm mesons[PDG 98]. Although there has been study of charm baryon lifetimes and branching fractions, this body of work is not as extensive as the work on charm mesons.

However, there is a considerable amount of information to be found from the study of charm baryon decays, such as the relative importance of exchange and spectator diagrams.*In charm meson decays, the exchange diagrams are inhibited at the quark level, because of helicity and form factor suppression, but this is not necessarily the case for the charm baryon decay. This inhibiting would cause the charm meson lifetime to be longer than the charm baryon lifetime, as has been seen experimentally. As will be seen later in the dissertation, in the decay $\Lambda_c^+ \to \mathrm{pK}^-\pi^+$ (and charge conjugate decays which are implied throughout this dissertation), the nonresonant $\mathrm{pK}\pi$ decay, and the resonant $\mathrm{p}\overline{\mathrm{K}}^{*0}$ and $\Lambda(1520)\pi$ two-body decays can be described by both the spectator and exchange diagrams. However, another significant branch is the two-body decay to $\Delta^{++}\mathrm{K}^-$ which can only occur via the exchange diagram. Thus, not only are the charm baryon lifetimes expected to be shorter than charm meson lifetimes, but we expect to find a significant fraction of $\mathrm{pK}^-\pi^+$ decays via the Δ^{++} resonance.

This dissertation also offers a new and better technique for measuring branching fractions. Although measurements of charm baryon branching fractions are difficult even in the copious modes such as $\Lambda_c^+ \to \mathrm{pK}^-\pi^+$, E791 offers the first experiment with sufficient statistics to do it well. Also, a proper analysis is far more sophisticated than previous researchers have tried[Bas 81, Boz 93]. This is because charm baryons carry spin and may be polarized upon production; also, their decay products always include a baryon with spin. Most three-body decay analyses study structure in the two-dimensional space of decay product energies, as in the Dalitz plot analysis, but the spin effects just described require five kinematic variables for a complete description. While this complicates the analysis, it affords greater sensitivity to the parameters of interest. This analysis also offers the chance to determine the polarization of the Λ_c concurrently with the other fit parameters given a convenient choice for the polarization axis. This analysis is the first to use all of these effects and, as such, is unique.

*The exchange diagram describes a decay in which a W mediator is emitted in the transformation of a quark and absorbed by another quark which then transforms. The spectator diagram refers to a decay in which the W decays into a quark and antiquark. See figures starting on page 2 for examples of each kind of diagram.

Chapter 2

Theory of Decay

2.1 Decay of $\Lambda_c^+ \to pK^-\pi^+$

As mentioned in the Introduction, the Λ_c decay can be described by exchange and spectator diagrams. As Λ_c decays it can take several paths as seen below in figures 2.1 - 2.7. When reading the figures, note that time travels from left to right (just follow the arrows).

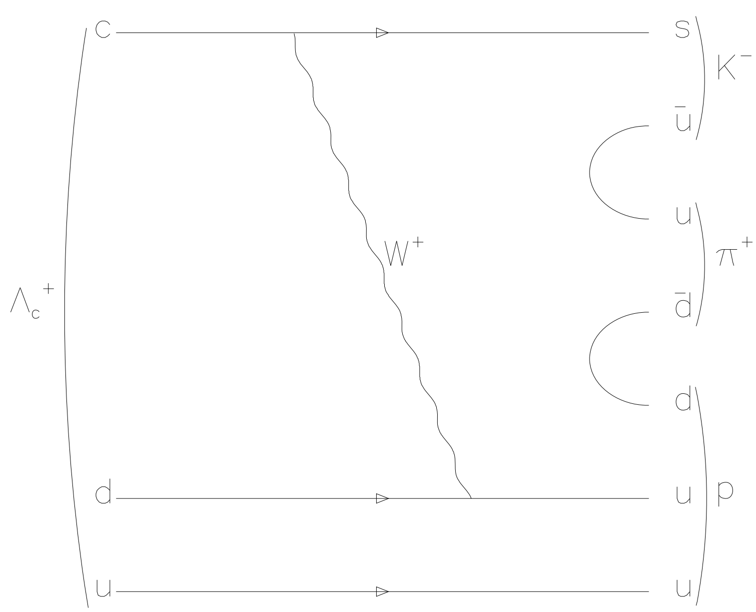

Figure 2.1: An exchange diagram for $\Lambda_c^+ \to pK^-\pi^+$ nonresonant decay.

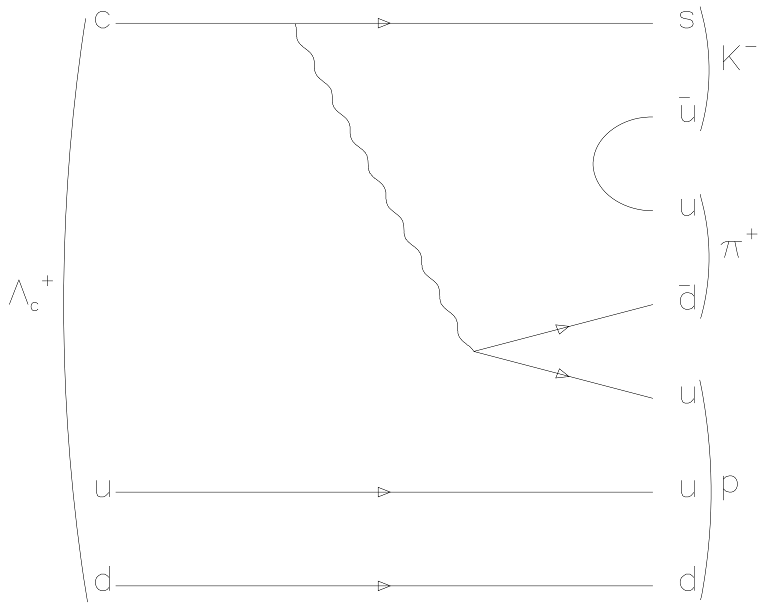

Figure 2.2: A spectator diagram for $\Lambda_c^+ \to \mathrm{pK}^-\pi^+$ nonresonant decay.

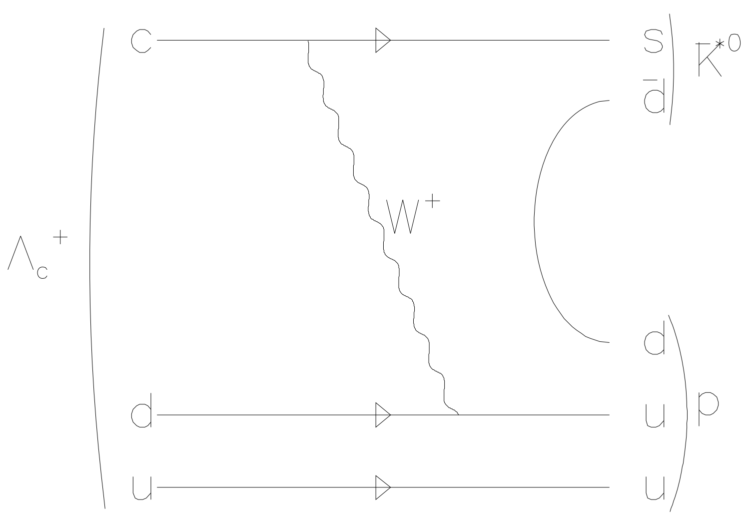

Figure 2.3: An exchange diagram for $\Lambda_c^+ \to \overline{\mathrm{K}}^{*0}(\to \mathrm{K}^-\pi^+)\mathrm{p}$ resonant decay.

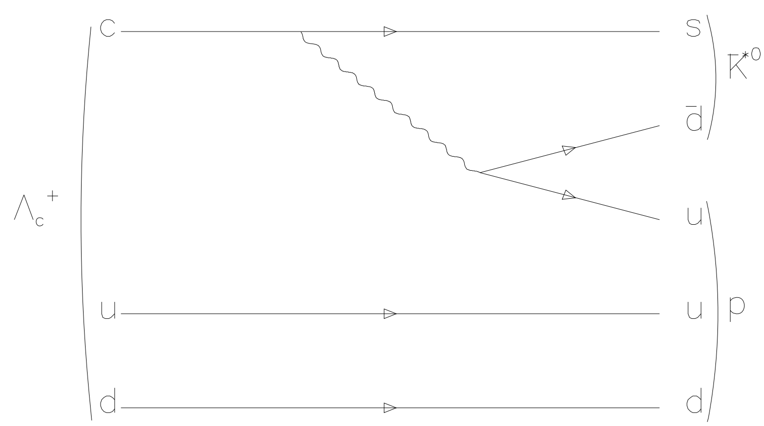

Figure 2.4: A spectator diagram for $\Lambda_c^+ \to \overline{K}^{*0}(\to K^- \pi^+)p$ resonant decay.

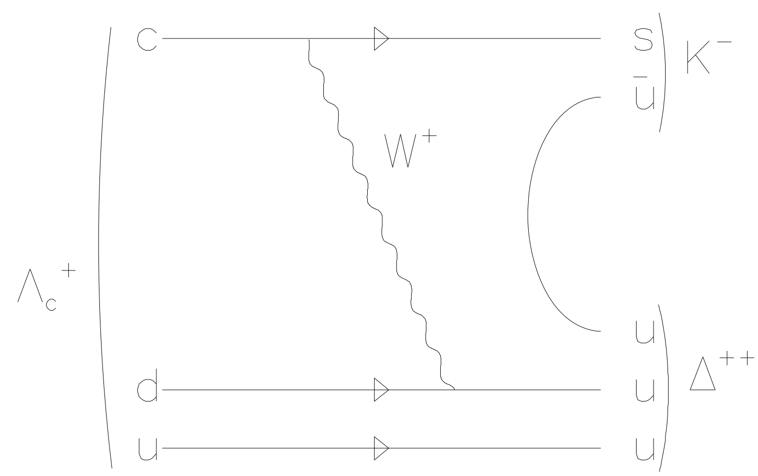

Figure 2.5: An exchange diagram for $\Lambda_c^+ \to \Delta^{++}(\to p\pi^+)K^-$ resonant decay.

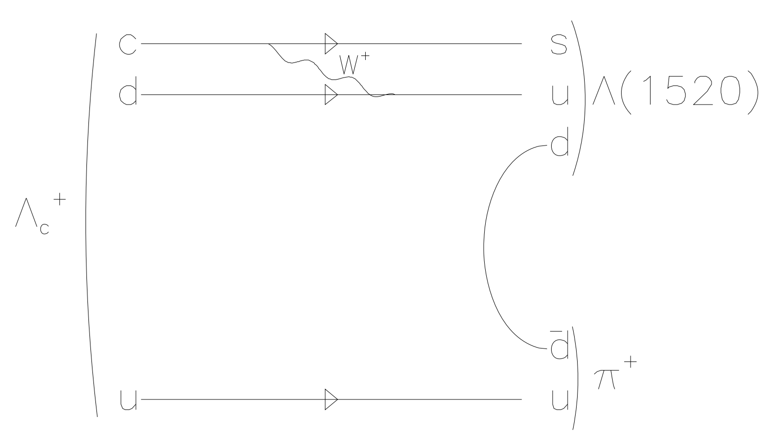

Figure 2.6: An exchange diagram for $\Lambda_c^+ \to \Lambda(1520)(\to pK^-)\pi^+$ resonant decay.

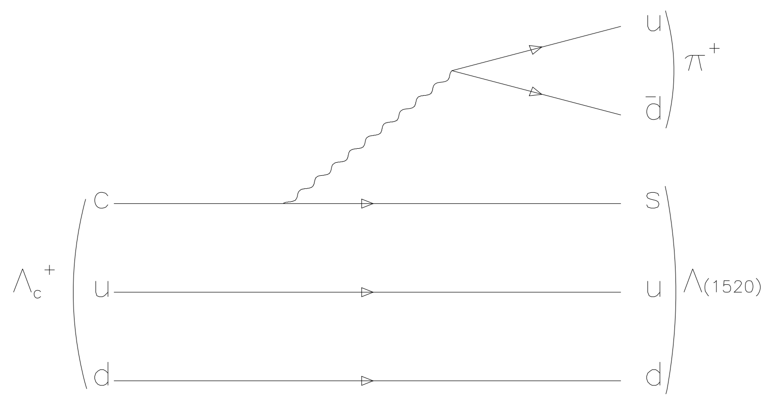

Figure 2.7: A spectator diagram for $\Lambda_c^+ \to \Lambda(1520)(\to pK^-)\pi^+$ resonant decay.

2.2 Helicity Formalism

In conducting any analysis involving particle interaction, one must first choose an appropriate basis in which to operate.[Hab 94] The traditional basis states involve simultaneous eigenstates of $\vec{J}^2$, J_z, $\vec{L}^2$, and $\vec{S}^2$ or simultaneous eigenstates of $\vec{L}^2$, L_z, $\vec{S}^2$, and S_z.*It is also relatively simple to go between one and the other through the use the Clebsch-Gordon coefficients. However, a different basis - the helicity basis - has certain advantages over the two previously mentioned, in that the helicity states are

1. invariant under spatial rotations,
2. invariant under a boost in the direction of the particle's momentum (therefore, we can work in the rest frame of the Λ_c), and
3. convenient for describing both massive and massless particles.

In this basis state, one can construct simultaneous eigenstates of $\vec{J}^2$, J_z, Λ_1 and Λ_2 where Λ is the helicity operator (with eigenvalue λ) defined by

$$\Lambda = \vec{S} \cdot \hat{p} \tag{2.1}$$

where $\hat{p}$ = the direction of the particle's linear momentum. As implied in equation 2.1, helicity is just the component of the spin in the direction of the particle's linear momentum.

2.2.1 Two Body Decay

Generalization: A→BC

If particle A decays into two particles, B and C, which can also be written as A→BC and seen in figure 2.8, then the differential decay rate, dΓ, can be written using Fermi's Golden Rule[PDG 98]

* $\vec{J} = \vec{L} + \vec{S}$ is the total angular momentum operator of the particle with eigenvalue j, J_z is the projection operator of the total angular momentum on some arbitrary z-axis with eigenvalue m_j, $\vec{L}$ is the orbital angular momentum operator with eigenvalue l, L_z is its projection operator on the z-axis with eigenvalue m_l, $\vec{S}$ is the intrinsic spin operator of the particle with eigenvalue s, and S_z is its projection operator on the z-axis with eigenvalue m_s.

as

$$\mathrm{d}\Gamma = \frac{(2\pi)^4}{2\mathrm{M}}|\mathcal{M}|^2 \mathrm{d}\Phi_{\mathrm{n}} \tag{2.2}$$

where M is the mass of the parent particle (which is constant in our case after the mass constraint is enforced), $\mathrm{d}\Phi_{\mathrm{n}}$ is an element of n-body phase space, and and $\mathcal{M}$ is the transition amplitude. With an appropriate set of coordinates for phase space, which in the case of this analysis is two two-body masses and three decay angles (as can be seen in more detail in chapter 7), $\mathrm{d}\Phi_{\mathrm{n}}$ can be constant within the kinematic boundaries. Thus $\mathrm{d}\Gamma$ can be expressed as

$$\mathrm{d}\Gamma \sim |\mathcal{M}|^2 = |\langle \mathrm{f}|\mathrm{T}|\mathrm{i}\rangle|^2 = |\langle \mathrm{BC}|\mathrm{T}|\mathrm{A}\rangle|^2 \tag{2.3}$$

where T = the transition operator, and $|\langle \mathrm{BC}|\mathrm{T}|\mathrm{A}\rangle|^2$ is the probability that A will decay into BC.

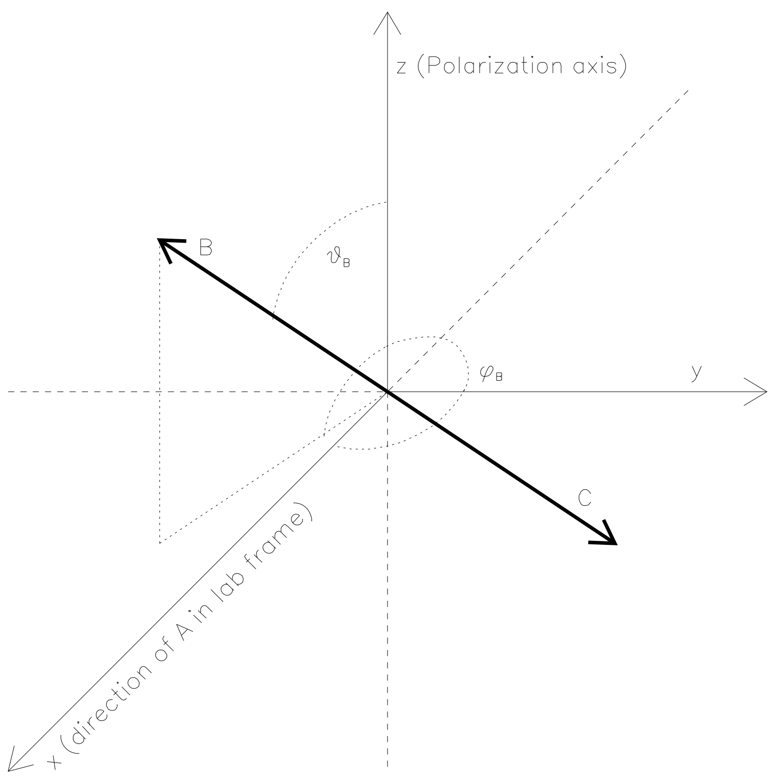

Figure 2.8: A view of the decay A→BC in the A rest frame.

In the rest frame of A, let m_{A} be the projection of the spin of A, j_{A}, along the z-axis. We denote the spin part of $|\mathrm{A}\rangle$ as $|j_{\mathrm{A}} m_{\mathrm{A}}\rangle$. In the rest frame of A, B is traveling in the $(\theta_{\mathrm{B}}, \phi_{\mathrm{B}})$ direction, and thus C must be traveling in the $(\pi - \theta_{\mathrm{B}}, \phi_{\mathrm{B}} + \pi)$ direction. If the helicities of B and C are λ_{B} and λ_{C}, then we can denote the spin part of $|\mathrm{BC}\rangle$ as $|\theta_{\mathrm{B}}\phi_{\mathrm{B}}\lambda_{\mathrm{B}}\lambda_{\mathrm{C}}\rangle$. Thus, we can write

$$\langle f|T|i\rangle = \langle \theta_{\mathrm{B}}\phi_{\mathrm{B}}\lambda_{\mathrm{B}}\lambda_{\mathrm{C}}|T|j_{\mathrm{A}} m_{\mathrm{A}}\rangle \tag{2.4}$$

Since $\langle \theta_{\mathrm{B}}\phi_{\mathrm{B}}\lambda_{\mathrm{B}}\lambda_{\mathrm{C}}|$ is not an eigenstate of $\vec{J}^2$ or J_{z}, we need to construct a relationship which can relate $|\mathrm{BC}\rangle$ in its plane wave helicity state, $|\theta_{\mathrm{B}}\phi_{\mathrm{B}}\lambda_{\mathrm{B}}\lambda_{\mathrm{C}}\rangle$, to its spherical wave state, $|JM\lambda_{\mathrm{B}}\lambda_{\mathrm{C}}\rangle$. As seen in [Per 74, p.228], this can be written as

$$|\theta_{\rm B}\phi_{\rm B}\lambda_{\rm B}\lambda_{\rm C}\rangle = \sum_{JM}\sqrt{\frac{2J+1}{4\pi}}{\rm D}^{\rm J}_{{\rm M}\lambda_1}(\phi_{\rm B},\theta_{\rm B},-\phi_{\rm B})|{\rm JM}\lambda_{\rm B}\lambda_{\rm C}\rangle \tag{2.5}$$

where λ_1 = the total helicity of B and C = $\lambda_{\rm B} - \lambda_{\rm C}$, and J and M = the total angular momentum and its projection of $|{\rm BC}\rangle$. If we combine equations 2.4 and 2.5, we get

$$\langle f|T|i\rangle = \sum_{JM}\sqrt{\frac{2J+1}{4\pi}}{\rm D}^{\rm J*}_{{\rm M}\lambda_1}(\phi_{\rm B},\theta_{\rm B},-\phi_{\rm B})\langle{\rm JM}\lambda_{\rm B}\lambda_{\rm C}|{\rm T}|{\rm j_A m_A}\rangle \tag{2.6}$$

Since angular momentum must be conserved, $J = j_{\rm A}$ and $M = m_{\rm A}$, and thus

$$\langle f|T|i\rangle = \sqrt{\frac{2j_{\rm A}+1}{4\pi}}{\rm D}^{\rm j_A*}_{{\rm m_A}\lambda_1}(\phi_{\rm B},\theta_{\rm B},-\phi_{\rm B})\langle\lambda_{\rm B}\lambda_{\rm C}|{\rm T}|{\rm m_A}\rangle \tag{2.7}$$

where $|\lambda_1| \leq |m_{\rm A}|$. ${\rm D}^{\rm j_A}_{{\rm m_A}\lambda}(\phi,\theta,-\phi)$ is the rotation matrix where

$$\begin{aligned} {\rm D}^{\rm j}_{{\rm m}\lambda}(\phi,\theta,-\phi) &= {\rm e}^{-{\rm i}\phi{\rm m}}\langle{\rm m}|{\rm e}^{-{\rm i}\theta{\rm J_y}}|\lambda\rangle{\rm e}^{-{\rm i}(-\phi)\lambda} & (2.8)\\ &= {\rm e}^{-{\rm i}({\rm m}-\lambda)\phi}{\rm d}^{\rm j}_{{\rm m}\lambda}(\theta) & (2.9)\end{aligned}$$

where ${\rm d}^{\rm j}_{{\rm m}\lambda}(\theta)$ is a d-matrix which can be found in [PDG 98].

Therefore equation 2.7 becomes

$$\langle f|T|i\rangle = \sqrt{\frac{2j_{\rm A}+1}{4\pi}}{\rm e}^{{\rm i}({\rm m_A}-\lambda_1)\phi_{\rm B}}{\rm d}^{\rm j_A}_{{\rm m_A}\lambda_1}(\theta_{\rm B})\langle\lambda_{\rm B}\lambda_{\rm C}|{\rm T}|{\rm m_A}\rangle \tag{2.10}$$

Since $\langle\lambda_{\rm B}\lambda_{\rm C}|T|i\rangle$ is just some transition constant, it can be absorbed into the initial coefficient and the following simplification is produced:

$${\rm d}\Gamma \sim |\alpha_{\lambda_{\rm B}\lambda_{\rm C}}{\rm e}^{{\rm i}({\rm m_A}-\lambda_1)\phi_{\rm B}}{\rm d}^{\rm j_A}_{{\rm m_A}\lambda_1}(\theta_{\rm B})|^2 \tag{2.11}$$

where $\alpha_{\lambda_{\rm B}\lambda_{\rm C}}$ is the complex coefficient for that decay amplitude. Note that $\alpha_{\lambda_{\rm B}\lambda_{\rm C}}$ is implicitly a function of $j_{\rm A}$, and thus we could have written the coefficient as $\alpha^{j_{\rm A}}_{\lambda_{\rm B}\lambda_{\rm C}}$, but since $j_{\rm A}$ is a constant, we chose not to write it for convenience. Also note that $\alpha_{\lambda_{\rm B}\lambda_{\rm C}}$ is not dependent on $m_{\rm A}$, because it was fixed in equation 2.7.

If we want the full differential decay rate for all combinations of the spin projection of A and helicities of B and C, equation 2.11 becomes

$${\rm d}\Gamma \sim \sum_{\rm m_A}\sum_{\lambda_{\rm B}\lambda_{\rm C}}|\alpha_{\lambda_{\rm B}\lambda_{\rm C}}{\rm e}^{{\rm i}({\rm m_A}-\lambda_1)\phi_{\rm B}}{\rm d}^{\rm j_A}_{{\rm m_A}\lambda_1}(\theta_{\rm B})|^2 \tag{2.12}$$

particle	j^P
Λ_c	$\frac{1}{2}^+$
$\overline{\mathrm{K}}^{*0}$	1^-
p	$\frac{1}{2}^+$

Table 2.1: Particles, spins, and parities for the example decay.

Λ_c m_{Λ_c}	p λ_C	$\overline{\mathrm{K}}^{*0}$ λ_B	λ_1	amplitude
$\frac{1}{2}$	$\frac{1}{2}$	1	$\frac{1}{2}$	$\alpha_{\frac{1}{2}1} e^{i(\frac{1}{2}-\frac{1}{2})\phi_{\overline{K}^{*0}}} d^{\frac{1}{2}}_{\frac{1}{2}\frac{1}{2}}(\theta_{\overline{K}^{*0}}) = \alpha_{\frac{1}{2}1} d^{\frac{1}{2}}_{\frac{1}{2}\frac{1}{2}}(\theta_{\overline{K}^{*0}})$
$\frac{1}{2}$	$\frac{1}{2}$	0	-$\frac{1}{2}$	$\alpha_{\frac{1}{2}0} e^{i(\frac{1}{2}+\frac{1}{2})\phi_{\overline{K}^{*0}}} d^{\frac{1}{2}}_{\frac{1}{2}-\frac{1}{2}}(\theta_{\overline{K}^{*0}}) = \alpha_{\frac{1}{2}0} e^{i\phi_{\overline{K}^{*0}}} d^{\frac{1}{2}}_{\frac{1}{2}-\frac{1}{2}}(\theta_{\overline{K}^{*0}})$
$\frac{1}{2}$	$\frac{1}{2}$	-1	-$\frac{3}{2}$	forbidden
$\frac{1}{2}$	-$\frac{1}{2}$	1	$\frac{3}{2}$	forbidden
$\frac{1}{2}$	-$\frac{1}{2}$	0	$\frac{1}{2}$	$\alpha_{-\frac{1}{2}0} e^{i(\frac{1}{2}-\frac{1}{2})\phi_{\overline{K}^{*0}}} d^{\frac{1}{2}}_{\frac{1}{2}\frac{1}{2}}(\theta_{\overline{K}^{*0}}) = \alpha_{-\frac{1}{2}0} d^{\frac{1}{2}}_{\frac{1}{2}\frac{1}{2}}(\theta_{\overline{K}^{*0}})$
$\frac{1}{2}$	-$\frac{1}{2}$	-1	-$\frac{1}{2}$	$\alpha_{-\frac{1}{2}-1} e^{i(\frac{1}{2}+\frac{1}{2})\phi_{\overline{K}^{*0}}} d^{\frac{1}{2}}_{\frac{1}{2}-\frac{1}{2}}(\theta_{\overline{K}^{*0}}) = \alpha_{-\frac{1}{2}-1} e^{i\phi_{\overline{K}^{*0}}} d^{\frac{1}{2}}_{\frac{1}{2}-\frac{1}{2}}(\theta_{\overline{K}^{*0}})$
-$\frac{1}{2}$	$\frac{1}{2}$	1	$\frac{1}{2}$	$\alpha_{\frac{1}{2}1} e^{i(-\frac{1}{2}-\frac{1}{2})\phi_{\overline{K}^{*0}}} d^{\frac{1}{2}}_{-\frac{1}{2}\frac{1}{2}}(\theta_{\overline{K}^{*0}}) = \alpha_{\frac{1}{2}1} e^{-i\phi_{\overline{K}^{*0}}} d^{\frac{1}{2}}_{-\frac{1}{2}\frac{1}{2}}(\theta_{\overline{K}^{*0}})$
-$\frac{1}{2}$	$\frac{1}{2}$	0	-$\frac{1}{2}$	$\alpha_{\frac{1}{2}0} e^{i(-\frac{1}{2}+\frac{1}{2})\phi_{\overline{K}^{*0}}} d^{\frac{1}{2}}_{-\frac{1}{2}-\frac{1}{2}}(\theta_{\overline{K}^{*0}}) = \alpha_{\frac{1}{2}0} d^{\frac{1}{2}}_{-\frac{1}{2}-\frac{1}{2}}(\theta_{\overline{K}^{*0}})$
-$\frac{1}{2}$	$\frac{1}{2}$	-1	-$\frac{3}{2}$	forbidden
-$\frac{1}{2}$	-$\frac{1}{2}$	1	$\frac{3}{2}$	forbidden
-$\frac{1}{2}$	-$\frac{1}{2}$	0	$\frac{1}{2}$	$\alpha_{-\frac{1}{2}0} e^{i(-\frac{1}{2}-\frac{1}{2})\phi_{\overline{K}^{*0}}} d^{\frac{1}{2}}_{-\frac{1}{2}\frac{1}{2}}(\theta_{\overline{K}^{*0}}) = \alpha_{-\frac{1}{2}0} e^{-i\phi_{\overline{K}^{*0}}} d^{\frac{1}{2}}_{-\frac{1}{2}\frac{1}{2}}(\theta_{\overline{K}^{*0}})$
-$\frac{1}{2}$	-$\frac{1}{2}$	-1	-$\frac{1}{2}$	$\alpha_{-\frac{1}{2}-1} e^{i(-\frac{1}{2}+\frac{1}{2})\phi_{\overline{K}^{*0}}} d^{\frac{1}{2}}_{-\frac{1}{2}-\frac{1}{2}}(\theta_{\overline{K}^{*0}}) = \alpha_{-\frac{1}{2}-1} d^{\frac{1}{2}}_{-\frac{1}{2}-\frac{1}{2}}(\theta_{\overline{K}^{*0}})$

Table 2.2: Possible helicity combinations.

Example: $\Lambda_c^+ \to \overline{\mathrm{K}}^{*0}\mathrm{p}$

If $\Lambda_c^+ \to \mathrm{p}\overline{\mathrm{K}}^{*0}$, $\mathrm{d}\Gamma$ would be calculated by the following means. First we need to establish the spins and parities of the particles, as can be seen in table 2.1.

Then looking at all 12 helicity combinations we get table 2.2.

Therefore,

$$\begin{aligned}
\mathrm{d}\Gamma &\sim |\alpha_{\frac{1}{2}1}\mathrm{d}^{\frac{1}{2}}_{\frac{1}{2}\frac{1}{2}}(\theta_{\overline{\mathrm{K}}^{*0}})|^2 + |\alpha_{\frac{1}{2}0}\mathrm{e}^{\mathrm{i}\phi_{\overline{\mathrm{K}}^{*0}}}\mathrm{d}^{\frac{1}{2}}_{\frac{1}{2}-\frac{1}{2}}(\theta_{\overline{\mathrm{K}}^{*0}})|^2 \\
&+ |\alpha_{-\frac{1}{2}0}\mathrm{d}^{\frac{1}{2}}_{\frac{1}{2}\frac{1}{2}}(\theta_{\overline{\mathrm{K}}^{*0}})|^2 + |\alpha_{-\frac{1}{2}-1}\mathrm{e}^{\mathrm{i}\phi_{\overline{\mathrm{K}}^{*0}}}\mathrm{d}^{\frac{1}{2}}_{\frac{1}{2}-\frac{1}{2}}(\theta_{\overline{\mathrm{K}}^{*0}})|^2 \\
&+ |\alpha_{\frac{1}{2}1}\mathrm{e}^{-\mathrm{i}\phi_{\overline{\mathrm{K}}^{*0}}}\mathrm{d}^{\frac{1}{2}}_{-\frac{1}{2}\frac{1}{2}}(\theta_{\overline{\mathrm{K}}^{*0}})|^2 + |\alpha_{\frac{1}{2}0}\mathrm{d}^{\frac{1}{2}}_{-\frac{1}{2}-\frac{1}{2}}(\theta_{\overline{\mathrm{K}}^{*0}})|^2 \\
&+ |\alpha_{-\frac{1}{2}0}\mathrm{e}^{-\mathrm{i}\phi_{\overline{\mathrm{K}}^{*0}}}\mathrm{d}^{\frac{1}{2}}_{-\frac{1}{2}\frac{1}{2}}(\theta_{\overline{\mathrm{K}}^{*0}})|^2 + |\alpha_{-\frac{1}{2}-1}\mathrm{d}^{\frac{1}{2}}_{-\frac{1}{2}-\frac{1}{2}}(\theta_{\overline{\mathrm{K}}^{*0}})|^2
\end{aligned}$$

2.2.2 Three Body Decay

Generalization: A→B(→DE)C

In the case of three body resonant decay, such as A→B(→DE)C,

$$\mathrm{d}\Gamma \sim |\langle \mathrm{DE}|\mathrm{T}_2|\mathrm{B}\rangle\langle \mathrm{BC}|\mathrm{T}_1|\mathrm{A}\rangle|^2 \tag{2.13}$$

$\langle \mathrm{BC}|\mathrm{T}_1|\mathrm{A}\rangle$ is calculated the same as way as in section 2.2.1. In order to calculate $\langle \mathrm{DE}|\mathrm{T}_2|\mathrm{B}\rangle$, note that in a particle's rest frame, its helicity state coincides with its spin state, therefore if we analyze $\langle \mathrm{DE}|\mathrm{T}_2|\mathrm{B}\rangle$ in B's rest frame and set the z'-axis to be in the $(\theta_\mathrm{B}, \phi_\mathrm{B})$ direction, we can treat $\lambda_\mathrm{B} = m_{j_\mathrm{B}}$. Therefore

$$\langle \mathrm{DE}|\mathrm{T}_2|\mathrm{B}\rangle = \sqrt{\frac{2\mathrm{j}_\mathrm{B}+1}{4\pi}}\mathrm{e}^{\mathrm{i}(\lambda_\mathrm{B}-\lambda_2)\phi_\mathrm{D}}\mathrm{d}^{\mathrm{j}_\mathrm{B}}_{\lambda_\mathrm{B}\lambda_2}(\theta_\mathrm{D})\langle \lambda_\mathrm{D}\lambda_\mathrm{E}|\mathrm{T}_2|\mathrm{B}\rangle \tag{2.14}$$

which, when combined with equation 2.10 and simplified by combining constants and coefficients, yields equation 2.15.

$$\mathrm{d}\Gamma \sim \sum_{\mathrm{m_A}}\sum_{\lambda_\mathrm{C}\lambda_\mathrm{D}\lambda_\mathrm{E}}|\sum_{\lambda_\mathrm{B}}\alpha_{\lambda_\mathrm{B}\lambda_\mathrm{C}}\alpha_{\lambda_\mathrm{D}\lambda_\mathrm{E}}\mathrm{e}^{\mathrm{i}(\mathrm{m_A}-\lambda_1)\phi_\mathrm{B}}\mathrm{e}^{\mathrm{i}(\lambda_\mathrm{B}-\lambda_2)\phi_\mathrm{D}}\mathrm{d}^{\mathrm{j_A}}_{\mathrm{m_A}\lambda_1}(\theta_\mathrm{B})\mathrm{d}^{\mathrm{j_B}}_{\lambda_\mathrm{B}\lambda_2}(\theta_\mathrm{D})|^2 \tag{2.15}$$

where $\lambda_1 = \lambda_\mathrm{B} - \lambda_\mathrm{C}$, $(\theta_\mathrm{B}, \phi_\mathrm{B})$ describes the direction particle B is going after the first decay in A's rest frame with the z-axis perpendicular to the plane of production, and $\lambda_2 = \lambda_\mathrm{D} - \lambda_\mathrm{E}$, $(\theta_\mathrm{D}, \phi_\mathrm{D})$ describes the direction particle D is doing after the second decay in B's rest frame with the z'-axis in the $(\theta_\mathrm{B}, \phi_\mathrm{B})$ direction, and $\mathrm{j_B}$ is the intrinsic spin of the resonant particle. See figures 8.1 and 8.2 for an example of the definition of these angles in the case of $\Lambda_c^+ \to \overline{\mathrm{K}}^{*0}(\to \mathrm{K}^-\pi^+)\,\mathrm{p}$.

Simplifying the written expression for equation 2.15 by setting

$$\xi_{B,\mathrm{m_A},\lambda_\mathrm{B},\lambda_\mathrm{C},\lambda_\mathrm{D},\lambda_\mathrm{E}} = \alpha_{\lambda_\mathrm{B}\lambda_\mathrm{C}}\alpha_{\lambda_\mathrm{D}\lambda_\mathrm{E}}\mathrm{e}^{\mathrm{i}(\mathrm{m_A}-\lambda_1)\phi_\mathrm{B}}\mathrm{e}^{\mathrm{i}(\lambda_\mathrm{B}-\lambda_2)\phi_\mathrm{D}}\mathrm{d}^{\mathrm{j_A}}_{\mathrm{m_A}\lambda_1}(\theta_\mathrm{B})\mathrm{d}^{\mathrm{j_B}}_{\lambda_\mathrm{B}\lambda_2}(\theta_\mathrm{D}) \tag{2.16}$$

yields

$$\mathrm{d}\Gamma \sim \sum_{\mathrm{m_A}}\sum_{\lambda_\mathrm{C}\lambda_\mathrm{D}\lambda_\mathrm{E}}|\sum_{\lambda_\mathrm{B}}\xi_{\mathrm{B},\mathrm{m_A},\lambda_\mathrm{B},\lambda_\mathrm{C},\lambda_\mathrm{D},\lambda_\mathrm{E}}|^2 \tag{2.17}$$

In order to account for the ill-defined mass of the resonant particle, a relativistic Breit-Wigner amplitude multiplies each term, so equation 2.17 becomes

$$\mathrm{d}\Gamma \sim \sum_{\mathrm{m_A}} \sum_{\lambda_\mathrm{C}\lambda_\mathrm{D}\lambda_\mathrm{E}} |\sum_{\lambda_\mathrm{B}} \mathrm{BW}(\mathrm{m_B})\xi_{\mathrm{B},\mathrm{m_A},\lambda_\mathrm{C},\lambda_\mathrm{D},\lambda_\mathrm{E}}|^2 \tag{2.18}$$

where m_B is the two body mass of the resonant particle.

If there is more than one resonance, then equation 2.18 becomes

$$\mathrm{d}\Gamma \sim \sum_{\mathrm{m_A}} \sum_{\lambda_\mathrm{C}\lambda_\mathrm{D}\lambda_\mathrm{E}} |\sum_{\lambda_\mathrm{B}} \sum_{\mathrm{B}} \mathrm{BW}(\mathrm{m_B})\xi_{\mathrm{B},\mathrm{m_A},\lambda_\mathrm{C},\lambda_\mathrm{D},\lambda_\mathrm{E}}|^2 \tag{2.19}$$

Example: $\Lambda_\mathrm{c}^+ \to \overline{\mathrm{K}}^{*0} (\to \mathrm{K}^-\pi^+)\,\mathrm{p}$

For example, if $\Lambda_\mathrm{c}^+ \to \overline{\mathrm{K}}^{*0} (\to \mathrm{K}^-\pi^+)\,\mathrm{p}$, $\mathrm{d}\Gamma$ would be calculated in a similar fashion to above, noting that K and π are both spin 0 particles, so the summation over their helicities becomes greatly simplified, as well as $\alpha_{\lambda_\mathrm{D}\lambda_\mathrm{E}} = \alpha_{\lambda_\mathrm{K}\lambda_\pi} = \alpha_{00}$ which can be absorbed into an overall coefficient.

Applying the simplifications, equation 2.18 reduces to

$$\mathrm{d}\Gamma \sim \sum_{\mathrm{m}_{\Lambda_\mathrm{c}}} \sum_{\lambda_\mathrm{p}} |\sum_{\lambda_{\overline{\mathrm{K}}^{*0}}} \mathrm{BW}(\mathrm{m}_{\overline{\mathrm{K}}^{*0}})\alpha_{\lambda_{\overline{\mathrm{K}}^{*0}}\lambda_\mathrm{p}} \mathrm{e}^{\mathrm{i}(\mathrm{m}_{\Lambda_\mathrm{c}}-\lambda_1)\phi_{\overline{\mathrm{K}}^{*0}}+\mathrm{i}(\lambda_{\overline{\mathrm{K}}^{*0}})\phi_\mathrm{K}} \mathrm{d}^{\frac{1}{2}}_{\mathrm{m}_{\Lambda_\mathrm{c}}\lambda_1}(\theta_{\overline{\mathrm{K}}^{*0}}) \mathrm{d}^{\mathrm{j}_{\overline{\mathrm{K}}^{*0}}}_{\lambda_{\overline{\mathrm{K}}^{*0}}0}(\theta_\mathrm{K})|^2 \tag{2.20}$$

Λ_c m	p λ_C	$\overline{\mathrm{K}}^{*0}$ λ_B	λ_1	amplitude
$\frac{1}{2}$	$\frac{1}{2}$	1	$\frac{1}{2}$	$\alpha_{\frac{1}{2}1}\mathrm{e}^{\mathrm{i}\phi_\mathrm{K}}\mathrm{d}^{\frac{1}{2}}_{\frac{1}{2}\frac{1}{2}}(\theta_{\overline{\mathrm{K}}^{*0}})\mathrm{d}^1_{10}(\theta_\mathrm{K})$
$\frac{1}{2}$	$\frac{1}{2}$	0	-$\frac{1}{2}$	$\alpha_{\frac{1}{2}0}\mathrm{e}^{\mathrm{i}\phi_{\overline{\mathrm{K}}^{*0}}}\mathrm{d}^{\frac{1}{2}}_{\frac{1}{2}-\frac{1}{2}}(\theta_{\overline{\mathrm{K}}^{*0}})\mathrm{d}^1_{00}(\theta_\mathrm{K})$
$\frac{1}{2}$	$\frac{1}{2}$	-1	-$\frac{3}{2}$	forbidden
$\frac{1}{2}$	-$\frac{1}{2}$	1	$\frac{3}{2}$	forbidden
$\frac{1}{2}$	-$\frac{1}{2}$	0	$\frac{1}{2}$	$\alpha_{-\frac{1}{2}0}\mathrm{d}^{\frac{1}{2}}_{\frac{1}{2}\frac{1}{2}}(\theta_{\overline{\mathrm{K}}^{*0}})\mathrm{d}^1_{00}(\theta_\mathrm{K})$
$\frac{1}{2}$	-$\frac{1}{2}$	-1	-$\frac{1}{2}$	$\alpha_{-\frac{1}{2}-1}\mathrm{e}^{\mathrm{i}(\phi_{\overline{\mathrm{K}}^{*0}}-\phi_\mathrm{K})}\mathrm{d}^{\frac{1}{2}}_{\frac{1}{2}-\frac{1}{2}}(\theta_{\overline{\mathrm{K}}^{*0}})\mathrm{d}^1_{-10}(\theta_\mathrm{K})$
-$\frac{1}{2}$	$\frac{1}{2}$	1	$\frac{1}{2}$	$\alpha_{\frac{1}{2}1}\mathrm{e}^{-\mathrm{i}(\phi_{\overline{\mathrm{K}}^{*0}}-\phi_\mathrm{K})}\mathrm{d}^{\frac{1}{2}}_{-\frac{1}{2}\frac{1}{2}}(\theta_{\overline{\mathrm{K}}^{*0}})\mathrm{d}^1_{10}(\theta_\mathrm{K})$
-$\frac{1}{2}$	$\frac{1}{2}$	0	-$\frac{1}{2}$	$\alpha_{\frac{1}{2}0}\mathrm{d}^{\frac{1}{2}}_{-\frac{1}{2}-\frac{1}{2}}(\theta_{\overline{\mathrm{K}}^{*0}})\mathrm{d}^1_{00}(\theta_\mathrm{K})$
-$\frac{1}{2}$	$\frac{1}{2}$	-1	-$\frac{3}{2}$	forbidden
-$\frac{1}{2}$	-$\frac{1}{2}$	1	$\frac{3}{2}$	forbidden
-$\frac{1}{2}$	-$\frac{1}{2}$	0	$\frac{1}{2}$	$\alpha_{-\frac{1}{2}0}\mathrm{e}^{-\mathrm{i}\phi_{\overline{\mathrm{K}}^{*0}}}\mathrm{d}^{\frac{1}{2}}_{-\frac{1}{2}\frac{1}{2}}(\theta_{\overline{\mathrm{K}}^{*0}})\mathrm{d}^1_{00}(\theta_\mathrm{K})$
-$\frac{1}{2}$	-$\frac{1}{2}$	-1	-$\frac{1}{2}$	$\alpha_{-\frac{1}{2}-1}\mathrm{e}^{-\mathrm{i}\phi_\mathrm{K}}\mathrm{d}^{\frac{1}{2}}_{-\frac{1}{2}-\frac{1}{2}}(\theta_{\overline{\mathrm{K}}^{*0}})\mathrm{d}^1_{-10}(\theta_\mathrm{K})$

Table 2.3: Possible helicity combinations.

Therefore,

$$\mathrm{d}\Gamma \;\sim\; |BW(m_{\overline{\mathrm{K}}^{*0}})\alpha_{\frac{1}{2}1}\mathrm{e}^{\mathrm{i}\phi_\mathrm{K}}\mathrm{d}^{\frac{1}{2}}_{\frac{1}{2}\frac{1}{2}}(\theta_{\overline{\mathrm{K}}^{*0}})\mathrm{d}^1_{10}(\theta_\mathrm{K}) +$$

$$
\begin{aligned}
& BW(m_{\overline{\mathrm{K}}^{*0}})\alpha_{\frac{1}{2}0}\mathrm{e}^{\mathrm{i}\phi_{\overline{\mathrm{K}}^{*0}}}\mathrm{d}^{\frac{1}{2}}_{\frac{1}{2}-\frac{1}{2}}(\theta_{\overline{\mathrm{K}}^{*0}})\mathrm{d}^{1}_{00}(\theta_{\mathrm{K}})|^2 \\
+ \quad & |BW(m_{\overline{\mathrm{K}}^{*0}})\alpha_{-\frac{1}{2}0}\mathrm{d}^{\frac{1}{2}}_{\frac{1}{2}\frac{1}{2}}(\theta_{\overline{\mathrm{K}}^{*0}})\mathrm{d}^{1}_{00}(\theta_{\mathrm{K}}) + \\
& BW(m_{\overline{\mathrm{K}}^{*0}})\alpha_{-\frac{1}{2}-1}\mathrm{e}^{\mathrm{i}(\phi_{\overline{\mathrm{K}}^{*0}}-\phi_{\mathrm{K}})}\mathrm{d}^{\frac{1}{2}}_{\frac{1}{2}-\frac{1}{2}}(\theta_{\overline{\mathrm{K}}^{*0}})\mathrm{d}^{1}_{-10}(\theta_{\mathrm{K}})|^2 \\
+ \quad & |BW(m_{\overline{\mathrm{K}}^{*0}})\alpha_{\frac{1}{2}1}\mathrm{e}^{-\mathrm{i}(\phi_{\overline{\mathrm{K}}^{*0}}-\phi_{\mathrm{K}})}\mathrm{d}^{\frac{1}{2}}_{-\frac{1}{2}\frac{1}{2}}(\theta_{\overline{\mathrm{K}}^{*0}})\mathrm{d}^{1}_{10}(\theta_{\mathrm{K}}) + \\
& BW(m_{\overline{\mathrm{K}}^{*0}})\alpha_{\frac{1}{2}0}\mathrm{d}^{\frac{1}{2}}_{-\frac{1}{2}-\frac{1}{2}}(\theta_{\overline{\mathrm{K}}^{*0}})\mathrm{d}^{1}_{00}(\theta_{\mathrm{K}})|^2 \\
+ \quad & |BW(m_{\overline{\mathrm{K}}^{*0}})\alpha_{-\frac{1}{2}0}\mathrm{e}^{-\mathrm{i}\phi_{\overline{\mathrm{K}}^{*0}}}\mathrm{d}^{\frac{1}{2}}_{-\frac{1}{2}\frac{1}{2}}(\theta_{\overline{\mathrm{K}}^{*0}})\mathrm{d}^{1}_{00}(\theta_{\mathrm{K}}) + \\
& BW(m_{\overline{\mathrm{K}}^{*0}})\alpha_{-\frac{1}{2}-1}\mathrm{e}^{-\mathrm{i}\phi_{\mathrm{K}}}\mathrm{d}^{\frac{1}{2}}_{-\frac{1}{2}-\frac{1}{2}}(\theta_{\overline{\mathrm{K}}^{*0}})\mathrm{d}^{1}_{-10}(\theta_{\mathrm{K}})|^2
\end{aligned}
$$

Adding other resonances to the equation is done in the same manner where the two body mass is incorporated into a relativistic Breit-Wigner amplitude which multiplies each term. Finally, to analyze this decay, we would fit for the α coefficients.

2.3 Parity Conservation

In parity conserving decays, the relationship between the coefficients can be expressed as

$$\alpha_{\lambda_{\mathrm{D}}\lambda_{\mathrm{E}}} = (-1)^{s_{\mathrm{D}}+s_{\mathrm{E}}-j_{\mathrm{B}}}\eta_{\mathrm{B}}\eta_{\mathrm{D}}\eta_{\mathrm{E}}\alpha_{-\lambda_{\mathrm{D}}-\lambda_{\mathrm{E}}} \tag{2.21}$$

where η is the intrinsic parity of the particle.

Although the initial Λ_{c} decay is a weak decay and parity is not conserved, the secondary decay is strong, therefore parity is conserved. Using the parity relationship in equation 2.21, we can deduce that

$$\alpha_{\lambda_\pi\lambda_{\mathrm{K}}} = (-1)^{s_\pi+s_{\mathrm{K}}-j_{\overline{\mathrm{K}}^{*0}}}\eta_{\overline{\mathrm{K}}^{*0}}\eta_\pi\eta_{\mathrm{K}}\alpha_{-\lambda_\pi-\lambda_{\mathrm{K}}} \tag{2.22}$$

More specifically, this reduces to

$$\alpha_{\lambda_\pi\lambda_{\mathrm{K}}} = (-1)^{0+0-1}(-1)(-1)(-1)\alpha_{-\lambda_\pi-\lambda_{\mathrm{K}}} = \alpha_{-\lambda_\pi-\lambda_{\mathrm{K}}} = \alpha_{00} \tag{2.23}$$

Although, parity conservation does not reduce the number of coefficients in the $\overline{\mathrm{K}}^{*0}\mathrm{p}$ resonance mode, it does in the case of the $\Delta^{++}K^-$ decay mode. Since $\Delta^{++} \to p\pi^+$, equation 2.21 becomes

$$\alpha_{\lambda_{\mathrm{p}}\lambda_\pi} = (-1)^{s_{\mathrm{p}}+s_\pi-j_{\Delta^{++}}}\eta_{\Delta^{++}}\eta_{\mathrm{p}}\eta_\pi\alpha_{-\lambda_{\mathrm{p}}-\lambda_\pi} \tag{2.24}$$

$$\alpha_{\lambda_{\mathrm{p}}\lambda_\pi} = (-1)^{\frac{1}{2}+0-\frac{3}{2}}(+1)(+1)(-1)\alpha_{-\lambda_{\mathrm{p}}-\lambda_\pi} \tag{2.25}$$

$$\alpha_{\lambda_{\mathrm{p}}\lambda_\pi} = \alpha_{-\lambda_{\mathrm{p}}-\lambda_\pi} \tag{2.26}$$

Thus, the number of parameters needed to describe this decay mode is four instead of eight.

2.4 Polarization of the Λ_c

Polarization, P_A, of the decay can also be incorporated into the analysis. If the polarization axis is chosen to be perpendicular to the plane of production (as can been seen in figure 8.1 on page 55), then the spin-density matrix ($= \frac{1}{2}(\mathbf{1} + \vec{\sigma} \cdot \vec{\mathbf{P}})$) is represented by

$$\rho = \frac{1}{2} \begin{pmatrix} 1 + P_z & P_x - iP_y \\ P_x + iP_y & 1 - P_z \end{pmatrix}$$

However, because of parity conservation, if the polarization axis is chosen perpendicular to the plane of production, P_x and P_y must be 0, therefore there is only one polarization component and $P_A = P_z$.

So, equation 2.19 becomes

$$\begin{aligned} d\Gamma \quad & \sim \tfrac{1}{2}(1 + P_A) \textstyle\sum_{\lambda_C \lambda_D \lambda_E} |\sum_B BW(m_B)\xi_{B,\frac{1}{2},\lambda_C,\lambda_D,\lambda_E}|^2 \\ & + \tfrac{1}{2}(1 - P_A) \textstyle\sum_{\lambda_C \lambda_D \lambda_E} |\sum_B BW(m_B)\xi_{B,-\frac{1}{2},\lambda_C,\lambda_D,\lambda_E}|^2 \end{aligned} \tag{2.27}$$

2.5 Breit-Wigner Formula

In order to account more accurately for the shape of the resonance, as mentioned previously, a Breit-Wigner distribution is needed. Given the decay mode $\Lambda_c \to r(\to AB)C$, the relativistic shape with centrifugal barrier factors is determined by the equation[Fra 94]

$$(-2|p_C||p_A|)^L \frac{F_{\Lambda_c} F_r}{m_0^2 - m_r^2 - im_0\Gamma_r} \tag{2.28}$$

where

$$\Gamma_r = \Gamma_0 (\frac{q}{q_0})^{2L+1} \frac{m_0}{m_r} \frac{F_r^2(q)}{F_r^2(q_0)} \tag{2.29}$$

for resonance r at the reconstructed two body mass m_r, with the momentum of a daughter particle in the resonant particle's rest frame q (and q_0 when $m_r = m_0$), and with resonant mass and width m_0 and Γ_0 as found in [PDG 98]. Using this convention, we set the Breit-Wigner amplitude for the nonresonant decay to be 1.0.

F_x is the strong coupling factor at the appropriate decay vertex, and is in the Blatt-Weisskopf form: $F_x = 1$ (L=0), $F_x = (1 + R_x^2 q^2)^{-1/2}$ (L=1), and $F_x = (9 + 3R_x^2 q^2 + R_x^4 q^4)^{-1/2}$ (L=2). For R_x, the range of the strong interaction, we used $R_{\overline{K}^{*0}} = 3.4$ (GeV/c^2)$^{-1}$[Ast 88], $R_{\Delta^{++}} = 5.22$ (GeV/c^2)$^{-1}$[Koc 80], $R_{\Lambda(1520)} = 6.29$ (GeV/c^2)$^{-1}$[Wat 63], and $R_{\Lambda_c} = 5.07$ (GeV/c^2)$^{-1}$[Pil 67].

This shape includes the centrifugal barrier at the lower end of the resonance mass spectrum and the high energy solutions at the upper end. For example, in the decay $\Delta^{++} \to p\pi^+$, the lowest mass of the Δ^{++} is the sum of the masses of the p and π, which is 1078 MeV. As the resonant mass approaches this limit, there is less and less energy available to overcome the potential barriers within the Δ^{++}, thus the shape mass spectrum of the resonant particle must be altered from the Breit-Wigner shape.

2.6 Fit Fractions

After the parameters have been fit, fit fractions need to be calculated. Since this is a coherent analysis, the fit fraction for resonance r in this specific analysis is calculated by

$$F_{\mathrm{r}} = \frac{\int \Sigma_{m_{\mathrm{A}},\lambda_{\mathrm{p}}} |BW(m_{\mathrm{r}})\xi_{\mathrm{r},\mathrm{m_A},\lambda_{\mathrm{p}}}|^2 \, d\vec{x}}{\int \Sigma_{m_{\mathrm{A}},\lambda_{\mathrm{p}}} |\sum_{\mathrm{B}} BW(m_{\mathrm{B}})\xi_{B,m_{\mathrm{A}},\lambda_{\mathrm{p}}}|^2 \, d\vec{x}} \tag{2.30}$$

where $\int d\vec{x}$ indicates an integration over phase space.

2.7 Branching Ratios

Once the fit fractions of the decays have been determined, the branching ratio is useful to calculate, in order to compare to previous results listed in [PDG 98]. Since isospin is conserved in strong interactions, the branching ratios need to take into account the summation over isospin space. For this, one can use the Clebsch-Gordon coefficients.

The isospins of the particles involved in this analysis can be seen in table 2.4.

particle	I	Q	B	S	I_3
Λ_c	0	1	1	0	$\frac{1}{2}$
$\overline{\mathrm{K}}^{*0}$	$\frac{1}{2}$	0	0	-1	$\frac{1}{2}$
Δ^{++}	$\frac{3}{2}$	2	1	0	$\frac{3}{2}$
$\Lambda(1520)$	0	0	1	-1	0
p^+	$\frac{1}{2}$	1	1	0	$\frac{1}{2}$
K^-	$\frac{1}{2}$	-1	0	-1	$-\frac{1}{2}$
π^+	1	1	0	0	1

Table 2.4: Particles and isospins (I). Q is the charge of the particle in units of e, B is the baryon number, S is the strangeness number, I_3 is the projection of the isospin.

For example, in the decay $\overline{\mathrm{K}}^{*0} \to \mathrm{K}^-\pi^+$, the initial state has I=$\frac{1}{2}$ and I_3=$\frac{1}{2}$. The final state is a direct product of $|I = \frac{1}{2}, I_3 = -\frac{1}{2}\rangle$ and $|I = 1, \mathrm{I}_3 = 1\rangle$, which can be written in terms of the total isospin states as

$$|\frac{1}{2}\frac{1}{2}\rangle \to \sqrt{2/3}|\frac{1}{2} - \frac{1}{2}\rangle|11\rangle - \sqrt{1/3}|\frac{1}{2}\frac{1}{2}\rangle|10\rangle \tag{2.31}$$

Isospin conservation implies that 2/3 of the time $\overline{\mathrm{K}}^{*0}$ will decay to $\mathrm{K}^-\pi^+$ and 1/3 of the time it will decay to $\overline{\mathrm{K}}^0\pi^0$. Therefore the branching fraction of $\Lambda_c^+ \to \mathrm{p}\overline{\mathrm{K}}^{*0}$ will be 3/2 times more than the fit fraction for $\overline{\mathrm{K}}^{*0} \to \mathrm{K}^-\pi^+$, because 1/3 of the time $\Lambda_c^+ \to \mathrm{p}\overline{\mathrm{K}}^{*0}$ will be followed by $\overline{\mathrm{K}}^{*0} \to \overline{\mathrm{K}}^0\pi^0$.

Going through the same logical process, it can be determined that the branching ratio for $\Lambda_c^+ \to \mathrm{K}^-\Delta^{++}$ is the same as the fit fraction for $\Lambda_c^+ \to K^-\Delta^{++}(\to p\pi^+)$, and for $\Lambda_c^+ \to \pi^+\Lambda(1520)$ is 2 times the fit fraction for $\Lambda_c^+ \to \pi^+\Lambda(1520)(\to \mathrm{pK}^-)$.

Chapter 3

Neural Networks

3.1 Introduction

Another tool we used in the analysis was the Neural Network. Once a reasonable data sample had been selected, as will be discussed in chapter 6, we applied the data to a Neural Network (Neural Net or Net, for short) for the final data selection. This chapter discusses briefly how Neural Nets work and how we used them. We refer the reader to [Bea 91, Bis 95, Smi 93] for more detail.

Neural Nets can be used for many applications, including curve fitting, probability density estimation[Alc 93], and classification. Since my use of Neural Nets is solely for classification, we will concentrate on this aspect in my descriptions below.

Neural Nets offer the advantage of being able to look in N-dimensional space and optimize based on linear combinations of the input data. To use them, one would do the following steps:

1. create an input vector,
2. design the Neural Net architecture,
3. train the Net, and
4. test data using the trained Net.

3.2 Creating the Input Vector

The input vector is as large as is needed to describe an event. For example, if we wanted to determine the difference between the $\Lambda_c \rightarrow \mathrm{pK}\pi$ signal events and background events, we would decide what we needed to describe each decay, because all we have prior to running the Net is a lot of three body decays, some of which are signal and some are background. We could choose the lifetime of the parent or the Čerenkov probability of the assumed kaon. In the end, we chose 14 parameters to describe the event.*Once the input vector is established, we have defined the size of my phase space. In my case, we are working in 14 dimensional phase space. This means that the Neural Network is looking at a 14 dimensional coordinate system.

*The specifics of the 14 parameters can be found on page 42, but knowing what they are at this point is not essential.

By defining each event in this phase space, the Neural Net will be able to analyze this space and to determine which parts of it belong to one class and which parts belong to another. This takes place during training, which will be discussed later.

For example, if a vector, $\vec{x}$, represents an event, where $\vec{x}$ = (x_1, x_2, ..., x_n) for n characteristics of the event, a Neural Network may determine that when x_1+x_2 is high and x_3-x_4 is low, the input vector belongs to one particular class but if x_1+2*x_2 and $3*x_3-1.2*x_4$ are both high then the input vector belongs to a second class. In other words, the Neural Net finds the best combination of parameters and calculates a formula which best separates the classes. This offers a tremendous advantage over conventional data selection techniques, which forces the user to look at only one or two variables at a time. For the conventional analyzer to match the work of the Neural Net, he would need to know which linear combinations are significant or be able to look at more than two dimensions at a time, and that would take either incredible insight or looking over thousands of plots looking for the right combination. And this task becomes even more monstrous as the number of parameters increases.

3.3 Designing Neural Network Architecture

Architecture refers to how the Net is set up, from the number of layers to operations performed at each layer. The Neural Network has three basic layers: an input layer, a hidden layer, and an output layer. The known data goes into the input layer, and the answer comes out of the output layer. The hidden layer is the key to the whole process. It allows the Net to split phase space into disjoint regions so that items from a single class do not have to be near each other. In helping this process, there are also weights, biases, activation functions, error functions, and an updating methodology. Please, see figure 3.1 for a diagram of the Neural Net process.

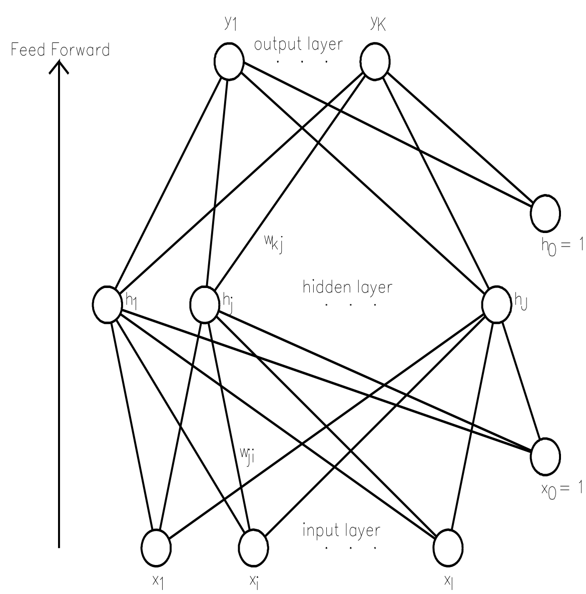

Figure 3.1: The basic structure of a Neural Network with I-J-K architecture. The data flows up when processing an event and the weight corrections flow backward after each epoch during training.

3.3.1 The Input Layer

The input layer is as big as the input vector. In my case the input layer has 14 nodes (or data sites).

3.3.2 The Hidden Layer

The next step is to determine the number of hidden nodes and layers of hidden nodes between the input parameters and the output node(s). Most applications just need one layer of hidden nodes, and it has been shown that there is no application for which more than 2 layers is needed.

With one layer, a collection of hyperplanes will be found which differentiate the different classes of events. These hyperplanes can be thought to be the locus of points where there is a 50/50 chance of being in one category or another. With two layers, a collection of hypersurfaces are found. These have the advantage of being able to form contours around certain regions in phase space. The disadvantage is the increase in computation time needed with the increase in the number of weights, and the increased possibility of training to statistical fluctuations.

3.3.3 The Output Layer

For classification purposes, there should be one fewer output node than types of classes. In other words, if the Net is being trained to differentiate between two classes (also known as binary classification) then there is only one output node. The output value will ideally be either 0 or 1, for our purposes. If the proper activation function is chosen then the output value will indicate the probability that the event is in class 1. In other words, if the output value for an unknown event is .34, then it has a 34% chance of being from the class with a value of 1 and a 66% chance of being from class 0.

3.3.4 Weights and Biases

Between any two nodes in consecutive layers, there is a weight value, w_{ji} and w_{kj} in figure 3.1. The number of weights determines the complexity of the dividing hyperplanes and surfaces. For example, for a 4 - 7 - 1 Neural Net (4 input nodes, 7 hidden nodes in a single hidden layer, and 1 output node) there would be 4x7 + 7x1 = 35 weights.

Also, for each node not in the input layer there is a bias, w_{j0} or w_{k0}, which is added to the value coming into that node. For example, in the 4 - 7 - 1 net, there would be 7 + 1 = 8 biases. This would bring the total of variables in the configuration to 35 + 8 = 43 variables. Note that the biases can be considered weights with an input of 1.0.

Therefore, the 4-7-1 architecture would give us the power to match the data to a 43 variable non-linear equation. In the beginning of the training, these values are arbitrarily set, and the training consists of updating the weights to match the data.

The direct effect of the weights and biases is that they affect the actual value that is inputed into the hidden and output nodes. Looking at figure 3.1, there are several lines leading to each hidden node. This indicates that the value inputed into each of these nodes is a linear combination of the values leaving the nodes of the previous layer. More specifically, the input into node h_1 is $\Sigma_{i=0}^{I} w_{1i} x_i$.

3.3.5 Activation Functions

The previous section discussed the value entering a node, but what exits the node is important to the understanding of the output, and key to the output's interpretation is Bayes Theorem.

Bayes Theorem

Bayes Theorem constructs a probability relationship between different classes of information. If there are two classes of information, C_1 and C_2, then the probability that an arbitrary event is in class C_1 is $P(C_1)$. Since this probability is based solely on the frequency that C_1 tends to occur, this is called a "prior probability". Given a class C_1 with a set of events $\vec{x}$, the probability that we could select $\vec{x}$ from C_1 is $P(\vec{x}|C_1)$. This is called the "class conditional probability". Given an event $\vec{x}$, the probability that it belongs to C_1 is $P(C_1|\vec{x})$, and this is called the "posterior probability". Bayes Theorem states, for a two class problem, that

$$P(C_1|\vec{x}) = \frac{P(\vec{x}|C_1)P(C_1)}{P(\vec{x}|C_1)P(C_1) + P(\vec{x}|C_2)P(C_2)} \tag{3.1}$$

The Activation Function

Taking equation 3.1, and dividing top and bottom by $P(\vec{x}|C_1)P(C_1)$, we get

$$P(C_1|\vec{x}) = \frac{1}{1 + \frac{P(\vec{x}|C_2)P(C_2)}{P(\vec{x}|C_1)P(C_1)}} \tag{3.2}$$

If we let $-2x = ln(\frac{P(\vec{x}|C_2)P(C_2)}{P(\vec{x}|C_1)P(C_1)})$ then Bayes Theorem reduces to

$$g(x) = \frac{1}{1 + exp(-2x)} \tag{3.3}$$

This offers several distinct advantages. Using exp(-2x), means that the input range from $(-\infty, \infty)$ is mapped onto the range (0,1). Secondly, if x = the input into a node, then $g(x)$ would represent the posterior probability as an output, which means that the output could be interpreted as a probability of an event being in class C_1. Although there are other activation functions which can be used, equation 3.3 is sufficient for my purposes.

3.3.6 Error Functions

When training the Net, there needs to be some way to adjust the weights and biases so that the Net better reflects the problem at hand. Crucial in this adjusting is the choice of the error function. The error function should match the purpose of the training, which accurately implies that there are as many equations as there are applications.

If the Net is being trained to distinguish between two classes, then an appropriate error function can be found starting with this purpose. Ultimately we want to determine if $\vec{x}$ is part of C_1 or C_2 ($P(C_1|\vec{x})$ and $P(C_2|\vec{x})$). Since $P(C_1|\vec{x}) + P(C_2|\vec{x}) = 1$, then if $y = P(C_1|\vec{x})$ as found by the Net then $1-y = P(C_2|\vec{x})$. If we are training the Net so that y = t (= 0 or 1 in most binary classification problems), then the probability of getting either target value is $p(t|\vec{x}) = y^t(1-y)^{1-t}$.

If there are n events then the maximum likelihood of a data set reaching its target values is $\prod_n (y_n)^{t_n}(1-y_n)^{1-t_n}$. We want the Net to optimize this but it is easier to minimize the negative logarithm. Thus we produce the error function to minimize as

$$E = E(x_n) = \Sigma_n\{-(1-t_n)ln(1-y_n) - t_n ln(y_n)\}. \tag{3.4}$$

3.3.7 Updating

Once an output value has been found for each of the events during the training phase (i.e. after each epoch), the weights at each node need to be updated in an attempt to minimize the error function. This is done by propagating the error backwards through the Net in order to minimize the error. After each epoch, this is done, so that the Net will differentiate between the classes better and better.

In general, each hidden node receives an input, $a_j = \Sigma_i w_{ji} x_i$. The effect that node has on the error of a particular event, E_n, is

$$\frac{\partial E_n}{\partial w_{ji}} = \frac{\partial E_n}{\partial a_j}\frac{\partial a_j}{\partial w_{ji}} \tag{3.5}$$

Let $\delta_{j_n} = \frac{\partial E_n}{\partial a_j}$. Since $\frac{\partial a_j}{\partial w_{ji}} = x_i$, equation 3.5 becomes

$$\frac{\partial E_n}{\partial w_{ji}} = \delta_j x_i. \tag{3.6}$$

Therefore, we can update the weights by

$$\Delta w_{ji} = \Sigma_n \delta_{jn} x_{in}. \tag{3.7}$$

There are of course, other ways to propagate the error back through the Net for updating. The sophistication of the technique depends on the programmer and the power of the computer. For example, in some cases it is inadvisable to adjust the weight as much as equation 3.7 suggests - as may be the case if the error function is fluctuating greatly with small adjustments to the weight. A learning rate can be added. This could ensure that the weight is adjusted faster in the beginning of the training and less later on as the Net approaches a convergence. In this case, equation 3.7 becomes

$$\Delta w_{ji} = \eta \Sigma_n \delta_{jn} x_{in}. \tag{3.8}$$

Various other terms can be added to control the rate at which the weights are changed. In this analysis, we used Rprop updating, which used the method described in equation 3.8 except the learning rate was different for each weight depending how “well” the actual weight is doing. Please, see [Pet 93, p.6-7] for more detail and additional references.

3.4 Training the Neural Network

When training the Net, one must put in information which is known. The Net will devise a mathematical formula which separates the classes and keep the formula for later use. The known information we used came from two sources. The signal events were from Monte Carlo. The collaboration created seven million idealized signal events which we sent through a simulation of the detector. We assumed that whatever survived was indicative of the real signal events. For background, we took the events in the wings of the real data, i.e. those events more than 3σ from the Λ_c mass.

When we trained the Net, we programmed the Net to try and devise a formula which would produce an output of 1.0 for the MC events, and an output of 0.0 for the background events. If we chose the input vector well enough then the Net would come up with a clear separation between the two classes, but in reality, there is a lot of cross over and some signal events are confused as background and vice versa.

3.4.1 Validation Set

One of the big problems with using Neural Nets is knowing when to stop training. Although updating improves performance, the training session programs the Net to differentiate between two known classes of data. If trained too much, then the statistical fluctuations start to be treated as normal. This problem of overfitting can be minimized with the use of a validation set. It is a set of known data which is not used for training. By testing it occasionally, one can determine if the fitting is general enough, and not specific to the set of training data.

3.5 Testing the Neural Network

After training is done, we are able to put in an unknown event and decide if the event is signal or background. If the event is signal then the output should be close 1.0, and if the event is background, the output should be close to 0.0. Ultimately, as will be discussed later, we chose that 0.94 to be the cut off from background to signal.

3.6 An Example of Using the Neural Network

If we want to classify the two data samples seen in figure 3.2, we would create a two dimensional data vector, corresponding to the two dimensional data.

Using a 2-20-1 architecture and Rprop updating, we trained the net using 1500 class 0 data events and 1500 class 1 data events. For a validation set we used 456 events from each set. Updating of the weights took place after each training session, where a training session consisted of using the entire training set. A measure for the progress of training can be seen by points where the output = 0.5. Because we are looking at data which should have an output of 0.0 or 1.0, an output of 0.5 would be the boundary between the classes. See figure 3.3 for scatter plots of the evolution of the boundaries. These figures were created by generating random points within the confines of the plot, and testing the output. If the output were greater than 0.496 and less than 0.504, then the point was plotted. As one can see, the boundaries evolved over time until the optimum boundary was reached.

The updating process is designed so that the error on the training decreases. The error on the validation set is not necessarily going to decrease. We would want to stop the training at the point at which the error on the validation set is no longer improving. See figure 3.4 for a comparison of

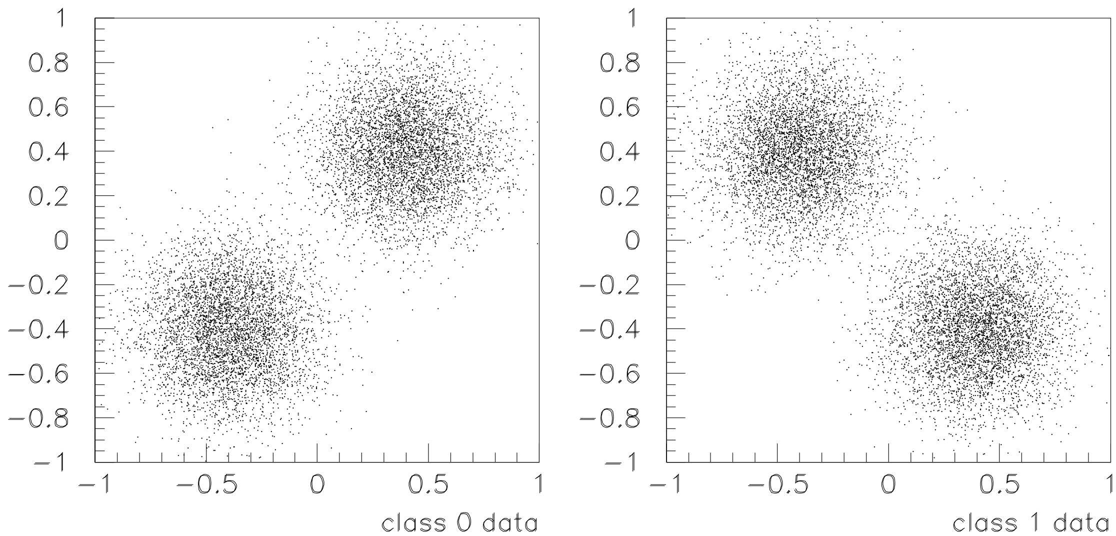

Figure 3.2: The two classes of data being used in this example.

the training and testing errors. Notice in the figure that the two errors are close to the same, but there is a slight increase in the validation set error, which was at its minimum at epoch 225.

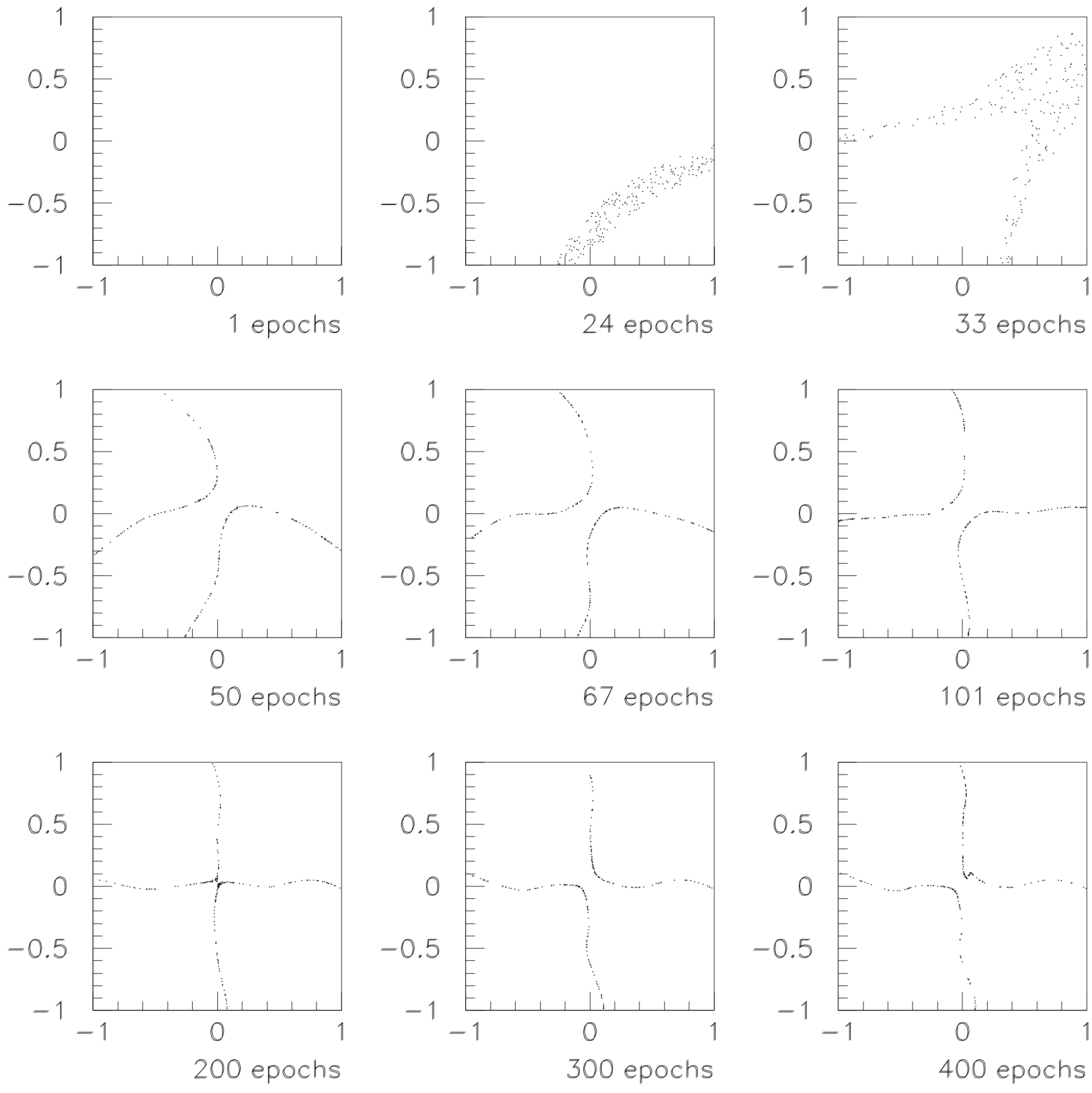

Figure 3.3: The evolution of the boundary between the classes. The points plotted have an output value between 0.496 and 0.504. Note the squiggle near the center of the 400 epoch plot which indicates a noticeable training to a statistical fluctuation.

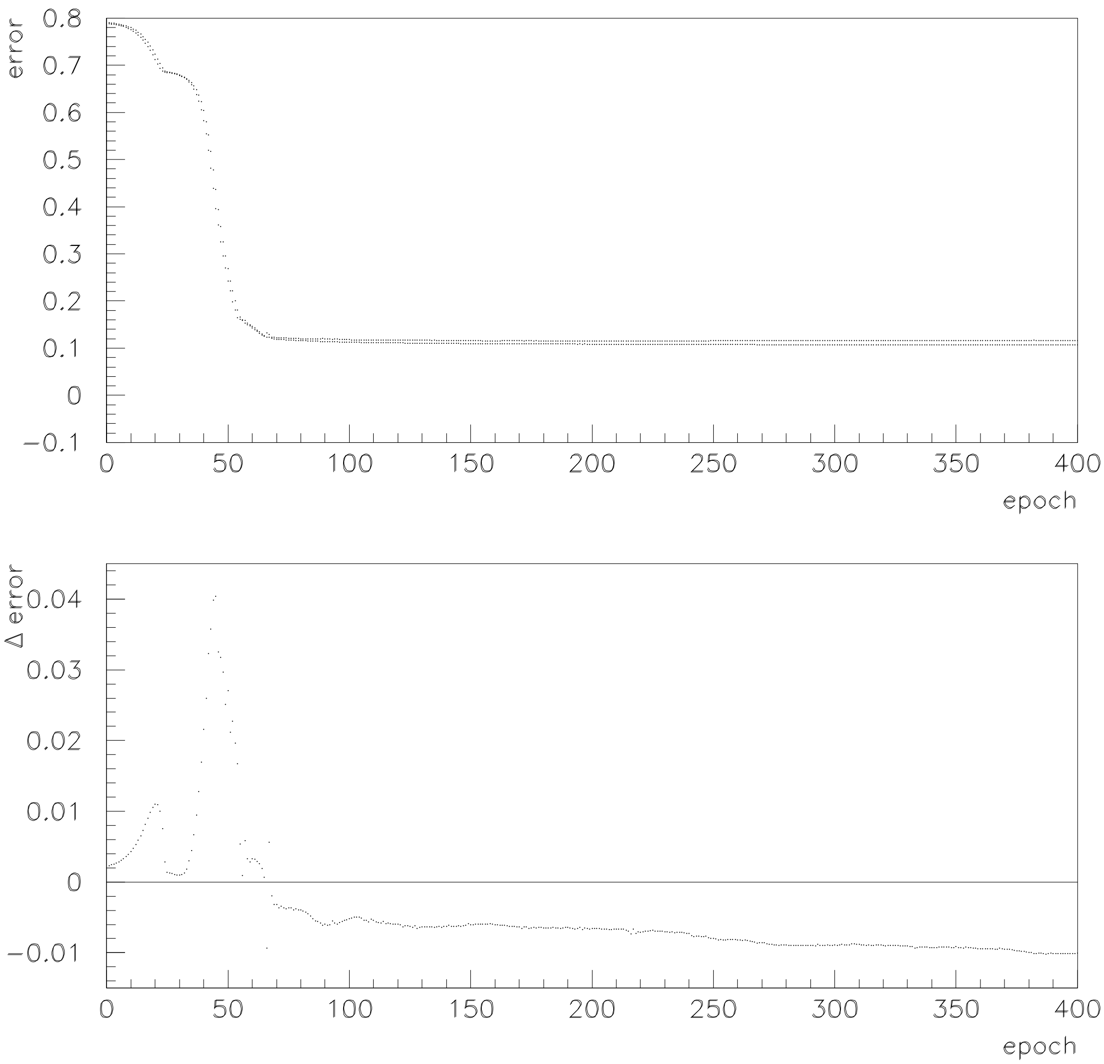

Figure 3.4: The error on the training and validation sets. The top plot represents the average error on both sets of data. The bottom plot represents the difference between the two errors. Note that the validation set reached its minimum at epoch 225.

Chapter 4

E791: A Continued Study of Heavy Flavors

The run of the E791 experiment took place at the Tagged Photon Lab (TPL) facility in the P-East fixed target experimental area at Fermilab, in Batavia, Illinois from July 1991 to January 1992.[Les 96, Per 95] During the course of this run, 20 billion pion-nucleon (πN) interactions were recorded, including 200,000 reconstructed charm events. This charm data sample was the largest in the world until recently. The analysis of the data collected is still continuing and probably will for another couple of years.

4.1 Introduction

In this chapter, I discuss the beam, the target and the E791 Spectrometer - the detector used in this experiment.*In order to find as many charm particles as possible, the detector had three main goals:

1. To find the primary and secondary vertices,
2. To determine the path and momentum of each particle, and
3. To calculate the probability that the identity of each final daughter particle is an electron, muon, pion, kaon, or proton.

The identification of the parent particles (both neutral and charged) would be done preliminarily during reconstruction and more specifically during the individual analyses.

4.2 The Beam

The source of the Λ_c's starts with 800-900 GeV/c protons (as energized by the Tevatron) being aimed at a 30 cm thick Beryllium target. About 2 trillion protons per spill were allocated to the TPL.

*The E791 detector is just an updated version of the detector used in the previous Fermilab experiments: E516 (1979), E691 (1985), and E769 (1988). The main upgrade is the increased number of silicon microstrip detectors used in tracking and the improved data acquisition system.

The shower of particles which was produced in the collision was then separated into positively and negatively charged particles by magnets, then filtered by its momentum and collimated by another magnet to produce a 94% pure beam of 500 GeV/c π^-'s which was then guided down the TPL beam line - about 40 million per spill (which lasted about 23 seconds). As the 500 GeV/c π^- beam approached the target, it passed through eight planes of proportional wire chambers far upstream from the target and six planes of silicon microstrip devices near the target, which were used to track the beam. See table 4.1 for details of the devices used to track the beam. In the language of E791, X refers to the west, X' also refers to west but slightly shifted, Y refers to up, and Z refers to the north (also the direction of the beam). The xz-plane was parallel to the floor of the lab. See figure 4.1 for another display of the orientations of the planes.

	PWC Assembly 1	PWC Assembly 2	SMD Assembly 1	SMD Assembly 2
number of planes	4	4	3	3
number of instrumented wires/strip	64	64	384,384,448	448,416,416
view ordering	X,Y,X',W	X,Y,X',W	Y,X,W'	W',Y,X
wire/strip spacing	1.0 mm	1.0 mm	25/50 μm	25/50 μm
z position (cm)	-3117 to -3114	-1212 to -1209	-80.25 to -74.52	-33.16 to -29.48

Table 4.1: The details of the Proportional Wire Chambers (PWC) and Silicon Microstrip Detectors (SMD) in the beam tracking mechanism. This information was taken from [Les 96, Per 95].

The beam stayed well collimated along the z-axis, with a Gaussian spread in the X direction of a mean$\pm\sigma$ of -0.2$\pm$0.2cm and a spread in the Y direction of -0.7$\pm$0.2cm. The spread in the xy-plane was -0.3$\pm$0.3 mrad and in the yz-plane, 0.9$\pm$0.1 mrad.

4.3 The Target

After passing through these planes, the beam hit the circular target foils which consisted of one $\sim$0.5 mm thick platinum foil, followed by four $\sim$1.6 mm thick industrial diamond foils, with a $\sim$15 mm center to center distance between the foils. See table 4.2 for details on the target. The relatively large spacing between the foils allowed for greater reconstruction of the short lived charmed particles which decay prior to the last foil. Ultimately, the π^- beam had $\sim$2% chance of interacting with any of the targets. Although not done in this dissertation, the different atomic masses of the targets also allowed for study of the charm cross section dependence on nuclear targets.

After interacting, the πN produced a shower of particles which passed through 17 planes of SMD's, used to measure the tracks downstream of the primary vertex. The particles would then pass through a series of two PWC's, 35 DC's and two dipole magnets used to measure the momentum and slopes of the tracks.

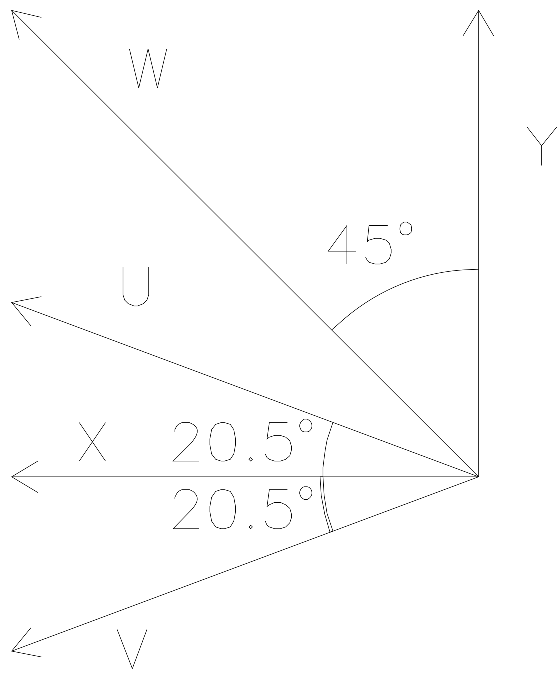

Figure 4.1: The orientations and views of the detector pieces. Z goes into the page.

foil number	1	2	3	4	5
material	Pt	C	C	C	C
z position (cm)	-8.191	-6.690	-5.154	-3.594	-2.060
thickness (mm)	0.52	1.57	1.57	1.53	1.58
proton interaction length (%)	0.584	0.589	0.586	0.582	0.582
diameter (cm)	1.61	1.37	1.38	1.37	1.36
radiation length (%)	16.9	1.2	1.2	1.2	1.2
density (g/cm^3)	21	3			
atomic mass	195	12			

Table 4.2: The details of the target. This information was taken from [Les 96, Per 95].

4.4 The Detector

The spectrometer[Ait 98, Ama 93, E791] consisted of several components (see figure 4.2 for the schematic):

1. Twenty-three planes of silicon microstrip detectors (SMD) split between upstream and downstream of the target,
2. Thirty-five planes of drift chambers (DC),
3. Eight proportional wire chambers (PWC) split between upstream and downstream of the target,
4. Two magnets,
5. Two segmented gas threshold Čerenkov detectors,
6. Two Calorimeters: hadronic and electromagnetic,
7. Steel Plate,
8. Two planes on scintillation counters, and
9. One plastic scintillator.

The SMD, DC, and PWC were used for tracking charged particles; the Čerenkov detectors were used for identifying particles; the magnets, in conjunction with the DC's were used for determining momentum; the calorimeters were used for measuring energies; and the plastic scintillator was used for detecting muons.

Two Čerenkov detectors mixed in with the above were used to identify μ, e, π, K, and p in the 6 - 60 GeV/c range.

After this, the tracks passed through two calorimeters: the first being a SLIC used to determine the EM energies, and the second being a hadrometer used to determine the hadronic energies.

After the calorimeters, came a steel plate to stop all particles except muon's which were detected by the plastic scintillator (muon wall) at the end.

4.4.1 Silicon Microstrip Detectors

The Silicon Microstrip Detector (SMD) is one of the most important parts of E791. The SMD is key in reducing the amount of background in the analysis. Since the primary focus of the SMD is to determine the vertices, it allows us to eliminate any track that does not come from a well defined vertex. With the 6 SMD's prior to the target and 17 downstream from the target, an unprecedented accuracy and precision in locating vertices was achieved.

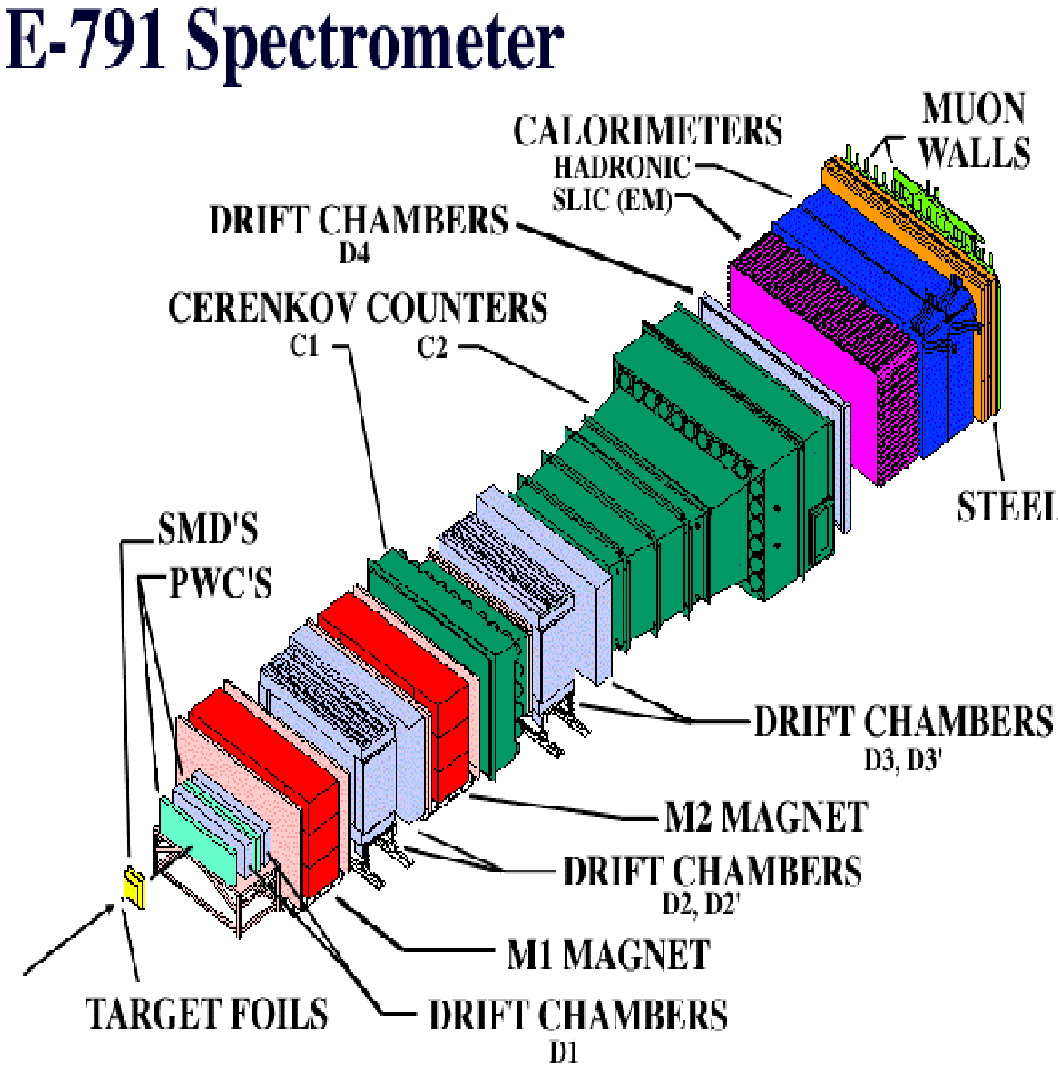

Figure 4.2: E791 Spectrometer.

Design

The SMD works under the basic principle that semiconductors will conduct in the presence of a moving charged particle. As the charged particle goes by it allows the high energy electrons in the semiconductor to jump the energy gap in to the conducting zone. Thus a current is induced, and a particle is detected.

With many layers of SMD planes placed behind one another at different angles, if a single charged particle goes through, its path can be detected. However, many charged particles pass by the SMD's in a short amount of time. Later, when reconstructing the events, physicists must study all the SMD wires which detected an event. Using combinatoric techniques, in combination with information determined downstream, a picture as to the number of particles and their paths can be sketched out. See section 5.1.1 for more detail on this technique.

Specifics

The planes of SMD's were constructed as an array of reversed biased p-n junctions. Each SMD was 300 μm thick, and the planes were arranged in groups of three oriented so that a near exact location could be determined. The orientation in the xy plane put two SMD's at a right angle to one another and the third was set so that it was 20.5^o from one and 110.5^o from the other as seen in figure 4.1. See table 4.3 for more detail on the SMD configuration.

plane	z-position(cm)	strip spacing(μm)	number of strips	view
7	0.670	25;50	688	Y
8	1.000	25;50	688	X
9	1.931	50	512	X
10	3.015	50	512	Y
11	6.684	50	512	V
12	11.046	50	884	Y
13	11.342	50	884	X
14	14.956	50	884	V
15	19.915	50	1000	X
16	20.254	50	1000	Y
17	23.878	50	1000	V
18	27.558	50;200	864	V
19	31.848	50;200	864	X
20	34.548	50;200	864	Y
21	37.248	50;200	864	X
22	39.948	50;200	864	Y
23	45.508	50;200	864	V

Table 4.3: The details of the silicon microstrips. The table was taken from [Per 95].

Overall, the geometric acceptance was ~100 mrad, the efficiency of all 23 planes was 83% - 99%, and the spatial resolution ranged from 7 - 15 μm.

4.4.2 Drift Chambers

The Drift Chamber (DC)[Hei 96] operates under the basic principle that a charged particle traveling through a gas will ionize that gas. The released electrons will then travel, if the DC is ideal, to the nearest anode wire. If those electrons can be detected, several important characteristics of the initial charged particle can be determined, such as its presence, and its energy and position.

Design

In order to perform its chosen task, the DC must have an anode wire surrounded by a cathode. Once the ionized electron is released, it will, in an absence of a stronger potential, tend to latch onto the nearest positively charged ion. Therefore, a potential must be present in the chamber, in order to cause the ionized electrons to drift toward an anode wire for detection. Once the charged particle travels through the detector and releases the electrons, the electron travels toward the anode, it will in turn ionize more gas, and a shower of electrons is created, all of which will ideally drift toward the anode.

Setting the initial time, t_0, by a triggering mechanism, the DC can time how long it takes for the rest of the shower to reach it (at time t). Fortunately, electron drift velocity is reasonably well known for particular gases, and therefore, based upon the time it takes for the shower to travel, an initial position can be determined.

There are, of course, complications to this. It is possible that the drift velocity is not constant through the DC, ultraviolet photons are released, or the wire has deposits built up on it through use. However, these problems can be minimized by an appropriate choice of gas, care of the detector, or thorough study of the DC prior to its intensive use.

Like the PWC's, the resolution of the position of the particle can be influenced by $t-t_0$. If the drift time is long, then the errors on the time are less significant and the position is better known. But this means increased dead time before the next particle can be detected. A shorter drift time will shorten the dead time, but add to the imprecision of the position. Although, the choice of gas influences these factors, position problems can be further reduced by several planes of DC.

By having the wires in the planes at angles to each other, three dimensional coordinates can be determined.

Momentum can also be determined by the DC in conjunction with the magnets. The magnets are oriented so that the charged particle's path will bend in the xz-plane. Using a simplistic model, if we know the strength of the magnet, B, and the charge of the particle, q, then by looking at how much the path of the particle deviated (calculated by the radius of curvature, r) when passing through the magnetic field, the momentum, p, of the particle can be determined by $p = qrB$.

Specifics

The 35 DC planes were split into four modules, each consisting of one to four assemblies, each of which was made from three or four planes. See table 4.4 for more detail on how the DC's were organized. The gas used was a mixture of 89% Ar, 10% C and 1% CF_4. The spatial resolution of the DC's ranged from 250 - 350 μm, which is two times better than that of the PWC and 20-40 times worse than that of the SMD.

There was a problem with excess ionization at the point where the beam hit the DC. As the time of the experiment went on, this created a drop in efficiency for certain parts of the DC. This problem area is referred to as the DC hole. As time went on this hole increased in size. This was treated by incorporating this hole into the analysis of the data.

DC group	D1	D2	D3	D4
dimensions (cm)	160 x 120	230 x 200	330 x 200	550 x 300
view ordering	X,X',U,V	X,U,V	X,U,V	X,U,V
number of planes	8	12	12	3
number of channels	1536	2400	1952	416
U and V cell size (cm)	0.446	0.892	1.487	2.97
X cell size (cm)	0.476	0.953	1.588	3.18
z-position first plane (cm)	142.49	381.43	928.14	1737.99
z-position last plane (cm)	183.66	500.80	1047.10	1749.42

Table 4.4: The details of the drift chambers. The table was taken from [Per 95].

4.4.3 Proportional Wire Chambers

The PWC's are also used for tracking and are similar in principle to the DC's. They offer the advantage over other tracking devices by being relatively easy to use and to maintain.

Design

Sets of parallel wires are set up perpendicular to a plane of another parallel set of wires with the opposite potential. The PWC's are filled with a gas that ionozes after the passage of a charged particle. If this occurs, the ions drift towards charged wires causing a pulse which is detected.

Although timing can be alos determined with PWC's, greater timing resolution can be found using the DC's so this is not an issue.

Specifics

The two downstream PWC planes were placed at z=120.4cm and z=162.9cm. They had a wire spacing of 2.0mm, a gas composition of 82.7% Ar, 17% $C0_2$, and 0.3% freon. They were oriented to determine the y position of the particles. This in conjunction with the magnets would be used for determining the momentum of the particle. The resolution of the PWC's was 600 μm, which is 40-80 times worse than the resolution for the SMD's and twice the resolution of the DC.

4.4.4 Analysis Magnets

The magnets were copper coil magnets which provided a transverse boost of 212 MeV/c and 320 MeV/c, respectively. See table 4.5 for a more detailed look at the magnets.

4.4.5 Gas Čerenkov Detectors

The Čerenkov detectors[Bar 87] are based on the principle that when a charged particle travels through a gas faster than photons can, it will produce its own light. Since the speed of a photon

	M1	M2
z-position front (cm)	222.5	566.9
z-position center (cm)	273.5	617.7
z-position back (cm)	324.1	668.5
aperture (cm^2)	183.2 x 81	182.9 x 85.6
length (cm)	101.6	101.6
current (A)	2500	1800
$\int B_y(0,0,z)dz$ (gauss-cm)	711,097	1,077,242
p_T kick (MeV/c)	212	324
maximum strength (kG)	5	7

Table 4.5: The details of the magnets. The information was taken from [Les 96, Per 95].

(whose speed in a vacuum is c) in a gas with index of refraction n, is $c' = \frac{c}{n}$, the particles threshold speed, v, and the angle at which its radiation is emitted, θ ($\theta = cos^{-1}(\frac{c'}{v})$), are dependent on the gas. So if the properties of the gas are well known, then particle identification becomes possible, which is fortunate because that is the primary purpose of the Čerenkov detector.

In E791, there are two detectors (C1 and C2 in figure 4.2) with different gases in each. Thus, if a particle emits light in one and not the other, there is a strong clue as to the identity of the particle. Thus, with an increased accuracy in the identification of electrons, muons, pions, kaons, and protons, there is an increased identification of charmed particles over the background. Since charm particles decay predominantly into strange particles, such as the K mesons and hyperons (such as Λ and Σ) which, in turn, quickly decay into protons and pions, it is essential that the detector have the capacity to discriminate between these daughter particles.

Design

The two most essential parameters in the effectiveness of the Čerenkov detectors are the gas composition and mirror segmentation. The gases chosen for the two detectors are nitrogen (n=1.000290) and a mix of nitrogen and helium (4:1) (n=1.000086), where the indices of refraction were calculated for a particle of wavelength 3500 Angstroms and STP environment. The radiation emitted by a charged particle is predicted by the equation:

$$\frac{\mathrm{dN}}{\mathrm{dl}} = 2\pi\alpha \int (1 - \frac{1}{\beta^2 n^2(\lambda)})\epsilon(\lambda)\frac{\mathrm{d}\lambda}{\lambda^2} \tag{4.1}$$

where $\frac{\mathrm{dN}}{\mathrm{dl}}$ = the number of photons per unit length; $\alpha = 1/137$; n(λ) = index of refraction at the wavelength, λ; β = P/E where P and E are the momentum and energy, respectively, of the charged particle; and $\epsilon(\lambda)$ = the detector efficiency at λ.

Therefore, a proton with a momentum of 40 GeV/c would approximately produce 13 photons/meter in the first detector. Since the first detector is 3.75 m long this would mean that under an ideal situation, it would count 49 photons. But once correct efficiencies and wavelength dependencies are taken into account, we would only detect ~15 photons. Note that with the second detector at its lower index of refraction, a 40 GeV/c proton would not generate any photons.

The mirror segmentation was designed to minimize identification confusion. The radius of the light cone is characterized by the following equation:

$$R = L\tan(\theta) \tag{4.2}$$

$$\sin(\theta) = (1 - \frac{1}{\beta^2 \mathrm{n}^2(\lambda)})^{1/2} \tag{4.3}$$

Therefore, for our 40 GeV/c proton, the predicted radius is approximately 3.1 cm. Although this information is not used in the threshold detectors, like those used in the experiment, in the same way as the ring-imaging detectors, the radius is useful for determining the appropriate size of the mirrors.

Specifics

See table 4.6 for a detailed look at the Čerenkov counters.

	C1	C2
length (m)	3.7	6.6
number of mirrors	28	32
gas mixture	100% N_2	80% He, 20% N_2
δ = (n-1)	290 x 10^{-6}	86 x 10^{-6}
pion momentum threshold (GeV/c)	5.8	10.6
kaon momentum threshold (GeV/c)	20.5	37.6
proton momentum threshold (GeV/c)	38.9	71.5

Table 4.6: The details of the Čerenkov counters. The table was taken from [Per 95].

4.4.6 Calorimeters

There are two basic types of calorimeters[App 86]: hadronic and electromagnetic. Although they are designed for different particles, their overall purpose and operating principles are the same. The purpose of a calorimeter is to measure the energy of a particle. The basic principle is that a particle enters the calorimeter and produces a shower and the total light output is proportional to the incident particle's energy.

Design

As the shower is detected, several characteristics can be measured. As implied above, the total energy of the shower is measured, which is proportional to the energy of the particle. But also measured are the width of the shower, which is related to the particle's momentum, and the position of the shower, which is obviously related to the particle's position.

With both calorimeters, the particle's identification can be narrowed down as well. Since hadrons will dump most of their energy in the hadronic calorimeter and the photons, electrons and positrons will dump most of their energy in the electromagnetic calorimeter, both pieces of information can be used to eliminate the non-hadrons.

Specifics

The electromagnetic calorimeter was a SLIC which is short for “segmented liquid ionization calorimeter”. See table 4.7 for detail on the SLIC and table 4.8 for detail on the hadrometer.

	u channels	v channels	y channels
number of channels	109	109	116
orientation	-20.5^o	+20.5^o	90^o
number of layers	20	20	20
single channel width (cm)	3.17/6.35	3.17/6.35	3.17/6.35
channel length (cm)	260	260	244
view ordering	U,V,Y		
upstream z-position (cm)	1866.		
downstream z-position	1962.		
active area (cm^2)	488 x 244		
total radiation length	21.5		
total interaction length	2.07		
energy resolution	$(\frac{\delta E}{E})^2 \approx (\frac{17.4\%}{E})^2 + (11.5\%)^2$		
position resolution (cm)	0.65		

Table 4.7: The details of the SLIC. The table was taken from [Per 95].

	X channels	Y channels
number of channels	66	76
number of layers	36	36
single channel width (cm)	14.5	14.5
view ordering	X,Y	
absorber thickness (cm)	2.54	
total interaction length	6	
upstream z-position (cm)	1973.	
downstream z-position (cm)	2131	
active area (cm^2)	490. x 270.	
energy resolution	$\frac{\Delta E}{E} \approx \frac{75\%}{\sqrt{E}}$	

Table 4.8: The details of the hadrometer. The table was taken from [Per 95].

4.4.7 The Trigger

There were two triggers for data collection in the E791 spectrometer. The first trigger was placed near the target and used to determine if there was anything to detect. More specifically, there had to be a π^- detected upstream of the target and at least four charged tracks downstream from the detector. This decision took 160 ns.

The second trigger was based on the calorimeter measurements. Since the transverse energy for charm particles is greater than the transverse energy for lighter particles, the trigger was set to go if the transverse energy exceeded 4.2 GeV. The transverse energy was calculated by summing the total energy found by both calorimeters weighted by sinθ, where θ is the angle between the beam direction and the line connecting the target to the collector on the calorimeter.

In order to remove multiple beam pions in a single event, all events with a total energy greater than 700 GeV were thrown out. Of the events which were recorded, 90% satisfied both triggers.

4.4.8 Data Acquisition

The incident pions interacted with a target nucleon about every 25 μs. About half of these met the trigger requirements, so a recordable incident took place every 50 μs. The digitization process took $\sim$50 μs, so there was about 50% dead time.

An event segment was typically 2.5 kB in size and written to the 8mm tapes in a bank of 42 Exabyte tape drives and 54 ACP 1 processors. A 640 MB buffer allowed writing during the next event. Overall the acquisition averaged 9.6 MB/s.

When done, there were 20 billion events stored on 24,000 8mm tapes at 2.2 GB per tape.

Chapter 5

Event Reconstruction

The reconstruction and analysis of the data took place in several steps: reconstructing, filtering, stripping, substripping, and microstripping. The reconstruction and filtering were done at 4 farms throughout the western hemisphere, and the remaining stages were done at individual machines. The purpose of the reconstruction phase was to get a sense of what happened and to establish the parameter values for each event. There were two formats for these values, called within E791 "Release 5" and "Release 7". See appendix B for the listing of the Release 7 data structure. These releases contained the same basic information, but organized it differently according to how the data were to be used in analysis. The subsequent steps were designed to reduce the number of events for easier analysis. See table 5.1 for the number of events at each stage in the process.

Process	Tapes	Events
Raw Data	24,000	20 billion
Reconstruction/ Filter	7,500	4 billion
Strip: Stream A	2,000	1.2 billion
Strip: Stream B	2,000	800 million
Substrip (KSUSS)	33	20 million
Microstrip	1	2,271

Table 5.1: The number of tapes and events at each stage in the selection process.

5.1 Reconstructing and Filtering

All events were partially reconstructed based on the certain parameters, then filtered. Events which survived the filter were then fully reconstructed. Reconstruction included reconstructing the tracks, finding the primary and secondary vertices, analyzing the calorimetry and Čerenkov data, and identifying muons.

5.1.1 Track Reconstruction

Tracks were first reconstructed using the software package STR which used the SMD hits. The first set of SMD's which was placed upstream of the target were used for beam reconstruction, and the SMD's downstream from the target were used for post-interaction tracks. The SMD tracking algorithm fit straight lines to the hits in each view using a minimum χ^2 fit. Each line of flight required four hits in each of the X and Y views and three hits in the V view.

If a track was found in the SMD's, then this path was extended to the DC. The track was considered good if it lined up with D3 hits in all three views. Since the particles were deflected by a magnet in the xz-plane, the Y view was used for identifying a good track. A final decision as to the actual path was determined if the good track also went through D1 and D2 hits in all three views. Since not every track is properly detected or more likely some particles decay after one region and before another, a classification system, as can be seen in table 5.2, was developed to catalog the tracks.

region	hits
0	SMD's
1	D1
2	D2
3	D3,D4

Table 5.2: The regions used for identifying tracks.

The track category was determined by $\Sigma 2^i$, where i = the region where the hits occurred. For example, if a track was detected in only regions 0 and 1, then it was a category 3 track. Obviously category 15 tracks would be the most reliable.

If an event were detected in region 0 and another region, it was called in E791 a SESTR track. After reconstructing the SESTR tracks, the remaining tracks, called ESTR tracks, were then reconstructed. Note that about a third of the category 3 tracks were later found to be false tracks found by the tracking algorithm and were later discarded.

5.1.2 Vertex Reconstruction

After reconstructing the SESTR tracks, the vertices were determined. In determining the primary vertex, the tracks were followed upstream. If two tracks came from the same point (or as close as possible) at a target foil, then it was considered to be a primary vertex. Then other tracks were added as long as the χ^2 / degree of freedom stayed reasonably low. Tracks which were not linked to a primary vertex were considered to have come from a secondary vertex and were reconstructed as such, as long as the χ^2 per degree of freedom stayed low.

Once the vertices had been determined, the SDZ, the distance between the primary and secondary vertices divided by their errors in quadrature, and DCA, the distance of closest approach between a track and a vertex, could be calculated. Both of these variables would be involved in the filtering criteria.

5.1.3 Čerenkov Reconstruction

The process for particle identification was a 3 step process.

1. Calculate the measured amount of radiation in each mirror,

2. Predict the number of photoelectrons expected from a particle of a given mass in that mirror, and

3. Determine the particle identification probabilities.

Number of Photoelectrons

The measured number of photoelectrons (NMEAS) produced by the light off mirror k is found by:

$$NMEAS_k = \frac{ADC_k - PED_k}{SPEP_k} \tag{5.1}$$

where ADC is the actual number of photoelectrons measured, PED is the number of background photoelectrons, and SPEP is a measure of the gain for that mirror.

The total number of photons measured is $N = \sum_k NMEAS_k$.

Predicted Number of Photoelectrons

In predicting the average number of photoelectrons ($\overline{NPRED}$), one must take into account the geometry of the detector F^{geo} - which factors in mirror angles, gaps between the mirrors and the mirror that is actually used - as well as F^{rad} - a parameter dependent on the amount of radiation emitted which is dependent on the mass and velocity of the particle - and average number of photoelectrons for the specific mirror $\overline{PE}$. This prediction can be formalized in the equation:

$$\overline{NPRED}_{mass,track,mirror} = \mu_{m,t,k} = F^{\text{geo}}_{m,t,k} \times F^{\text{rad}}_{m,t}(\beta) \times \overline{PE}_k \tag{5.2}$$

Particle Identification

From the above calculations, we can determine the compound Poisson PDF.

$$P_{m,t}(N, \mu, b) = \frac{\mu^N}{N!}(1 + b\mu)^{-N-1/b} \times \prod_{q=1}^{N-1}(1 + qb) \tag{5.3}$$

where $\mu = \overline{\mu}_{m,t} = \Sigma_k \overline{\mu}_{m,t,k}$; and the width parameter, $b = \overline{b}_{m,t} = \Sigma_k b_k \overline{\mu}^2_{m,t,k} / \overline{\mu}^2_{m,t}$ which is a measure of deviation of this distribution from a pure Poisson Distribution.

From this PDF, we calculate a consistency probability for each detector: $PC1_{m,t} = P(NMEAS_{C1}, \mu, b)$ and $PC2_{m,t} = P(NMEAS_{C2}, \mu, b)$. From these and an a priori likelihood*, A_m, that a particular particle is produced in this collision, we calculate the overall Čerenkov probability, $CPRB_{m,t}$, for hypothesized mass, m, and track, t, to be

$$CPRB2_{m,t} = \frac{PC1_{m,t} \times PC2_{m,t} \times A_m}{\sum_m PC1_{m,t} \times PC2_{m,t} \times A_m} \tag{5.4}$$

5.1.4 Filtering

After partial reconstruction, an event passed the filter if it had a primary vertex and satisfied one of the following criteria:

1. a secondary vertex with a good separation from the primary vertex,

*For this analysis the a priori probabilities were 0.02, 0.01, 0.81, 0.12, 0.04 for μ, e, π, K, p respectively.

2. a K_s or Λ from the ESTR tracks, or

3. a ϕ from two SESTR tracks.

See table 5.3 for the specific criteria used in the filtering selection process.

Filter	Requirement	Cut Made	Survival
SMD Vertex	well separated secondary	SDZ > 6 for two prongs SDZ > 4 for three or more prongs	9%
ESTR vertex	presence of K_s	track χ^2/DOF < 5 0.5 < track momentum < 500 DCA of two tracks < 0.5cm 0.470 GeV < $M(\pi^+\pi^-)$ < 0.520 GeV in region 1 0.465 GeV < $M(\pi^+\pi^-)$ < 0.525 GeV in region 2	9%
	presence of Λ	track χ^2/DOF < 5 0.5 < track momentum < 500 DCA of two tracks < 0.7cm 1.106 GeV < $M(p\pi^-)$ < 1.125 GeV in region 1 1.100 GeV < $M(\pi^+\pi^-)$ < 1.130 GeV in region 2	
ϕ	presence of ϕ	track χ^2/DOF < 5 0.5 < track momentum < 500 DCA of two tracks < 0.5cm Joint Kaon Probability > 0.05 1.015 GeV < $M(K^+K^-)$ < 1.025 GeV	1%

Table 5.3: The specifics of the filtering process.

5.2 Stripping

As the data which survived the filter were fully reconstructed, it was tagged based upon certain characteristics of the event. In all there were sixteen different categories of events, of which, the first nine tags sent the event into Stream A, and the last seven tags sent the event into Stream B. In general, the difference between the streams is that stream A events are possible charm events and stream B events are not considered possible charm events. We used stream A events in my analysis (with the exception of the Λ's we used as a proton source in my exploration of the Čerenkov probability systematic errors in chapter 10). See appendix C for the list of tags used. Stripping reduced the amount of information down to 2000 tapes.

5.3 Substripping

Analysts at this point substripped the data one of two ways: the grand canonical substrip (GCSS) or the Kansas State University substrip (KSUSS). Since we used the KSUSS, we will discuss it and not the GCSS. For the details of the cuts used, see appendix D.

Chapter 6

Final Event Microstrip Selection and Signal Optimization

After reconstructing, filtering, stripping and substripping the data from the E791 experiment, we were left with enough data to fill 33 tapes. Given these 33 KSUSS tapes from the experiment, we made the following loose cuts to pare the number of events to 392,742 events (which fit onto 1 tape):

1. the decay vertex must have 3 decay tracks,
2. the Čerenkov probability of the identified kaon being a kaon ≥ 0.13,
3. the Čerenkov probability of the identified proton being a proton ≥ 0.05, and
4. the reconstructed Λ_c mass must be between 2.18 and 2.58 GeV/c^2.

We determined which of the three tracks was a kaon by assuming that the track with the opposite charge of the other two was the kaon. Of the remaining two tracks, we assumed the track with the greater probability of being a proton was the proton, and the remaining track was the pion.

From this group of events, we added some more loose cuts:

1. every daughter track must be from category 3,7, or 15,
2. every vertex, when reconstructed minimizing the transverse χ^2, must be good with χ^2 per degree of freedom < 10.0, and

At this point, we checked to see if we could extract any more Λ_c's from the data from the two prong vertices. Starting with 100,000 reconstructed MC events, we assumed that some of the two prong vertices were actually from the $\Lambda_c \rightarrow \mathrm{pK}\pi$, but were misfit. For each of these two track vertices, we added all of the other tracks (with $\chi^2 < 8.0$) from the event, one at a time, to the two prong vertex. If this newly formed vertex had $\chi^2/DOF < 8.0$, we plotted the reconstructed pKπ mass. See figure 6.1 for the display of the reconstructed masses. With ideal MC data there was a peak, but considering the amount of background present, we assumed that it would be much worse for the real data events, and this line of exploration was stopped.

We also pared the number by cutting data from the mid-plane region where our Čerenkov counters had no mirrors and a poor efficiency[Yos 96]. This translates specifically to cutting any

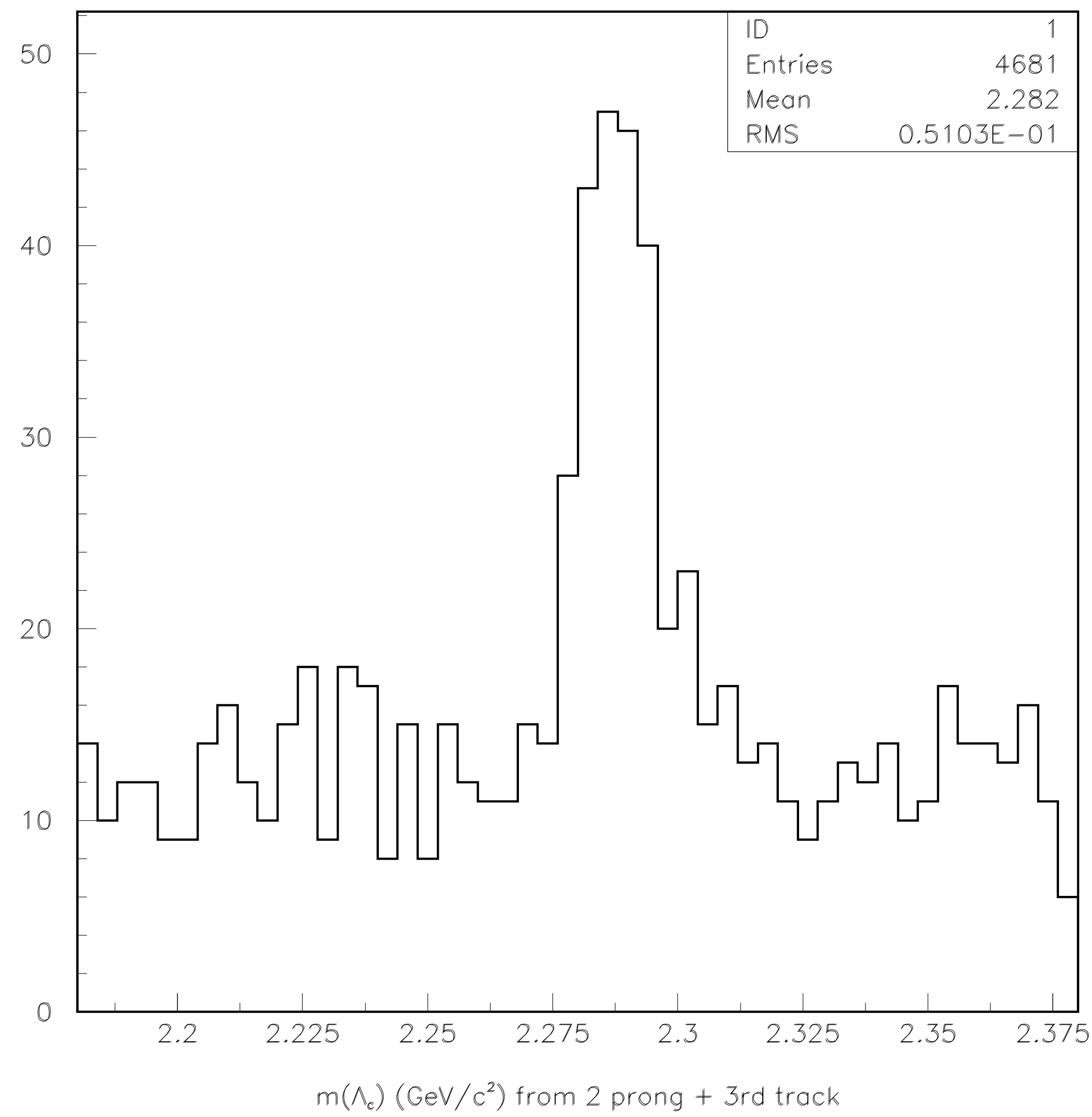

Figure 6.1: Reconstructed masses of Monte Carlo data extracted by adding a third track to all two prong vertices.

event in which the proton had a 70% probability or greater of being a proton and the slope in the y direction of the track was between -0.0021 and 0.007 was cut. We had 228,900 events, of which 133,305 were within the mass range of 2.18 and 2.38 GeV/c^2.

We also generated 7 million Monte Carlo $\Lambda_c \to pK\pi$ events uniformly distributed in phase space. *This process pared the number of MC events to 226,865. Sending these events through the above cuts pared the number to 31,361 events within the mass range 2.18 and 2.58 GeV/c^2, of which 26,718 events were less than 2.38 GeV/c^2.

For the sake of optimization, we looked at events only within the mass range of 2.18 and 2.38 GeV/c^2. (The events with the reconstructed mass between 2.38 and 2.58 GeV/c^2 could be used later to look for the decay $\Xi \to pK\pi$. See appendix M for a display of the findings.) We optimized the projected significance using a Neural Net based on the following variables (as suggested by Simon Kwan[Kwa 95]):

1. JC, the joint Čerenkov probability for the proton being a proton and the kaon being a kaon,
2. SDZ, the distance between the z-coordinate of the primary and secondary vertices divided by their errors in quadrature,
3. DIP, the distance between the primary vertex and the line of flight of the reconstructed Λ_c in the xy-plane,
4. PT2DK, the sum of all the p_T^2 of all the secondary tracks with respect to the flight path (as determined by a line of flight from the primary vertex to the secondary vertex) of the reconstructed Λ_c,
5. PTBAL, the absolute value of the p_T of the vector sum of all the secondary tracks with respect to the flight path of the reconstructed Λ_c,
6. SIGMA, the number of standard errors the secondary vertex is from the closest target foil edge,
7. TAU, the calculated proper lifetime of the reconstructed Λ_c,
8. RAT(3), the ratio of the distance in the xy-plane of the decay track from the secondary vertex to its distance in the xy-plane from the primary vertex (there is one value for each track),
9. RATMIN, the minimum of all the above ratios,
10. RATIO, the product of the above three ratios,
11. CHISQS, the χ^2 per degree of freedom for the secondary vertex, and
12. CHISQP, the χ^2 per degree of freedom for the primary vertex.

*Of these, 5 million were generated at Fermilab in release 5 mode. The remaining 2 million were generated in release 7 mode at University of Mississippi and University of South Carolina. All events were generated with half assuming the target nucleon was a proton and half assuming a neutron. They were also generated so that an equal amount of MC data was reconstructed using each of the DC holes. The 7 million events were then filtered and stripped. The stream A events were sent to USC for KSU Substripping. There was no essential difference in all the data sets which were generated.

Since the KSUSS applied a restriction that SDZ $\geq$ 6.0 and PTBAL $\leq$ 0.4 we also cut any events which violated these boundaries. See figures 6.2 and 6.3 for the real and MC data after the above cuts and reconstructed as pKπ, KKπ, and K$\pi\pi$.

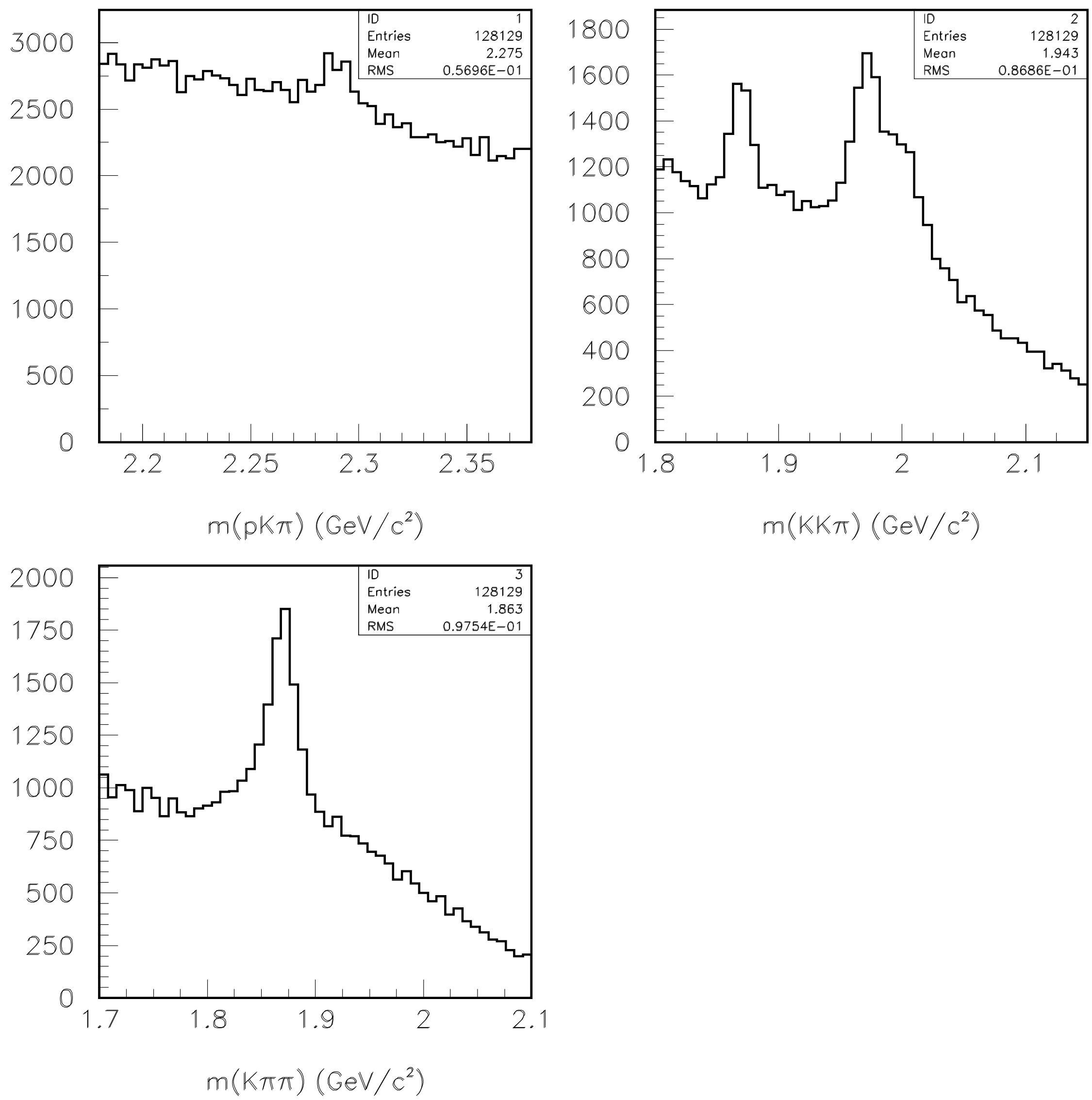

Figure 6.2: Reconstructed masses of real data before Neural Net and D mass cuts.

The last cut we made before using the Neural Net, was to eliminate the D resonances. There are three decays which are more likely to be reconstructed as false $\Lambda_c^+ \rightarrow pK^-\pi^+$ than other decays. They are

1. $D^+ \rightarrow K^+K^-\pi^+$

2. $D^+ \rightarrow K^-\pi^+\pi^+$

3. $D_s^+ \rightarrow K^+K^-\pi^+$

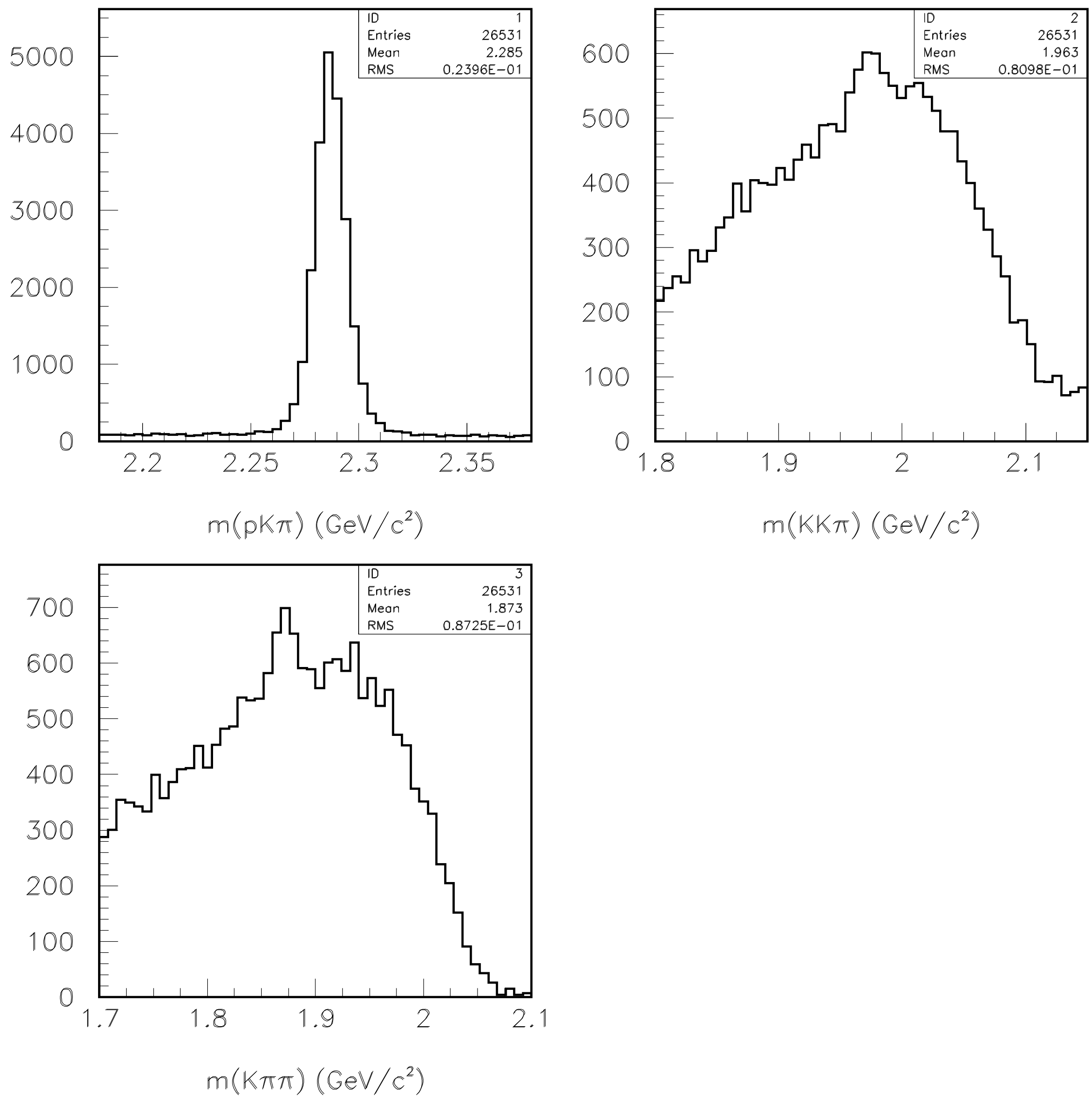

Figure 6.3: Reconstructed masses of Monte Carlo data before Neural Net and D mass cuts.

To avoid confusion in later analysis, we cut all events whose reconstructed KKπ mass was within the mass range of 1.85 to 1.89 GeV/c^2 and 1.95 to 1.99 GeV/c^2 and whose reconstructed K$\pi\pi$ mass was within the range of 1.85 to 1.89 GeV/c^2. See appendix E for the display and more discussion of the D mass cuts.

This gave us 108,366 candidate decays (see figure 6.4 for the mass plot of the candidates) and 19,348 Monte Carlo decays with which to work.

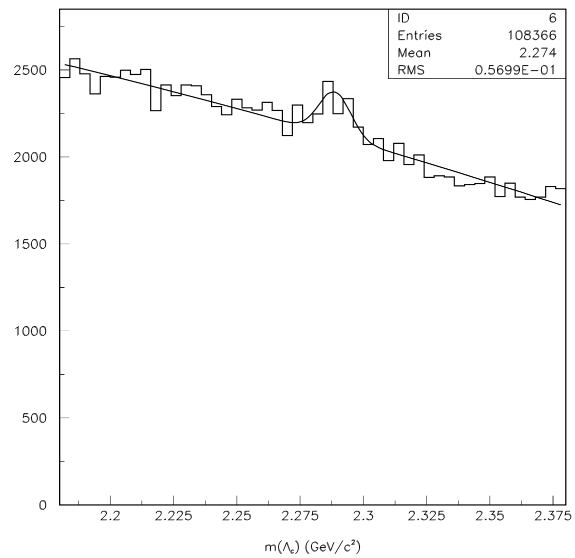

Figure 6.4: Mass(pKπ) of the real data set after filter, strip. KSU substrip, good 3-prong vertex and track cuts, Soichi cuts, SDZ and PTBAL cuts. It has a significance of 5.97σ. There are 998$\pm$167 signal events and 107368$\pm$366 background events assuming that the peak is Gaussian and the background is quadratic.

To optimize the significance of our Λ_c signal, we sent both the reconstructed real data and the reconstructed Monte Carlo data through the same cuts mentioned above. We then fit the real data to a Gaussian peak and a quadratic background and established that the signal initially has a significance of 5.97σ with 998 $\pm$ 167 signal events and 107,368 background events.

Given this, for our optimization, we set the signal region to be from 2.26 GeV/c^2 to 2.32 GeV/c^2 and the background region to be outside this. We then trained a Neural Network with a 5-20-1 architecture with Rprop updating (page 18). For training, we used 12,912 MC events and 12,912 real background events. For a validation set we used 4,260 of each type of event and stopped training when the error on the validation set stopped decreasing steadily.

After training was complete, we determined the Neural Net cut to be the one which optimized $\frac{n_s}{\sqrt{n_s+n_b}}$. The number of signal events, n_s, was estimated by $n_s = 998$ initial signal events $\times$ efficiency of MC.† Background, n_b, was estimated by performing a binned quadratic fit on the surviving events in the wings and integrating over the signal region. From these estimates, it was determined that the optimum NN cut should be 0.94 which predicted 632 signal events, 451 background events in the signal region and a significance of 19.2σ. Applying this cut, 2271 real events survived (see figure 6.5 for the mass plot of the final data set) which corresponded to 886.4$\pm$43.4 signal events and

†998 came from the fit on the data prior to using the Neural Net. See figure 6.4 for the histogram of the data

1384.1±48.8 background events and a significance of 20.4σ. See table 6.1 for detail on significance and alternate ways of calculating it.

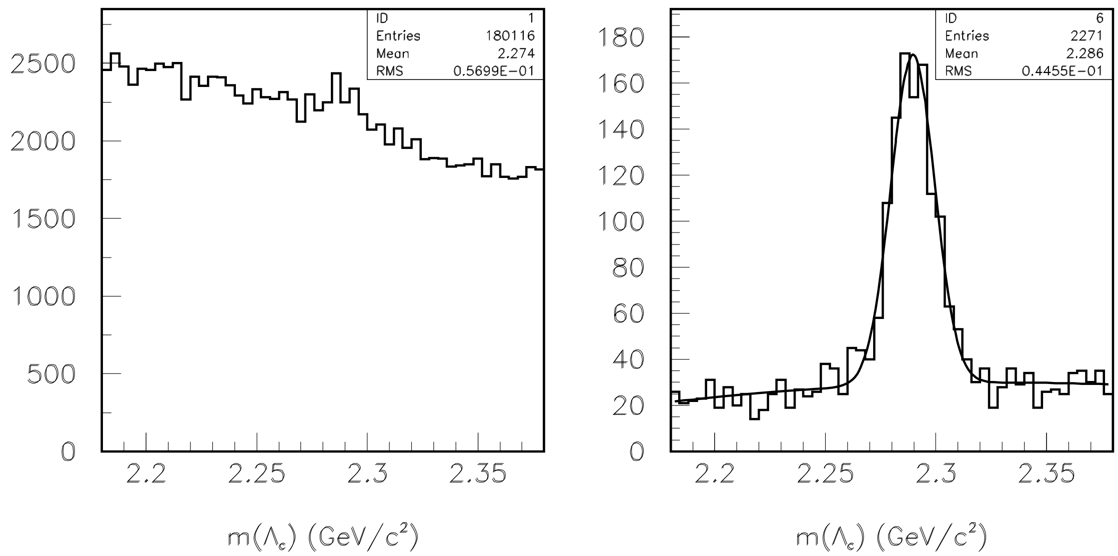

Figure 6.5: (left) Mass(pKπ) of the real data set before Neural Net cuts and (right) after. It has a significance of 20.4σ. There are 886±43 signal events and 1384 background events assuming that the peak is Gaussian, the background is quadratic and the number of signal and background events are variables.

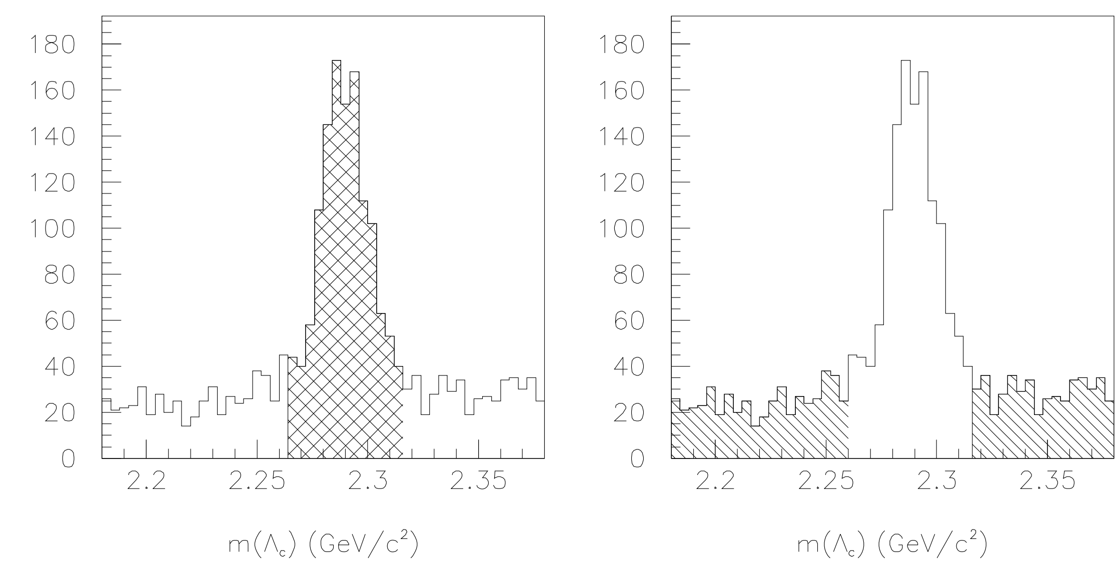

Figure 6.6: Mass(pKπ) of the real data set after the Neural Net cut. For future reference: the shaded area on the left refers to the signal region and on the right to the background regions.

Background $\rightarrow$ $\downarrow$ Number of Events	Quadratic	Linear
Allowed to Float	20.4σ	23.2σ
Not Allowed to Float	22.6σ	26.5σ

Table 6.1: The significance of the fit depending on the technique of fitting. As the background model simplifies, from quadratic to linear, the significance goes up. And also, as the more dramatic effect can be caused by setting the number of background events from a floating variable (as in the 6 variable case) to a number directly dependent on the total number of events minus the number of signal events (as in the 5 variable case).

Applying this cut to the reconstructed Monte Carlo, 11,454 MC events survived with a significance of 99.4σ. See figure 6.7 for a mass plot of the surviving reconstructed MC.

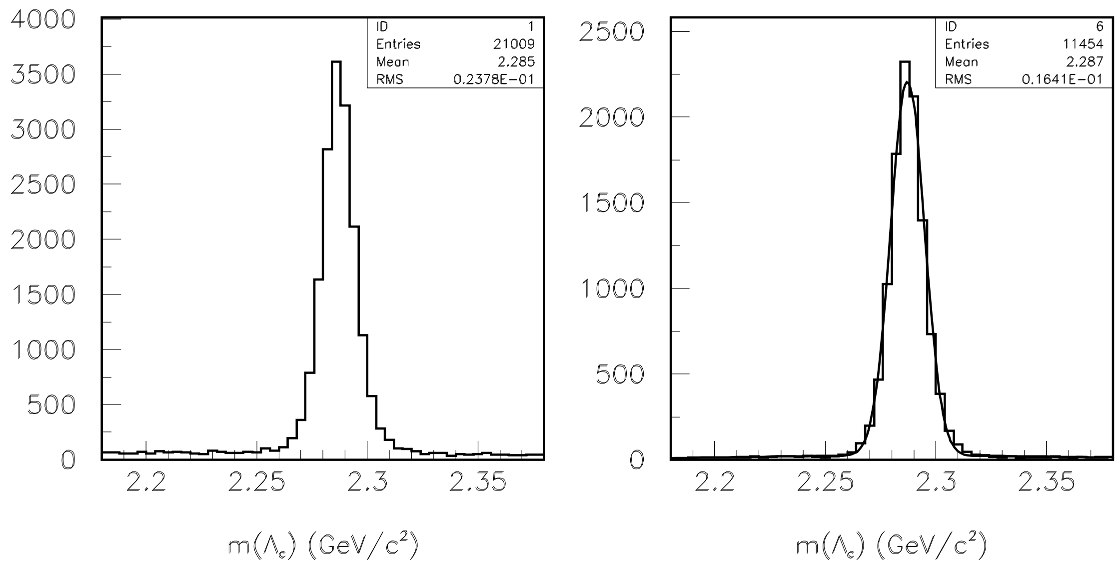

Figure 6.7: (left) Mass(pKπ) of the MC data set before Neural Net cuts and (right) after. It has a significance of 99σ. There are 10510 ± 106 signal events and 944 background events assuming that the peak is Gaussian, the background is quadratic and the number of signal and background events are variables. The central mass is 2.287 GeV/c^2 with σ = 7.65 MeV/c^2.

Refer to figures 6.8 and 6.9 for a look at the final data sets (real and MC) reconstructed as other reflections.

Also note that if we varied the Neural Network cut, we would get the histograms as seen in figure 6.10. The common structure to the nine plots indicates that the cut we used is not a bizarre statistical fluctuation. Note that the cut of 0.94 does not produce the most significant data set, but it does produce the largest predicted significance for a data set.

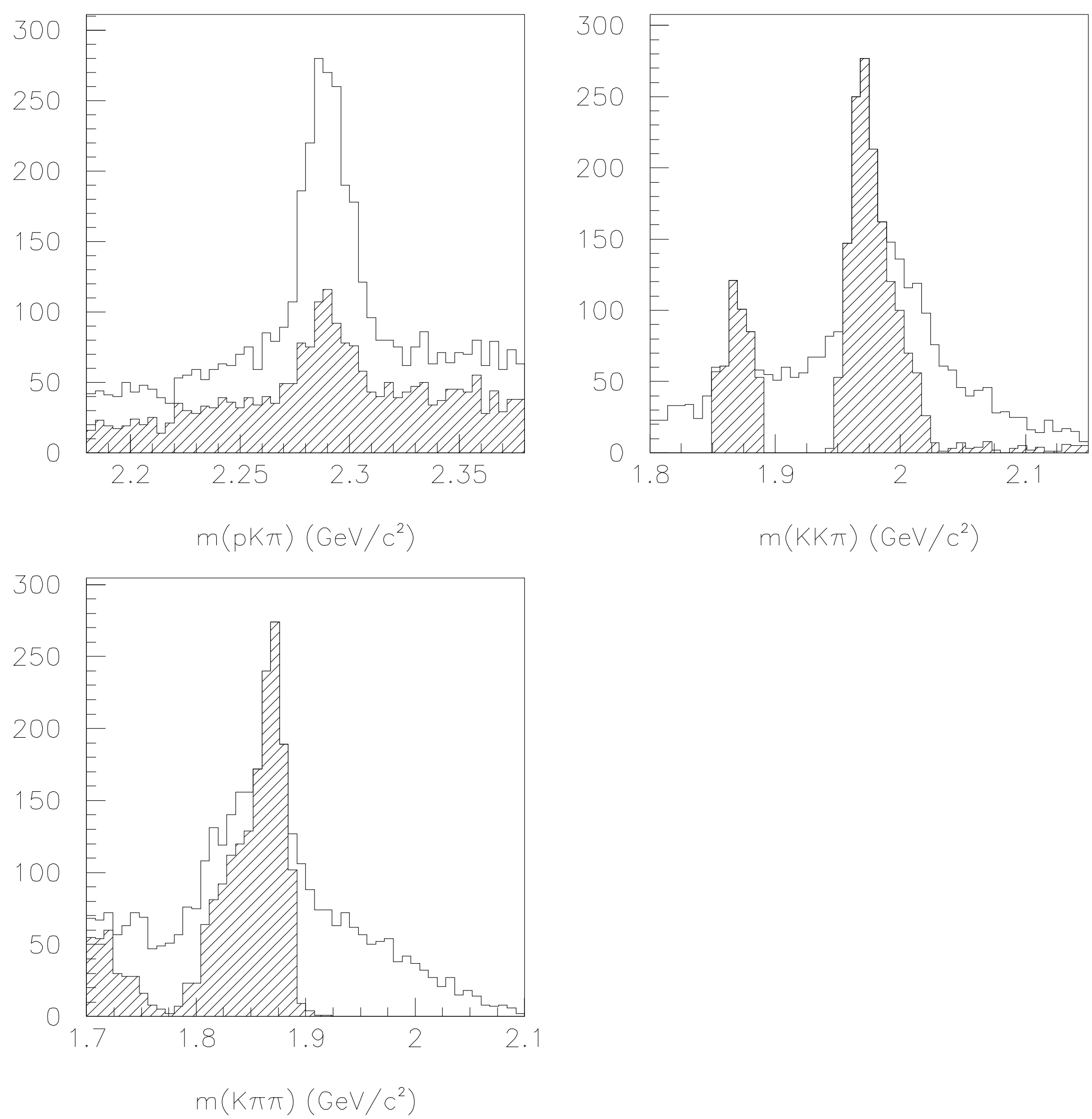

Figure 6.8: Reconstructed masses of real data after the Neural Net cuts are made. The shaded region is the region cut by the D mass cuts. This data set was produced by running the 19,763 events, which were in the D mass range and cut, through the Neural Net cut. The 2137 events of the 19,763 which survived are in the shaded region. These events are not used in the analysis. The larger outline is the total of the D region (2137 events) and the final data set (2271 events).

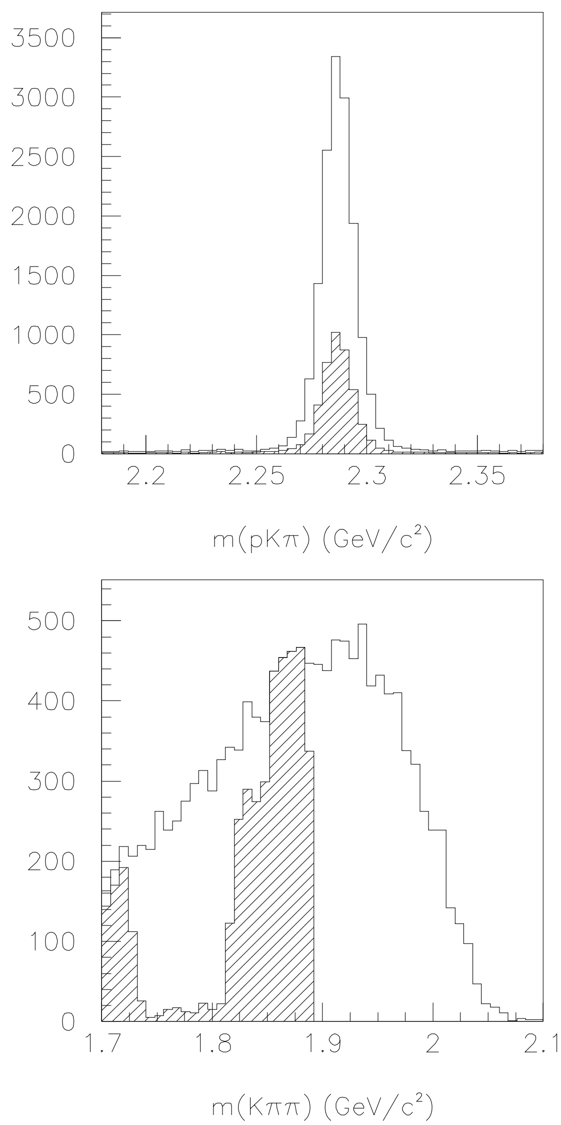

Figure 6.9: Reconstructed masses of MC data after the Neural Net cuts are made. The shaded region is the region cut by the D mass cuts. The larger outline is the total of the D region (4730 events) and the final data set (11454 events).

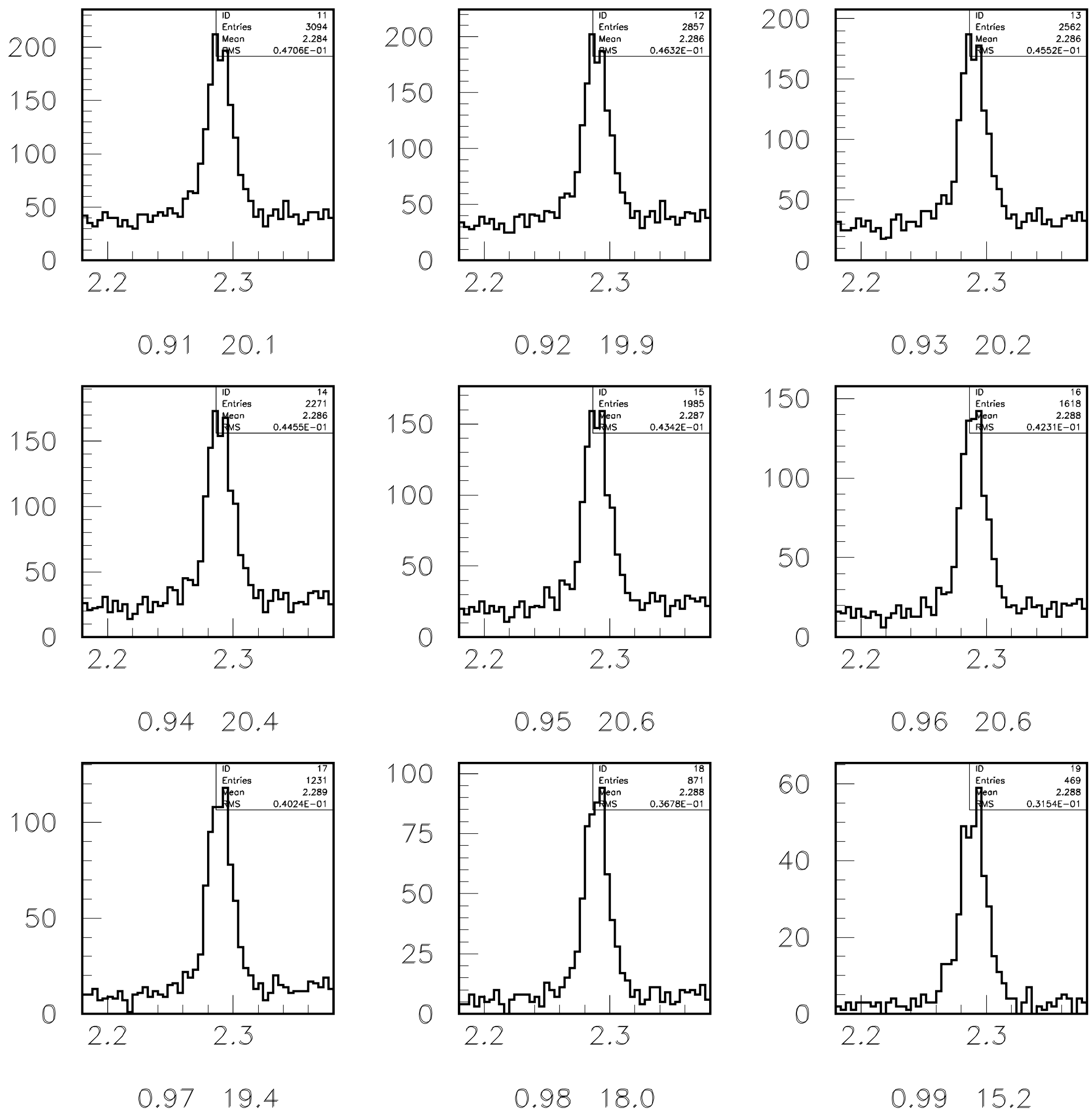

Figure 6.10: Mass(pKπ) (GeV/c^2) The first number in each caption is the NN cut used to create the histogram. The second number is the significance found by MINUIT assuming a Gaussian peak and quadratic background.

Chapter 7

The Signal Density

For the final fit, we used the fitting software, MINUIT, to perform an extended maximum likelihood fit. The likelihood was assumed to have the form

$$\ln \mathcal{L} = \sum_i \ln \mathcal{L}_i - \left(\frac{1}{2} \ln\left[2\pi \mathrm{n_{pred}}\right] + \frac{[n_{\mathrm{pred}} - n_{\mathrm{obs}}]^2}{2n_{\mathrm{pred}}} \right), \tag{7.1}$$

where $n_{\mathrm{pred}} = n_{\mathrm{s}} + n_{\mathrm{b}}$ and n_{obs} are the predicted and observed number of events, respectively, and $\mathcal{L}_i$ is the likelihood of each event defined by a joint probability density in the five-dimensional space of decay kinematics and the one-dimensional space of $m_{pK\pi}$.

The likelihood for an individual event is given by:

$$\mathcal{L}_i = \frac{n_{\mathrm{s}}}{n_{\mathrm{s}} + n_{\mathrm{b}}} G(m_i) S(\vec{x}_i) A(\vec{x}_i) + \frac{n_{\mathrm{b}}}{n_{\mathrm{s}} + n_{\mathrm{b}}} Q(m_i) B(\vec{x}_i) \tag{7.2}$$

where
$G(m_i) = \frac{e^{(m_i - m_0)^2/(2\sigma^2)}}{N_G \sigma \sqrt{2\pi}}$ = a Gaussian description of the Λ_c mass peak with normalization N_G,
$S(\vec{x}_i)$ = signal density,
$A(\vec{x}_i)$ = acceptance,
$Q(m_i) = \frac{1 + b_{\mathrm{l}}(m_i - 2.28) + b_{\mathrm{q}}(m_i - 2.28)^2}{N_Q}$ = a quadratic description of the background with normalization N_Q,
$B(\vec{x}_i)$ = background density, and
$\vec{x} = (m_{12}^2, m_{23}^2, cos(\theta_{\mathrm{p}}), \phi_{\mathrm{p}}, \phi_{K\pi})$ = the vector which describes each event. It is defined more specifically for this problem in chapter 8. The normalizations fixed $\int_{2.18}^{2.38} G\,\mathrm{dm} = 1.0$ and $\int_{2.18}^{2.38} B\,\mathrm{dm} = 1.0$

To find the signal density, S, we used the helicity formalism as described in chapter 2, and outlined more explicitly in [Pur 96]. As seen previously as equation 2.27,

$$\begin{aligned} \mathrm{d}\Gamma \quad & \sim \tfrac{1}{2}(1 + P_{\mathrm{A}}) \textstyle\sum_{\lambda_{\mathrm{C}}\lambda_{\mathrm{D}}\lambda_{\mathrm{E}}} |\sum_{\mathrm{B}} BW(m_{\mathrm{B}}) \xi_{B,\frac{1}{2},\lambda_{\mathrm{C}},\lambda_{\mathrm{D}},\lambda_{\mathrm{E}}}|^2 \\ & + \tfrac{1}{2}(1 - P_{\mathrm{A}}) \textstyle\sum_{\lambda_{\mathrm{C}}\lambda_{\mathrm{D}}\lambda_{\mathrm{E}}} |\sum_{\mathrm{B}} BW(m_{\mathrm{B}}) \xi_{B,-\frac{1}{2},\lambda_{\mathrm{C}},\lambda_{\mathrm{D}},\lambda_{\mathrm{E}}}|^2 \end{aligned} \tag{7.3}$$

for the decay A→B(→DE)C.

We used the relativistic Breit-Wigner amplitude (previously seen in equations 2.28 and 2.29) for the decay mode $\Lambda_{\mathrm{c}} \to \mathrm{r}(\to \mathrm{AB})\mathrm{C}$,

$$(-2|p_{\mathrm{C}}||p_{\mathrm{A}}|)^L \frac{F_{\Lambda_{\mathrm{c}}} F_{\mathrm{r}}}{m_0^2 - m_{\mathrm{r}}^2 - i m_0 \Gamma_{\mathrm{r}}} \tag{7.4}$$

where

$$\Gamma_{\rm r} = \Gamma_0(\frac{q}{q_0})^{2L+1}\frac{m_0}{m_{\rm r}}\frac{F_{\rm r}^2(q)}{F_{\rm r}^2(q_0)} \tag{7.5}$$

for resonance r at the reconstructed two body mass $m_{\rm r}$, with the momentum of a daughter particle in the resonant particle's rest frame q (and q_0 when $m_{\rm r} = m_0$), and with resonant mass and width m_0 and Γ_0 as found in [PDG 98]. Using this convention, we set the Breit-Wigner amplitude for the nonresonant decay to be 1.0. The Breit-Wigner amplitude squared was normalized numerically within the MINUIT fit.

Deriving $\xi_{\rm B,m_A,\lambda_B,\lambda_C,\lambda_D,\lambda_E}$ for several resonances yields tables 7.1-7.4[Pur 96]. Because two of the three daughter particles are spin 0 particles, the problem simplifies greatly. Also note that the number of coefficients in tables 7.2 and 7.3 are reduced to two because of parity conservation.

m	$\lambda_{\rm p}$	Amplitude
$\frac{1}{2}$	$\frac{1}{2}$	$E_1e^{i\phi_{E_1}}d^{\frac{1}{2}}_{\frac{1}{2}\frac{1}{2}}(\theta_{\overline{\rm K}^{*0}})d^1_{10}(\theta'_{\rm K})e^{i\phi'_{\rm K}} + E_2e^{i\phi_{E_2}}d^{\frac{1}{2}}_{\frac{1}{2}-\frac{1}{2}}(\theta_{\overline{\rm K}^{*0}})d^1_{00}(\theta'_{\rm K})e^{i\phi_{\overline{\rm K}^{*0}}}$
$\frac{1}{2}$	-$\frac{1}{2}$	$E_3e^{i\phi_{E_3}}d^{\frac{1}{2}}_{\frac{1}{2}\frac{1}{2}}(\theta_{\overline{\rm K}^{*0}})d^1_{00}(\theta'_{\rm K}) + E_4e^{i\phi_{E_4}}d^{\frac{1}{2}}_{\frac{1}{2}-\frac{1}{2}}(\theta_{\overline{\rm K}^{*0}})d^1_{-10}(\theta'_{\rm K})e^{i(\phi_{\overline{\rm K}^{*0}}-\phi'_{\rm K})}$
-$\frac{1}{2}$	$\frac{1}{2}$	$E_1e^{i\phi_{E_1}}d^{\frac{1}{2}}_{-\frac{1}{2}\frac{1}{2}}(\theta_{\overline{\rm K}^{*0}})d^1_{10}(\theta'_{\rm K})e^{-i(\phi_{\overline{\rm K}^{*0}}-\phi'_{\rm K})} + E_2e^{i\phi_{E_2}}d^{\frac{1}{2}}_{-\frac{1}{2}-\frac{1}{2}}(\theta_{\overline{\rm K}^{*0}})d^1_{00}(\theta'_{\rm K})$
-$\frac{1}{2}$	-$\frac{1}{2}$	$E_3e^{i\phi_{E_3}}d^{\frac{1}{2}}_{-\frac{1}{2}\frac{1}{2}}(\theta_{\overline{\rm K}^{*0}})d^1_{00}(\theta'_{\rm K})e^{-i\phi_{\overline{\rm K}^{*0}}} + E_4e^{i\phi_{E_4}}d^{\frac{1}{2}}_{-\frac{1}{2}-\frac{1}{2}}(\theta_{\overline{\rm K}^{*0}})d^1_{-10}(\theta'_{\rm K})e^{-i\phi'_{\rm K}}$

Table 7.1: Amplitudes for $\Lambda_{\rm c}^+(\frac{1}{2}^+) \to (\overline{\rm K}^{*0}(1^-) \to {\rm K}^-\pi^+)$ p $(\frac{1}{2}^+)$ decay mode.

m	$\lambda_{\rm p}$	Amplitude
$\frac{1}{2}$	$\frac{1}{2}$	$F_1e^{i\phi_{F_1}}d^{\frac{1}{2}}_{\frac{1}{2}\frac{1}{2}}(\theta_{\Delta^{++}})d^{\frac{3}{2}}_{\frac{1}{2}\frac{1}{2}}(\theta'_{\rm p}) + F_2e^{i\phi_{F_2}}d^{\frac{1}{2}}_{\frac{1}{2}-\frac{1}{2}}(\theta_{\Delta^{++}})d^{\frac{3}{2}}_{-\frac{1}{2}\frac{1}{2}}(\theta'_{\rm p})e^{i(\phi_{\Delta^{++}}-\phi'_{\rm p})}$
$\frac{1}{2}$	-$\frac{1}{2}$	$F_1e^{i\phi_{F_1}}d^{\frac{1}{2}}_{\frac{1}{2}\frac{1}{2}}(\theta_{\Delta^{++}})d^{\frac{3}{2}}_{\frac{1}{2}-\frac{1}{2}}(\theta'_{\rm p})e^{i\phi'_{\rm p}} + F_2e^{i\phi_{F_2}}d^{\frac{1}{2}}_{\frac{1}{2}-\frac{1}{2}}(\theta_{\Delta^{++}})d^{\frac{3}{2}}_{-\frac{1}{2}-\frac{1}{2}}(\theta'_{\rm p})e^{i\phi_{\Delta^{++}}}$
-$\frac{1}{2}$	$\frac{1}{2}$	$F_1e^{i\phi_{F_1}}d^{\frac{1}{2}}_{-\frac{1}{2}\frac{1}{2}}(\theta_{\Delta^{++}})d^{\frac{3}{2}}_{\frac{1}{2}\frac{1}{2}}(\theta'_{\rm p})e^{-i\phi_{\Delta^{++}}} + F_2e^{i\phi_{F_2}}d^{\frac{1}{2}}_{-\frac{1}{2}-\frac{1}{2}}(\theta_{\Delta^{++}})d^{\frac{3}{2}}_{-\frac{1}{2}\frac{1}{2}}(\theta'_{\rm p})e^{-i\phi'_{\rm p}}$
-$\frac{1}{2}$	-$\frac{1}{2}$	$F_1e^{i\phi_{F_1}}d^{\frac{1}{2}}_{-\frac{1}{2}\frac{1}{2}}(\theta_{\Delta^{++}})d^{\frac{3}{2}}_{\frac{1}{2}-\frac{1}{2}}(\theta'_{\rm p})e^{-i(\phi_{\Delta^{++}}-\phi'_{\rm p})} + F_2e^{i\phi_{F_2}}d^{\frac{1}{2}}_{-\frac{1}{2}-\frac{1}{2}}(\theta_{\Delta^{++}})d^{\frac{3}{2}}_{-\frac{1}{2}-\frac{1}{2}}(\theta'_{\rm p})$

Table 7.2: Amplitudes for $\Lambda_{\rm c}^+(\frac{1}{2}^+) \to (\Delta^{++}(\frac{3}{2}^+) \to {\rm p}\pi^+){\rm K}^-$ decay mode.

m	$\lambda_{\rm p}$	Amplitude
$\frac{1}{2}$	$\frac{1}{2}$	$H_1e^{i\phi_{H_1}}d^{\frac{1}{2}}_{\frac{1}{2}\frac{1}{2}}(\theta_{\Lambda(1520)})d^{\frac{3}{2}}_{\frac{1}{2}\frac{1}{2}}(\theta'_{\rm p}) + H_2e^{i\phi_{H_2}}d^{\frac{1}{2}}_{\frac{1}{2}-\frac{1}{2}}(\theta_{\Lambda(1520)})d^{\frac{3}{2}}_{-\frac{1}{2}\frac{1}{2}}(\theta'_{\rm p})e^{i(\phi_{\Lambda(1520)}-\phi'_{\rm p})}$
$\frac{1}{2}$	-$\frac{1}{2}$	-$(H_1e^{i\phi_{H_1}}d^{\frac{1}{2}}_{\frac{1}{2}\frac{1}{2}}(\theta_{\Lambda(1520)})d^{\frac{3}{2}}_{\frac{1}{2}-\frac{1}{2}}(\theta'_{\rm p})e^{i\phi'_{\rm p}} + H_2e^{i\phi_{H_2}}d^{\frac{1}{2}}_{\frac{1}{2}-\frac{1}{2}}(\theta_{\Lambda(1520)})d^{\frac{3}{2}}_{-\frac{1}{2}-\frac{1}{2}}(\theta'_{\rm p})e^{i\phi_{\Lambda(1520)}})$
-$\frac{1}{2}$	$\frac{1}{2}$	$H_1e^{i\phi_{H_1}}d^{\frac{1}{2}}_{-\frac{1}{2}\frac{1}{2}}(\theta_{\Lambda(1520)})^{\frac{3}{2}}_{\frac{1}{2}\frac{1}{2}}(\theta'_{\rm p})e^{-i\phi_{\Lambda(1520)}} + H_2e^{i\phi_{H_2}}d^{\frac{1}{2}}_{-\frac{1}{2}-\frac{1}{2}}(\theta_{\Lambda(1520)})d^{\frac{3}{2}}_{-\frac{1}{2}\frac{1}{2}}(\theta'_{\rm p})e^{-i\phi'_{\rm p}}$
-$\frac{1}{2}$	-$\frac{1}{2}$	-$(H_1e^{i\phi_{H_1}}d^{\frac{1}{2}}_{-\frac{1}{2}\frac{1}{2}}(\theta_{\Lambda(1520)})d^{\frac{3}{2}}_{\frac{1}{2}-\frac{1}{2}}(\theta'_{\rm p})e^{-i(\phi_{\Lambda(1520)}-\phi'_{\rm p})} + H_2e^{i\phi_{H_2}}d^{\frac{1}{2}}_{-\frac{1}{2}-\frac{1}{2}}(\theta_{\Lambda(1520)})d^{\frac{3}{2}}_{-\frac{1}{2}-\frac{1}{2}}(\theta'_{\rm p}))$

Table 7.3: Amplitudes for $\Lambda_{\rm c}^+(\frac{1}{2}^+) \to (\Lambda(1520)(\frac{3}{2}^-) \to {\rm pK}^-)\pi^+$ decay mode.

The method used to find the acceptance and the background are outlined in chapter 8.

m	λ_{p}	Amplitude
$\frac{1}{2}$	$\frac{1}{2}$	$N_{++}e^{i\phi_{N_{++}}}$
$\frac{1}{2}$	-$\frac{1}{2}$	$N_{+-}e^{i\phi_{N_{+-}}}$
-$\frac{1}{2}$	$\frac{1}{2}$	$N_{-+}e^{i\phi_{N_{-+}}}$
-$\frac{1}{2}$	-$\frac{1}{2}$	$N_{--}e^{i\phi_{N_{--}}}$

Table 7.4: Amplitudes for nonresonant $\Lambda_{\mathrm{c}}^{+}(\frac{1}{2}^{+}) \rightarrow \mathrm{pK}^{-}\pi^{+}$ decay mode.

Chapter 8

Acceptance and Background Model

Once the final data set was established, we used the constrained data for the models, i.e. we constrained the pKπ reconstructed mass to be the Λ_c PDG mass value.

Using the surviving Λ_c Monte Carlo as acceptance and all events more than 3.0σ from the mean of the peak as background (see figure 6.6), we then set out to model these distributions. We used the frame of reference to be the Λ_c rest frame with the x-axis being the direction the Λ_c traveled in the lab frame, the z-axis to be the polarization axis as defined by the cross product of the beam axis and the x-axis, and the y-axis to be the z-axis cross the x-axis. See figures 8.1 and 8.2 for the coordinate system used. Note that the polarization axis is perpendicular to the production plane and is the reference from which we determine the orientation of the Λ_c spin. For each of these events, we established (by the convention established in [Kor 91]) the independent variables to be:

1. $m^2(K\pi)$,
2. $m^2(p\pi)$,
3. the cosine of polar angle, θ_p, of the momentum of the daughter proton relative to the polarization axis,
4. the angle, ϕ_p, between the x-axis and the xy plane projection of the momentum of the daughter proton, and
5. the orientation angle, $\phi_{K\pi}$, of the plane with Kπ daughter pair relative to the plane of the daughter proton and the polarization axis.

8.1 Phase Space

The phase space is defined by the allowed values of the above kinematic variables. In order to account for the shape of this phase space in the analysis, it becomes essential to be able to model it. This can be done in two ways. One way is to use the points used in the truth tables of the 7 million generated MC events. The other way is to assume that the phase space is evenly (uniformly) distributed within the allowed limits of the above variables and to generate quickly a set of random points within this range. This second method is referred to as “fast Monte Carlo”. In order to

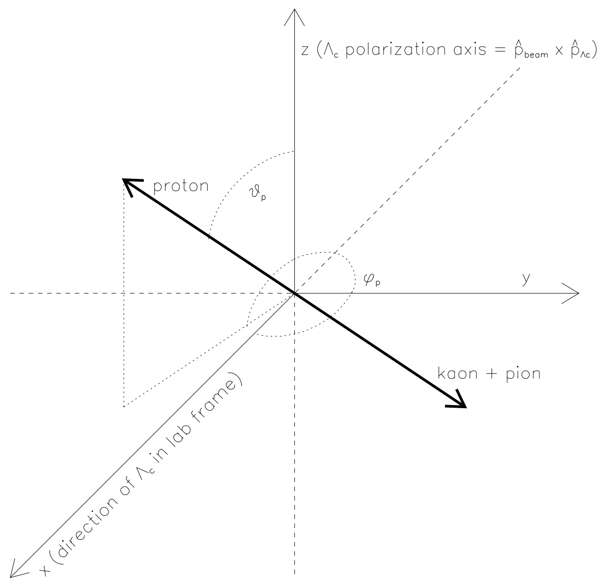

Figure 8.1: $\Lambda_c \rightarrow pK\pi$ in Λ_c rest frame. (θ_p, ϕ_p) define the proton direction in the Λ_c rest frame. Note that the xy plane is the plane of production.

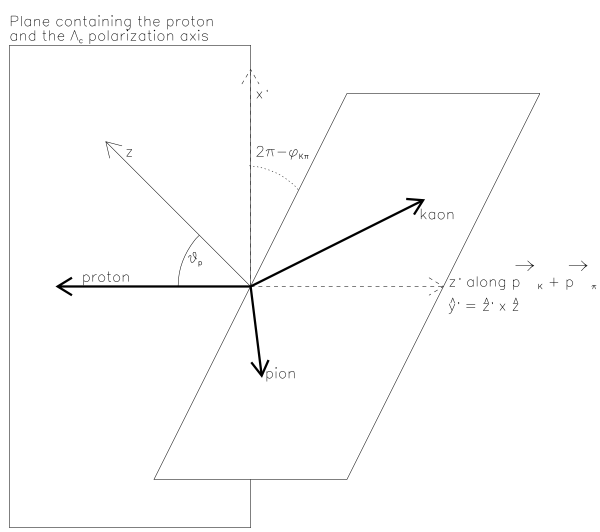

Figure 8.2: $\Lambda_c \rightarrow pK\pi$ in Λ_c rest frame.

show that these methods are equivalent, we used 1 million fast MC points and 1,000,126 truth table points*, binned them in the one dimensional projections and compared them. See figure 8.3 for the comparison of the one dimensional projections.

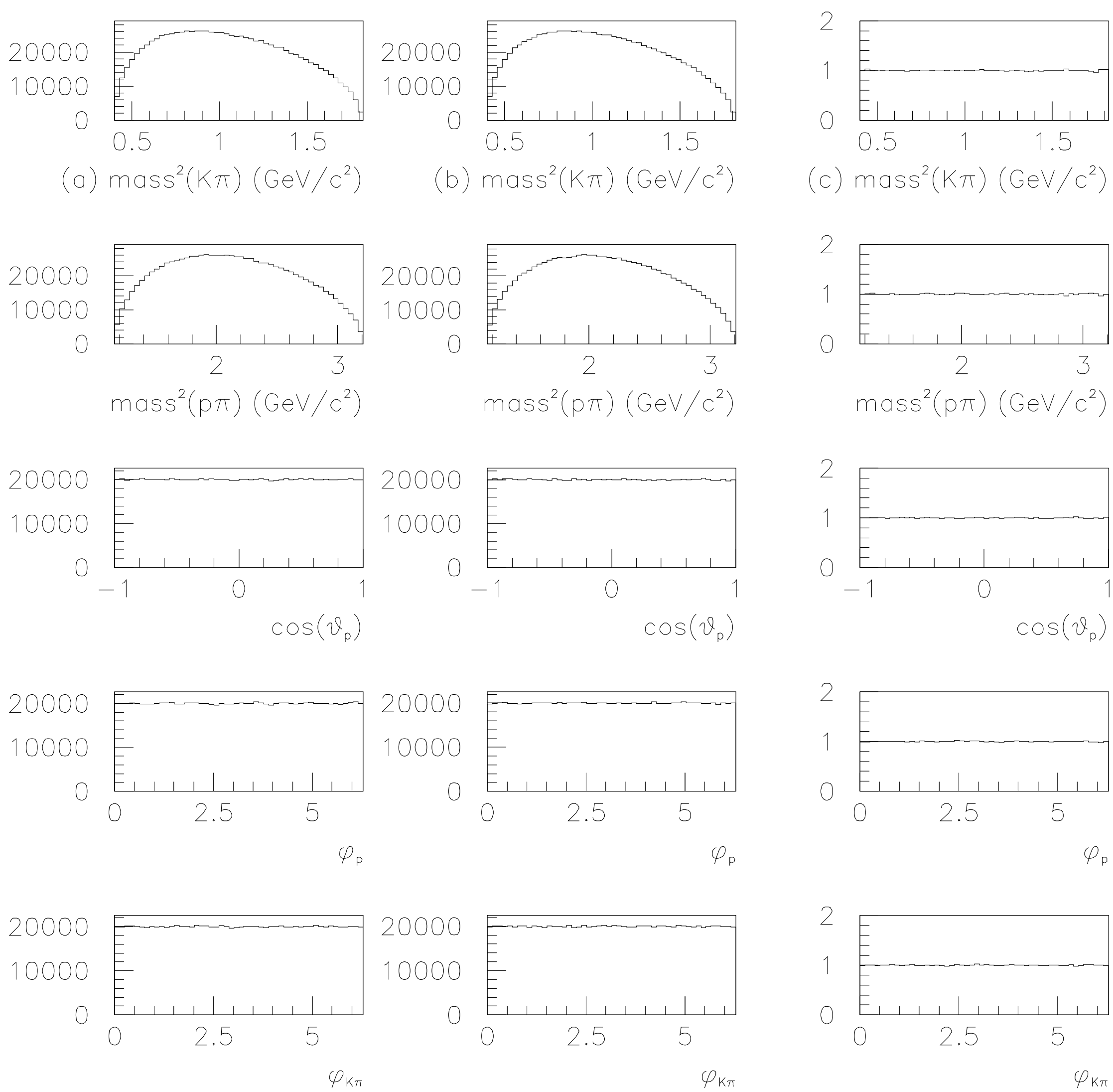

Figure 8.3: (a) The one dimensional projections of the fast MC phase space, (b) The one dimensional projections of the truth table MC phase space, and (c) the result of dividing the contents of each bin of (a) by the content of the respective bin in (b).

As can be seen in figure 8.3, the ratio of the two samples is near 1.0 in all cases. From this we assume that the use of either set is valid.

With these fast MC points, we can model the shape of phase space. Later in this dissertation, when we refer to "uniform phase space", we are referring to this distribution of 1 million points.

*These truth table points are from the Release 7 MC generations produced at USC.

The boundaries of phase space are defined kinematically in [PDG 98], but in reality, the boundaries are blurred, by the resolution of the detector. In order to offset these resolution problems , we constrained the reconstructed pKπ mass to be the PDG value of the Λ_c. This forced all of the reconstructed data points to be within the same phase space. See appendix F for more justification of constraining the events.

8.2 Modeling

8.2.1 K-Nearest-Neighbors: Basics

For modeling the five dimensional distribution of acceptance (background), we used the K-nearest-neighbors technique as outlined in [Bis 95]. To find the probability density at a point in phase space, we would find the minimum spherical volume which encompassed the fixed number, K, of points. We then estimated the unnormalized probability density to be K divided by the volume. This technique is based on the following line of reasoning:

The probability, P, that an event $\vec{x}$ which is drawn from some unknown density function, $p(\vec{x})$, will fall in a region of space, R, can be described mathematically as

$$P = \int_R p(\vec{x'})d\vec{x'} \tag{8.1}$$

If we independently draw N data points from p($\vec{x}$), the probability, $Pr(K)$, that K of them will fall within R can be expressed as

$$Pr(K) = \frac{N!}{K!(N-K)!}P^K(1-P)^{N-K} \tag{8.2}$$

where the mean fraction of points falling in R is <K/N> = P. The variance around this point is $< K/(N-P)^2 >= P(1-P)/N$. As $N \to \infty$, the variance drops to zero and

$$P \simeq K/N \tag{8.3}$$

Assuming $p(\vec{x})$ is continuous and varies little in R, equation 8.2.1 can be approximated by

$$P = \int_R p(\vec{x'})d\vec{x'} \simeq p(\vec{x})V \tag{8.4}$$

where V = the volume of R and $\vec{x}$ is some point lying in R. Equating 8.2.1 with 8.2.1, gives us

$$p(\vec{x}) \simeq K/NV \tag{8.5}$$

If the density is unnormalized, equation 8.2.1 can be reduced to

$$p(\vec{x})_{unnormalized} \simeq K/V \tag{8.6}$$

Choosing to fix the number of points, K, or the encompassing volume, V, is a matter of the user's choice. For this dissertation, we chose to fix the number of points.

8.2.2 Implementation

To implement this method, we first reduced the bias in each dimension. In other words, we linearly transformed all data sets so that each dimension of the uniform phase space had a mean of 0.0 and a standard deviation of 1.0. For example, let $\vec{x}$ be one decay event, where $\vec{x}$ = (0.89, 2.42, 0.12, 1.98, 5.97). After transforming it, $\vec{x} \to \vec{x_t}$ = (-0.43, 0.57, 0.21, -0.64, 1.56).

Next, we found the distance in this transformed space from every point in the acceptance (background) set to each point in the set of real data points (those from the experimental data set which survived all of the cuts). The 4 nearest-neighbors were 0.43, 0.47, 0.49, and 0.54 from $\vec{x_t}$.

We then found the volume needed to enclose each nearest-neighbor by seeing how many randomly generated points were within the corresponding distance and phase space and scaling the number to the volume which encompassed the generated points. For $\vec{x_t}$, the volumes which encompassed the 4 nearest-neighbors were 0.069, 0.10, 0.12, and 0.20.

The last step in the K-nearest-neighbors method was to establish the optimum value of K. We did this by setting up a measure of closeness. Our measure was the sum of the absolute value of differences in each bin of the five histograms of the acceptance (background) and its model when normalized to the same value. by doing this we found that K = 4 for acceptance and background. We ran the 100,000 fast MC points through this process followed by the real data points. Again, for the case of $\vec{x_t}$, this would correspond to an estimated unscaled acceptance of 4/0.20 = 19.9[†], and since the transformation of coordinates was linear, this is also the unnormalized probability density of $\vec{x}$.

A comparison of the model as found by this technique and the acceptance (background) can be seen in figures 8.4 and 8.5.

8.2.3 Tweaking

At this point, the correlations between the variables is incorporated into the estimated probability densities. Our next step is to tweak each probability for greater accuracy. To do this, we tried to optimize the one dimensional projections of the model, i.e. we minimized the total absolute difference between each bin in the acceptance (background) histograms and the model. This optimization is similar to before, except we added a new histogram and assumed that the corrections can ignore the correlations.

The new histogram is for $\mathrm{m}^2(\mathrm{pK})$. Our justification for using it is as follows: In three body decay, it really does not matter which 2 pairs of daughter particles we pick for analysis, since the third pair is directly related to the first two. In our case

$m^2(\mathrm{pK}) = m^2(\mathrm{pK}\pi) + m^2(\mathrm{p}) + m^2(\mathrm{K}) + m^2(\pi)$ - $m^2(\mathrm{p}\pi)$ - $m^2(\mathrm{K}\pi)$.

Also, if we assume the variables are uncorrelated then the probability can be factored. For example,

$A = A(m^2_{\mathrm{K}\pi}, m^2_{\mathrm{p}\pi}, cos(\theta_\mathrm{p}), \phi_\mathrm{p}, \theta_{\mathrm{K}\pi}) = A_1(m^2_{\mathrm{K}\pi})A_2(m^2_{\mathrm{p}\pi})A_3(cos(\theta_\mathrm{p}))A_4(\phi_\mathrm{p})A_5(\theta_{\mathrm{K}\pi})$

But since the choice of pairs to use is arbitrary, $A_1(m^2_{\mathrm{K}\pi})$ is just as significant as $A_2(m^2_{\mathrm{p}\pi})$ which is just a significant as $A_3(m^2_{\mathrm{pK}})$, so we can rewrite A to be:

[†]Technically, this is not an acceptance, but it is proportional to acceptance. In order to find the true acceptance, we would need to know the number, N, of MC points which were generated. Since this value is the same for every location in phase space, there is no need to incorporate it into the formula at this point. All the densities will be off by the same factor and this will be taken care of when the density is normalized later.

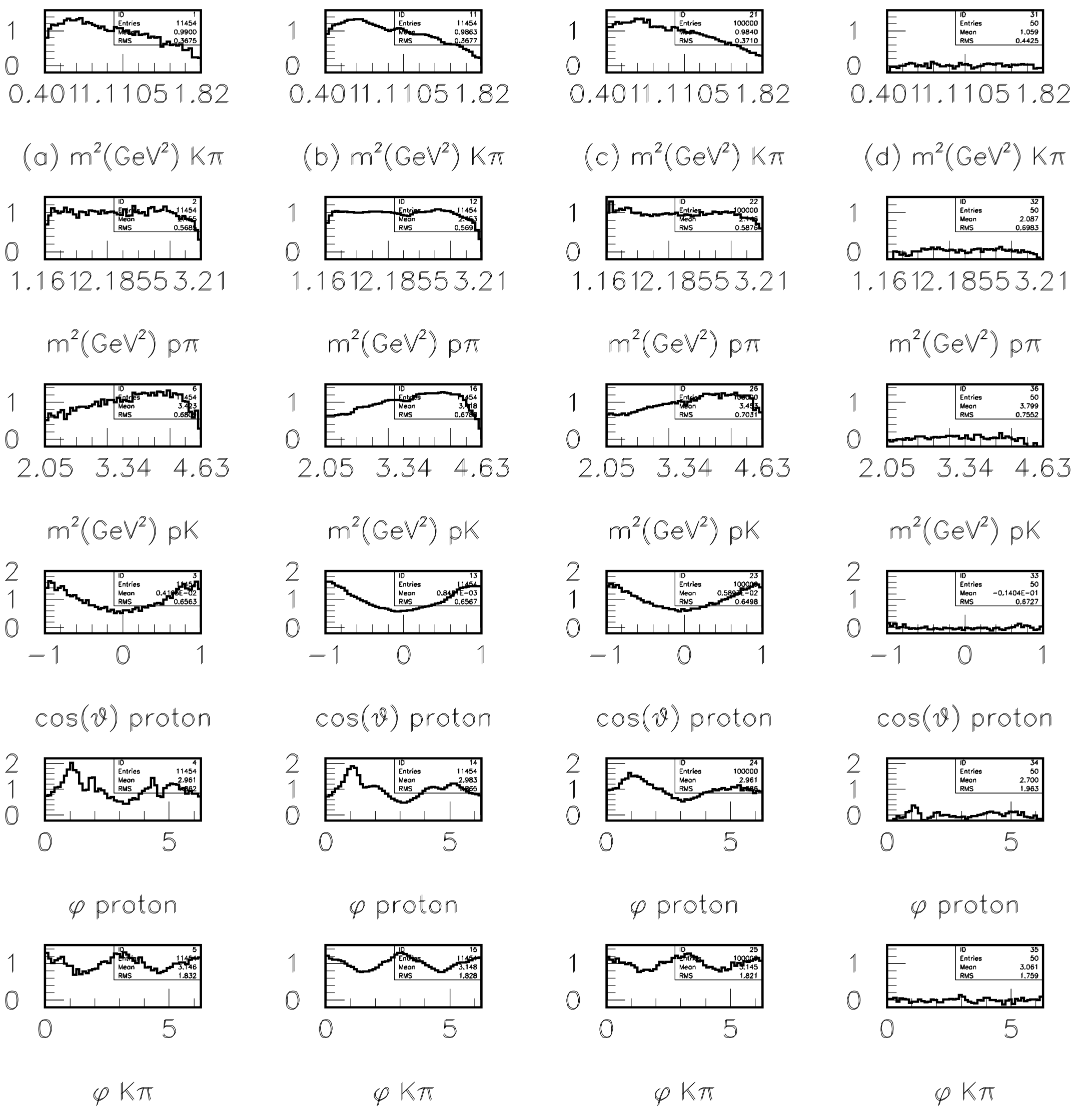

Figure 8.4: Acceptance. (a) The one dimensional projections of the surviving Monte Carlo divided by uniform phase space, (b) The one dimensional projections of the surviving Monte Carlo divided by uniform phase space after smoothing with HSMOOF, (c) The model of the acceptance as found by the nearest-neighbors technique, (d) the difference between the real acceptance and the model.

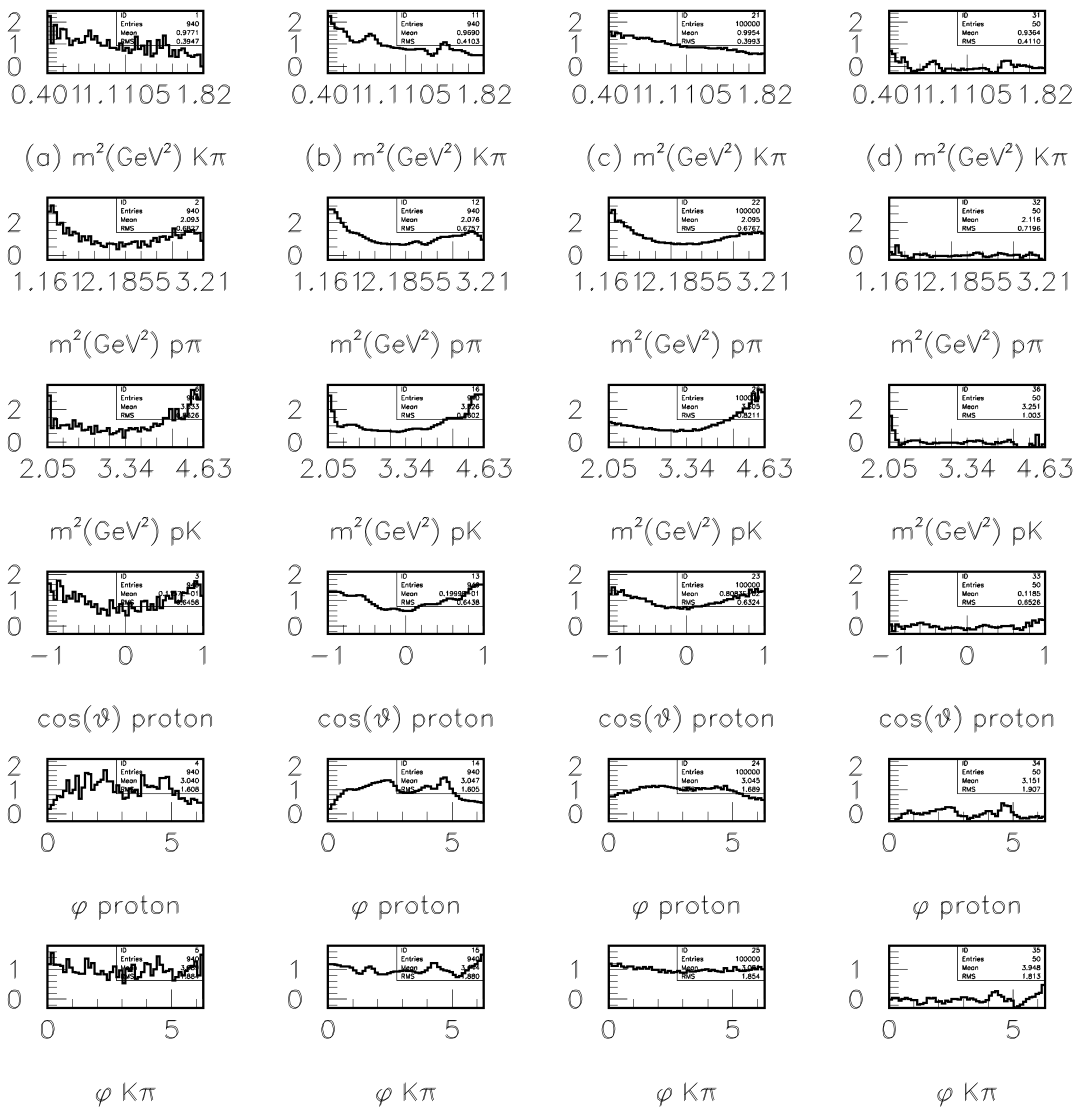

Figure 8.5: Background. (a) The one dimensional projections of the background divided by uniform phase space, (b) The one dimensional projections of the background divided by uniform phase space after smoothing with HSMOOF, (c) The model of the background as found by the nearest-neighbors technique, (d) the difference between the real background and the model.

$A = A_1(m^2_{K\pi})^{\frac{2}{3}} A_2(m^2_{p\pi})^{\frac{2}{3}} A_6(m^2_{pK})^{\frac{2}{3}} A_3(\cos(\theta_p)) A_4(\phi_p) A_5(\theta_{K\pi})$

This offers the advantage of one more piece of information used for accuracy.

We then scaled each probability so that the model would be normalized to the same value as the acceptance (background). In the case of $\vec{x}$, the K-nearest acceptance needed to be multiplied by 0.311, thus making the initial estimated acceptance to be 6.20.

Looking a figures 8.4 and 8.5, one can see that the nearest-neighbor technique smoothed out some of the fluctuations seen in column (a).[‡]Because some of the fluctuations are real (as opposed to statistical), we refrained from tweaking our acceptance and background to match the smoothed projections.

We adjusted by multiplying each weight by the ratio of the size of the corresponding histogram's bin for the acceptance (background) to the model. Note that $\vec{x}$'s acceptance changed from 6.20 to 5.93. See figure 8.6 for a look at the effect of the tweaking on the acceptance.

After several corrections, we achieved a result in one dimensional projections of the data and model which matched very well (see figures 8.7 and 8.8 for the comparison of the one dimensional projections), and two dimensional projections which matched reasonably well. See figures 8.9 and 8.10 for a comparison of the two dimensional projections. Notice that the discrepancies in the one dimensional projections are too small for the naked eye, while the basic two dimensional structures are still modeled well.

The measure of difference for acceptance dropped from 24.02 after just using the nearest-neighbor technique to 0.016 after tweaking the results. The measure of difference for background dropped from 62.46 after just using the nearest neighbor technique to 0.060 after tweaking the results. For a two dimensional χ^2 comparison of the acceptance to model, see appendix H.

8.3 Confidence

Comparing multidimensional data sets can be tricky. The classic one dimensional comparison tests, like the χ^2 test or the Kolmogorov-Smirnov tests do not translate well to multi-dimensions. There is one test however which is suited for such a task: The Permutation Test as described by F. James [Jam 81].

As F. James describes it, the permutation test allows for a comparison between two multidimensional data sets with the freedom to use any distance metric. Given two sets which one wants to compare, one makes a choice of metric, which defines a distance between these two sets. After finding this distance, the two sets are combined to form a larger set which is then split randomly into two new mixed sets.[§]The idea of the method is that if the two original sets are indeed drawn from the same underlying density then the mixed sets will also be drawn from the same underlying density. Therefore, one finds the distance between these two mixed sets and compares it to the original distance. If this distance is larger (or smaller, depending on the choice of metric) than the original, there is some indication that the two original sets are from the same underlying distribution. By combining and mixing these sets several times and counting the number of times the

[‡]Exploring whether some of those fluctuations are more than statistical, we looked at whether or not they came from the cutting of the D resonances as described in chapter 6. Our study can be seen in appendix E.

[§]An illustration of this would be to start with a deck of cards which is divided into two sets. one set could be the black suits and the other the red suits. After finding a way of measuring the difference between these two stacks, the cards are shuffled randomly, then split into two new stacks, where each new stack is a mix of red and black suits.

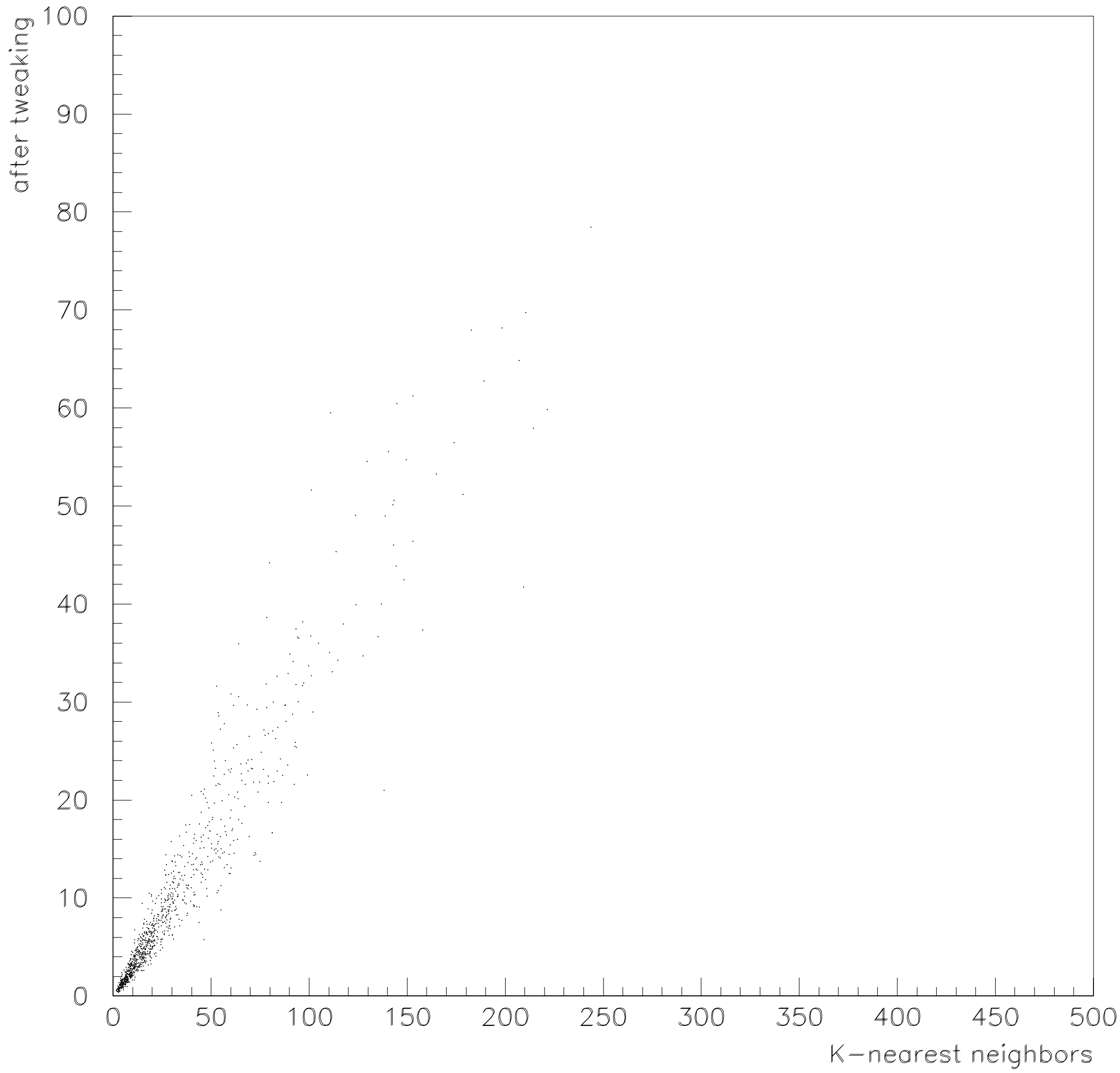

Figure 8.6: A comparison of the 1000 acceptance values before and after tweaking.

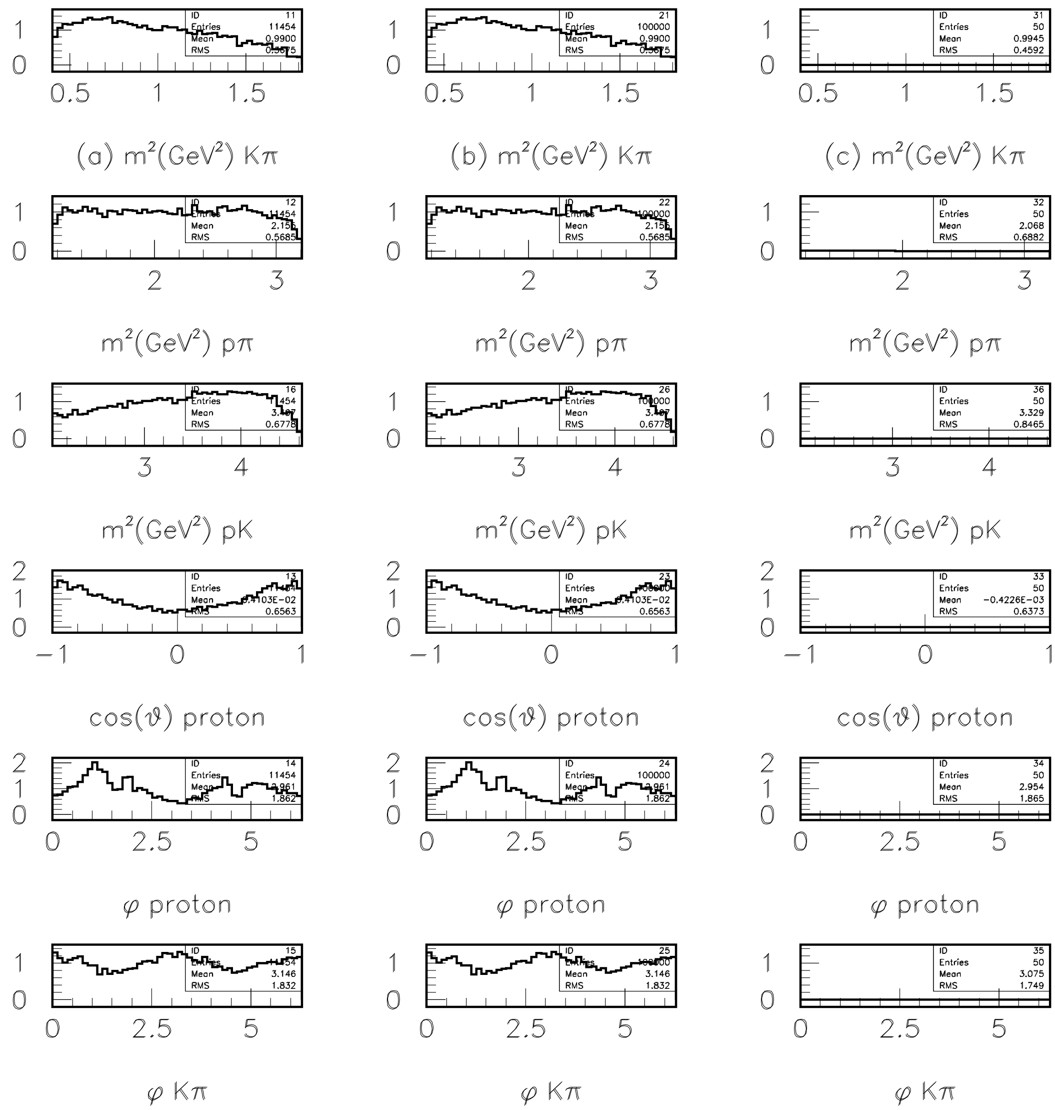

Figure 8.7: Acceptance. (a) The one dimensional projections of the surviving Monte Carlo divided by uniform phase space, (b) The model of the acceptance, (c) the difference between the real acceptance and the model.

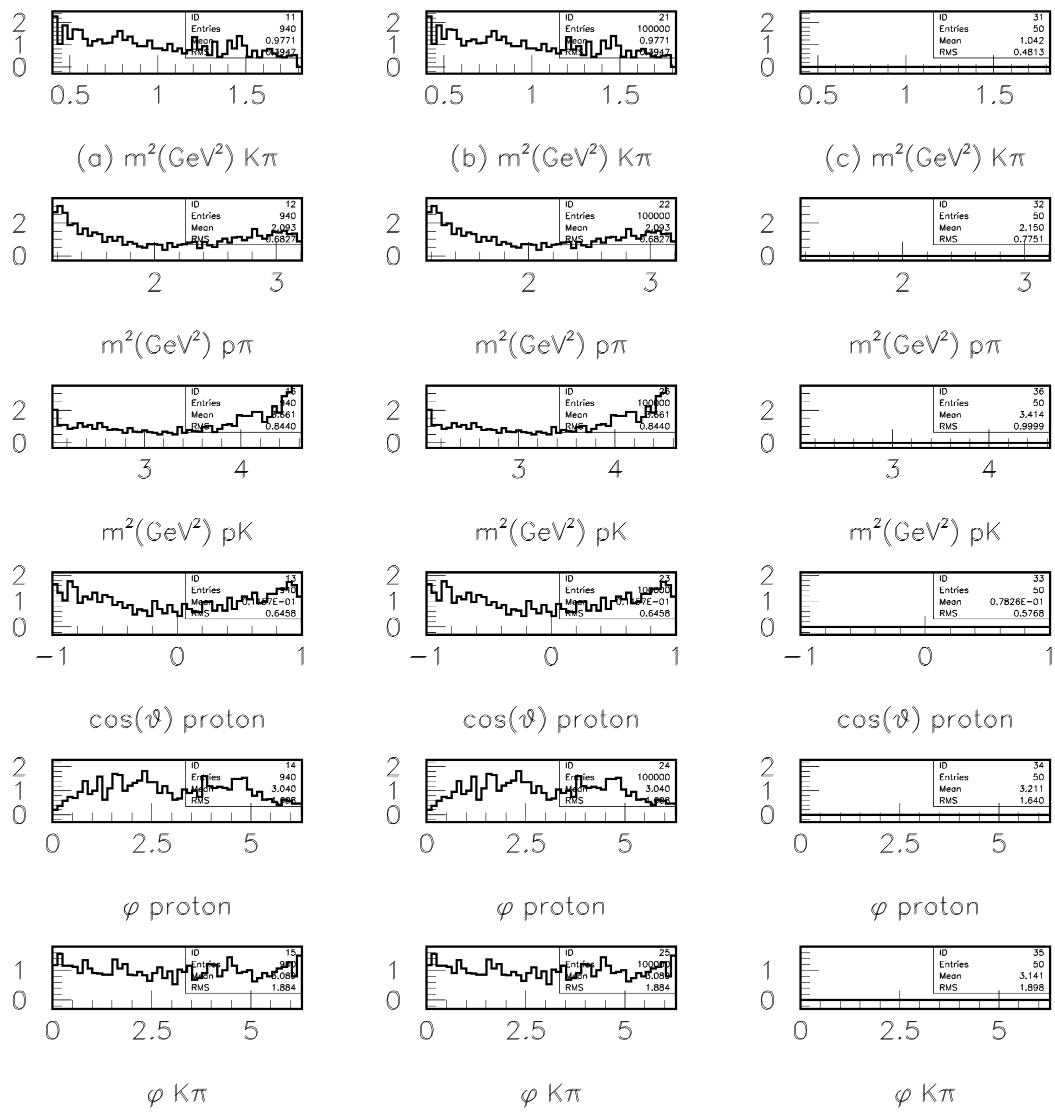

Figure 8.8: Background. (a) The one dimensional projections of the background divided by uniform phase space, (b) The model of the background, (c) the difference between the real background and the model.

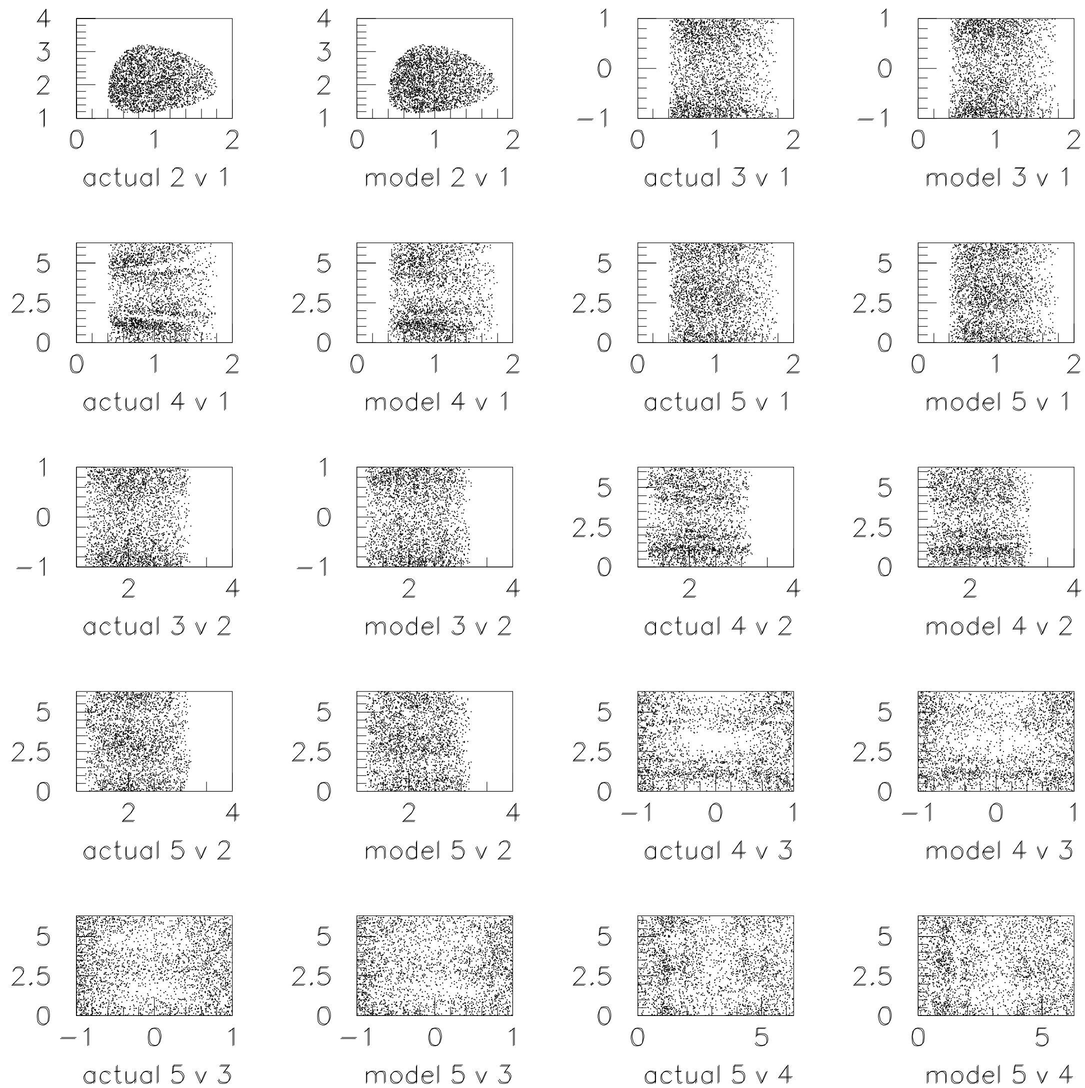

Figure 8.9: The two dimensional projections of the Acceptance, where the numbers 1 - 5 represent the dimensions outlined in the beginning of this section. Notice that the basic structure of the surviving reconstructed MC is present in the model. Note that in order to keep the size of this plot reasonable for printing, we projected only around 15% of the real acceptance points to represent the total data set.

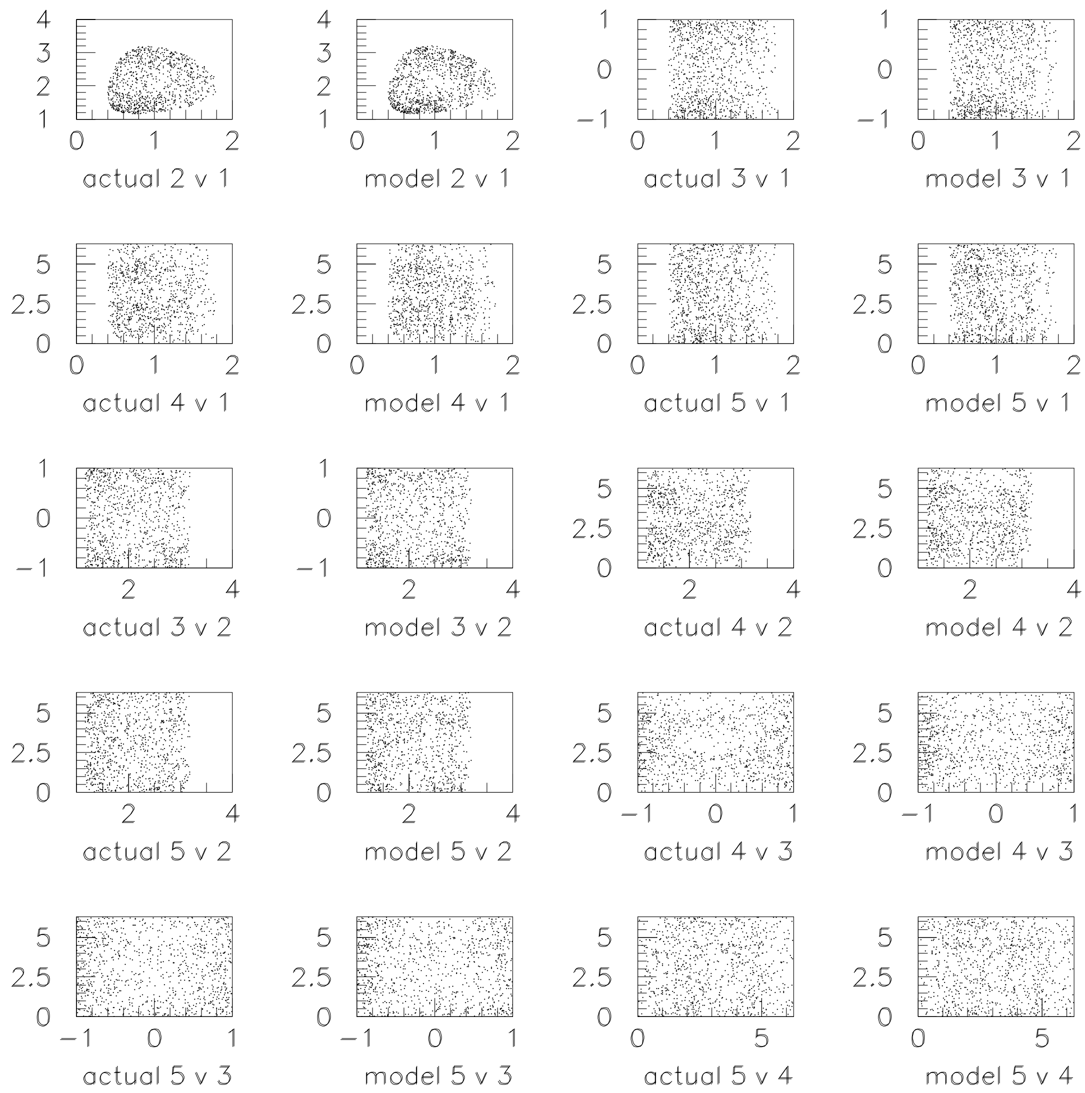

Figure 8.10: The two dimensional projections of the Background, where the numbers 1 - 5 represent the dimensions outlined in the beginning of this section. Notice that the basic structure of the data from the wings is present in the model.

distance exceeds the original, one can get a picture of a confidence level for the hypothesis.

If the two original sets are known to be from identical underlying densities then one expects that this procedure will yield a 50% confidence level because of the random nature of the selecting events for the mixed sets.

In our application of the permutation test, we chose our distance metric to be the average number of points from the set 2 within a radius of 0.2 units of each tested point of set 1. The dimensions were scaled from 0.0 to 1.0. If the sets are completely separate, then for a small enough radius, there would be, on average, no points from set 2 within this radius of any point in set 1. As the two sets are mixed, the average number of points should increase. Therefore, in our case the confidence is measured by the percent of the distance below the original distance.

To find our distance between the two sets, we used every point from the "real" set and the "modeled" set. Next, we mixed the two sets, as prescribed, split them into 2 sets, and chose 18 points randomly from set 1. We then proceeded to find the average number of points from set 2 within 0.2 units of each of these 18 points from set 1. If this distance were less than the initial distance, the confidence increased. We mixed, chose and measured 500 times, and then produced the confidence for this 500 cycle run. We then did the above nine more times and looked at the distribution of confidences, from which we found an overall average confidence as well as a standard deviation.

See table 8.1 for the confidences that we calculated. In this table, "v. uniform" refers to comparing the actual distribution to a uniformly distributed set of fast MC points. The label "v. uncorrelated model" refers to the comparison of the actual distribution to a model which assumed no correlation between the variables. The label "v. model" refers to the comparison of the actual distribution to the model as seen in figures 8.7 - 8.10. The label "v. self" refers to a comparison of the actual data set with itself. To do this, we randomly assigned each point into one of the two sets. We insured that the sets were of the same size by looking at a pair of points at a time.

Real	Acceptance(%)	Background(%)
v. uniform	6.8±1.0	19.0±3.2
v. uncorrelated model	22.3±2.6	30.0±3.0
v. model	51.4±3.8	51.1±2.9
v. self	51.0±2.0	53.4±4.5

Table 8.1: The confidences for the acceptance and the background.

Chapter 9

The Fit

We fit the data with the probability density function of chapter 7 using the physics software, MINUIT. The equation was normalized numerically using 100,000 uniformly distributed phase space points.

We fit the data with the following resonances:

Fit 1:	Nonresonant, $\overline{\mathrm{K}}^{*0}$, and Δ^{++}
Fits 2a and 2b:	Nonresonant, $\overline{\mathrm{K}}^{*0}$, Δ^{++}, and $\Lambda(1520)$
Fit 3:	Nonresonant, $\overline{\mathrm{K}}^{*0}$, Δ^{++}, $\Lambda(1520)$, plus the mass plot fit parameters outlined in chapter 7
Fit 3p:	Nonresonant, $\overline{\mathrm{K}}^{*0}$, Δ^{++}, $\Lambda(1520)$, plus the mass plot fit parameters outlined in chapter 7 and three values of polarization to match increasing values of p_{T}.

While fitting, the amplitude parameters of the fit were numerically normalized. For Fit 1, we did not fit the $\Lambda(1520)$. For Fits 1, 2a, and 2b, we fixed the mass plot parameters to their PDG values, thereby excluding the width dependence on $\mathrm{x_F}$. Please, see table 9.1 for the central masses and widths used in during the fitting process. For Fit 3, we added the reconstructed $m_{\mathrm{pK}\pi}$ parameters to the fit, and for Fit 3p, we added the p_{T} dependence on the polarization of the Λ_{c}

When we fit the data, we had to choose a variable to be a reference. All the phases had to be relative to a single phase, and all the magnitudes to a single magnitude. For fits 1 and 2a, we chose to fix one of the $\overline{\mathrm{K}}^{*0}$ amplitudes. For fits 2b, 3 and 3p, we chose to fix a nonresonant amplitude.

9.1 Search for Resonances

For the Fits 1, 2a, 2b, and 3, see appendix I.

9.1.1 Fit 3p: Nonresonant, $\overline{\mathrm{K}}^{*0}$, Δ^{++}, $\Lambda(1520)$, plus the mass plot fit parameters and polarization as a function of p_{T}.

Fits 1, 2a, and 2b (in appendix I) were good for getting a feel for which modes were present. However, the proper fit should include additional factors. One of these factors is that the errors in

Particle	Mass (GeV/c^2)	Width (MeV/c^2)
Λ_c	2.2896	9.888
$\overline{K}^{*0}$	0.8961	50.50
Δ^{++}	1.2309	111.0
$\Lambda(1520)$	1.5195	15.60
p	0.9383	
K	0.4937	
π	0.1396	

Table 9.1: The masses and widths used for each of the particles in the analysis. These values, except for the Λ_c, were given by the [PDG 98]. The Λ_c mass and width were found by a MINUIT fit on the final data set, and these values were used in Fits 1, 2a, and 2b, only. Fits 3 and 3p used the mass and width calculated for that fit.

the mass plot fit needed to be propagated throughout the fit, so the mass plot fit was incorporated into the process (as seen in Fit 3). Also, it had been noticed within the Collaboration that the width of the Λ_c depended on x_F (also seen in Fit 3). This, too, was incorporated. A further consideration is the polarizations dependence on the transverse momentum[Dha 96]. Taking this, too, into account makes Fit 3p the most accurate of these fits.

In order to determine if there is a relationship between the polarization of the Λ_c and the transverse momentum, p_T, of the Λ_c, we broke the data set into three divisions of p_T so that roughly the same number of events were in each division. The boundaries of these bins and the number of events in each can be seen in table 9.2.

bin	1	2	3
p_T range (GeV/c^2)	0.00 - 0.71	0.71 - 1.24	1.24 - 5.21
$\overline{p_T}$ (GeV/c^2)	0.45	0.96	1.80
Number of events	758	757	756

Table 9.2: Information on the bins of p_T.

For a one dimensional projection comparison of the model and data, see figure 9.1. For a two dimensional comparison, see figure 9.2. Again, one can see the $\overline{K}^{*0}$ and the Δ^{++} resonances. The $\Lambda(1520)$ resonance seems to be there, but its presence is still not as obvious from the plot. The breakdown of the contribution from each of these modes in the model can be seen in figure 9.3. Again, we subtracted the one dimensional projections of the model from the real data projections and We divided these by phase space. The results of this subtraction can be seen in figures 9.4 and 9.5. A plot of the Fit 3p values of polarization can be seen in figure 9.6.

Note that since the mass plot fit was included the projection of the fit has changed from figure 6.5 (p.46). The new projection of the mass plot with the new values can be seen in figure 9.7. The increase in the number of signal events can be attributed to the increase in the width of the Gaussian from 9.89 MeV/c^2 to a function depepdent on x_F.

There is also another comparison of this fit in appendices H.2 and H.3. Appendix H.2 contains a two dimensional χ^2 comparison for the full mass region, and appendix H.3 contains a two dimensional χ^2 comparison for just the signal region, as defined as a reconstructed Λ_c mass from 2.265

GeV/c^2 to 2.315 GeV/c^2. See figure 6.6 for a visual of this region.

Also note that the $\overline{\mathrm{K}}^{*0}$ in the real data is slightly more prominent than in the model, as seen in figure 9.2. This can be explained by the fact that the width of the $\overline{\mathrm{K}}^{*0}$ in the real data is 20% narrower than the PDG value[PDG 98], as will be explained in section 9.3.

The Breit-Wigner resonance formula we used is the corrected formula as is seen in equations 2.28 and 2.29

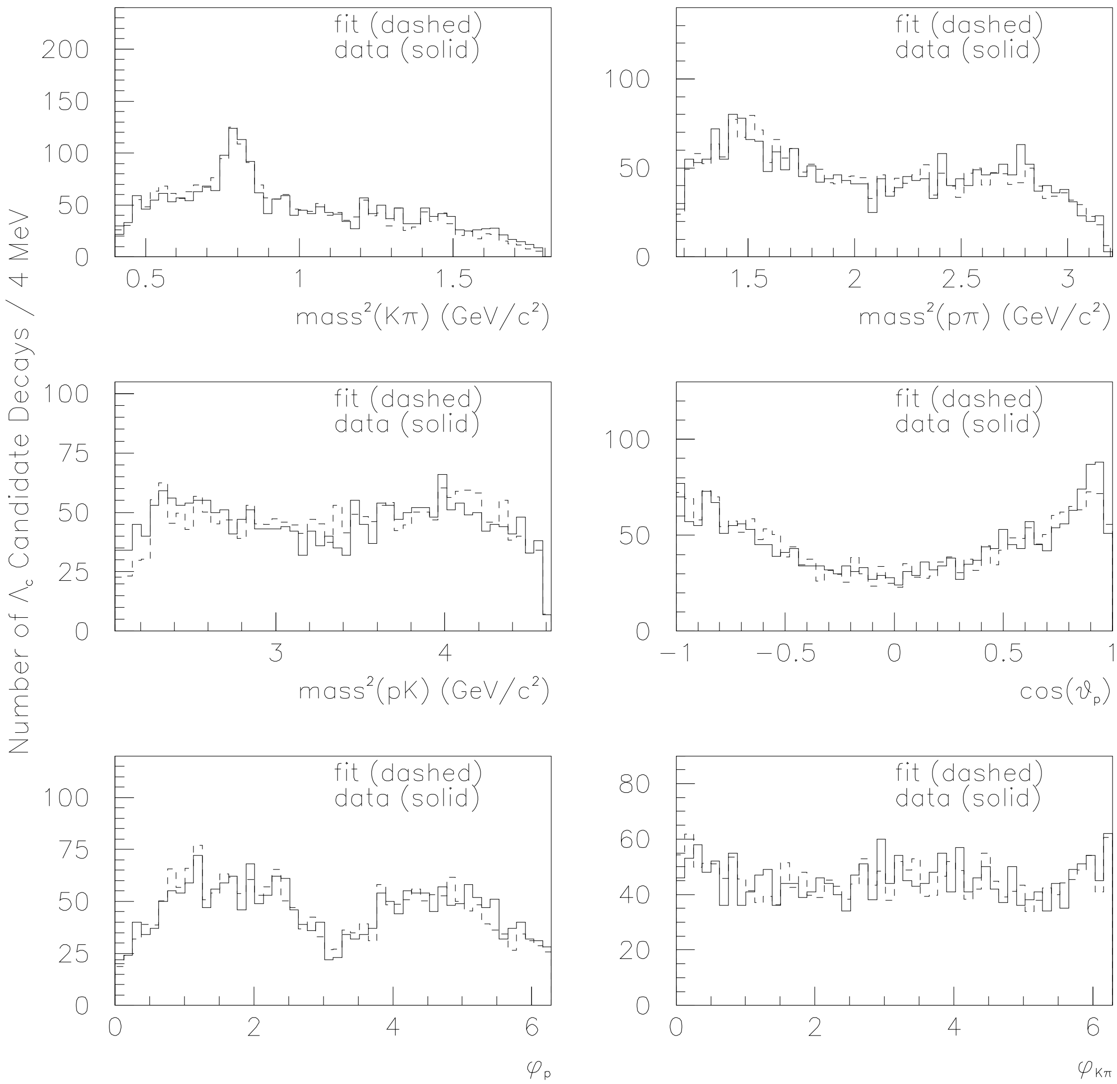

Figure 9.1: Projections of the real data and Fit 3p superimposed for comparison purposes.

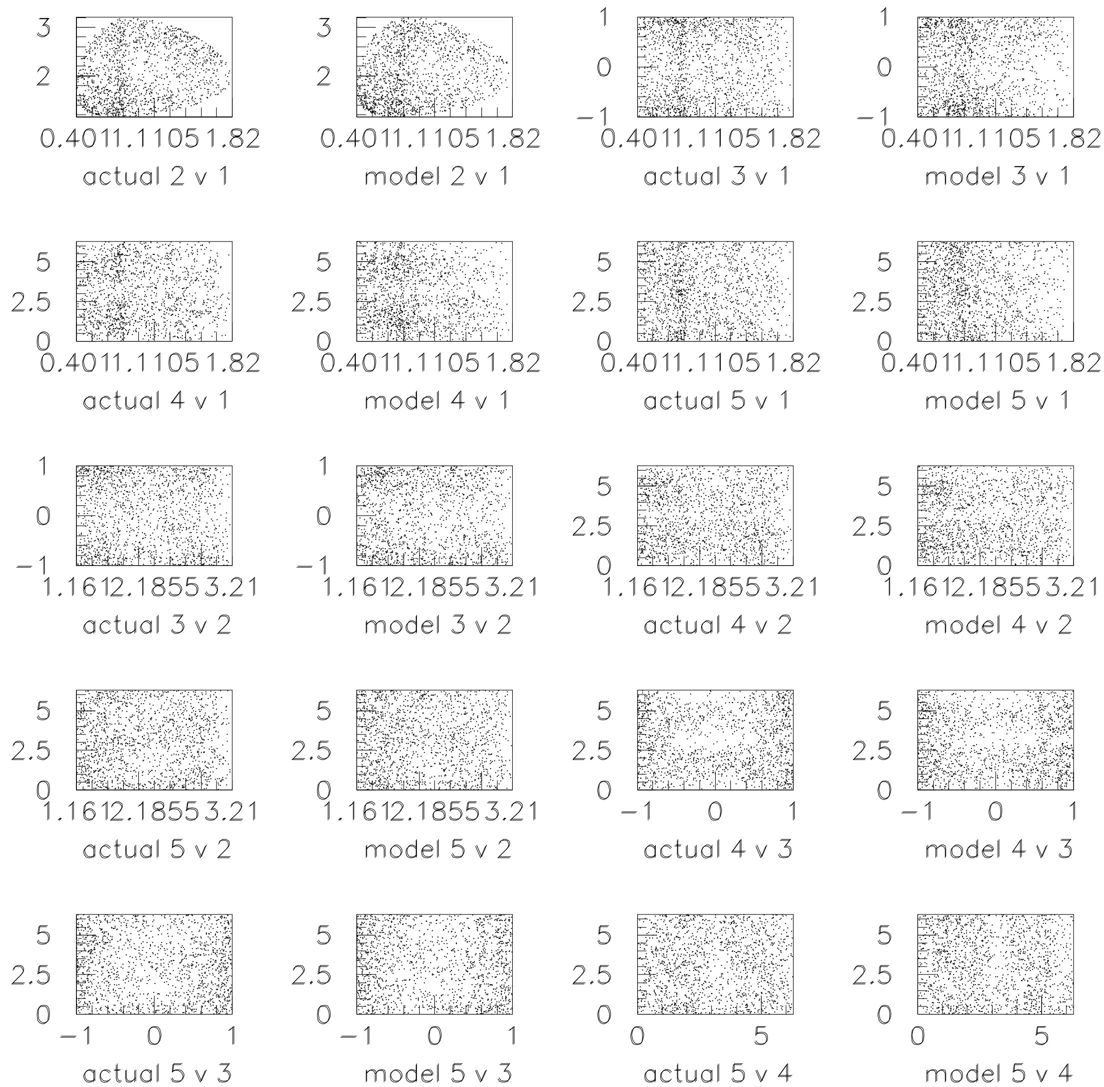

Figure 9.2: The two dimensional projections of Fit 3p and real data, where the numbers 1 - 5 represent the dimensions outline in the beginning of the previous section. Note the $\overline{\mathrm{K}}^{*0}$ band in the first eight plots, and the hole in “4 v 3” is in both the model and actual.

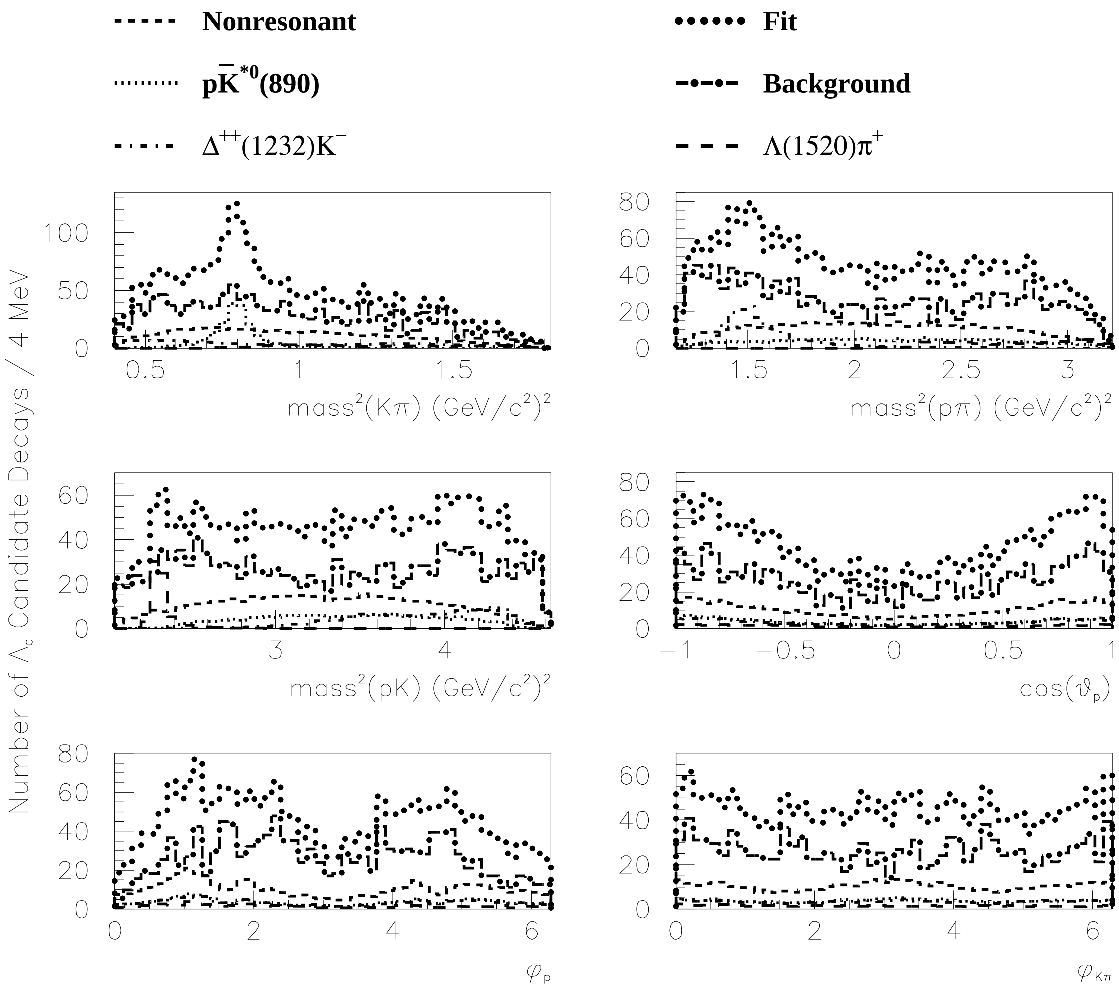

Figure 9.3: Projections of the model broken down by resonance mode for Fit 3p.

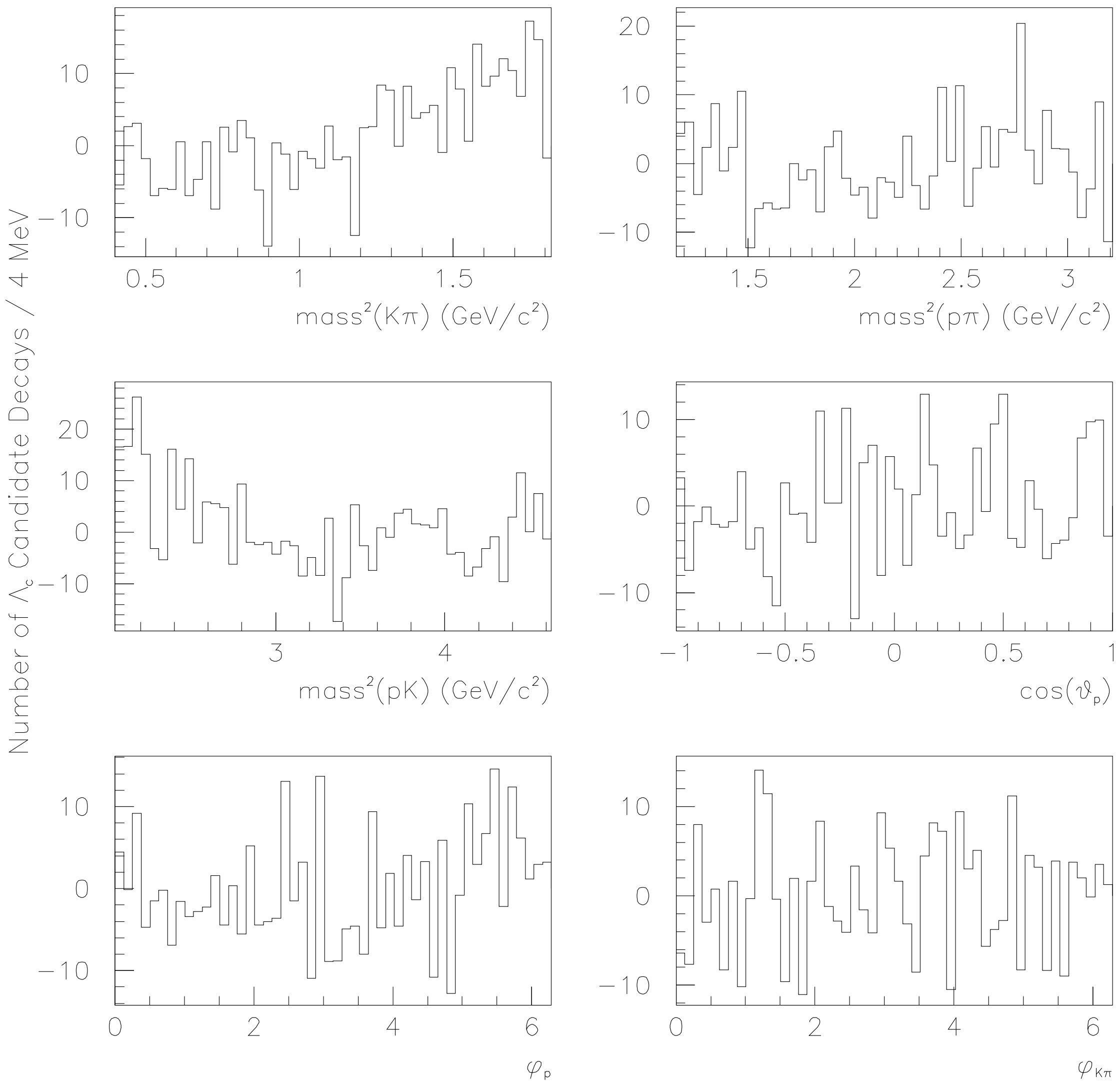

Figure 9.4: Projections of the real data minus Fit 3p and divided by phase space.

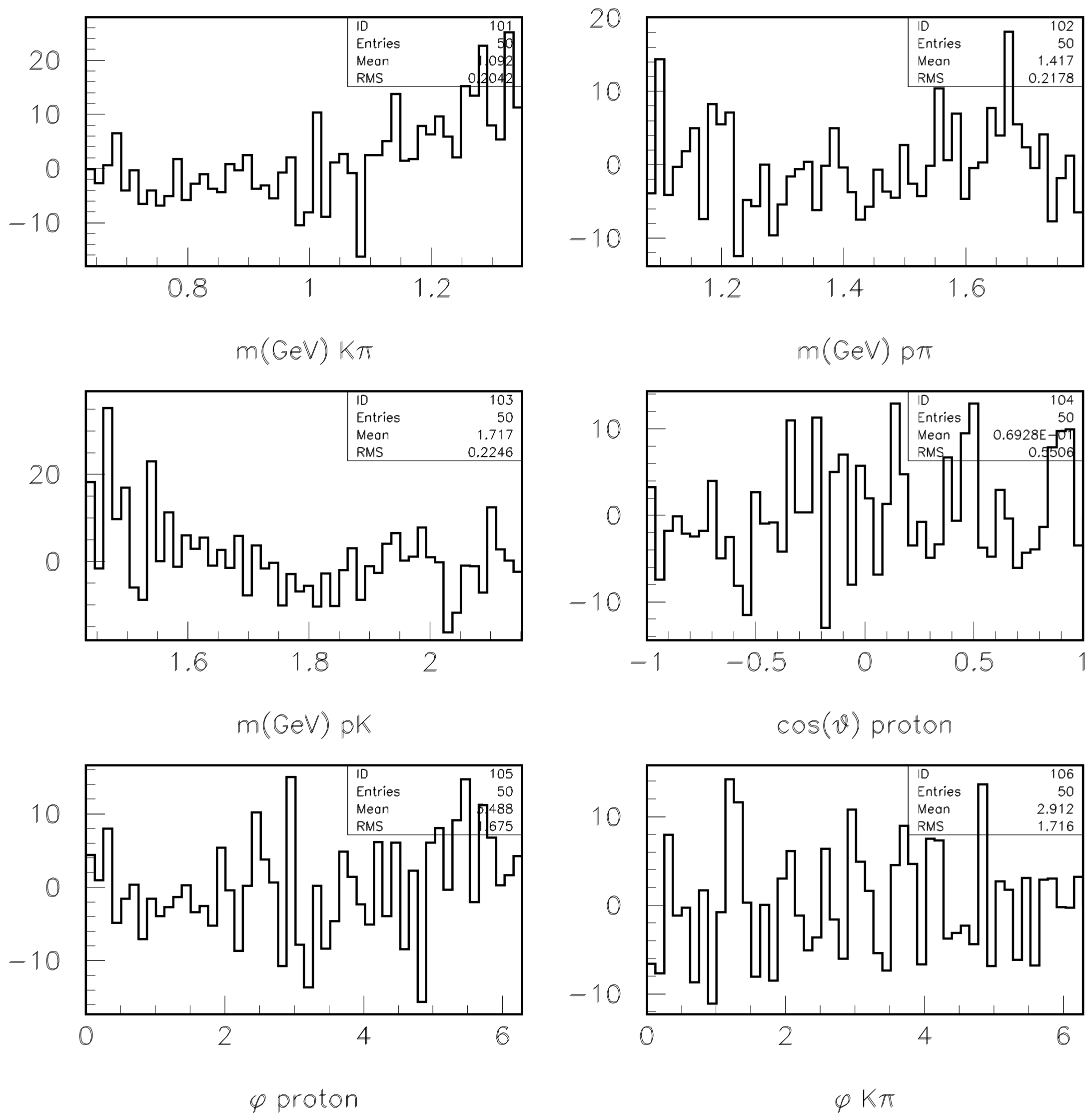

Figure 9.5: Projections of the real data minus Fit 3p and divided by phase space. Note that the first 3 histograms are mass and not mass^2.

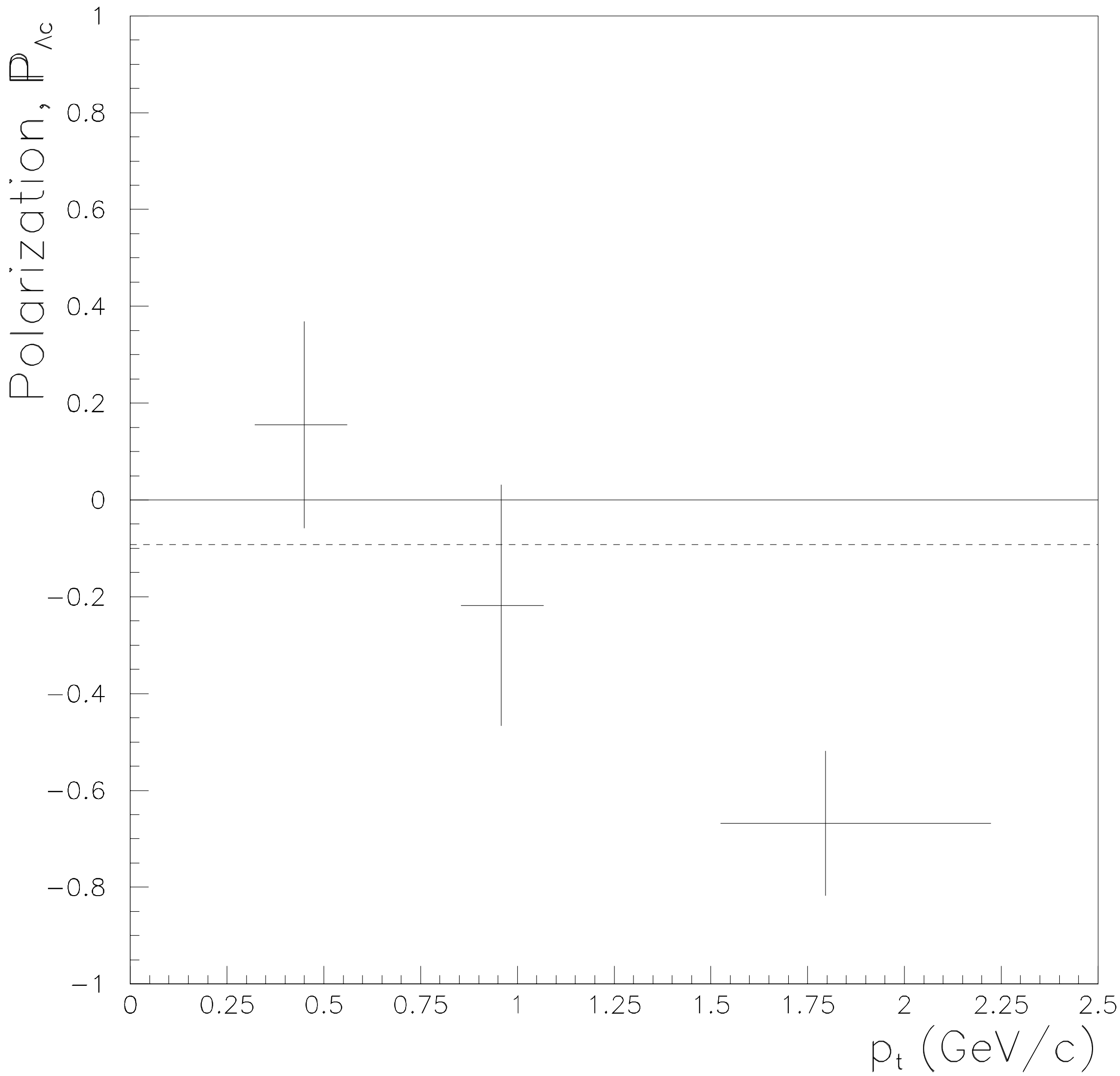

Figure 9.6: The polarization of the Λ_c as a function of the Λ_c's transverse momentum. The vertical bars represent the error as found by MINUIT. They are placed at the average p_T value for that region. The horizontal bars represent the standard deviation of p_T from the mean for each particular bin. The dotted line represents the value of the polarization when it was assumed constant for all data events.

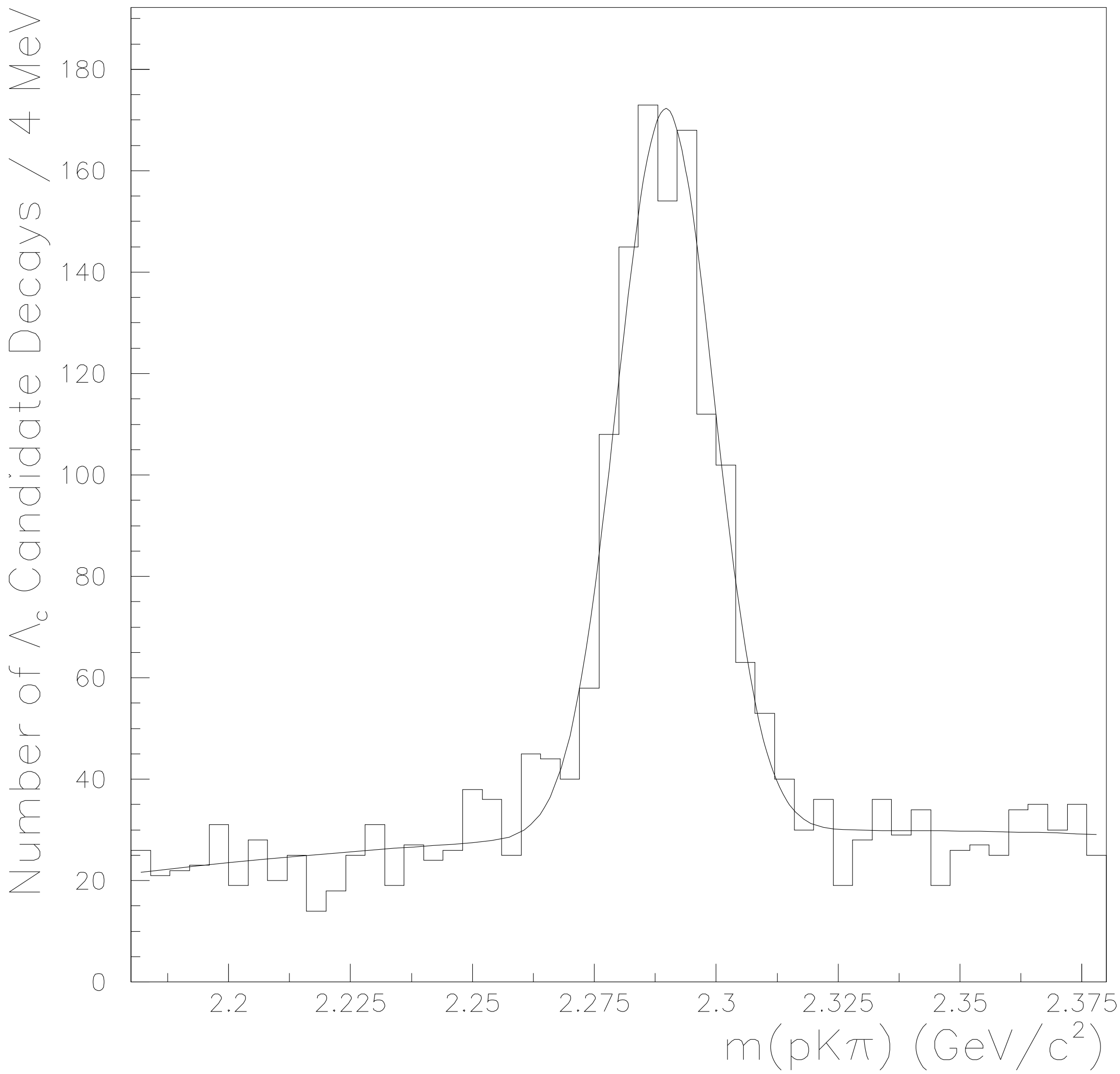

Figure 9.7: Mass(pKπ) of the real data set after Neural Net cuts and the MINUIT Fit 3. There are 946$\pm$38 signal events and 1324$\pm$43 background events assuming that the peak is Gaussian, the background is quadratic and the number of signal and background events are variables.

9.2 Statistical Results

In the tables below, the variable ϕ represents the phase of the decay with respect to one of the nonresonant amplitudes which was assumed to have $\phi = 0.0$ and a magnitude of 1.0.

In table 9.4, FCN refers to the function value found by MINUIT. It has only a relative meaning, in that it is the value that MINUIT is minimizing. It is presented for those who want to draw a conclusion. χ^2 refers to the χ^2 fit found for each of the dimensions used in the fit, as defined in chapter 8.

Terms	Parameter	Value
$\mathrm{p}\overline{\mathrm{K}}^{*0}(890)$	E_1	0.52± 0.17
	ϕ_{E_1}	-1.01± 0.48
	E_2	0.20± 0.10
	ϕ_{E_2}	2.35± 0.67
	E_3	0.21± 0.10
	ϕ_{E_3}	3.46± 0.42
	E_4	0.16± 0.10
	ϕ_{E_4}	5.29± 0.55
$\Delta^{++}(1232)\mathrm{K}^-$	F_1	0.17± 0.07
	ϕ_{F_1}	4.98± 0.41
	F_2	0.38± 0.13
	ϕ_{F_2}	4.88± 0.40
$\Lambda^*(1520)\pi^+$	H_1	0.18± 0.09
	ϕ_{H_1}	5.93± 0.52
	H_2	0.20± 0.07
	ϕ_{H_2}	-0.06± 0.55
Nonresonant	N_{++}	0.46± 0.26
	$\phi_{N_{++}}$	3.48± 0.54
	N_{+-}	1.00
	$\phi_{N_{+-}}$	0.00
	N_{-+}	0.18± 0.15
	$\phi_{N_{-+}}$	0.75± 0.71
	N_{--}	0.94± 0.45
	$\phi_{N_{--}}$	1.13± 0.36
Polarization (bin 1)	$\mathbf{P}_{\Lambda_c,1}$	0.15± 0.21
Polarization (bin 2)	$\mathbf{P}_{\Lambda_c,2}$	-0.22± 0.25
Polarization (bin 3)	$\mathbf{P}_{\Lambda_c,3}$	-0.67± 0.15
# Signal Events	$\mathrm{n_s}$	946.22± 38.38
# Background Events	$\mathrm{n_b}$	1324.28± 43.01
Background Quad Term	b_q	-0.98± 10.51
Background Linear Term	b_l	1.34± 0.48
$\mathrm{Mass}_{\Lambda_c}$ (GeV/c^2)	m_0	2.29± 0.00
$\mathrm{Width}_{\Lambda_c}$ (MeV/c^2)	σ_l	20.08± 4.77
$\mathrm{Width}_{\Lambda_c}$ (MeV/c^2)	σ_c	9.28± 0.55

Table 9.3: The result of the MINUIT fit. Note that the width of the Λ_c peak = σ = $\sigma_\mathrm{l} x_\mathrm{F} + \sigma_\mathrm{c}$.

	Fit 3p
$\mathrm{FCN_{total}}$	12485.87
$\chi^2 : m^2_{\mathrm{K}\pi}$	43.3
$\chi^2 : m^2_{\mathrm{p}\pi}$	43.4
$\chi^2 : m^2_{\mathrm{pK}}$	58.2
$\chi^2 : cos(\theta_{\mathrm{p}}]$	39.3
$\chi^2 : \phi_{\mathrm{p}}$	41.4
$\chi^2 : \phi_{\mathrm{K}\pi}$	42.6
χ^2: $\mathrm{sum_1}$	219.9
$\chi^2 : m(\mathrm{pK}\pi)$	63.8
$\chi^2 : sum_{\mathrm{total}}$	283.7
$\mathrm{DOF_{total}}$	268

Table 9.4: The result of the MINUIT fit. χ^2 $\mathrm{sum_1}$ was found by taking $\frac{2}{3}$ the sum of the first 3 values plus the sum the of the next 3. Each of the first 6 χ^2's was found by comparing the model and real histograms spread out over 50 bins.

The values which are displayed in table 9.3 along with the covariant matrix generated by MINUIT, give us the fit fraction for each decay, as seen in table 9.5. The errors on fit fraction k were calculated by $E_k = \sqrt{\sum_{ij} \frac{df_k}{dx_i}\frac{df_k}{dx_j} V_{ij}}$ where f = f($\vec{x}$) = the fit fraction (as described in equation 2.30 on page 13), x_i is the i^{th} element of $\vec{x}$, and V_{ij} is an element from the covariant matrix.

Mode	Fit 3p (%)
$\overline{\mathrm{K}}^{*0}$	19.5±2.6
Δ^{++}	18.0±2.9
$\Lambda(1520)$	7.7±1.8
Nonresonant	54.8±5.5

Table 9.5: The Fit Fraction with statistical errors for the decay $\Lambda_c \rightarrow \mathrm{pK}\pi$ from the MINUIT fit.

9.3 A Comment on the $\overline{\mathrm{K}}^{*0}$ Width

The width of the $\overline{\mathrm{K}}^{*0}$ is well established with a PDG value of 50.5 MeV. To see the effect of the resolution of the detector on this width, we weighted the surviving reconstructed MC by a signal density assuming only a $\overline{\mathrm{K}}^{*0}$ resonance. The Breit-Wigner amplitude used the truth table values associated with each event. We then fit the resulting peak in the m(Kπ) projection with a an unbinned MINUIT fit using the reconstructed m(Kπ). See figure 9.8 for the unconstrained mass and the constrained mass. The width for the unconstrained masses was 51.3±0.4 MeV and for the constrained masses was 51.1±0.4 MeV.

We also ran Fit 3 with the $\overline{\mathrm{K}}^{*0}$ mass and width floating. The converged value for the mass was 0.893±0.003 GeV and the width was 40.8±7.0 MeV. This may be due to a statistical fluctuation. Other possibilities include poor modeling of the acceptance near the $\overline{\mathrm{K}}^{*0}$ mass, but this does not seem likely looking at the top 8 plots in figure 8.9 on page 65. There may also be possible interference effects with the nonresonant components, but this seems unlikely given the total fit fraction is around 100%.

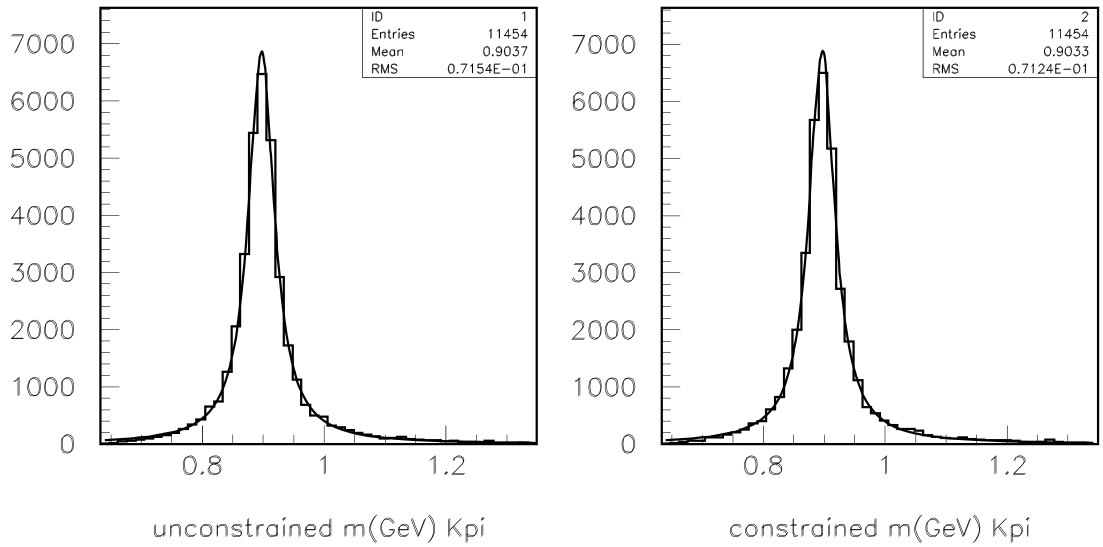

Figure 9.8: Projection of $\overline{\mathrm{K}}^{*0}$ with fit using unconstrained (left) and constrained (right) masses.

Because the width is so well established and the constrained width is not too far off of the accepted value, we used the PDG values in our fits.

9.4 A Comment on the $\Lambda(1520)$ Width

Looking at figures 9.1 - 9.3, it may seem that the $\Lambda(1520)$ width is too narrow. The PDG value is 15.6 MeV, but the questions arises as to whether that is what we should use. To see the effect of the resolution of the detector on the width, we weighted the surviving reconstructed MC by a signal density assuming only a $\Lambda(1520)$ resonance. The Breit-Wigner amplitude used the truth table values associated with each event. We then fit the resulting peak in the m(pK) projection with a an unbinned MINUIT fit using the reconstructed m(pK). See figure 9.9 for the unconstrained mass and the constrained mass. The width for the unconstrained masses was 17.1 MeV and for the constrained masses was 16.7 MeV.

We also ran Fit 3 with the $\Lambda(1520)$ mass and width floating. The converged value for the mass was 1.46$\pm$0.03 GeV and the width was 172$\pm$40 MeV. This may be due to a weak $\Lambda(1520)$ signal or the presence of an unknown resonance.

Given these findings we concluded that the constraining counterbalanced some of the resolution problems of the detector and reconstruction. Also, since the floated width was far too large, we used the PDG value for the width.

9.5 The Search for Other Resonances

As seen in figures 9.1 (p.71) and 9.5 (p.75), there seems to be some other resonance in the low pK mass phase space. To explore this region, we decided to look for a particle with a mass within the

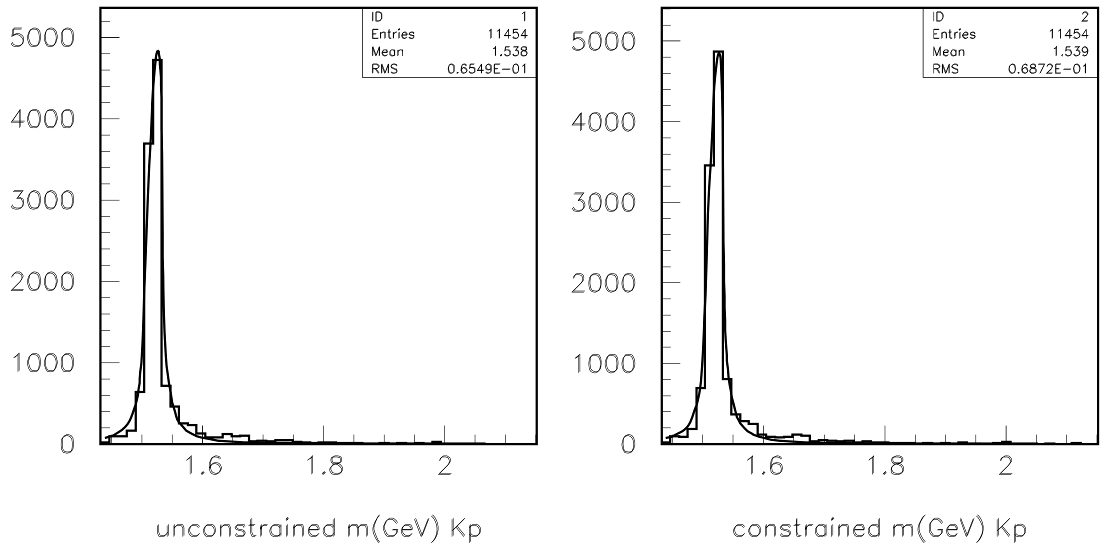

Figure 9.9: Projection of $\Lambda(1520)$ with fit using unconstrained (left) and constrained (right) masses.

range of 1.5 GeV - 1.7 GeV, a width on the order of 100 MeV, and a decay mode $\rightarrow \mathrm{N}\overline{\mathrm{K}}$. Two such candidates are $\Lambda(1600)$ and $\Sigma(1660)$. See table 9.6.

Particle	J^P	PDG mass range (GeV)	PDG width range (MeV)
$\Lambda(1600)$	$\frac{1}{2}^+$	1.560-1.700	50-250
$\Sigma(1660)$	$\frac{1}{2}^+$	1.630-1.690	40-200

Table 9.6: The PDG values for two potential resonances.

To search for these resonances, we floated the mass and width of an unnamed spin $\frac{1}{2}^+$ particle. This was done with and without the $\Lambda(1520)$ resonance (just in case its presence in the formula was hiding another resonance).

We also searched for a spin $\frac{1}{2}^-$ resonance, by floating the mass and width of the particle with and without the $\Lambda(1520)$ was present. See appendix K for more detail on these models as well as the possible resonance of $\Lambda(1405)$ which has a center of mass below the pK threshhold but whose upper tail extends into the pK mass range.

Overall, there is weak (if any) evidence of any specific additional resonance present in the decay. However there is evidence of something else in the low pK mass range, as discussed in appendix K.

9.6 Confidence

Subjecting the models to the permutation test used on the acceptance and background, we found the following confidence levels found in table 9.7. In this table, "uniform" refers to a comparison of the model to a uniformly distributed set of points; "real" refers to a comparison of the model to the actual distribution of 2,271 points; and "self" refers to a comparison of the half of the model to the other half when split randomly into two equally sized sets.

model vs.	Fit 3p (%)
uniform	12.1±1.3
real	54.1±3.3
self	52.8±2.8

Table 9.7: The Confidence of the MINUIT fit using the permutation test described earlier. In this table, "uniform" refers to a comparison of the model to a uniformly distributed set of points; "real" refers to a comparison of the model to the actual distribution of 2,271 points; and "self" refers to a comparison of the half of the model to the other half when split randomly into two equally sized sets.

Chapter 10

Systematic Errors

In any analysis of data, there will be more errors than just statistical. The purpose of systematic errors is to explore potential problems in the modeling of the data. For example, the acceptance was based on the surviving reconstructed MC. If the detector simulation strayed from how the real detector operated, this would cause a problem in the acceptance model and the subsequent fitting procedures. Note that all systematic errors were calculated using fit 3p.

Given this, we considered two types of systematic errors to explore: acceptance related and background related. The acceptance related systematic errors stem from the Čerenkov probabilities, the production model, the DC hole parameters, and the affect of tweaking. In these cases, we looked at the difference in appropriate data and MC parameters, and weighted the surviving reconstructed MC to account for the difference. Once weighted, we recalculated the acceptance, and redid the fitting procedure.

The background systematic errors possibly stem from the straight cut of the D^+ and D_s decay reflections. When done, we determined that problems with the background were already taken into account in the initial fitting.

After redoing Fit 3p with the new acceptances, we estimated the effect of the systematic error by the change in the central value for the fit fractions. After all the scenarios were studied, the total systematic error was the sum in quadrature of the individual changes from Fit 3p. The fit fractions for each of the fits seen in table 10.1 can be seen in table 10.2. The total systematic error can be seen in table 10.3.

	Fit 3p	Čerenkov	Production	DC hole	2D Tweak
E_1	0.52± 0.17	0.51± 0.18	0.52± 0.19	0.57± 0.26	0.51± 0.18
ϕ_{E_1}	-1.01± 0.48	5.33± 0.47	5.20± 0.47	5.28± 0.48	5.32± 0.49
E_2	0.20± 0.10	0.19± 0.10	0.21± 0.10	0.22± 0.12	0.20± 0.10
ϕ_{E_2}	2.35± 0.67	2.46± 0.66	2.32± 0.65	2.49± 0.66	2.29± 0.73
E_3	0.21± 0.10	0.19± 0.09	0.20± 0.10	0.26± 0.13	0.19± 0.09
ϕ_{E_3}	3.46± 0.42	3.58± 0.45	3.49± 0.44	3.61± 0.45	3.47± 0.47
E_4	0.16± 0.10	0.14± 0.09	0.18± 0.10	0.20± 0.12	0.17± 0.09
ϕ_{E_4}	5.29± 0.55	5.35± 0.58	5.34± 0.53	5.38± 0.54	5.30± 0.54
F_1	0.17± 0.07	0.17± 0.07	0.17± 0.08	0.20± 0.10	0.15± 0.07
ϕ_{F_1}	4.98± 0.41	5.02± 0.40	4.97± 0.41	4.96± 0.43	5.10± 0.44
F_2	0.38± 0.13	0.36± 0.13	0.39± 0.14	0.44± 0.20	0.37± 0.13
ϕ_{F_2}	4.88± 0.40	4.90± 0.40	4.82± 0.40	4.81± 0.43	4.86± 0.42
H_1	0.18± 0.09	0.19± 0.10	0.18± 0.10	0.18± 0.11	0.18± 0.08
ϕ_{H_1}	5.93± 0.52	5.98± 0.53	5.98± 0.52	6.03± 0.57	5.88± 0.51
H_2	0.20± 0.07	0.20± 0.07	0.21± 0.07	0.22± 0.09	0.18± 0.07
ϕ_{H_2}	-0.06± 0.55	6.27± 0.56	6.21± 0.54	6.29± 0.54	6.23± 0.58
N_{++}	0.46± 0.26	0.43± 0.25	0.51± 0.28	0.54± 0.36	0.48± 0.27
$\phi_{N_{++}}$	3.48± 0.54	3.52± 0.56	3.43± 0.52	3.60± 0.54	3.51± 0.54
N_{+-}	1.00	1.00	1.00	1.00	1.00
$\phi_{N_{+-}}$	0.00	0.00	0.00	0.00	0.00
N_{-+}	0.18± 0.15	0.18± 0.15	0.21± 0.16	0.32± 0.22	0.14± 0.14
$\phi_{N_{-+}}$	0.75± 0.71	0.82± 0.71	0.69± 0.64	1.01± 0.55	0.61± 0.86
N_{--}	0.94± 0.45	0.93± 0.48	0.95± 0.47	0.99± 0.60	0.91± 0.44
$\phi_{N_{--}}$	1.13± 0.36	1.20± 0.37	1.13± 0.36	1.18± 0.38	1.10± 0.38
$\mathbf{P}_{\Lambda_c,1}$	0.15± 0.21	0.14± 0.21	0.14± 0.21	0.12± 0.20	0.11± 0.22
$\mathbf{P}_{\Lambda_c,2}$	-0.22± 0.25	-0.22± 0.25	-0.24± 0.25	-0.25± 0.23	-0.25± 0.26
$\mathbf{P}_{\Lambda_c,3}$	-0.67± 0.15	-0.66± 0.15	-0.69± 0.15	-0.67± 0.16	-0.71± 0.14
$\mathrm{n_s}$	946.22± 38.38	951.28± 38.55	956.08± 38.52	912.56± 37.83	918.55± 37.43
$\mathrm{n_b}$	1324.28± 43.01	1319.22± 43.05	1314.43± 42.91	1357.94± 43.30	1351.96± 42.82
$\mathrm{b_q}$	-0.98± 10.51	0.11± 10.68	1.39± 10.82	-8.22± 9.61	-7.51± 9.61
$\mathrm{b_l}$	1.34± 0.48	1.34± 0.48	1.35± 0.49	1.39± 0.46	1.31± 0.46
$\mathrm{m_0}$	2.29± 0.00	2.29± 0.00	2.29± 0.00	2.29± 0.00	2.29± 0.00
σ_l	20.08± 4.77	20.38± 4.84	19.75± 4.79	21.04± 4.80	19.60± 4.65
σ_c	9.28± 0.55	9.35± 0.55	9.42± 0.56	9.07± 0.55	9.14± 0.54

Table 10.1: The parameter values from the MINUIT fit for Fit 3p and each systematic study.

Mode	Fit 3p	Čerenkov(%)	Production(%)	DC hole(%)	2d Tweak(%)
$\overline{K}^{*0}$	19.5±2.6	18.9±2.7	19.5±2.7	21.2±3.0	19.8±2.8
Δ^{++}	18.0±2.9	16.8±2.8	18.1±2.9	20.5±3.3	17.3±2.9
$\Lambda(1520)$	7.7±1.8	8.3±1.9	7.6±1.8	6.8±1.7	7.3±1.8
Nonresonant	54.8±5.5	55.9±5.8	54.9±5.7	51.6±6.5	55.7±5.8

Table 10.2: The fit fractions for the decay $\Lambda_c \rightarrow pK\pi$ from the MINUIT fit.

Mode	Čkv(%)	Prod(%)	DC hole(%)	2d Tweak(%)	Syst Error (%)
$p\overline{K}^{*0}$	-0.6	0.0	+1.7	+0.3	1.8
$\Delta^{++}K^-$	-1.2	+0.1	+2.5	-0.7	2.9
$\Lambda(1520)\pi^+$	+0.5	-0.1	+0.9	-0.4	1.1
Nonres	+1.1	+0.1	-3.2	+0.9	3.5

Table 10.3: Deviations from the fit 3p fit fractions for the Systematic Errors.

10.1 Estimated Čerenkov Probabilities

To determine the effect of the Čerenkov probabilities of the kaons and protons on the final fit, we needed to determine the difference between the probabilities in MC and real data. It had already been determined in the collaboration that there was a dependence in the probabilities on the momentum (p) and transverse momentum (p_{T}) of the particles.

So we first looked at p and p_{T} in the background subtracted real data of each type particle to determine the bins for p_{T}. (We were trying to create bins which would have roughly the same number of data points.) We then found as pure a source of kaons and protons as we could find to determine the efficiency of the Neural Network cut on the respective Čerenkov probability. We then let the total weight of the Čerenkov probabilities be the product of the kaon weight and the proton weight.

Once this product was established, we normalized the weights to an average of 1.0. We then recalculated the acceptance using the nearest-neighbor technique but instead of dividing 4 by the volume required to encompass those points, as was described in chapter 8, we divided the weighted sum by the volume. With this new acceptance, we ran our base fit through the analysis and recalculated the fit fractions with errors.

10.1.1 Kaons

Given the third row from figure 10.1, we selected 3 bands in p_{T} which contained roughly the same number of events. See table 10.4 for the numbers used. We then looked at reference [Bar 87] for appropriate bands for p. These bands were selected by the momentum at which the two Čerenkov detectors would start to identify a new particle. See figure 10.2 for a visual of the bands.

p_{T} (GeV/c)	0.0-0.4	0.4-0.6	0.6-			
p (GeV/c)	6-10	10-15	15-20	20-25	25-35	35-

Table 10.4: The bands used for binning the events by p and p_{T}.

Once the bands were established, we needed a kaon source. Using a sample of $\mathrm{D} \to \mathrm{K}\pi\pi$, we cleaned it up using DIP and PTBAL[*]cuts of 0.0029 cm and 0.1624 GeV/c, respectively, which reduced the data set to an estimated 20,000 signal events. See figure 10.3 for a display of the reconstructed $\mathrm{K}\pi\pi$'s before and after the cuts.

To determine the weights needed for the new acceptance, we had to look at the efficiencies of the Čerenkov probability cuts on the Λ_c MC data in each bin of p and p_{T}. Looking at figure 10.4, we found a third order polynomial curve to model the way the data were cut. Note that the probabilities start at 0.13.

Therefore, we looked at the Kaons from the D source and calculated how many K's survived by a hard cut at 0.13 and a weighted cut corresponding to the curve. In other words, if the kaon has a p_{T} greater than 0.6 GeV/c, a p between 25 GeV/c and 35 GeV/c, and a probability of 0.5, then it was assumed that the efficiency for that event was $\sim$0.70. Using this technique we established a

[*]As defined earlier on page 42 with an adjustment from Λ_c to D, DIP is the distance in the xy-plane between the primary vertex and the line of flight of the reconstructed D and PTBAL is the absolute value of the p_{T} of the vector sum of all the secondary tracks with respect to the flight path of the reconstructed D

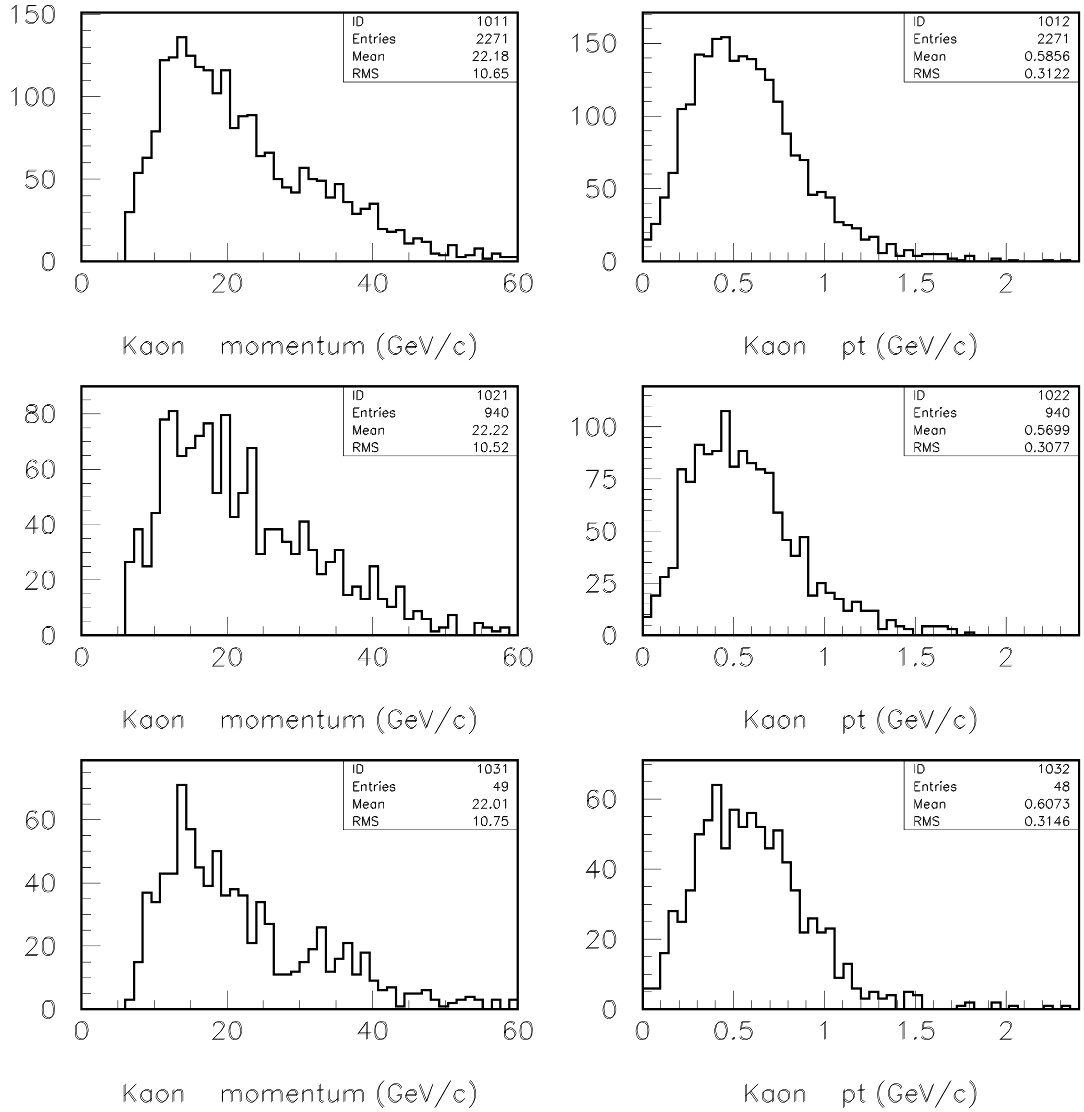

Figure 10.1: Kaons from Λ_c data. Row 1: Full real data set. Row 2: Background data scaled up to 1384 events (as predicted by MINUIT). Row 3: Background subtracted real data.

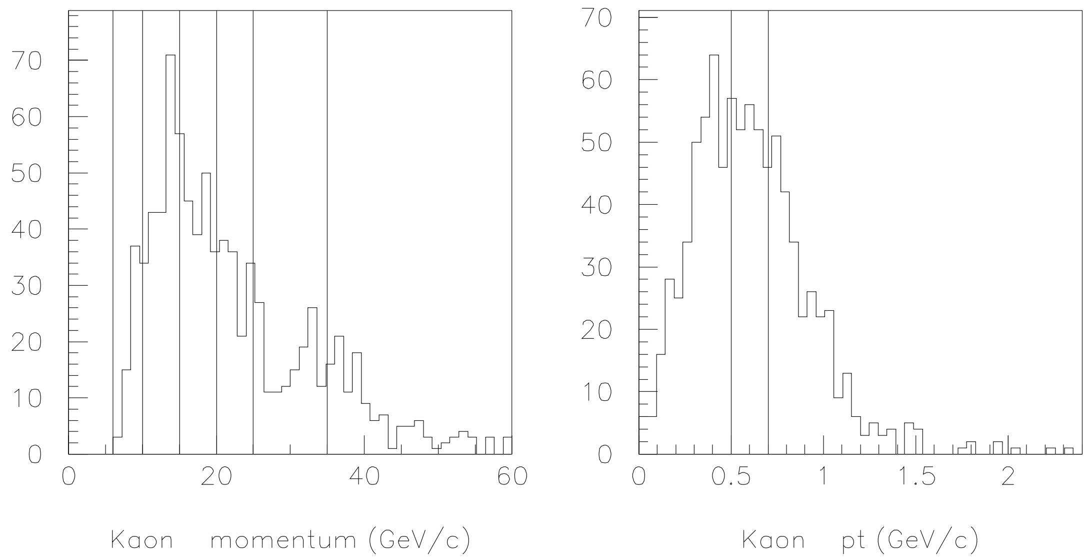

Figure 10.2: The boundaries of the bins chosen displayed on background subtracted Kaons from Λ_c data.

weight for any event within a particular band of p and p_T. Note that if the weight based on the fitted polynomial greater than 1.0 the weight was set to 1.0, and if less than 0.0, the weight was set to 0.0. See tables L.1-L.12 in appendix L for the progression of results, and tables 10.5-10.7 for the final efficiencies. The weights for the surviving MC were then averaged to 1.0.

The error on the efficiencies is $\Delta\epsilon = \sqrt{\frac{\epsilon(1-\epsilon)}{N}}$ where ϵ is the efficiency of the cut and N is the number of events prior to the cut. The error on the ratio is the errors of the efficiencies added in quadrature.

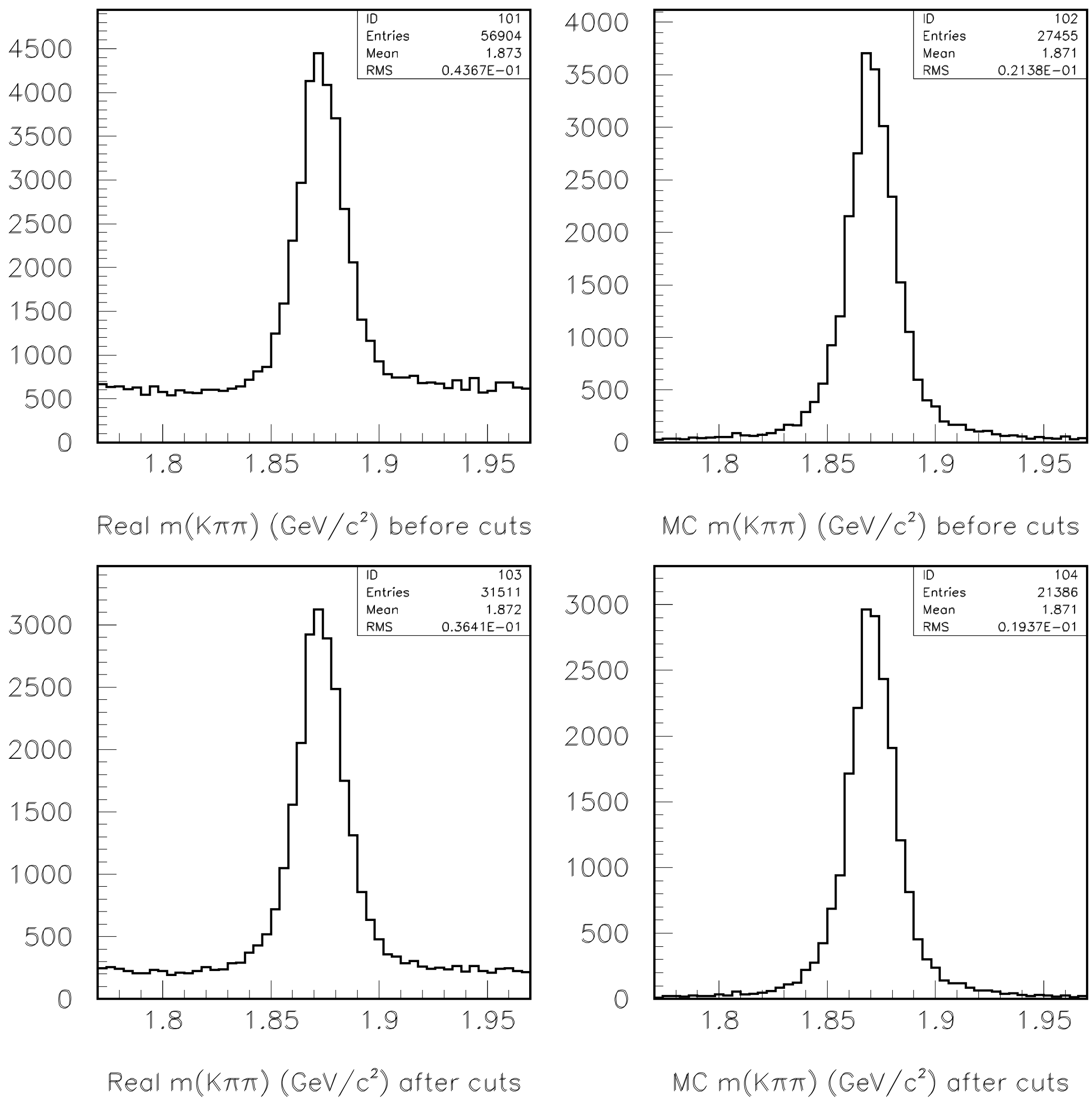

Figure 10.3: Mass of D $\rightarrow$ K$\pi\pi$ before and after the dip and ptb cuts.

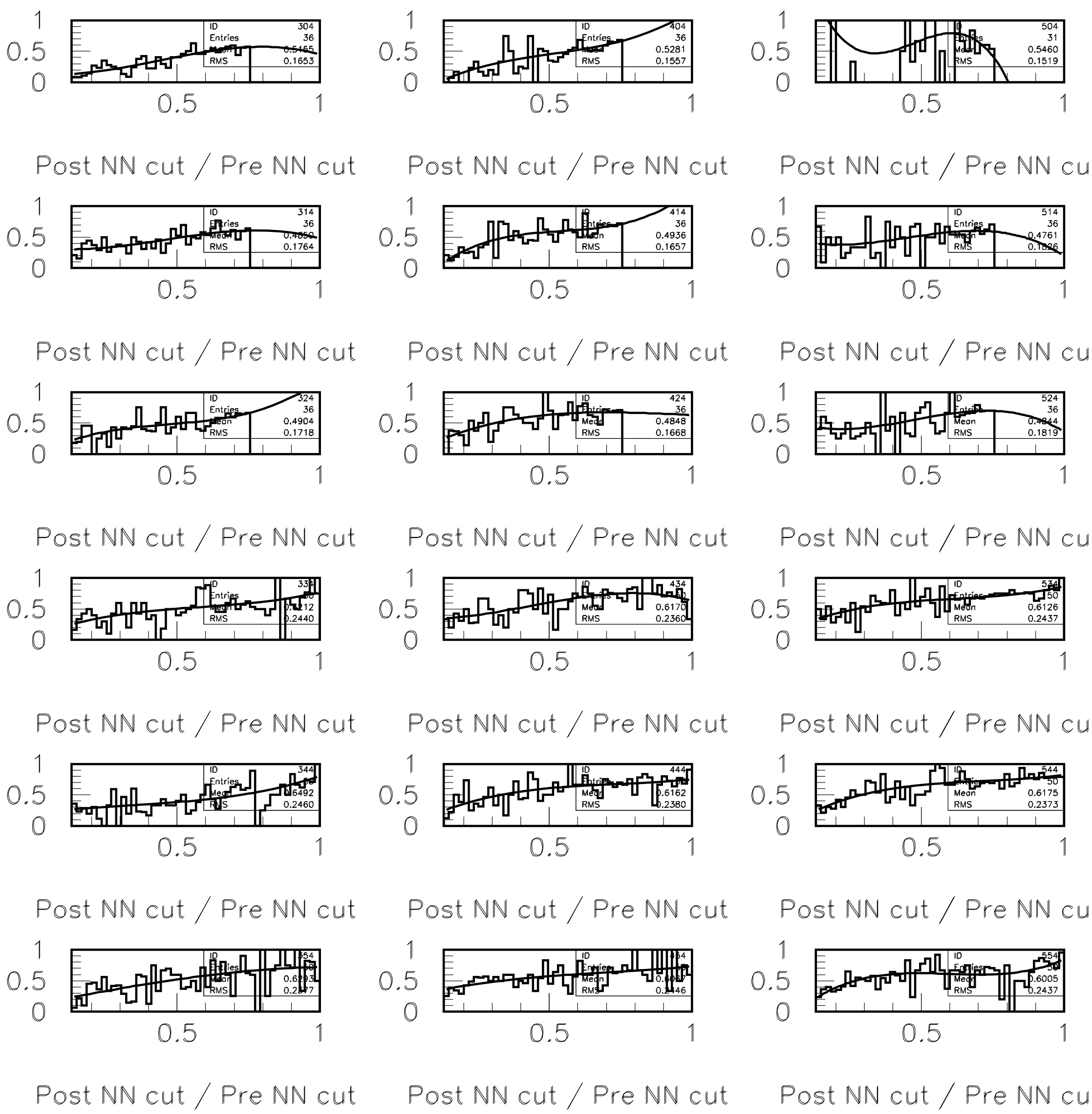

Figure 10.4: The effect of the Neural Net cut on the Kaon Čerenkov probabilities as demonstrated by Λ_c MC. The rows and columns represent the different bins of p and p_{T}.

	p_{T} (GeV)		
p (GeV)	0.0-0.4	0.4-0.6	0.6-
6-10	0.33±0.03	0.43±0.03	0.26±0.03
10-15	0.46±0.02	0.58±0.02	0.45±0.02
15-20	0.53±0.02	0.56±0.02	0.59±0.01
20-25	0.40±0.02	0.53±0.02	0.58±0.01
25-35	0.30±0.02	0.43±0.02	0.54±0.01
35-	0.22±0.02	0.27±0.01	0.24±0.01

Table 10.5: Efficiency of the NN cut on real $\rightarrow$ K$\pi\pi$ data within the m(K$\pi\pi$) of 1.84 GeV/c^2 - 1.92 GeV/c^2.

	p_{T} (GeV)		
p (GeV)	0.0-0.4	0.4-0.6	0.6-
6-10	0.26±0.03	0.36±0.04	0.28±0.04
10-15	0.39±0.03	0.57±0.03	0.46±0.02
15-20	0.51±0.03	0.52±0.02	0.59±0.02
20-25	0.37±0.03	0.49±0.02	0.55±0.02
25-35	0.29±0.02	0.38±0.02	0.48±0.01
35-	0.13±0.01	0.13±0.01	0.12±0.00

Table 10.6: Efficiency of the NN cut on MC $\rightarrow$ K$\pi\pi$ data within the m(K$\pi\pi$) of 1.84 GeV/c^2 - 1.92 GeV/c^2.

	p_{T} (GeV)		
p (GeV)	0.0-0.4	0.4-0.6	0.6-
6-10	1.26±0.19	1.19±0.16	0.92±0.16
10-15	1.18±0.10	1.02±0.06	1.00±0.06
15-20	1.03±0.07	1.07±0.06	1.00±0.04
20-25	1.09±0.10	1.07±0.07	1.05±0.04
25-35	1.06±0.09	1.14±0.07	1.12±0.03
35-	1.60±0.17	2.03±0.14	2.00±0.08

Table 10.7: The ratio of the real data efficiency to the MC data efficiency.

10.1.2 Proton's

Given the third row from figure 10.5, we selected 3 bands which contained roughly the same number of protons from the real Λ_c data events. See table 10.8 for the numbers used. See figure 10.6 for a visual of the bands.

p_T (GeV/c)	0.0-0.6	0.6-0.9	0.9-		
p (GeV/c)	6-20	20-30	30-40	40-50	50-

Table 10.8: The bands used for binning the events by p and p_T.

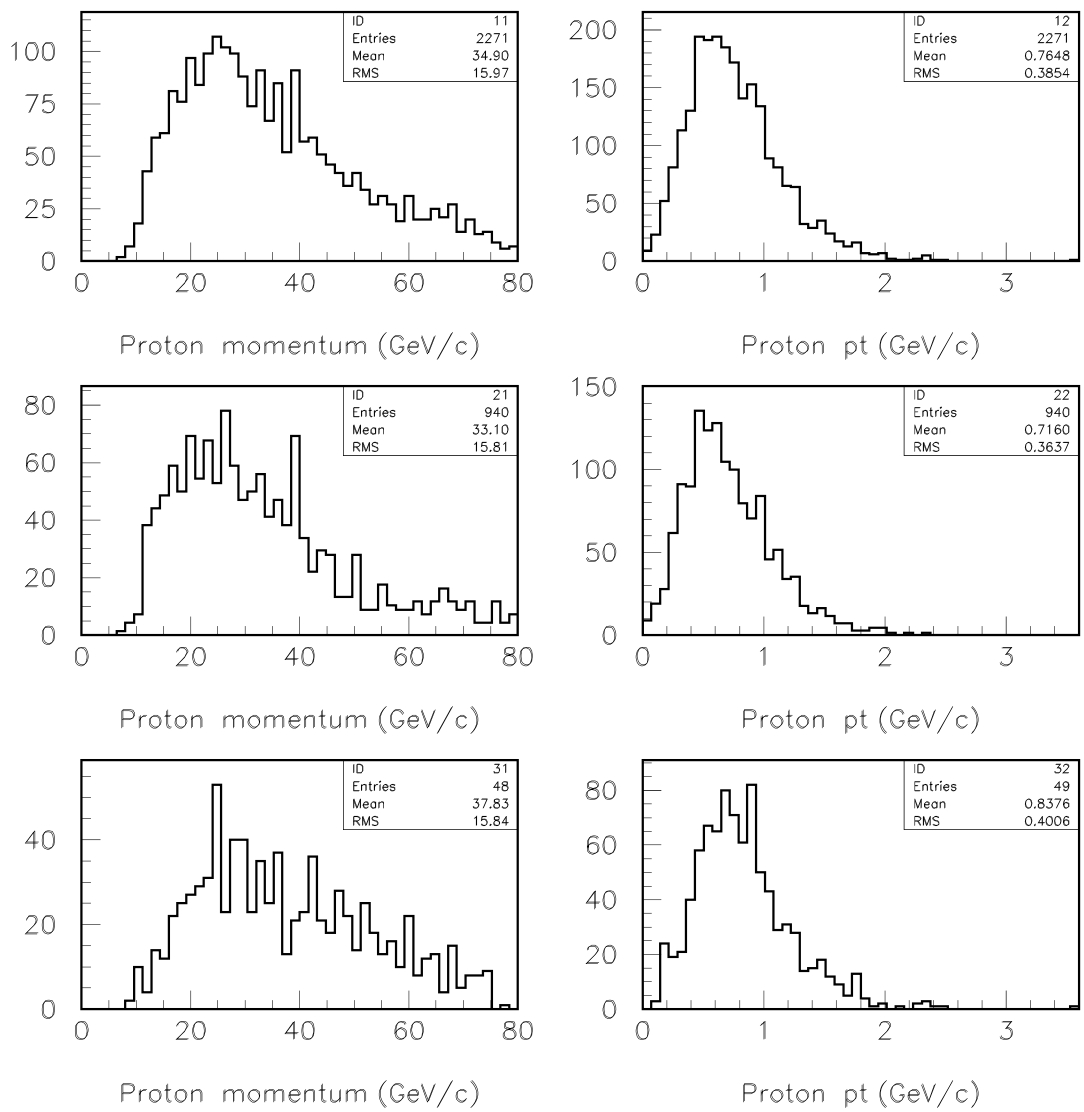

Figure 10.5: Protons from real Λ_c data. Row 1: Real data from full data set. Row 2: Background data (from wings) scaled up to 1384 events (as predicted by MINUIT). Row 3: Background subtracted real data.

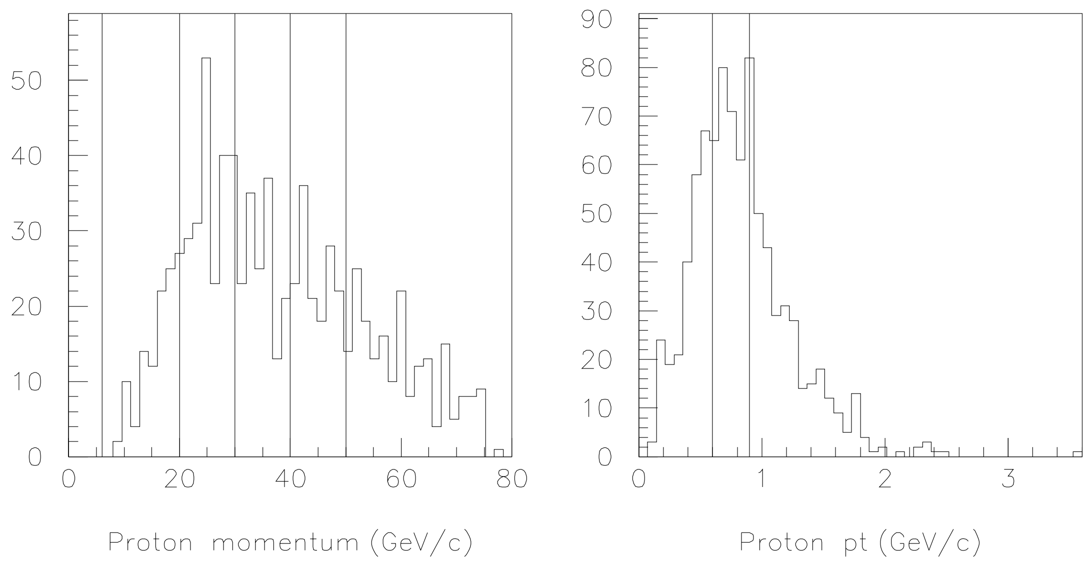

Figure 10.6: The boundaries of the bins chosen displayed on background subtracted protons from real Λ_c data.

Once the bands were established, we needed a proton source. For this, we selected the decay mode, $\Lambda \rightarrow \mathrm{p}\pi$. †See figure 10.7 for the plot of the reconstructed $\mathrm{p}\pi$. The requirements that we applied to the proton and pion tracks were:

1. $\chi^2 < 5.0$
2. 0.5 GeV/c $\leq p < 500.0$ GeV/c
3. total charge $= 0.0$
4. $3 <$ jcatsg ≤ 15
5. 1.08 GeV/c^2 $< \mathrm{m}_{\Lambda\rightarrow\mathrm{p}\pi} < 1.16$ GeV
6. $\mathrm{m}_{\mathrm{K}\rightarrow\pi\pi}$ is outside range of 0.49 GeV/c^2 - 0.51 GeV/c^2

The last item is to eliminate the possible $\mathrm{K} \rightarrow \pi\pi$ reflections in the data.

To determine the weights needed for the new acceptance, we had to look at the efficiencies of the Čerenkov probability cuts on the data. Looking at figure 10.8, we found a third order polynomial curve to model the way the data were cut in each bin of p and p_{T}. See tables L.13-L.24 in appendix L for the progression of results, and tables 10.9-10.11 for the final efficiencies.

The error on the efficiencies is $\Delta\epsilon = \sqrt{\frac{\epsilon(1-\epsilon)}{N}}$ where ϵ is the efficiency of the cut and N is the number of events prior to the cut. The error on the ratio is the errors of the efficiencies added in quadrature.

†The real data came from the tape internally labelled LA1068 which had been produced at the University of Mississippi. For MC, we generated our own.

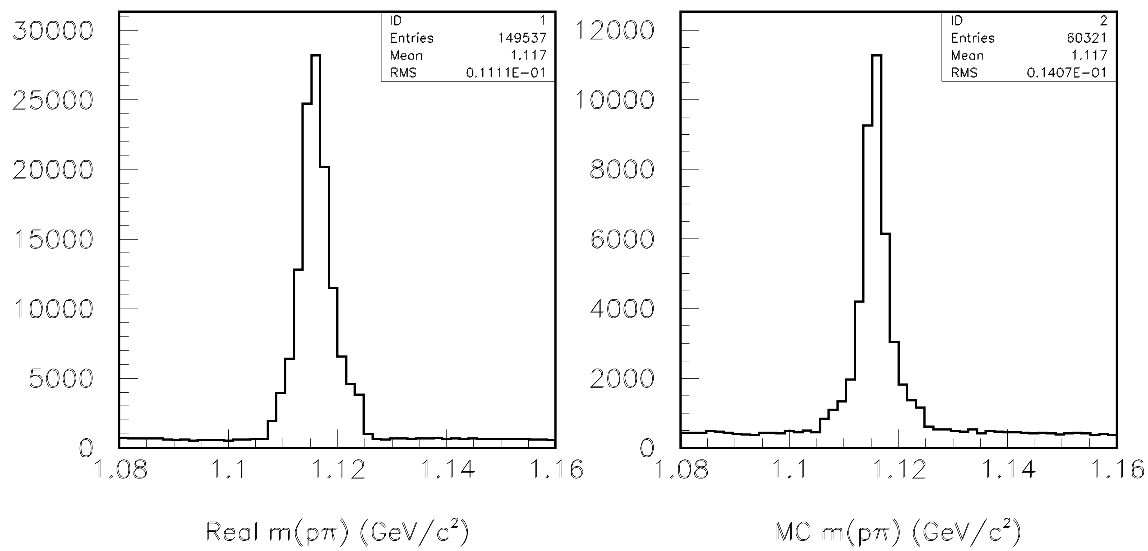

Figure 10.7: Mass of $\Lambda \rightarrow p\pi$.

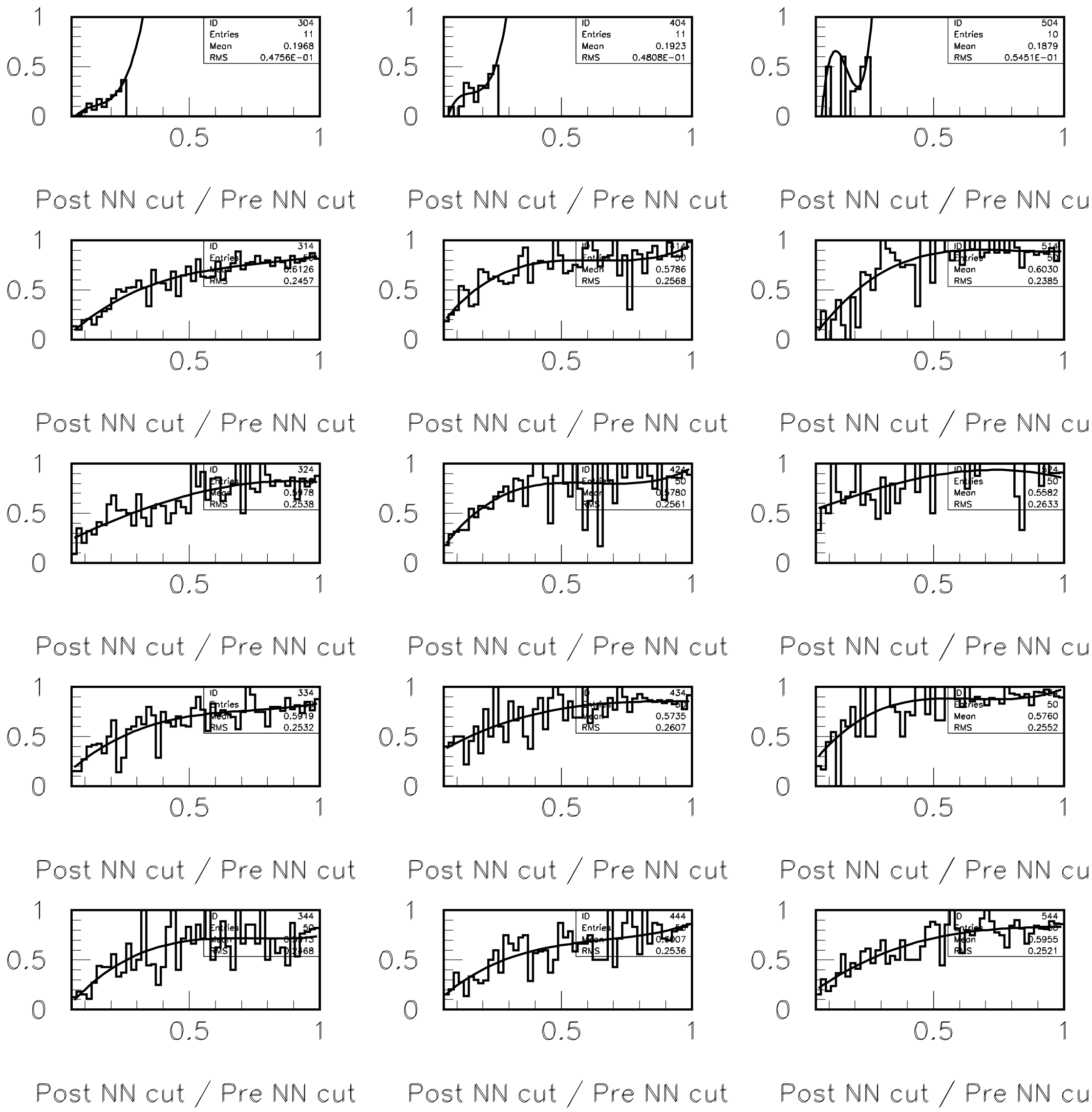

Figure 10.8: The effect of the Neural Net cut on the Proton Čerenkov probabilities as demonstrated by the MC Λ_c data.

	p_{T} (GeV)		
p (GeV)	0.0-0.6	0.6-0.9	0.9-
6-20	0.27±0.00	0.46±0.00	0.60±0.01
20-30	0.50±0.01	0.69±0.01	0.73±0.01
30-40	0.60±0.01	0.74±0.01	0.82±0.01
40-50	0.70±0.02	0.79±0.01	0.88±0.01
50-	0.66±0.02	0.76±0.02	0.76±0.01

Table 10.9: The efficiency of NN cut on the protons from Real $\Lambda \to \mathrm{p}\pi$ data within the mass range of 1.1056 GeV/c^2 - 1.1264 GeV/c^2.

	p_{T} (GeV)		
p (GeV)	0.0-0.6	0.6-0.9	0.9-
6-20	0.17±0.00	0.37±0.01	0.50±0.01
20-30	0.39±0.01	0.53±0.01	0.60±0.01
30-40	0.46±0.02	0.52±0.02	0.64±0.02
40-50	0.48±0.03	0.58±0.03	0.65±0.03
50-	0.32±0.05	0.52±0.04	0.47±0.02

Table 10.10: The efficiency of the NN cut on the protons from MC $\Lambda \to \mathrm{p}\pi$ data within the mass range of 1.1056 GeV/c^2 - 1.1264 GeV/c^2.

	p_{T} (GeV)		
p (GeV)	0.0-0.6	0.6-0.9	0.9-
6-20	1.59±0.03	1.24±0.03	1.20±0.03
20-30	1.28±0.03	1.29±0.04	1.22±0.03
30-40	1.30±0.05	1.44±0.07	1.27±0.04
40-50	1.46±0.10	1.37±0.08	1.34±0.05
50-	2.08±0.35	1.45±0.12	1.61±0.08

Table 10.11: The ratio of the efficiencies from the NN cut of the Real $\Lambda \to \mathrm{p}\pi$ data to the MC data.

10.2 The Production Model

To explore the production model, we looked at the Feynman x (x_{F}) and the square of the transverse momentum (p_{T}^2) of each decay. We first found x_{F} and p_{T}^2 for each of the 2,271 final decay events and the 11,454 MC events used for modeling the acceptance. From the final decay events, we plotted the projection of these variables for the 940 events used to model the background, scaled these events to simulate the 1,384 background events calculated by MINUIT, and subtracted the background from the full sample. We then smoothed the background subtracted and MC projections and found the ratio of background subtracted to MC for each bin. See figure 10.9 and 10.10 for the projections of the above explanations. The large bin size for p_{T}^2 was chosen to avoid statistical fluctuations.

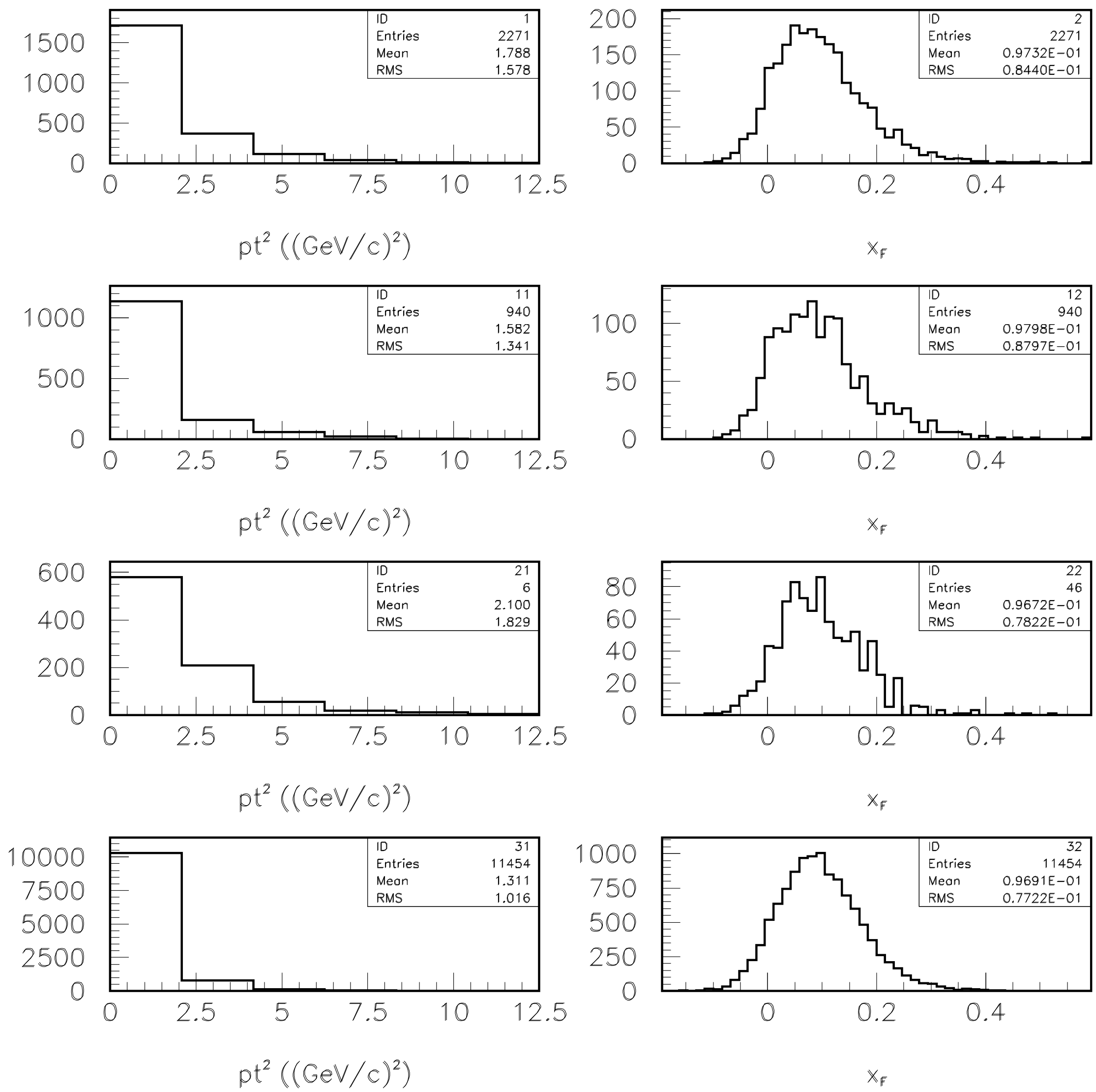

Figure 10.9: p_{T}^2 and x_{F} for Λ_c. Row 1: Real data. Row 2: Background data scaled up to 1384 events (as predicted by MINUIT). Row 3: Background subtracted real data. Row 4: Surviving reconstructed MC.

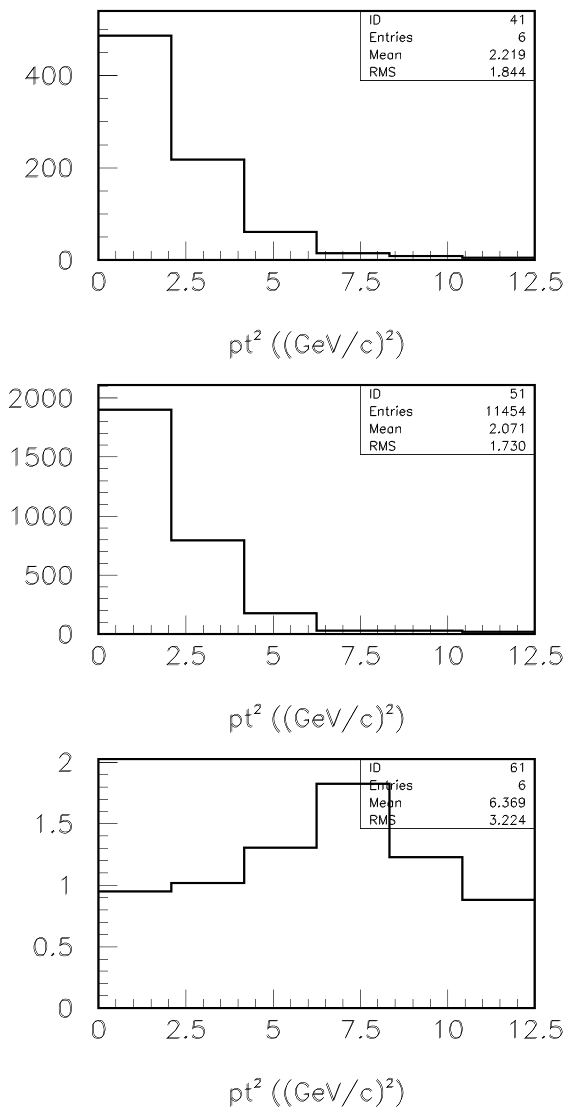

Figure 10.10: p_{T}^2 and x_{F} for Λ_c. Row 1: Smoothed background subtracted real data. Row 2: Smoothed MC. Row 3: The ratio of normalized background subtracted real data to normalized MC.

The weight used for the 11,454 events was the product of the size of the corresponding bin for each event in each projection. The weights were then averaged to 1.0. We then recalculated the acceptance using the nearest-neighbor technique but instead of dividing 4 by the volume required to encompass those points, as was described in chapter 8, we divided the weighted sum by the volume. With this new acceptance, we ran our base fit through the analysis and recalculated the fit fractions with errors.

10.3 DC hole Parameters

In order to explore the effect of the drift chamber (DC) holes[‡] , we looked at all the surviving reconstructed MC to see the survival rate as a function of the hole. See figure 10.11 for a histogram of the relationship between the hole parameter and the survival rate. Since an equal number of MC were generated with each hole parameter the relative number of surviving MC is the same as the relative efficiency for each hole. We then used the events from the first two holes and used it to model the acceptance using the nearest-neighbor technique again.

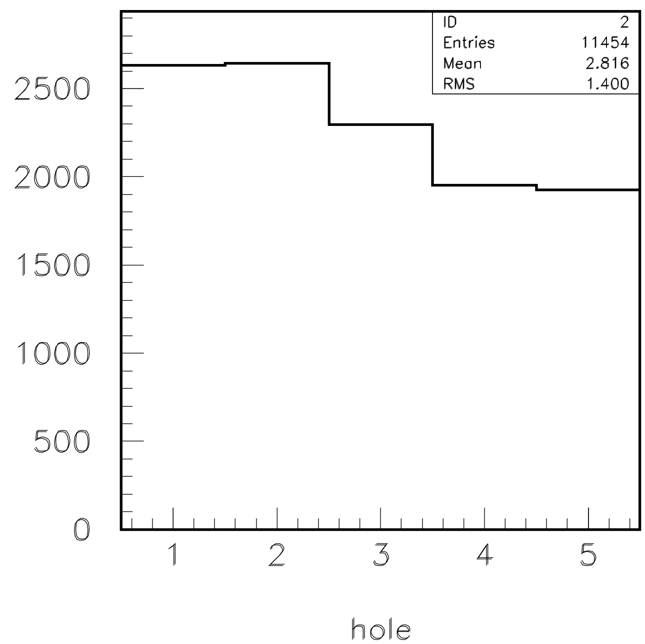

Figure 10.11: The number of surviving reconstructed MC by DC hole.

[‡]There was a problem with excess ionization at the point where the beam hit the DC. As the time of the experiment went on, this created a drop in efficiency for certain parts of the DC. This problem area is referred to as the DC hole. As time went on this hole increased in size. This was treated by incorporating this hole into the analysis of the data. See page 30.

10.4 Tweaking

When adjusting the acceptance model to match the one dimensional projections, we ignored the possibility of adjusting to match the two dimensional projections. Unsure of the potential effect of this new adjustment, we treated it as a possible systematic error. We, therefore, tweaked the K-nearest-neighbor model to match the two dimensional projection if each projection was binned in a 12x12 histogram. we then reran the fit with this new acceptance model. See appendix J for a χ^2 comparison of the surviving reconstructed MC (the acceptance) and the new model.

10.5 Reflections in the Background

One of the early cuts made was to remove the D reflections from the data set. After all the cuts were made, did these reflections still seep their way into the analysis?

10.5.1 ϕ

Looking for a common D resonance of ϕ, we created figures 10.12 - 10.14. Although ϕ appears to have a small peak as seen in figure 10.12 (as it is not seen in figure 10.13), these decays are mostly seen in the the wings, noted by their diminished presence in figure 10.14. With approximately 20 ϕ's in the final data set, we would expect, assuming they are in the background, that there would be around 6 ϕ's in the signal region, which there seem to be. Thus, we assume that this reflected resonance is already taken into account in our background model.

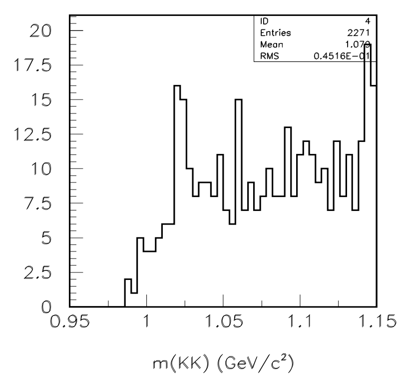

Figure 10.12: The KK mass from the final real data set.

10.5.2 $\overline{K}^{*0}$

Looking for $\overline{K}^{*0}$ in the signal region, we looked for the $\overline{K}^{*0}$'s in the signal region, the wings, and all of the data set. Fixing the $\overline{K}^{*0}$ mass and width, we projected the data set onto the $K\pi$ mass axis and fit the a Breit-Wigner resonance and quadratic background to the plots. From this MINUIT predicted 278±33 $\overline{K}^{*0}$ in the signal region, 58±24 in the wings, and 339±41 in the total set. See figure 10.15. 58 $\overline{K}^{*0}$ in the wings would correspond to 85±35 in the total sample and 27 in the signal region. This would indicate that the number of $\overline{K}^{*0}$ which are part of the signal is 251. Based

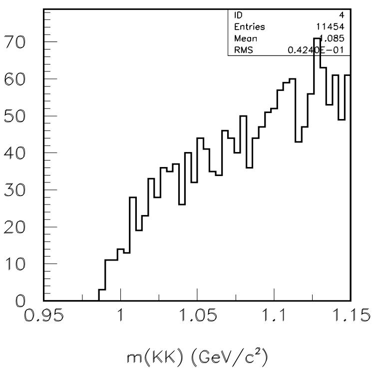

Figure 10.13: The KK mass from the surviving reconstructed MC set.

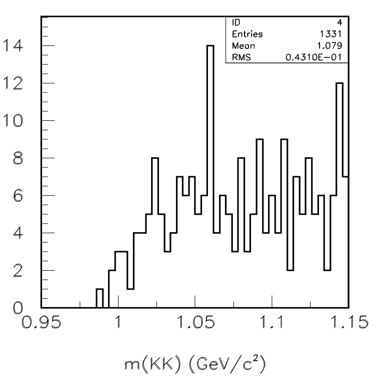

Figure 10.14: The KK mass from the signal region of the final data set.

on the fit fraction in the model, there should be 232±36 $\overline{\mathrm{K}}^{*0}$'s. This also indicates that the number of $\overline{\mathrm{K}}^{*0}$'s in the signal region is less than a σ and therefore should be taken into account properly by the background model.

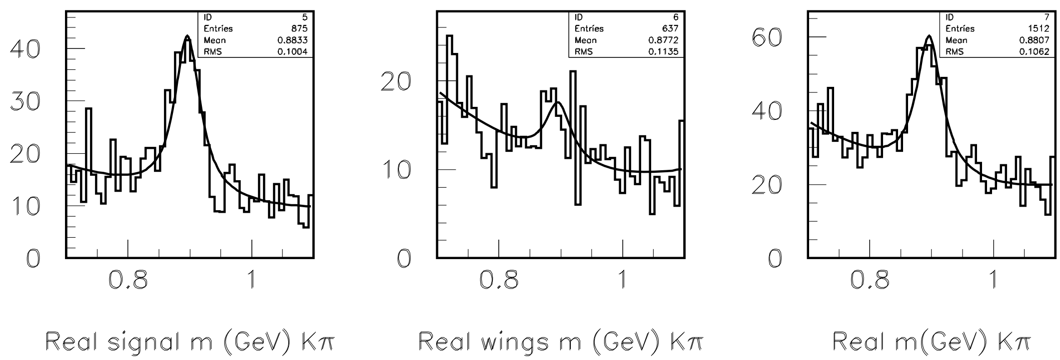

Figure 10.15: $\overline{\mathrm{K}}^{*0}$ as seen in the signal region, the wings, and the combined signal region and wings.

10.5.3 $\Delta^{++}(1232)$

We also looked for $\Delta^{++}(1232)$ in the background but referring to figure 10.16, none can be see in the wings (the middle plot).

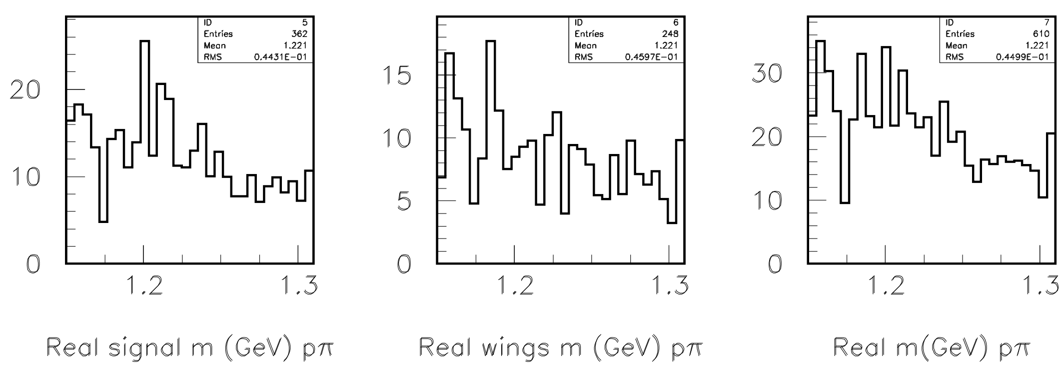

Figure 10.16: Δ^{++} as seen in the signal region, the wings, and the combined signal region and wings.

Chapter 11

Conclusion

Our final fit fractions can be found in table 11.1.

Mode	Fit Fraction (%)
$p\overline{K}^{*0}(890)$	19.5±2.6±1.8
$\Delta^{++}(1232)K^-$	18.0±2.9±2.9
$\Lambda(1520)\pi^+$	7.7±1.8±1.1
Nonresonant	54.8±5.5±3.5

Table 11.1: The decay fractions for $\Lambda_c^+ \to pK^-\pi^+$ with statistical and systematic errors from the final fit.

In addition to the nonresonant decays, the $p\overline{K}^{*0}$ and the $\Delta^{++}K^-$ modes definitely exist with significant branching fractions. This demonstrates that the exchange diagram contributes significantly in charm baryon decays. The fit prefers a $\Lambda(1520)$ contribution at around the 3 σ level. We also allowed for the $\Lambda(1600)$ and $\Sigma(1660)$ resonances in our data and found no significant evidence for either of them. We did find that the fit favored a spin $\frac{1}{2}^-$ particle with a mass of 1.565 GeV/c^2 and a width of 332 MeV/c^2, but there is no known particle with this description. We also found some evidence for the upper tail of the $\Lambda(1405)$ ($\to$ pK) but believe a higher statistics experiment can comment more conclusively.

Comparing our branching ratios (not fit fractions - see section 2.7 for the difference) to previous experiments, as seen in Table 11.2, one can note that the the NA32 values are similar to ours. Although we used a more sophisticated approach to the problem, this decay does not demonstrate much interference, as is also demonstrated by the fit fractions in Table 9.5 adding up close to 100%.

Mode	E791	NA32[Boz 93]	ISR[Bas 81]
$p\overline{K}^{*0}(890)$	0.29±0.04±0.03	$0.35^{+0.06}_{-0.07}\pm0.03$	0.42± 0.24
$\Delta^{++}(1232)K^-$	0.18±0.03±0.03	$0.12^{+0.04}_{-0.05}\pm0.05$	0.40±0.17
$\Lambda(1520)\pi$	0.15±0.04±0.02	$0.09^{+0.04}_{-0.03}\pm0.02$	
Nonresonant	0.55±0.06±0.04	$0.56^{+0.07}_{-0.09}\pm0.05$	

Table 11.2: Branching ratios relative to $\Lambda_c^+ \to pK^-\pi^+$. The NA32 and ISR values were calculated from the projections only and do not include the phase uncertainty.

Appendix A

The E791 Collaboration

Centro Brasileiro de Pesquisas Físicas, Rio de Janeiro RJ, Brazil
S. Amato, J. C. Anjos, I. Bediaga, H. S. Carvalho, C. Gobel, J. Magnin, J. R. T. de Mello Neto, J. M. de Miranda, A. C. dos Reis, A. F. S. Santoro, J. Solano

University of California, Santa Cruz, California 95064
P. Gagnon, J. Leslie, K. O'Shaughnessy

University of Cincinnati, Cincinnati, Ohio 45221
S. Devmal, B. Meadows, A. B. d'Oliveira, L. P. Perera A. K. S. Santha, A. J. Schwartz, M. D. Sokoloff

CINVESTAV, 07000 Mexico City, DF Mexico
G. Herrera, M. Sheaff

Fermilab, Batavia, Illinois 60510
J. A. Appel, S. Banerjee, T. Carter, K. Denisenko, A. M. Halling, C. James, S. Kwan, B. Lundberg, R. J. Stefanski, K. Thorne

Illinois Institute of Technology, Chicago, Illinois 60616
R. A. Burnstein, P. A. Kasper, K. C. Peng, H. A. Rubin

Kansas State University, Manhattan, Kansas 66506
D. Mihalcea, A. Nguyen, N. W. Reay, R. A. Sidwell, N. R. Stanton, A. K. Tripathi, N. Witchey, S. M. Yang, S. Yoshida, C. Zhang

University of Massachusetts, Amherst, Massachusetts 01003
G. Blaylock

University of Mississippi, University, Mississippi 38677
E. M. Aitala, L. M. Cremaldi, K. Gounder, B. Quinn, A. Rafatian, J. J. Reidy, D. A. Sanders, D. J. Summers, D. Yi

Princeton University, Princeton, New Jersey 08544
J. Wiener

Universidad Autonoma de Puebla, Puebla, Mexico
A. Fernandez, A. B. d'Oliveira

University of South Carolina, Columbia, South Carolina 29208
N. K. Copty, G. F. Fox, D. C. Langs, M. V. Purohit

Stanford University, Stanford, California 94305
P. R. Burchat, R. Zaliznyak

Tel Aviv University, Tel Aviv, 69978 Israel
D. Ashery, G. Hurvits, S. MayTal-Beck, R. Weiss-Babai

Box 1290, Enderby, British Columbia, V0E 1V0, Canada
S. B. Bracker

Tufts University, Medford, Massachusetts 02155
R. H. Milburn, A. Napier

University of Wisconsin, Madison, Wisconsin 53706
S. Radeztsky, M. Sheaff, K. Stenson, S. Watanabe

Yale University, New Haven, Connecticut 06511
C. Darling, A. J. Slaughter, S. Takach, E. Wolin

Appendix B

E791 Data Summary Tape Format Version 7 for Farm Release 7

```
November 1993
ENDCOMM

DST Version             7        10
Bank & Packing Source   Variable
======================= ==============================
 1)HEADER:              9
/runid/    run_number   RUN NUMBER
/scaler791/event_number EVENT NUMBER HI
/scaler791/event_number EVENT NUMBER LO
/dst/      idstvn       DST TABLE VERSION NUMBER
/analys_info/filter_vsn Filter Code Version
/scaler791/spill_number SPILL NUMBER
/scaler791/time_in_spil TIME IN SPILL HI
/scaler791/time_in_spil TIME IN SPILL LO
/dst/      dsterr       PACKING ERROR
 2)TRACKS:              33
/tracks/   ntrk         TRACKS (N)
/tracks/   ierpm2       LINKED SMD TRACKS
/r1sort/   incer        TRACKS IN CERENKOVS
/r1sort/   incal        TRACKS IN CALORIMETERS
/r1sort/   linked,nstubsLINKED SMD CAT 3,7,15,28;0
/strint/   nx,nyview    STR TRACKS
/strout/   nv,n3view    STR TRACKS
/tracks/   dof          DEGREES OF FREEDOM
/tracks/   q,jcatsg     Q & JCATSG
/tracks/   xis          CHI SQUARE
/r1sort/   xisqvx       VX CHI SQR CONTR
/r1sort/   sorted       XINTERCEPT R1
```

```
/r1sort/   sorted       DXDZ       R1
/r1sort/   sorted       YINTERCEPT R1
/r1sort/   sorted       DYDZ       R1
/tracks/   pp           Q=1/P
/etrxcm/   errtrx(15)   DQ
/r1sort/   sermat       ERR MAT DIAG
/r1sort/   sermat       ERR MAT OFF-DIAG
/etrxcm/   errtrx(11)   ERR MAT MOM-CORR
/etrxcm/   errtrx(12)   ERR MAT MOM-CORR
/etrxcm/   errtrx(13)   ERR MAT MOM-CORR
/r1sort/   xissmd       CHI SQUARE FROM SMD
/strout/   iuniq3       UNIQUE HITS
/r1cand/   r1cand_chi   REFITTED SMD CHI SQUARE
/r1cand/   r1cand_dof   REFITTED SMD DOF
/etrxcm/   errtrx(14)   ERR MAT MOM-CORR
/r1sort/   ndfsmd       SMD DEGREES OF FREEDOM
/r1cand/   r1cand_par   STUBS XINTERCEPT R1
/r1cand/   r1cand_par   STUBS DXDZ       R1
/r1cand/   r1cand_par   STUBS YINTERCEPT R1
/r1cand/   r1cand_par   STUBS DYDZ       R1
/strout/   iuniq3       STUBS UNIQUE HITS
 3)NEUTRAL HADRONS:     12
/calsum/   nhadn        NEUTRAL HADRONS (N)
/calsum/   ical         PARTICLE TYPE
/calsum/   jcal         PARTICLE INDEX
/calsum/   iuscal       CALORIMETER FLAG
/calsum/   p4cal        ENERGY
/calsum/   decal        ERROR IN ENERGY
/calsum/   xcal         X CENTROID
/calsum/   ycal         Y CENTROID
/calsum/   zcal         Z CENTROID
/calsum/   dxcal        ERROR IN X CENTROID
/calsum/   dycal        ERROR IN Y CENTROID
/calsum/   probha       HADRON PROBABILITY
 4)PHOTONS:             12
/calsum/   nfoton       PHOTONS (N)
/calsum/   ical         PARTICLE TYPE
/calsum/   jcal         PARTICLE INDEX
/calsum/   iuscal       CALORIMETER FLAG
/calsum/   p4cal        ENERGY
/calsum/   decal        ERROR IN ENERGY
/calsum/   xcal         X CENTROID
/calsum/   ycal         Y CENTROID
/calsum/   dxcal        ERROR IN X CENTROID
```

```
/calsum/   dycal        ERROR IN Y CENTROID
/calsum/   testb        RATIO OF 2 LOWEST ENERGIES
/calsum/   testc        CALCULATED U POSITION
 5)PIZEROS:             14
/pizout/   npiz         PI ZEROS (N)
/pizout/   igmpiz       POINTER TO PHOTONS
/pizout/   icomp        COMPETING PI ZEROS
/pizout/   itpiz        PI ZERO TYPE
/pizout/   prpiz2       PAIR QUALITY
/pizout/   ampiz        MASS
/pizout/   dmpiz        ERROR IN MASS
/pizout/   p4piz        X MOMENTUM
/pizout/   p4piz        Y MOMENTUM
/pizout/   p4piz        Z MOMENTUM
/pizout/   depiz        ERROR IN ENERGY
/pizout/   dthpi        ERROR IN DECAY PLANE ANGLE
/pizout/   dphpi        ERROR OUT-OF-PLANE ANGLE
/pizout/   iqualpiz     PI ZERO QUALITY
 6)VERTICES:            14
/vtxpar/   nvert        20*NPRI+NSEC (N)
/tkpars/   ntkvtx       VERTEX TRACKS (M)
/vtxpar/   chvtx        CHI SQUARE
/vtxpar/   xyzvtx       X POSITION
/vtxpar/   xyzvtx       Y POSITION
/vtxpar/   xyzvtx       Z POSITION
/vtxpar/   errvtx       ERROR IN X
/vtxpar/   errvtx       ERROR IN Y
/vtxpar/   errvtx       ERROR IN Z
/vtxpar/   ndfofvtx     DEGREES OF FREEDOM
/vtxpar/   covvtx*      XY ERR / (X ERR * Y ERR)
/vtxpar/   covvtx*      XZ ERR / (X ERR * Z ERR)
/vtxpar/   covvtx*      YZ ERR / (Y ERR * Z ERR)
/tkpars/   itkvtx       POINTER TO SMD TRACKS
 7)PARENT TRACKS:       34
/parent_tr num_parent   NUMBER OF PARENTS (N)
/srtprt/   numpc2       NUMBER WITH PCATSG=2 (N2)
/xitrk/    numxitrk     NUMBER OR HYPERON TRACKS
/parent_tr typ_prnt(ip) HEP ID OF PARENT
/parent_tr pjcatsg(ip)  REC ID OF PARENT
/parent_tr num_dtrs(ip) DECAY MULTIPLICITY (M)
/parent_tr idx_trax(ip) POINTER TO TRACKS
/parent_tr typ_dtr(id,i HEP ID OF DAUGHTERS
/parent_tr idx_dtr(id,i POINTER TO SMD TRACKS
/srtprt/   iptpc2       POINTER TO PARENT
```

```
/parent_tr pdtr_m1      PX OF DAUGHTER 1
/parent_tr pdtr_m1      PY OF DAUGHTER 1
/parent_tr pdtr_m1      PX OF DAUGHTER 2
/parent_tr pdtr_m1      PY OF DAUGHTER 2
/parent_tr pdtr_m1      PZ OF DAUGHTER 1
/parent_tr pdtr_m1      PZ OF DAUGHTER 2
/parent_tr parvtx       VERTEX X POSITION
/parent_tr parvtx       VERTEX Y POSITION
/parent_tr parvtx       VERTEX Z POSITION
/parent_tr pardca       VERTEX DCA
/xitrk/    xitrk_par(1) X INTERCEPT
/xitrk/    xitrk_par(2) X SLOPE
/xitrk/    xitrk_par(3) Y INTERCEPT
/xitrk/    xitrk_par(4) Y SLOPE
/xitrk/    xitrk_err    ERR MAT DIAG
/xitrk/    xitrk_err    ERR MAT OFF-DIAG
/xitrk/    xitrk_chi    CHI SQUARE
/xitrk/    xitrk_eff    EFFICIENCY
/xitrk/    xitrk_qual   QUALITY
/xitrk/    xitrk_dof    DEGREES OF FREEDOM
/xitrk/    xitrk_fnd    NUMBER OF HITS FOUND
/xitrk/    xitrk_uniq   NUMBER OF UNIQUE HITS
/xitrk/    xitrk_to_prntPOINTER TO PARENT
/xitrk/    xitrk_flg    POINTER TO R1CAND
 8)BEAM TRACKS:         11
/beamout/  nbeam        BEAM TRACKS (N)
                        NOT USED
/beamout/  btracks      BEAM X INTERCEPT
/beamout/  btracks      BEAM X SLOPE
/beamout/  btracks      BEAM Y INTERCEPT
/beamout/  btracks      BEAM Y SLOPE
/beamout/  bchisq       CHI SQUARE
/r1sort/   nbhcod       10*SMD+PWC HITS
/beamout/  berr         ERR INTERCEPT
/beamout/  berr         ERR SLOPE
/beamout/  berr         ERR CROSS TERMS
 9)CERENKOV:            7
/r1sort/   incer        TRACKS ACCEPTED (N)
local                   POINTER TO TRACKS
/ckvid/    cprb2        PROBABILITY ELECTRON
/ckvid/    cprb2        PROBABILITY MUON
/ckvid/    cprb2        PROBABILITY PION
/ckvid/    cprb2        PROBABILITY KAON
/ckvid/    cprb2        PROBABILITY PROTON
```

```
10)CALORIMETRY:          18
/r1sort/   incal         TRACKS ACCEPTED (N)
local                    POINTER TO TRACKS
/calsum/   ical          PARTICLE TYPE
/calsum/   jcal          PARTICLE INDEX
/calsum/   iuscal        CALORIMETER FLAG
/calsum/   kev511        BIT PATTERN
/calsum/   esl           ENERGY IN SLIC
/calsum/   ehdm          ENERGY IN HADROMETER
/calsum/   decal         ERROR IN TOTAL ENERGY
/calsum/   emprob        EM PROBABILITY
/calsum/   probmu        MU PROBABILITY
/calsum/   xcal          X CENTROID
/calsum/   ycal          Y CENTROID
/caldst/   secmom        2ND MOMENT OF ENERGY DISTR
/caldst/   ehmin         HADROMETER VIEW ENERGY
/caldst/   iuvwid,hadco  2*IUVWID+HADCONG
/caldst/   caldx         TRACK TO SHOWER X SEPAR
/caldst/   caldy         TRACK TO SHOWER Y SEPAR
11)MUON:                 15
/mutrks/   mucands       NUMBER OF MU CANDIDATES (N)
/mutrks/   nmutrk        POINTER TO TRACKS
/mutrks/   mupadx        POINTER TO X PADDLES
/mutrks/   mupady        POINTER TO Y PADDLES
/mutrks/   mutdcx        X PADDLE TDC VALUES
/mutrks/   mutdcy        Y PADDLE TDC VALUES
/mutrks/   eslicu        CANDIDATE SLIC U ENERGY
/mutrks/   eslicv        CANDIDATE SLIC V ENERGY
/mutrks/   eslicy        CANDIDATE SLIC Y ENERGY
/mutrks/   ehadx         CANDIDATE HADR X ENERGY
/mutrks/   whadx         CANDIDATE HADR X WIDTH
/mutrks/   fthadx        HADR FRONT/TOTAL ENERGY
/mutrks/   ehady         CANDIDATE HADR Y ENERGY
/mutrks/   whady         CANDIDATE HADR Y WIDTH
/mutrks/   fthady        HADR FRONT/TOTAL ENERGY
12)MISCELLANEOUS:        26
/cam791/   muon_front    FRONT MUON LATCH
/cam791/   muon_back     BACK MUON LATCH-HI
/cam791/   muon_back     BACK MUON LATCH-LO
/esum791/  esum          BEAM SPOT ADC
/esum791/  esum          INTERACTION ADC
/esum791/  esum          ET ADC
/esum791/  esum          ETOT ADC
/etrig_recal/et          ET RECALCULATED
```

```
/etrig_recal/etot        ETOT RECALCULATED
/tag_count/itagbit       MASTER TAG BITS
/tag_count/jtagbit(1)    SUB    TAG BITS
/tag_count/jtagbit(2)    SUB    TAG BITS
/tag_count/jtagbit(3)    SUB    TAG BITS
/tag_count/jtagbit(4)    SUB    TAG BITS
/tag_count/jtagbit(5)    SUB    TAG BITS
/tag_count/jtagbit(6)    SUB    TAG BITS
/tag_count/jtagbit(7)    SUB    TAG BITS
/tag_count/jtagbit(8)    SUB    TAG BITS
/tag_count/jtagbit(9)    SUB    TAG BITS
/tag_count/jtagbit(10)   SUB    TAG BITS
/tag_count/jtagbit(11)   SUB    TAG BITS
/tag_count/jtagbit(12)   SUB    TAG BITS
/tag_count/jtagbit(13)   SUB    TAG BITS
/tag_count/jtagbit(14)   SUB    TAG BITS
/tag_count/jtagbit(15)   SUB    TAG BITS
/tag_count/jtagbit(16)   SUB    TAG BITS
```

Appendix C

Strip Criteria

This appendix was written by Arun Tripathi on Aug 17, 1999[Tri 93]. The wording is Arun's, thus "I" does not refer to George Fox. The rest of this appendix is verbatim with some mild format adjustments.

```
****************
PURPOSE of this document is to list all the cuts used by the
REL 6 strip code for each tag for STREAM A and B. Stream A contains
tags 1 through 9 and STREAM B contains tags 10 through 16. The
information is listed in the following sequence:

Tag Number
The Code that is used to get this tag
Author of the code (if this information is available)
What the code does.
The cuts used.

****************

There is one logical called ITPOK that is used to make some
simple cuts that is used by several of the following routines. I will
describe what ITPOK does here in the begining so that I don't have to
do it over and over again.

ITPOK(I): ITPOK is a logical, and its argument I is the vertex number
  from the vertex list. It is set to TRUE if and only if all of
  the following conditions are satisfied. It is set in the
   routine call TAG_CUTS.F:

1. Number of tracks at the vertex .gt. 0.
2. Number of tracks at the vertex .le. MAXITF( = 35 in
          release 6).
3. Track category of each track at the vertex .ge. 3.
```

```
4. Charge of each track at the vertex .ne. 0.
5. Momentum of each track at the vertex .gt. 0.
6. Track chi-square ( XIS ) for each track .le. 6.5.

In what follows, if the reference to ITPOK is made, it will be
understood that all the above mentioned cuts ( most of which
        are trivial) are being made.

******************

Tag Number: 1
    Code: TAG_RASV2.F
    Author: Ai Nguyen
    Purpose: Tag 2-prong candidates from the vertex list. There is a
             mass window cut, so that it is not suitable for
             unconstrained decays.
    Cuts:
    1. Number of tracks at the secondary vertex = 2.
    2. ITPOK .eq. TRUE
    3. Charge of secondary = 0.
    4. Pt-balance of the secondary .le. 1.0 GeV.
    5. SDZ .gt. 5.
    6. Invariant mass of the vertex .gt. 1.7 GeV, where the
       invariant mass is calculated based on KPi, PiK, pipi,
       and KK hypotheses. If any of these hypotheses gives an
       invariant mass greater than 1.7 GeV, the event is saved,
       if conditions 1 through 5 are also satisfied.

Tag Number: 2
    Code: TAG_RASC3.F
    Author: Ai Nguyen
    Purpose: Tag 3-prong secondaries from the vertex list.
    Cuts:
    1. Number of tracks at the secondary vertex = 3.
    2. Absolute value of the charge of secondary vertex = 1.
    3. ITPOK .eq. TRUE.
    4. Pt-balance of the secondary .le. 1.0 GeV.
    5. SDZ .gt. 5.
    6. Proper decay time .lt. 5.0 ps. The proper decay time is
       calculated assuming that the parent of the vertex was
       a D+(-).

Tag Number: 3
    Code: TAG_RASV4.F
```

```
    Author: Ai Nguyen
    Purpose: Tag 4-prong secondaries from the vertex list.
    Cuts:
    1. ITPOK .eq. TRUE
    2. Number of the tracks at the secondary vertex = 4.
    3. Charge of the secondary vertex = 0.
    4. Pt-balance of the secondary .le. 1.0 GeV.
    5. SDZ .gt. 5.

Tag Number: 4
    Code: TAG_NPRONGS.F
    Author: Ai Nguyen
    Purpose: Tag 5- and higher prong secondaries from the
     vertex list.
    Cuts:
    1. Number of tracks at the secondary .gt. 4.
    2. ITPOK .eq. TRUE.
    3. SDZ .gt. 5.
    4. Abs(dztarg) .gt. 0.1 cm, for targets 1 to 5;
       Abs(dztarg) .gt. 0.5 cm, for target # 6, i. e. the
       interaction counter.

Tag Number: 5
    Code: TAG_LEP.F
    Author: Penny K.,Pauline G., Arun T.
    Purpose: Tag All-prong semileptonic secondaries from the vertex
             list.
    Cuts:
    1. There must be at least one Rel 6 Muon or at least one
       track with EMPROB .gt. 80 in the vertex.
    2. ITPOK .eq. TRUE
    3. SDZ .gt. 5.

   The above three cuts are common to all vertices. Now in
   addition:

       If the vertex is two-prong then:
       a. Ptbalance .lt. 1.5 GeV.
       b. Chi-square of impact parameter w.r.t. the primary for
         each track .gt. 6.0.

       On 3- or higer prong vertices, only cuts 1, 2 and 3 are
       applied.
```

Tag Number: 6

Code: TAG_M_2ND.F

Author: Jean Slaughter, Ai Nguyen

Purpose: Tag events with multiple secondaries from the vertex list. Would be useful for beauty-studies.

Cuts:

1. ITPOK .eq. TRUE
2. At least two secondary vertices must be present.
3. SDZ .gt. 5.
4. Number of tracks at the secondary vertex .le. IERPM2 (the total number of all SMD tracks).
5. Number of tracks at the secondary vertex .le. MAXITF (= 35 for Rel 6).
6. The distance of the Z-position of the secondary vertex must be at leas 3.5 sigma(in Z-position) away from the edge of the nearest target.
7. M-min .gt. 1.5, where M-min is calculated as described below:

   For each secondary vertex, the invariant mass is calculated assuming that all the tracks at the vertex are pions. Then the Minimum Parent Mass (M-min) is calculated for each vertex assuming that the missing neutral was a pion too.

8. NCANDS .gt. 1., where NCANDS is the number of secondary vertices satisfying conditions 1 through 7 described above.

Tag Number: 7

Code: TAG_PROTON.F

Author: ?

Purpose: Tag secondary vertices (from vertex list) with a proton or anti-proton in it. Useful for study of Baryons.

Cuts:

If there is any track in the secondary vertex(all-prong) for which CPRB2 for being a kaon is less than 0.12 and that for being a proton is greater than 0.9, then the event is saved. In other words,

```
IF (CPRB2(track,4).lt.0.12).and.(CPRB2(track,5).gt.0.9)
then save the event.
```

Based on the charge of the track, protons and anti-protons
are tagged seperately.

Tag Number: 8
Code: SELECT_PAIR.F
Author: Simon K.
Purpose: Selects a pair of tracks at least one of which has to be
an identified K or Proton. It does not use the
vertex list.

Cuts: (Based on input from Simon)
1. A track is defined as K if:
K prob > 0.13 if track momentum .lt. 40 GeV.
K prob > 0.1 if track momentum .gt. 40 GeV.
2. A track is defined as Proton if P prob > 0.1.
3. Once a track pair is found, such that at least one of
them is a K or P, a vertex is formed. There is a SDZ cut
on this vertex:
SDZ > 5 if the pair is Kpi
SDZ > 3 otherwise (eg. KK, KP etc)
4. There is a cut on the ratio of the product of the impact
parameter of the tracks w.r.t. the secondary and that
w.r.t. the primary vertex, i.e.
ratio = product(ip wrt secondary)/product(ip wrt primary)
ratio < 0.1 for Kpi pair
ratio < 0.12 otherwise
5. Vertex chisquare .lt. 7.

Tag Number: 9
Code: TAG_DI_LEP.F
Author: Ai Nguyen
Purpose: Tag di- and multi-lepton events with certain mass cuts.
It does not use the vertex list.
Cuts: (Based on input from Ai Nguyen)
1. A muon is anything tagged by the Rel 6 muon
reconstruction code. An electron is a track passing the
following momentum dependent EMPROB cut:
0 < p < 6 GeV EMPROB > 89
6 < p < 9 GeV EMPROB > 90
9 < p < 15 GeV EMPROB > 85
15 < p < 20 GeV EMPROB > 81
p > 20 GeV EMPROB > 85
2. If any two lepton candidate track pair mass (mumu, mue,
ee, regardless of net cahrge) exceeds 1.5 GeV, then set

tag bit 9 and keep the event. In case of Muons, there
must be at least 2 muons present in the event.

****

STREAM B

This stream contains Tags 10 through 16.

Tag Number: 10
    Code: TAG_PHI.F
    Author: Sharon
    Purpose: Looks for phi-resonance using Cerenkov and mass cuts.
             Does not use vertex list.
    Cuts:
    This routine looks for a KK pair by looping over all the
    tracks and forming an ivariant mass for all two-K
    combinations.

1. XIS(track) .lt. 5.0
2. Track momentum .le. 500 GeV
3. Jcatsg(track) .ge. 3 .and. Jcatsg(track) .le.15
4. At least two good tracks, as defined by the previous
   three cuts.
5. The total charge of the two tracks should be 0.
6. Cprob(K) .gt.0.12 for both the tracks and at least one
   track must have Cprob(K) .gt. 0.13. In addition, the
   product of K-Cerencove probabilities (cprb2), for the
   the two tracks .ge. 0.05.
7. The minimum distance between the two tracks .lt.0.005 Cm
8. Invariant mass for KK combination should lie within 0.01
   GeV of the Phi mass (1.0194 GeV).

Tag Number: 11
    Code: SELECT_B.F
    Author: Mike Halling
    Purpose: Tags B-candidate events using vertex list. Assumption is
             that the B decayed to a charm meson plus all charged
             tracks and that both the B decay vertex and the charm
             decay vertex are in the vertex list.
    Cuts: (Based on input from Mike Halling)

1. The B vertex is the one with middle Z-position.
2. SDZ (B to D vertex seperation in sigma) > 5

```
    3. 2 < mass(B) < 10 GeV/C .
    4. dip < 100 micro-meters  ( for the B vertex).
    5. D vertex minimum mass < 2.5 GeV.

Tag Number: 12
    Code: TAG_SLAMBDA.F
    Author: Committee for Stripping Lambdas
    Purpose: Tags events with Lambdas.
    Cuts: ( Based on input from Cat James)
    Routine find_sestr_lm, called in tag_process, does a
    list-driven search for Lambdas, and loads them into the
    parent_tracks common. Routine tag_slambda searches
    parent_tracks for SESTR Lambdas and applies additional
    cuts. The list below just itemizes the cuts  from both
    routines.

    Release 6 cuts:
        Select 2-prongs from the vertex list.
        Each track in the pair must satisfy ---
            0.5<track momentum<500 GeV
            Track is category 3,7,15
            track chisq<5
        Then the pair of tracks must satisfy ---
            opposite charge
            SDZ>7 (track pair is NOT removed from primary)
            PTB>0.2 GeV
            ABS(Vee vertex - closest target) < 0.1cm
            1.108<mass of parent<1.125
        Stiff daughter track is "not pion" ---
            For momentum<=10GeV, CPRB2(pion)<0.83
            For momentum>10GeV,  CPRB2(pion)<0.40
            Momentum of lambda parent > 5 GeV
        Stiff daughter is boosted back into the parent CM, and the
            cosine of the angle between CM daughter vector and boost
            direction is found (function DECYNG)
            ABS(cosine)<0.98


Tag Number: 13
    Code: TAG_LAMBDA.F
    Author: Committee for Stripping Lambdas
    Purpose: Tags events with ESTR Lambdas ( at least one).
    Cuts: Based on input from Cat James
    Routine find_estr_vs, called in tag_process, does a
```

```
    candidate-driven search for Lambdas, and loads them into
    the parent_tracks common. Routine tag_lambda searches
    parent_tracks for ESTR Lambdas and applies additional cuts.
    The list below just itemizes the cuts from both routines.

    Release 6
        Loop over IERPM2+1 to NTRKS....each track must satisfy --
             0.5<track momentum<500 GeV
             Track is category 3,7,15
             track chisq<5
        There must be at least two such tracks
        Then the pair of tracks must satisfy ---
             opposite charge
             DCA of the secondary (TWOLF) < 0.7cm
             10cm < Z secondary < 200cm
             1.108<mass of parent<1.125
         Stiff daughter track is "not pion" ---
             For momentum<=10GeV, CPRB2(pion)<0.83
             For momentum>10GeV,  CPRB2(pion)<0.40
             Momentum of lambda parent > 5 GeV
         Stiff daughter is boosted back into the parent CM, and the
             cosine of the angle between CM daughter vector and boost
             direction is found (function DECYNG)
             ABS(cosine)<0.98


Tag Number: 14
    Code: TAG_KSLM_2ND.F
    Author: Attanagoda Santha
    Purpose: Tags events with a K-short or a Lambda, and another
          sestr secondary vertex. The secondary vertex is
             required to have more than two tracks.
     Uses vertex list.
    Cuts:

Tag Number: 15
    Code: TAG_AKSS_D0.F
    Author: Attanagoda Santha
    Purpose: Tags events with D0 decays into modes with a K-short.
    Cuts:

Tag Number: 16
    Code: TAG_MULTI_KS.F
    Author: Attanagoda Santha
```

Purpose: Tags events with multiple K-shorts.
Cuts:

Appendix D

Kansas State University Substrip Criteria

```
This file describes the tagging cuts used by the FCNC MICRO STRIP.
The name of the file is MICRO_STRIP_CUTS.TXT and can be found in
"~witchey/misc/" area.

Nick Witchey MAY-27-1994

======================================================================

D0 -> 2 prong
2 Tracks
|P| < 500 Gev
Zprim < -0.35cm
        Q = 0
        Pt Balance < 0.4 Gev
SDZ > 8.0
Life Time < 5.0 ps
ITPOK = .TRUE.
Tracks are ordered according to K ckv prob.
Mass and COS(theta) cut are used together since COS(theta) is
mass dependent:
(Mass > 1.7 Gev).and.(Cos(theta) < 0.995)
K pi pi K pi pi K K
mu e e mu mu mu   e e
D+ -> 3 prong
3 Tracks
|P| < 500 Gev
Zprim < -0.35 cm
|Q| = 1
```

```
Pt Balance < 0.35 Gev
SDZ > 8
Life Time < 5.0 ps
Distance of Closet Approach < 0.01 cm
ITPOK = .TRUE.
First track is the off signed charged track the remaining two are
ordered according to K ckv prob.
Mass > 1.7 Gev:
K pi pi K K pi K pi K
pi pi pi mu pi mu mu mu pi
e pi e e e pi e mu pi
e pi mu mu e pi  mu pi e
Ds -> 3 prong
3 Tracks
|P| < 500 Gev
Zprim < -0.35 cm
|Q| = 1
Pt Balance < 0.35 Gev
SDZ > 8
Life Time < 3.0 ps
Distance of Closet Approach < 0.01 cm
ITPOK = .TRUE.
First track is the off signed charged track the remaining two are
ordered according to K ckv prob.
Mass > 1.7 Gev:
K K K K K pi K pi K
pi pi pi mu K mu  mu mu K
e K e e e K e mu K
e K mu mu e K   mu K e
D0 -> 4 prong
4 Tracks
|P| < 500 Gev
Zprim < -0.35 cm
|Q| = 0
Pt Balance < 0.45 Gev
SDZ > 7
Life Time < 4.0 ps
Distance of Closet Approach < 0.012 cm
ITPOK = .TRUE.
        Tracks are ordered by K ckv prob for the 1st three hypothosis
then ordered by alternating charge but as close to K prob as
possible.  The ordering will be +-+- or -+-+, were the first
particle ALWAYS has the greatest K prob.  The second has the
highest K prob of OPPOSITE sign of the first and so on.
```

```
Mass > 1.7 Gev:
K pi pi pi pi K pi pi pi pi pi pi
                K pi pi K       pi K K pi       pi pi mu mu
                mu mu pi pi     mu pi pi mu     pi mu mu pi
                pi pi e e       e e pi pi       pi e e pi
                e pi pi e       pi pi e mu      pi pi mu e
                e mu pi pi      mu e pi pi      e pi pi mu
                mu pi pi e      pi e mu pi      pi mu e pi
/\c -> 3 prong
3 Tracks
|P| < 500 Gev
Zprim < -0.35 cm
|Q| = 1
Pt Balance < 0.4 Gev
SDZ > 6
Life Time < 2.0 ps
Proton CKV prob > 0.05
ITPOK = .TRUE.
First track is the off signed charged track the remaining two are
ordered according by Proton ckv prob.
Mass > 1.9 Gev:
K P pi K pi P mu P mu
                mu mu P         e P e           e e P
                e P mu          mu P e          e mu P
                mu e P
J/Psi -> e+ e- ; mu+ mu-
Loop through pairs of opposite signed tracks with EMPROB > 70
Mass Trk1 Trk2 > 2.5
Loop through Rel 6 muon candidates.
Mass Mu1 Mu2 > 2.5
```

Appendix E

The Missing D^+ and D_s

With a hard cut made to remove the resonances:

1. $D^+ \rightarrow K^+K^-\pi^+$,
2. $D^+ \rightarrow K^-\pi^+\pi^+$, and
3. $D_s^+ \rightarrow K^+K^-\pi^+$,

one may wonder as to the effect of these missing pieces.

Referring to figures E.1 and E.2, one can see the removed parts.

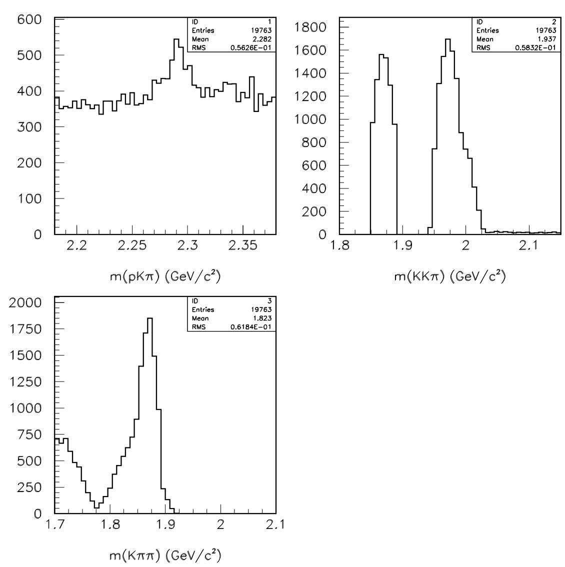

Figure E.1: Reconstructed masses of real data which were removed from the data set by the D cut.

We sent this data set through the trained Neural Net and applying the cut of 0.94. See figure E.3 for the mass plot.

The Monte Carlo results can be seen in figure E.4

We then looked at the acceptance from the MC data set and the background from the wings of the real data set. Figure E.5 shows the one dimensional projections of the data set with the D's,

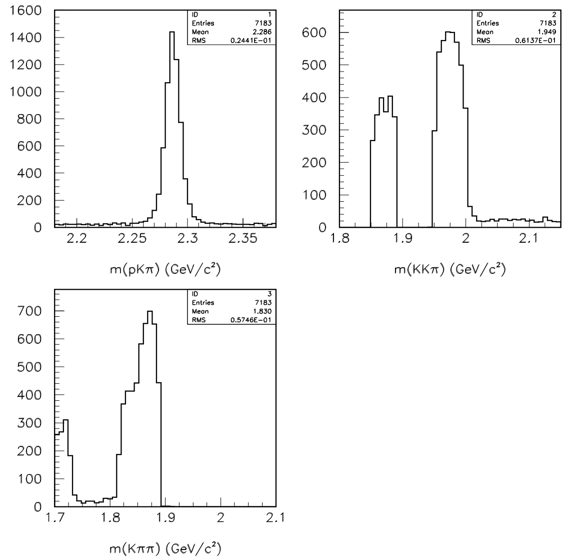

Figure E.2: Reconstructed masses of Monte Carlo data which were removed from the data set by the D cut.

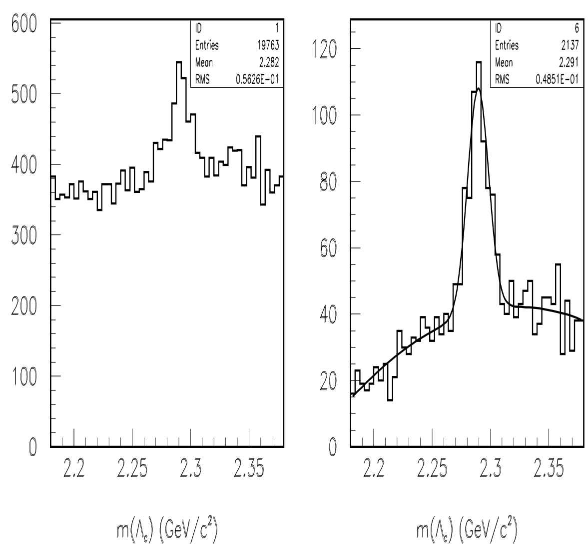

Figure E.3: Real data cut by the D cut: (left) Mass(pKπ) of the real data set before Neural Net cuts and (right) after. It has a significance of 10.7σ. There are 383±36 signal events and 1753 background events assuming that the peak is Gaussian, the background is quadratic and the number of signal and background events are variables.

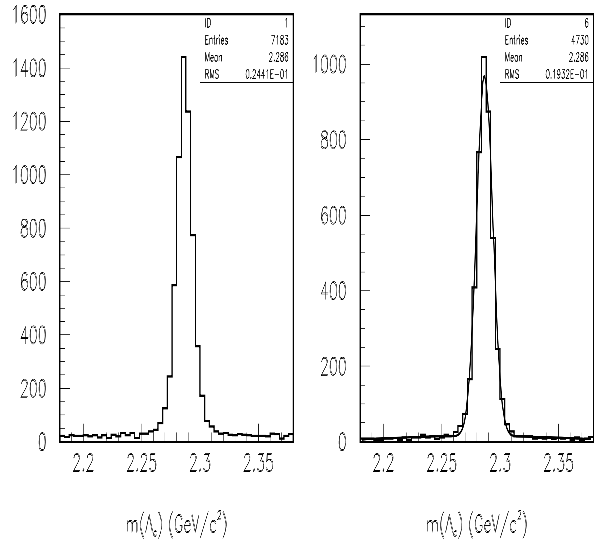

Figure E.4: MC data cut by the D cut: (left) Mass(pKπ) of the MC data set before Neural Net cuts and (right) after. It has a significance of 61.7σ. There are 4123$\pm$67 signal events and 607 background events assuming that the peak is Gaussian, the background is quadratic and the number of signal and background events are variables..

figure E.6 shows the one dimensional projections of the data set with the D's cut out (these can also be seen in chapter 8), and figure E.7 shows the one dimensional projections of the combined sets.

Note that the gaps which appear in the peak of ϕ proton acceptance in figure E.6 are matched by a peak in the corresponding plot in figure E.5, as is also shown by the lack of gaps in figure E.7.

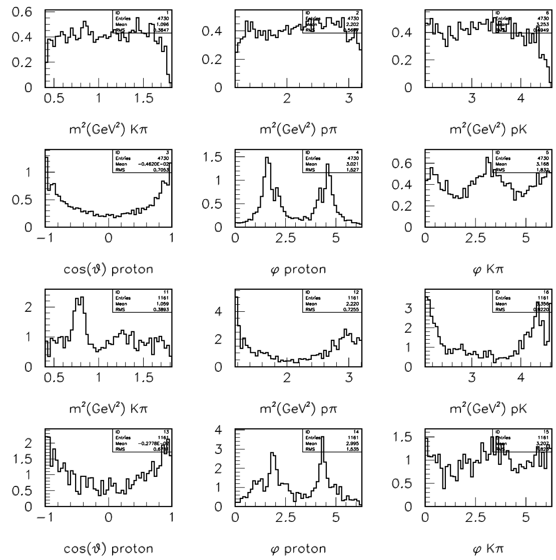

Figure E.5: Acceptance and Background of the D^+ and D_s resonances which had been cut by the D cut. The top 6 plots are the one dimensional projections of the Acceptance normalized to the number of reconstructed MC seen in the above figure, and the bottom 6 plots show the one dimensional projections of the Background normalized to the number of background events seen in one of the above figures. All projections were divided by uniform phase space.

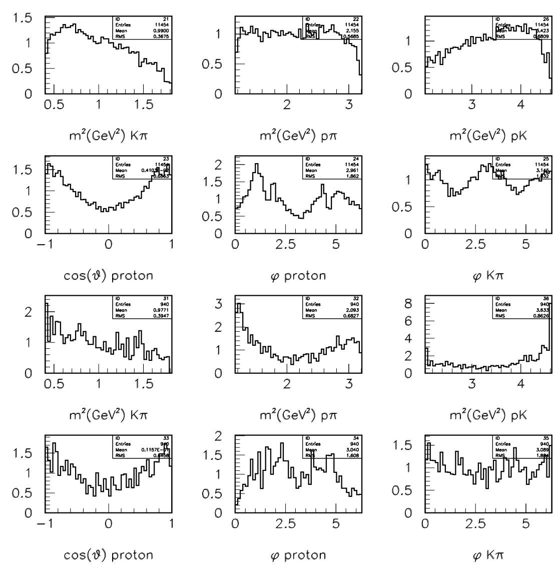

Figure E.6: Acceptance and Background of the optimized data set with the D^+ and D_s resonances removed. The top 6 plots are the one dimensional projections of the Acceptance and the bottom 6 plots show the one dimensional projections of the Background. All projections were divided by uniform phase space. Note that these plots are the same as seen in the Acceptance and Background chapter.

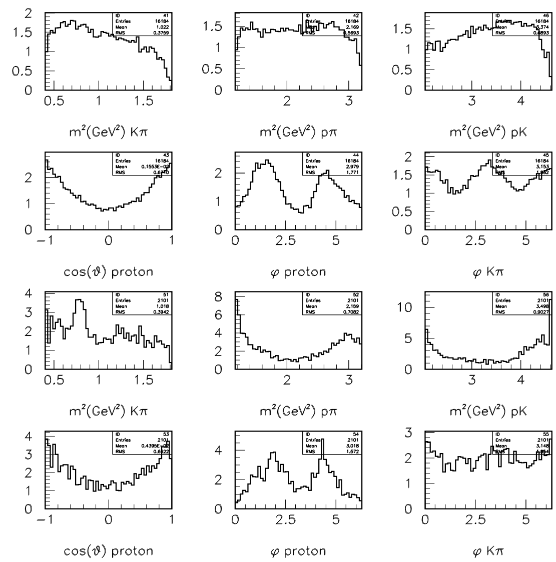

Figure E.7: Acceptance and Background of the combined optimized data set with D^+ and D_s resonances removed and the set of the D^+ and D_s resonances. These plots are the sums of the previous 2 figures. The top 6 plots are the one dimensional projections of the Acceptance and the bottom 6 plots show the one dimensional projections of the Background. All projections were divided by uniform phase space.

Appendix F

The Constrained Fit

For the final analyses, we used a constrained fit for the momenta of the p, K, and π. By constrained fit, we mean that the momenta were adjusted so the reconstructed mass of the Λ_c is the PDG value. This eliminated the problem of the drifting of phase space as a function of the Λ_c mass, and it brought the various calculated values closer to reality. In other words, it compensated for some of the smearing caused by the resolution of the detector.

From the momenta, we calculated $m^2_{K\pi}$ and $m^2_{p\pi}$. Using these values as a coordinate, we compared the truth table values of the surviving reconstructed Monte Carlo to their corresponding reconstructed unconstrained and constrained values. For comparison we evaluated the distance from the truth table value to the reconstructed values. See figure F.1 for the comparison.

Further evidence can be seen in the reconstructed widths of the various resonances. See figures 9.8 (p. 81) and 9.9 (p. 82). In both cases the constrained width was closer to the PDG width than the unconstrained width.

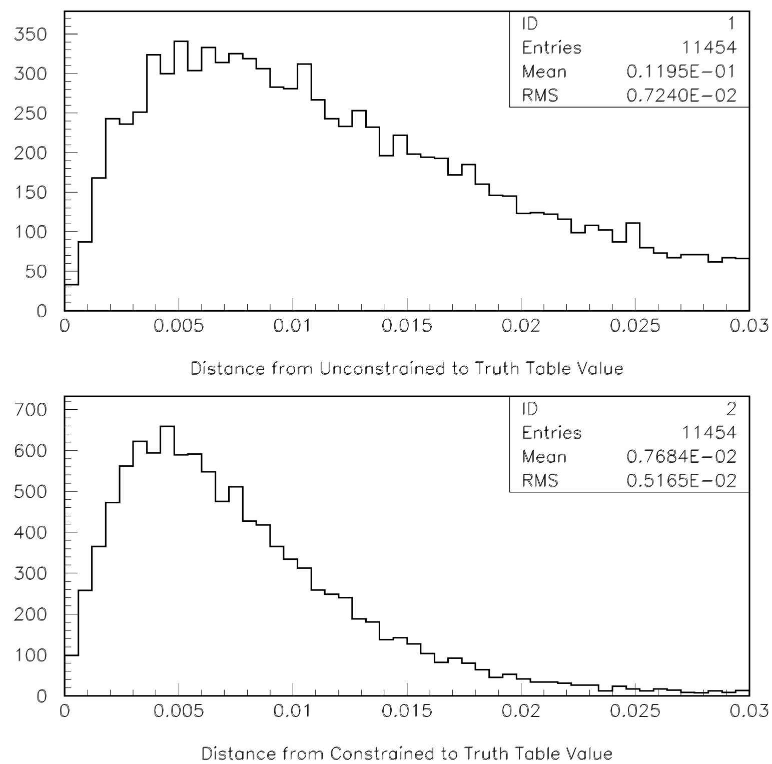

Figure F.1: The absolute distance from the Truth Table Dalitz plot coordinate to reconstructed coordinate for the surviving reconstructed MC.

Appendix G

The Test of the Fitting

G.1 Introduction

This chapter discusses our exploration of how well the fitting mechanism was constructed. It is not testing the validity of the physics, only the validity of the results from the MINUIT fit. To test this we need to generate Monte Carlo events which would simulate a decay with a certain resonant substructure going through a detector with a certain acceptance.

G.2 Generation

We first generated 9,042,568 fast Monte Carlo events, calculated a realistic signal density for each event, and used the elimination method to reduce that number to 2,000,000 events. The signal density is realistic in that we used fit parameters which came from a previous fit to real data. For the signal density, we assumed a nonresonant decay in addition to $\overline{\mathrm{K}}^{*0}$ and Δ^{++} resonant decays. The parameter values we used are found in table G.1.

From here we calculated the acceptance of each event assuming the 5 dimensions (as described in chapter 8) are uncorrelated and again used the elimination method to reduce the number of events to 83,481 events which should simulate $\Lambda_c \to \mathrm{pK}\pi$ going through a detector with some acceptance.

G.3 Full fit

If the fitting mechanism were correct, then using these 83,481 points as real data points, we should be able obtain the original parameter values. Sending these events through the MINUIT fitter that was used to determine the parameters, we got the results seen in table G.2. Note that we fit the data twice, starting from different points and arrived at the same final values.

See figure G.1 for a comparison of the projections of final sample and the fit obtained.

G.4 Further Testing

We then split this full set into 200 sets of 417 mutually exclusive events, 100 sets of 834 mutually exclusive events, and 50 sets of 1669 mutually exclusive events. We MINUIT fit each set and found

Mode	Variable	fit
$\overline{\mathrm{K}}^{*0}$	E_1	0.20
	ϕE_1	1.00
	E_2	0.54
	ϕE_2	2.46
	E_3	0.65
	ϕE_3	3.00
	E_4	1.00
	ϕE_4	0.00
Δ^{++}	F_1	0.75
	ϕF_1	2.83
	F_2	1.02
	ϕF_2	3.49
Nonresonant	+ +	0.39
	ϕ_{++}	3.10
	+ -	0.36
	ϕ_{+-}	1.73
	- +	1.47
	ϕ_{-+}	2.27
	- -	0.41
	ϕ_{--}	2.30
Polarization	α	-0.23

Table G.1: The parameter values used to generate a test sample for $\Lambda_c \to pK\pi$. Using the signal density which came from these, we reduced the number of events from over 9 million events to 2 million events.

Mode	Variable	fit
$\overline{\mathrm{K}}^{*0}$	E_1	0.189 $\pm$ 0.013
	ϕE_1	0.931 $\pm$ 0.080
	E_2	0.529 $\pm$ 0.019
	ϕE_2	2.488 $\pm$ 0.068
	E_3	0.684 $\pm$ 0.019
	ϕE_3	2.764 $\pm$ 0.067
	E_4	1.0
	ϕE_4	0.0
Δ^{++}	F_1	0.826 $\pm$ 0.019
	ϕF_1	2.756 $\pm$ 0.048
	F_2	0.969 $\pm$ 0.017
	ϕF_2	3.412 $\pm$ 0.057
Nonresonant	+ +	0.409 $\pm$ 0.040
	ϕ_{++}	2.860 $\pm$ 0.119
	+ -	0.378 $\pm$ 0.027
	ϕ_{+-}	1.769 $\pm$ 0.083
	- +	1.493 $\pm$ 0.022
	ϕ_{-+}	2.160 $\pm$ 0.051
	- -	0.362 $\pm$ 0.017
	ϕ_{--}	2.158 $\pm$ 0.059
Polarization	α	-0.242 $\pm$ 0.018

Table G.2: The result of the MINUIT fit on the 83,481 events.

Figure G.1: Projections of the (a) Fast MC data before acceptance, (b) Fast MC data after acceptance, (c) Signal fit to the "Fast MC data", (d) Acceptance, and (e) Signal fit to the "Fast MC data" times the acceptance. Ideally, columns (b) and (e) should be the same, as well as columns (a) and (c).

the average parameter value and average error. We then compared these averages to the values determined by fit the full 83,481 event sample. See table G.3 for a comparison of the parameter values, and see table G.4 for a comparison of the errors produced. For the histograms of the fit parameters and their errors see figures G.2-G.7.

Mode	Variable	Average from sets 200	100	50	Full fit
$\overline{\mathrm{K}}^{*0}$	E_1	0.41	0.28	0.22	0.19
	ϕE_1	2.70	1.81	1.43	0.93
	E_2	0.70	0.62	0.57	0.53
	ϕE_2	2.75	2.54	2.53	2.49
	E_3	0.65	0.64	0.66	0.68
	ϕE_3	2.73	2.59	2.73	2.76
	E_4	1.00	1.00	1.00	1.00
	ϕE_4	0.00	0.00	0.00	0.00
Δ^{++}	F_1	1.01	0.93	0.87	0.83
	ϕF_1	2.76	2.71	2.77	2.76
	F_2	1.00	0.96	0.96	0.97
	ϕF_2	3.39	3.40	3.43	3.41
Nonresonant	+ +	0.86	0.68	0.53	0.41
	ϕ_{++}	2.92	3.02	3.33	2.86
	+ -	1.00	0.66	0.49	0.38
	ϕ_{+-}	2.33	2.02	1.88	1.77
	- +	1.39	1.40	1.44	1.49
	ϕ_{-+}	2.27	2.11	2.16	2.16
	- -	0.52	0.43	0.41	0.36
	ϕ_{--}	2.45	2.14	2.19	2.16
Polarization	α	-0.39	-0.36	-0.29	-0.24

Table G.3: The average parameter values as found in the MINUIT fit. Note that the average from the 200 sets is actually an average of 193 sets, because 7 sets would not converge properly.

Mode	Variable	Average from sets					
		200		100		50	
		mean	RMS	mean	RMS	mean	RMS
$\overline{\mathrm{K}}^{*0}$	E_1	0.55	0.42	0.17	0.16	0.12	0.10
	ϕE_1	1.34	2.02	0.93	1.74	0.71	1.45
	E_2	0.40	0.37	0.21	0.17	0.14	0.14
	ϕE_2	0.97	1.21	0.71	0.72	0.51	0.35
	E_3	0.47	0.31	0.26	0.25	0.15	0.16
	ϕE_3	1.11	1.29	0.78	0.83	0.52	0.54
	E_4	0.00	0.00	0.00	0.00	0.00	0.00
	ϕE_4	0.00	0.00	0.00	0.00	0.00	0.00
Δ^{++}	F_1	0.37	0.33	0.21	0.21	0.14	0.14
	ϕF_1	0.74	0.98	0.51	0.61	0.37	0.35
	F_2	0.40	0.58	0.20	0.19	0.13	0.13
	ϕF_2	0.80	1.10	0.60	0.77	0.44	0.42
Nonresonant	+ +	1.44	0.72	0.94	0.47	0.42	0.27
	ϕ_{++}	1.74	1.53	1.44	1.27	1.16	1.12
	+ -	1.25	0.93	0.77	0.50	0.25	0.20
	ϕ_{+-}	1.19	1.54	1.13	1.10	0.63	0.59
	- +	0.47	0.54	0.26	0.27	0.17	0.16
	ϕ_{-+}	0.73	1.02	0.55	0.62	0.40	0.32
	- -	0.45	0.39	0.20	0.17	0.13	0.12
	ϕ_{--}	0.89	1.20	0.62	0.72	0.42	0.44
Polarization	α	0.27	0.34	0.21	0.24	0.14	0.15

Table G.4: The average errors found from the MINUIT fit and the RMS value from the spread of the parameter values. Ideally, the average error should equal the RMS value.

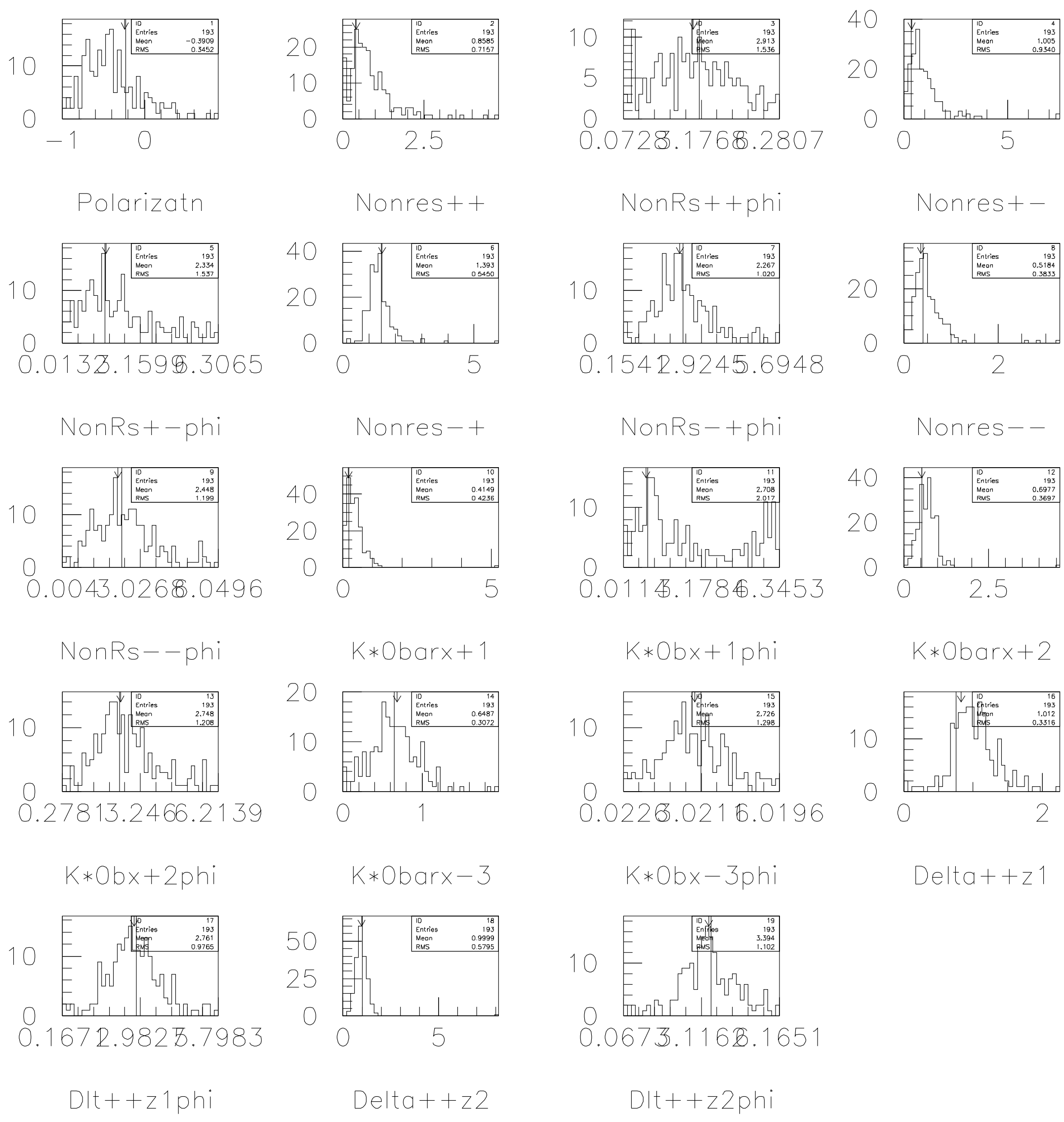

Figure G.2: The results from the MINUIT fit of the 200 sets. The solid line represents the initial value used to generate the data sample, and the arrow represents the values from the fit of the 83,481 events.

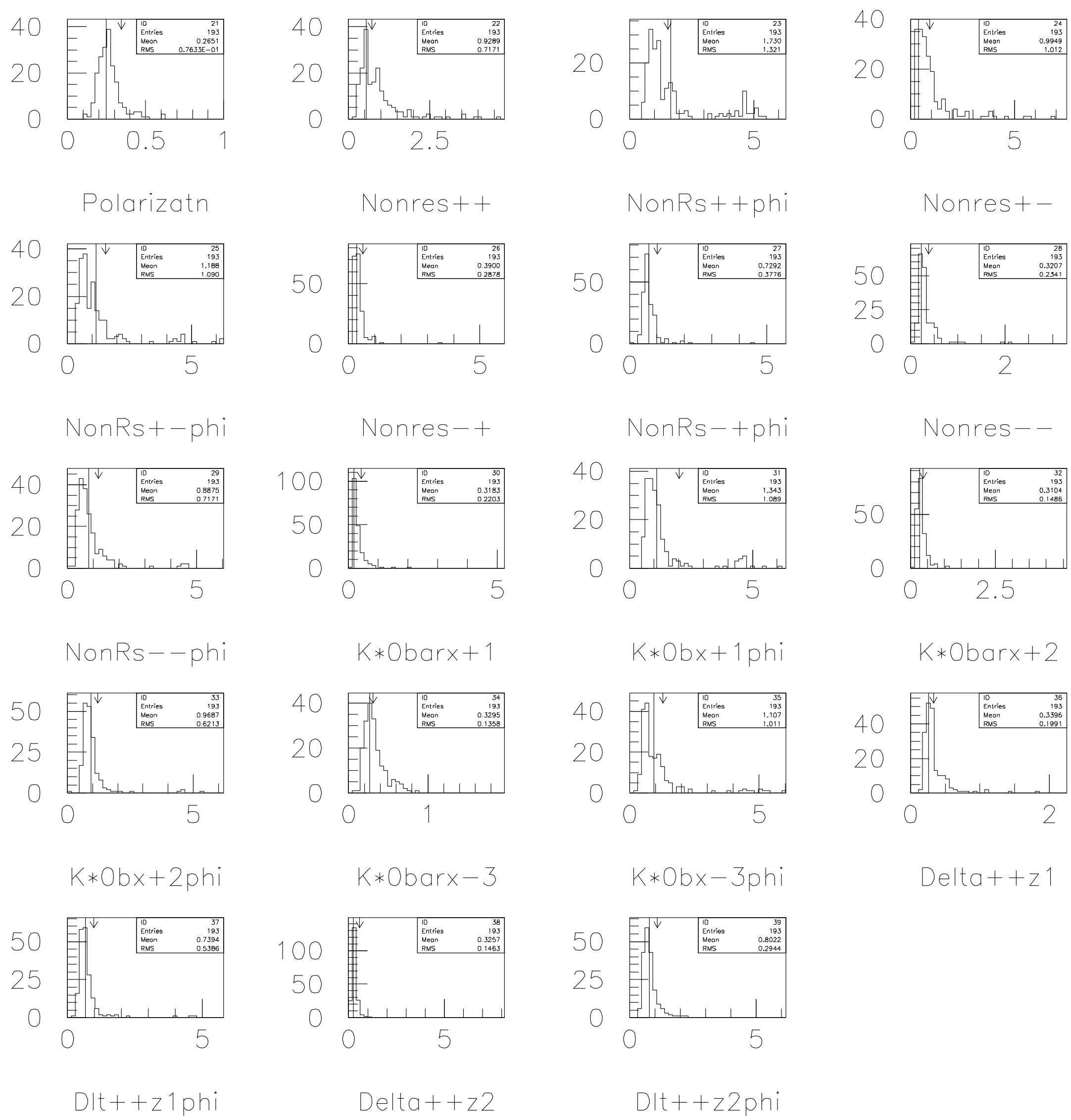

Figure G.3: The errors from the MINUIT fit of the 200 sets. The solid line represents the error from the full fit times the square root of the number of sets(193), and the arrow represents the RMS value from the spread of values on the previous page.

Figure G.4: The results from the MINUIT fit of the 100 sets. The solid line represents the initial value used to generate the data sample, and the arrow represents the values from the fit of the 83,481 events.

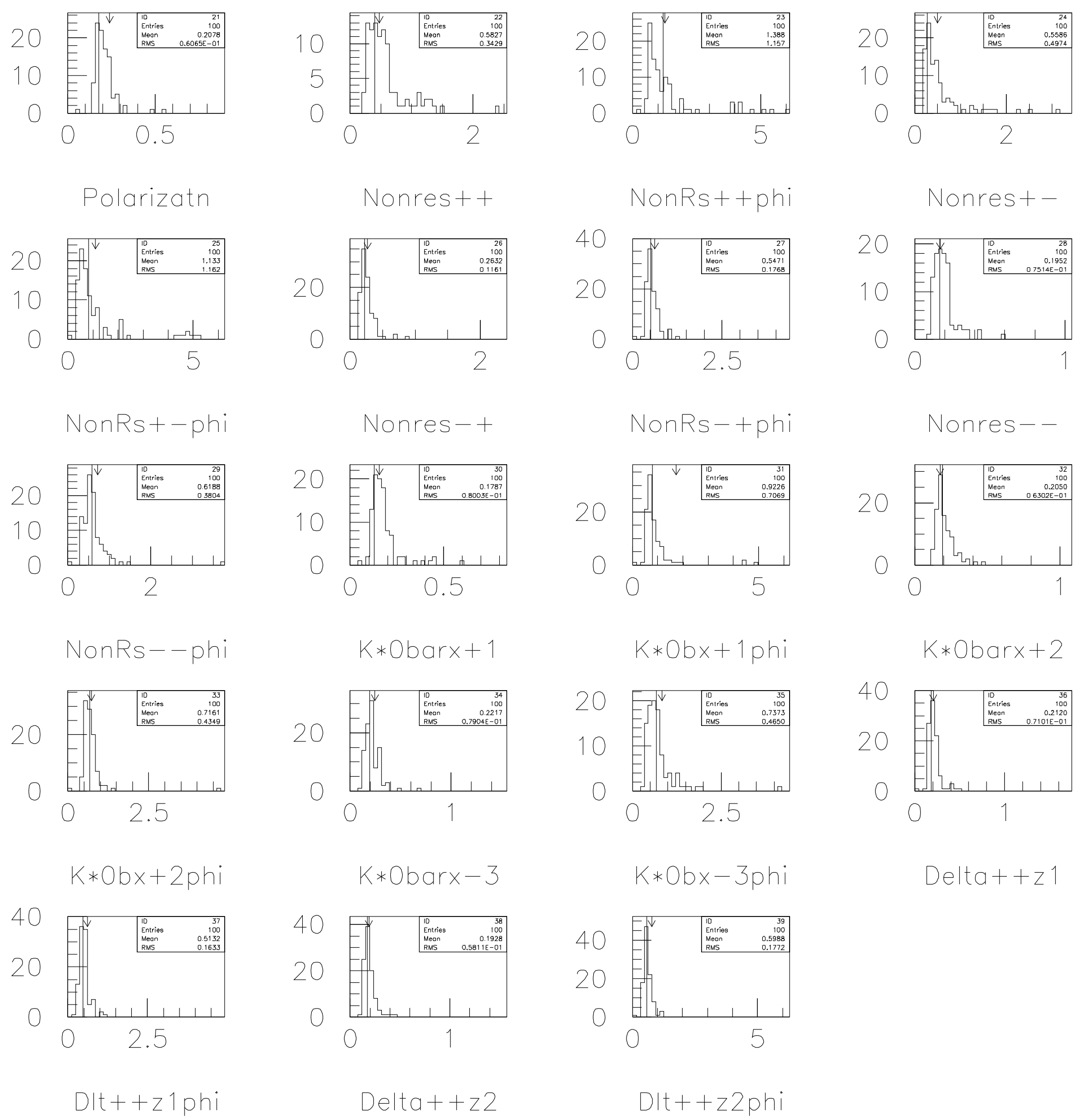

Figure G.5: The errors from the MINUIT fit of the 100 sets. The solid line represents the error from the full fit times the square root of the number of sets(100), and the arrow represents the RMS value from the spread of values on the previous page.

Figure G.6: The results from the MINUIT fit of the 50 sets. The solid line represents the initial value used to generate the data sample, and the arrow represents the values from the fit of the 83,481 events.

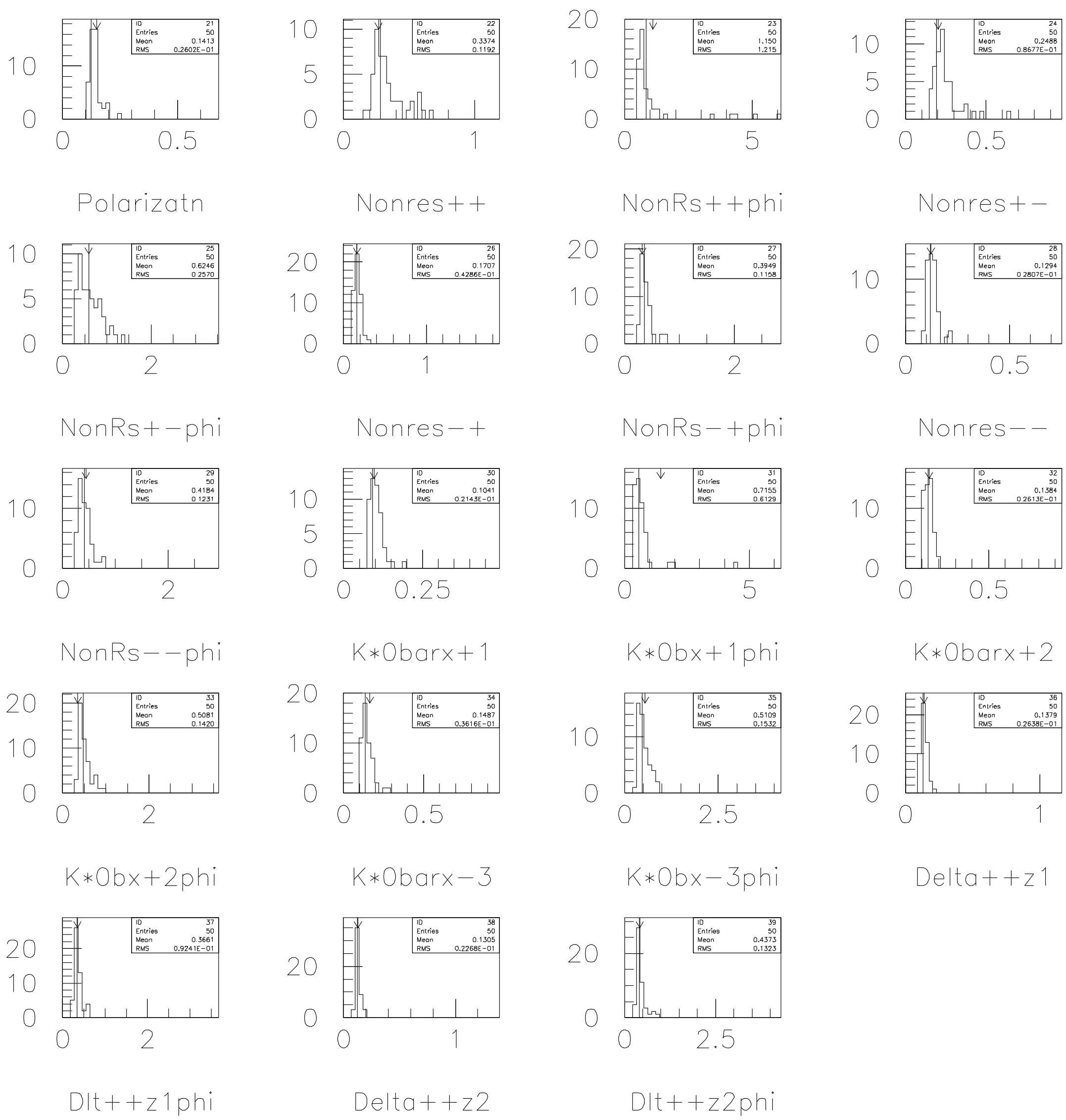

Figure G.7: The errors from the MINUIT fit of the 50 sets. The solid line represents the error from the full fit times the square root of the number of sets(50), and the arrow represents the RMS value from the spread of values on the previous page.

Appendix H

Two Dimensional χ^2 Comparisons

H.1 Acceptance

This chapter compares the two dimensional acceptance plot found on page 65.

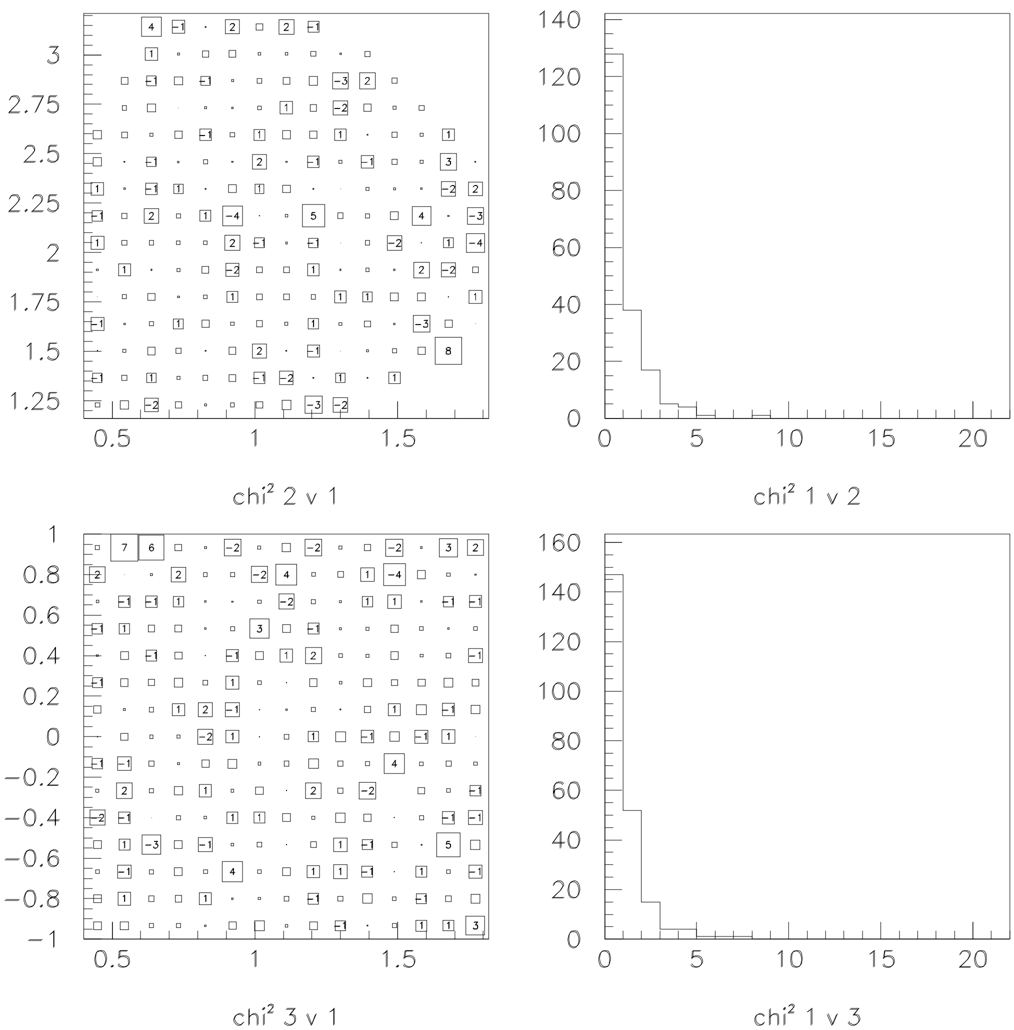

Figure H.1: One Dimensionally Tweaked Acceptance vs. Model as seen by χ^2 representation. The minus sign means that there were more points in the model than the actual distribution.

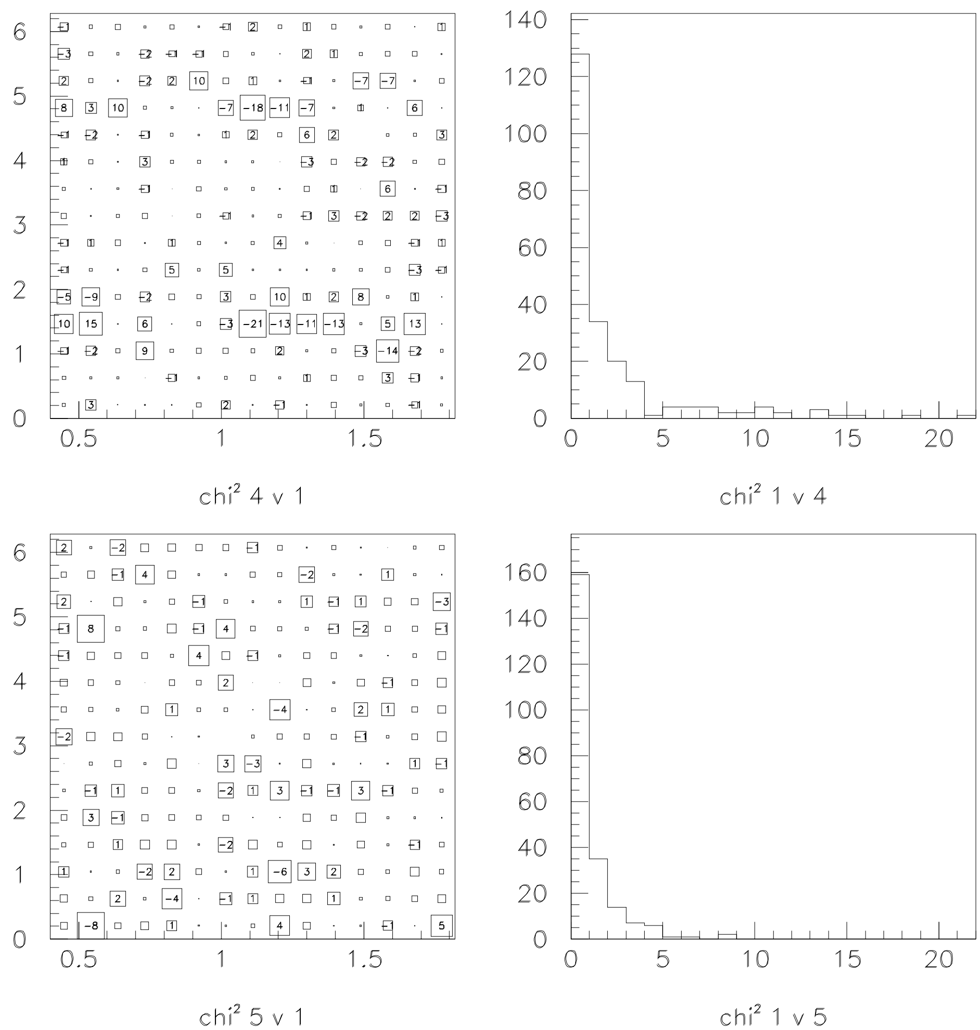

Figure H.2: One Dimensionally Tweaked Acceptance vs. Model as seen by χ^2 representation. The minus sign means that there were more points in the model than the actual distribution.

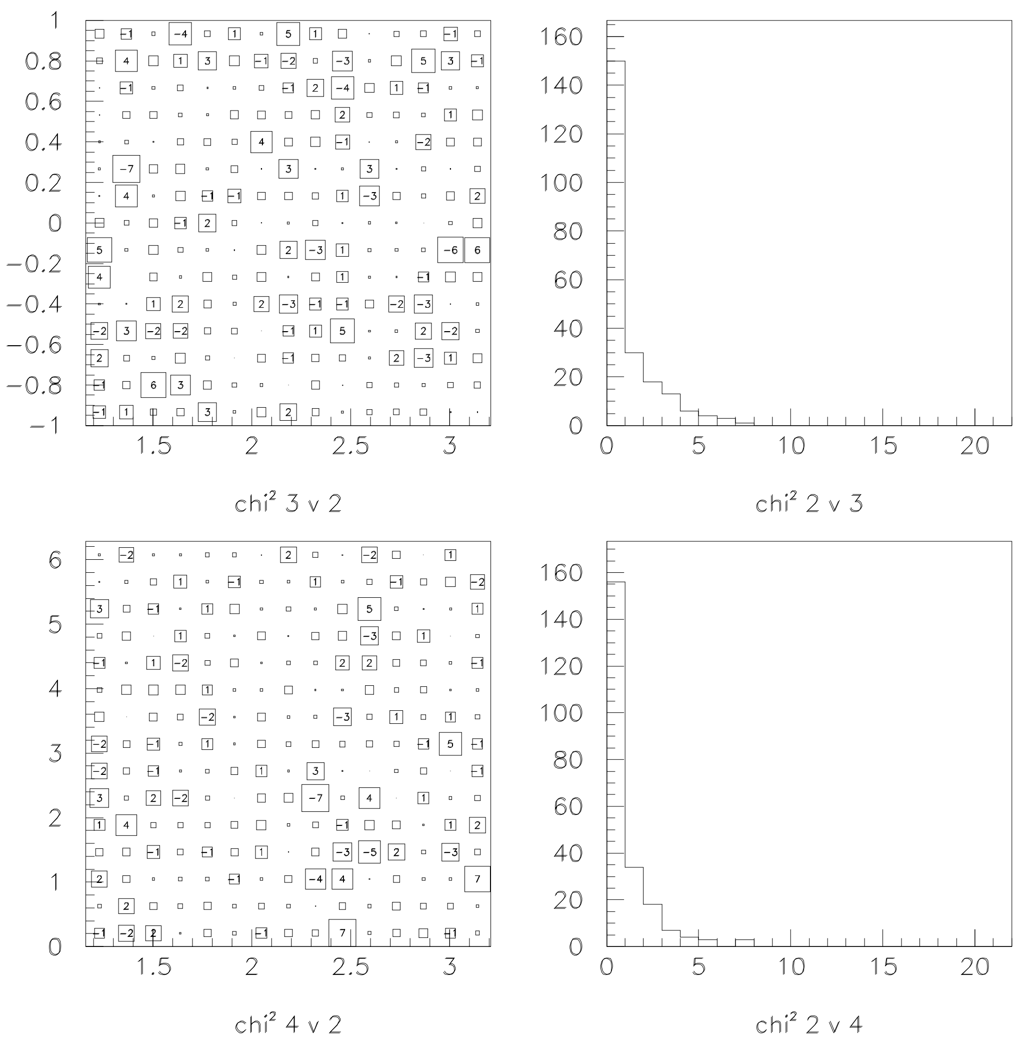

Figure H.3: One Dimensionally Tweaked Acceptance vs. Model as seen by χ^2 representation. The minus sign means that there were more points in the model than the actual distribution.

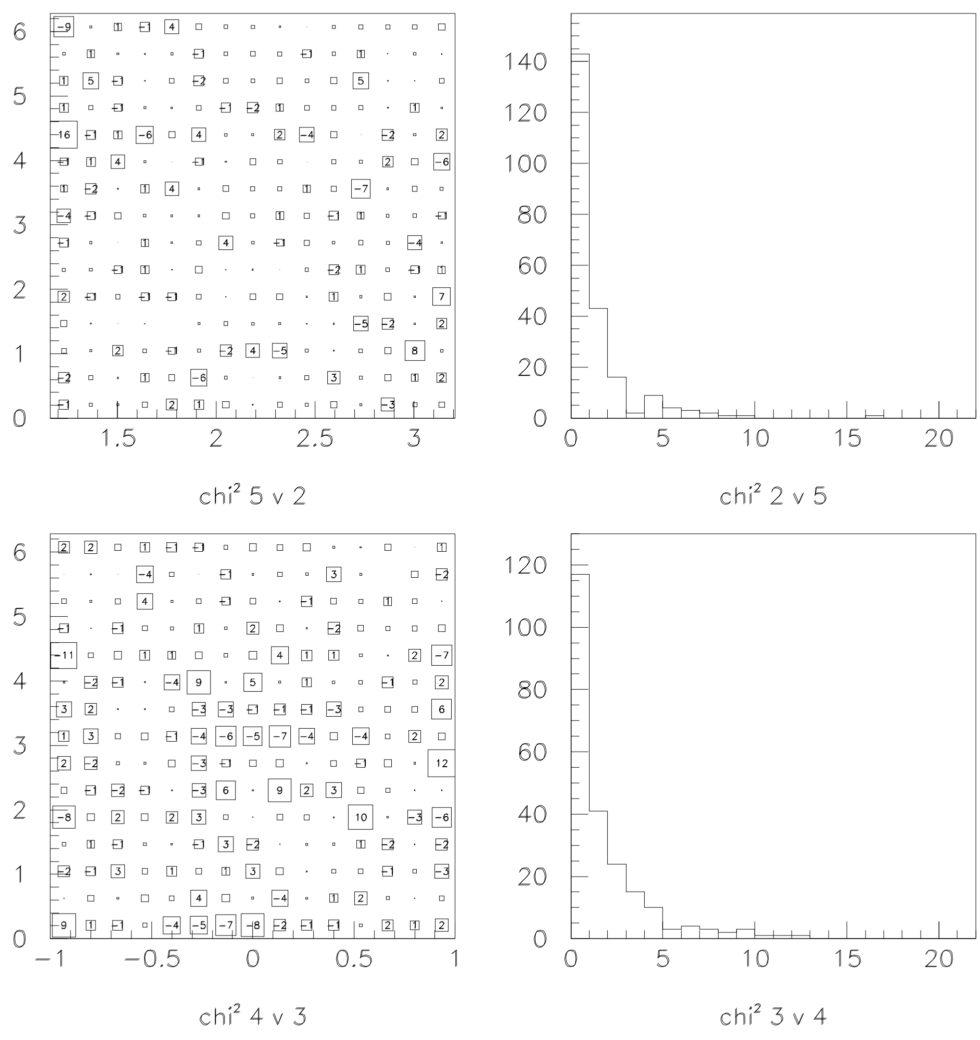

Figure H.4: One Dimensionally Tweaked Acceptance vs. Model as seen by χ^2 representation. The minus sign means that there were more points in the model than the actual distribution.

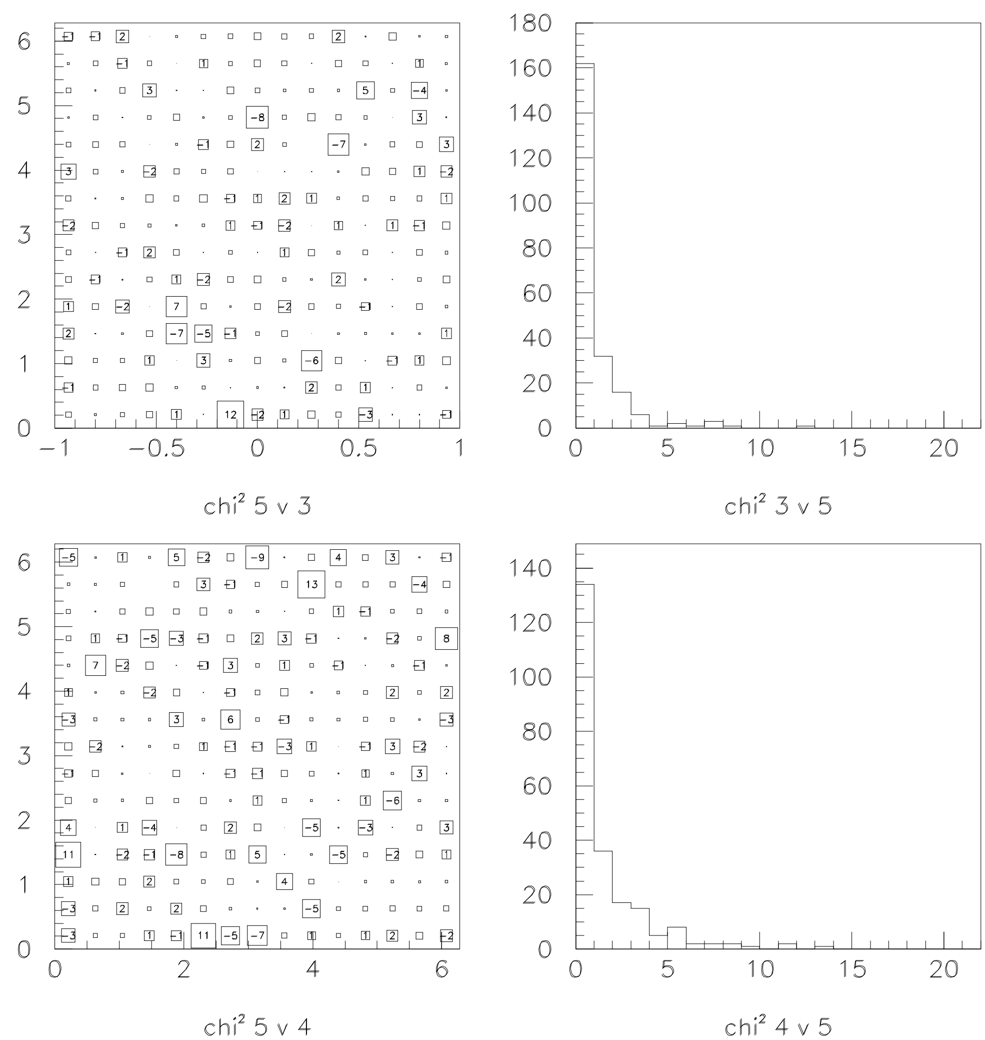

Figure H.5: One Dimensionally Tweaked Acceptance vs. Model as seen by χ^2 representation. The minus sign means that there were more points in the model than the actual distribution.

H.2 Fit 3: Full Mass Range

This section compares the final fit (as seen on page 72) over the full mass range.

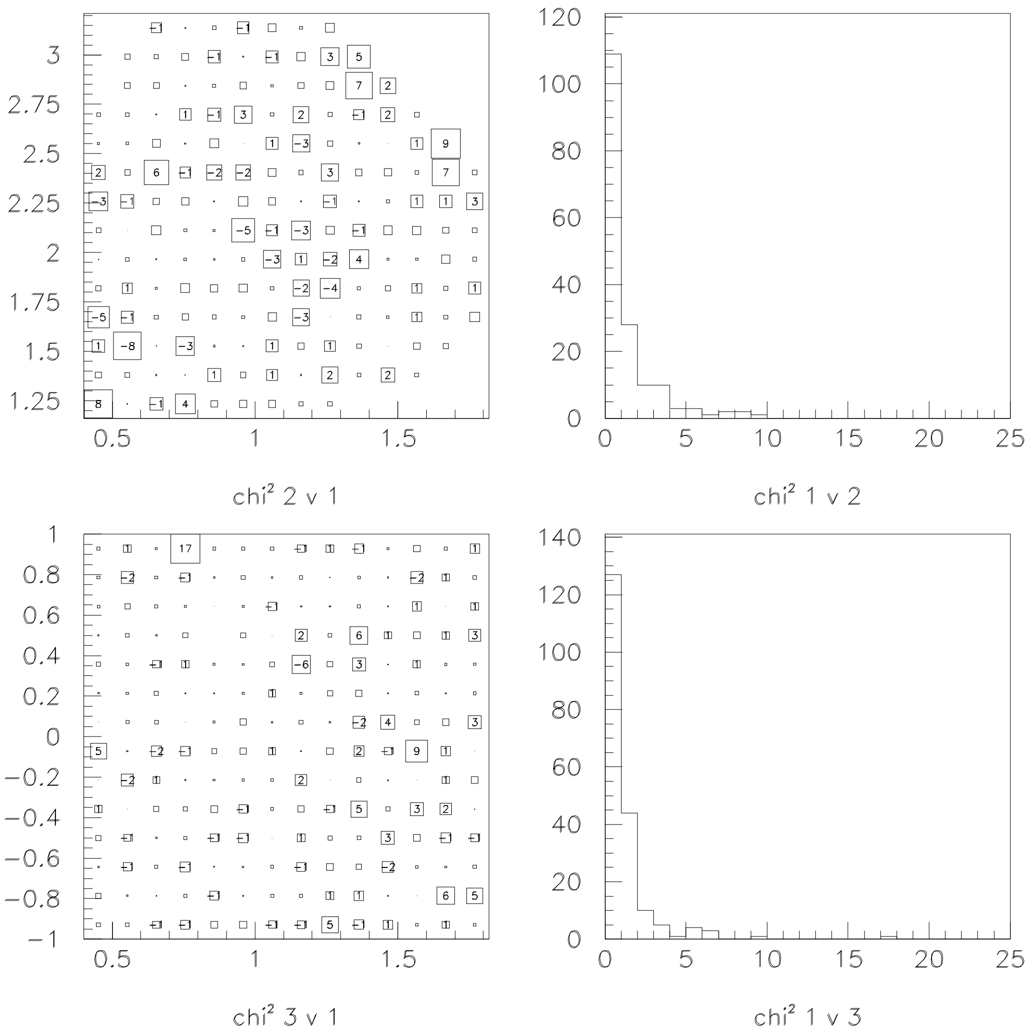

Figure H.6: Full mass range Real data set vs. Fit 3 Model as seen by χ^2 representation. The minus sign means that there were more points in the model than the actual distribution.

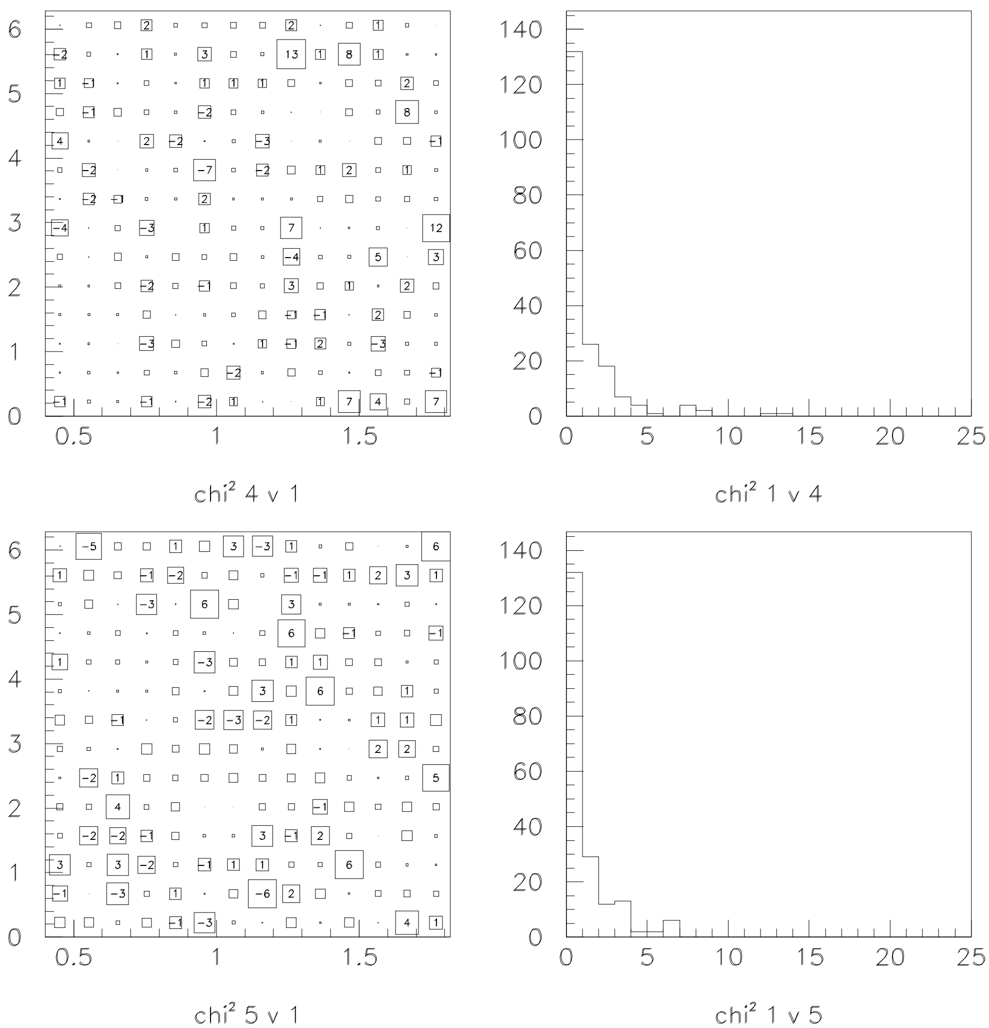

Figure H.7: Full mass range Real data set vs. Fit 3 Model as seen by χ^2 representation. The minus sign means that there were more points in the model than the actual distribution.

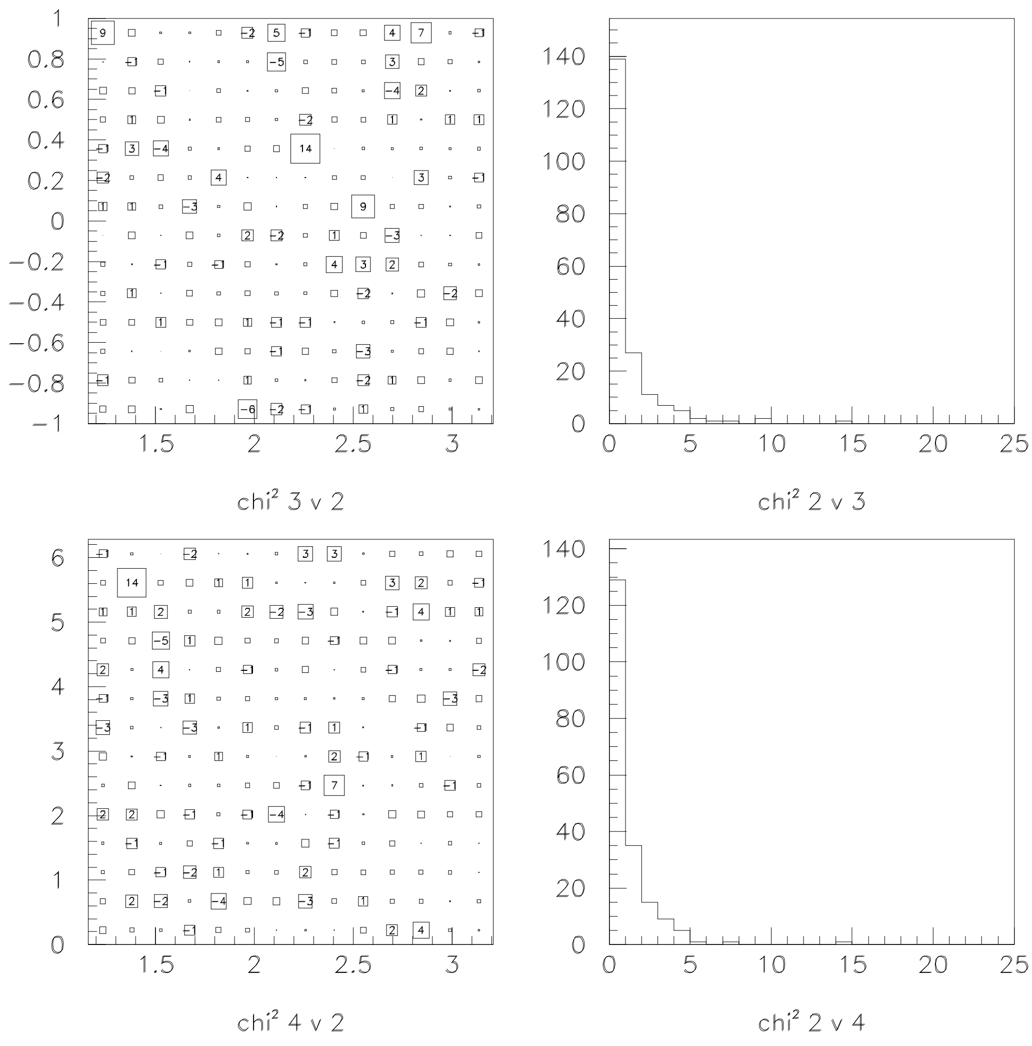

Figure H.8: Full mass range Real data set vs. Fit 3 Model as seen by χ^2 representation. The minus sign means that there were more points in the model than the actual distribution.

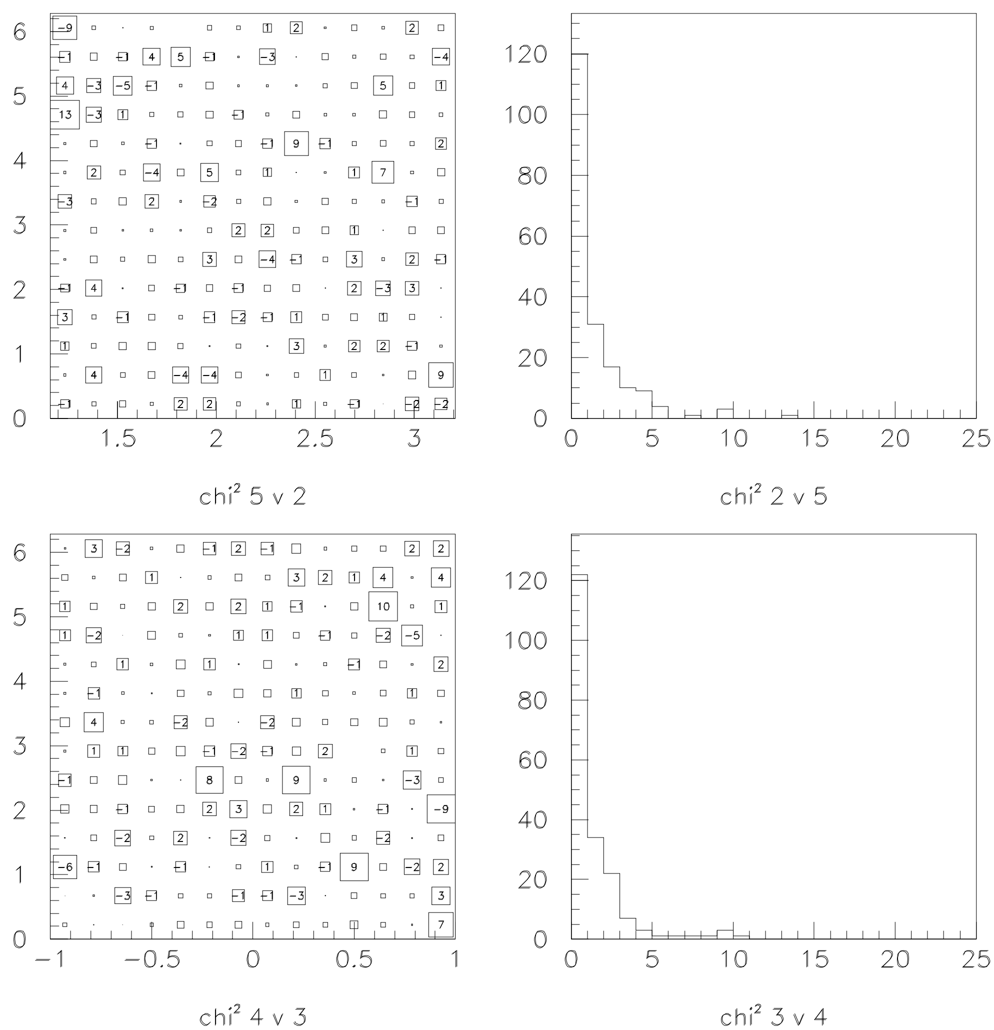

Figure H.9: Full mass range Real data set vs. Fit 3 Model as seen by χ^2 representation. The minus sign means that there were more points in the model than the actual distribution.

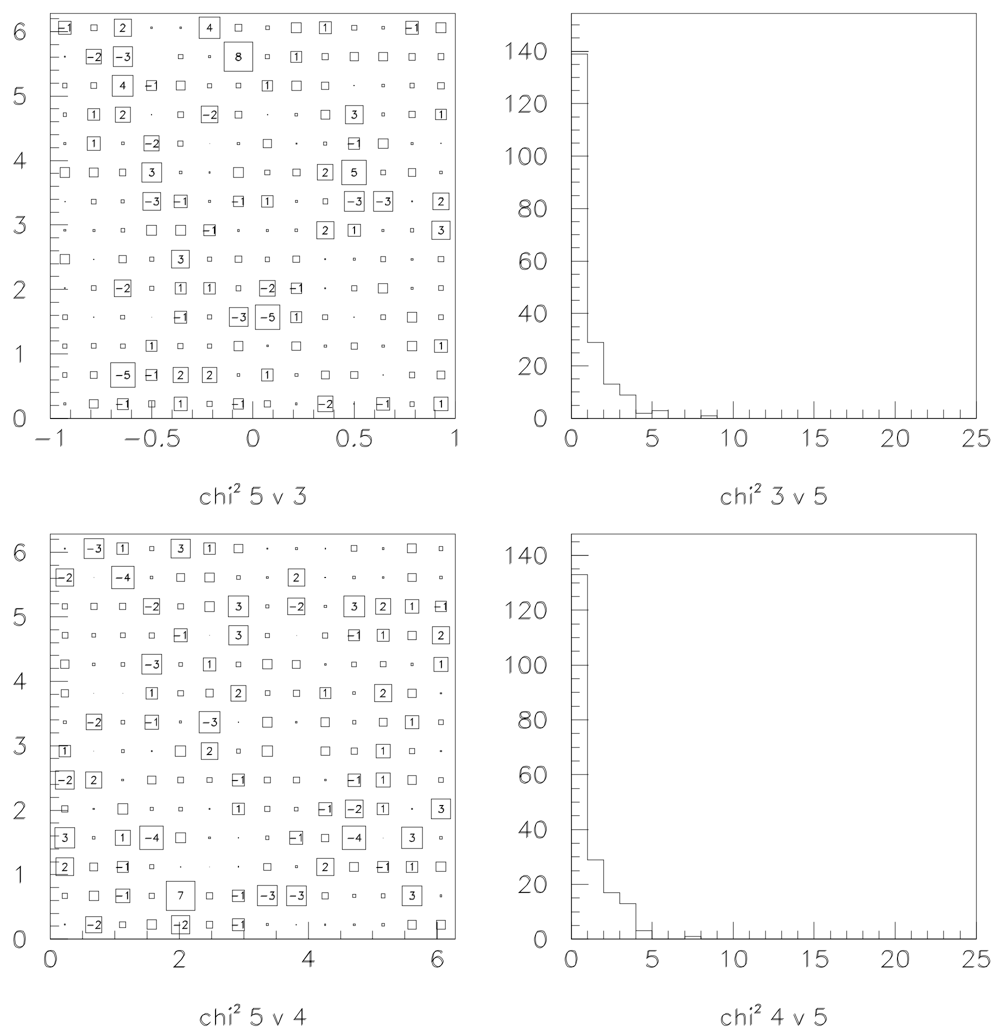

Figure H.10: Full mass range Real data set vs. Fit 3 Model as seen by χ^2 representation. The minus sign means that there were more points in the model than the actual distribution.

H.3 Fit 3: Signal Region

This section compares the final fit within the signal region. The scatter plot can be seen in figure H.11.

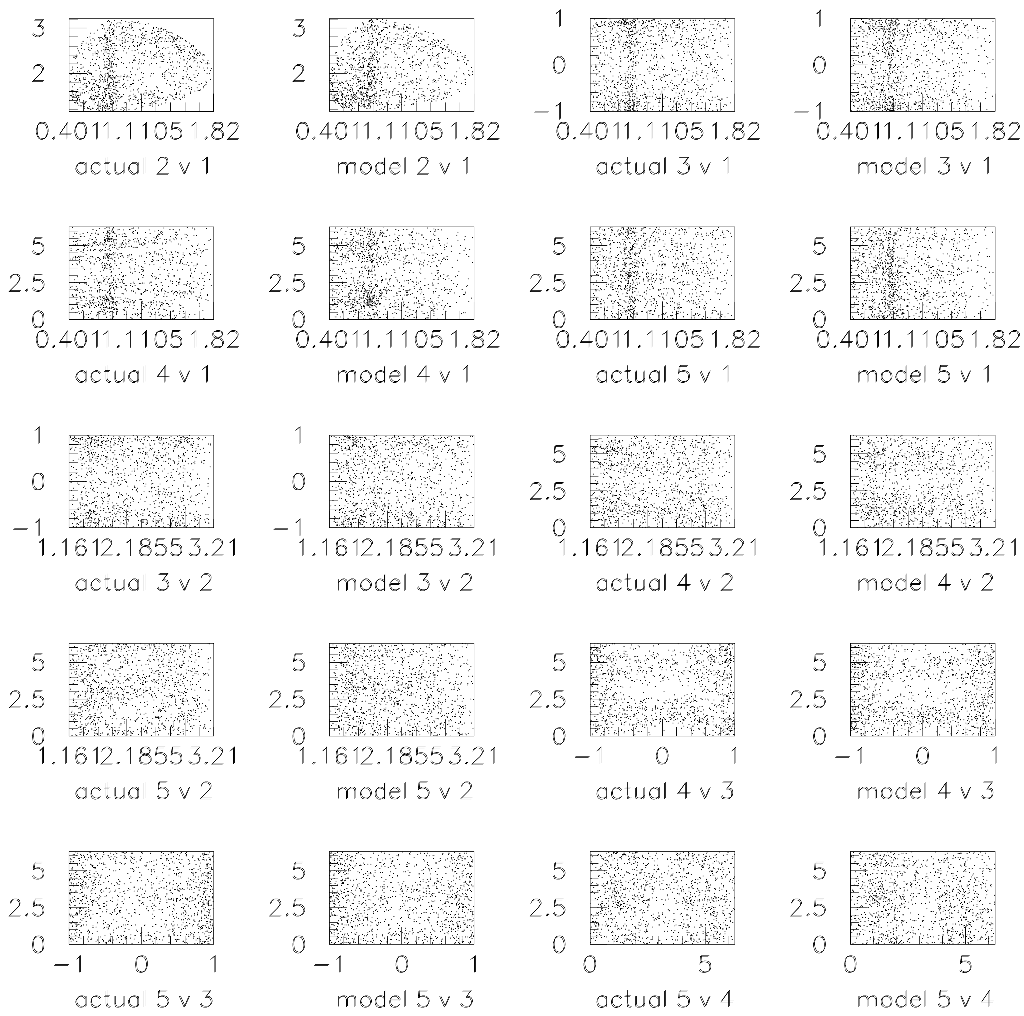

Figure H.11: Signal region of the Real data set vs. Fit 3 Model.

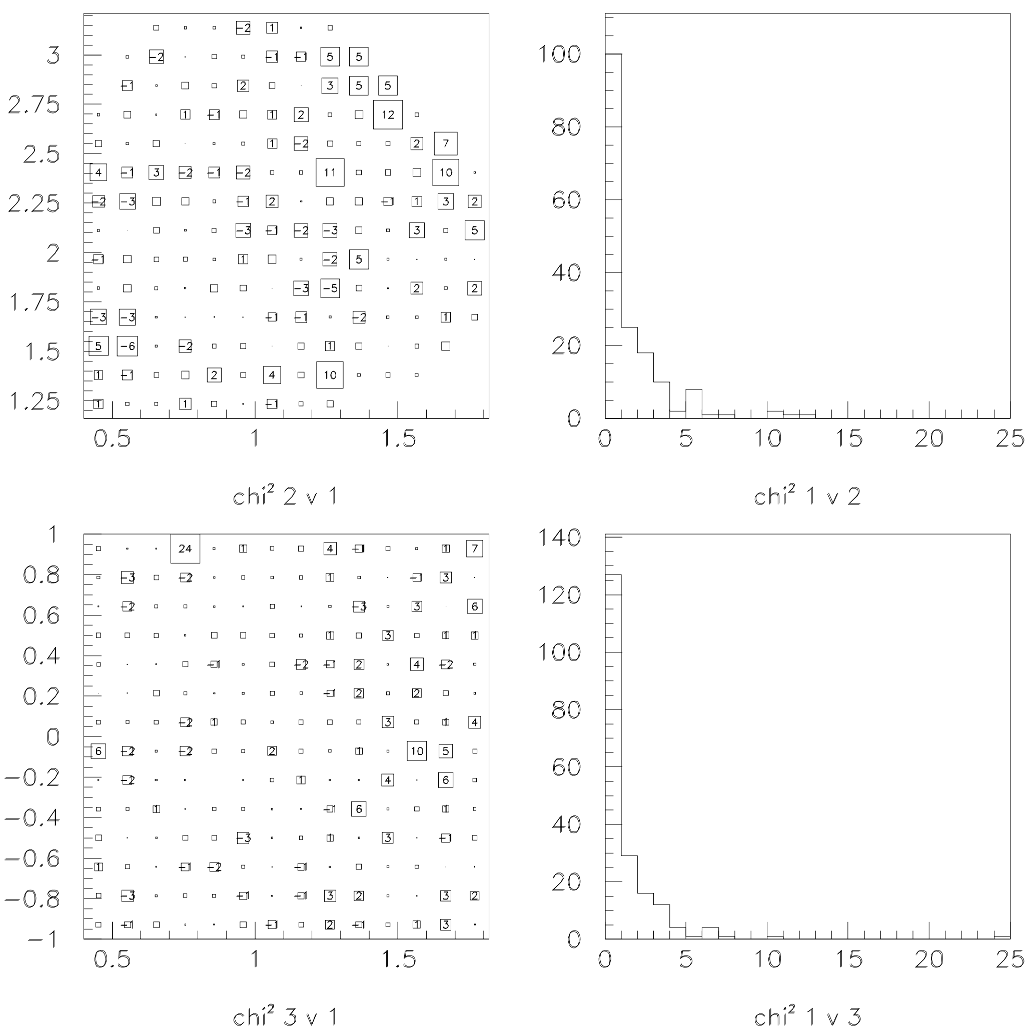

Figure H.12: Signal region of the Real data set vs. Fit 3 Model as seen by χ^2 representation. The minus sign means that there were more points in the model than the actual distribution.

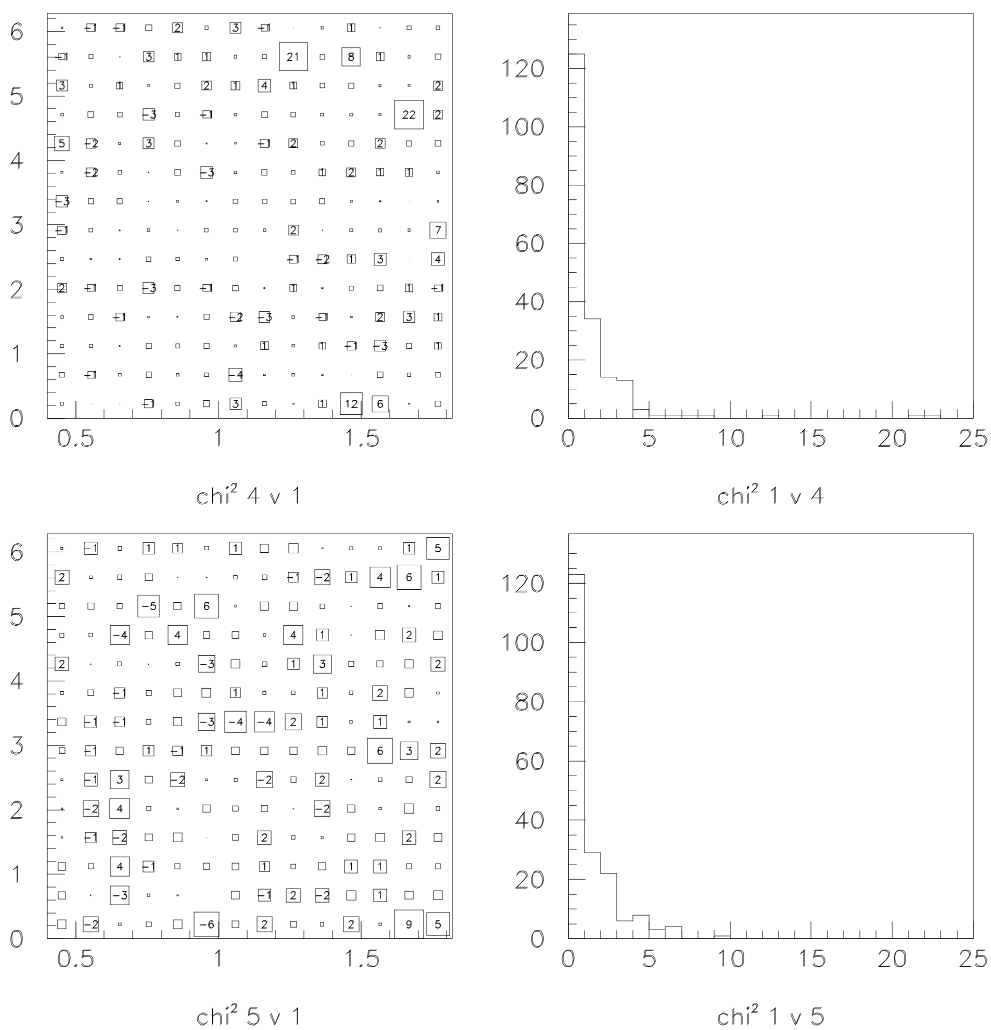

Figure H.13: Signal region of the Real data set vs. Fit 3 Model as seen by χ^2 representation. The minus sign means that there were more points in the model than the actual distribution.

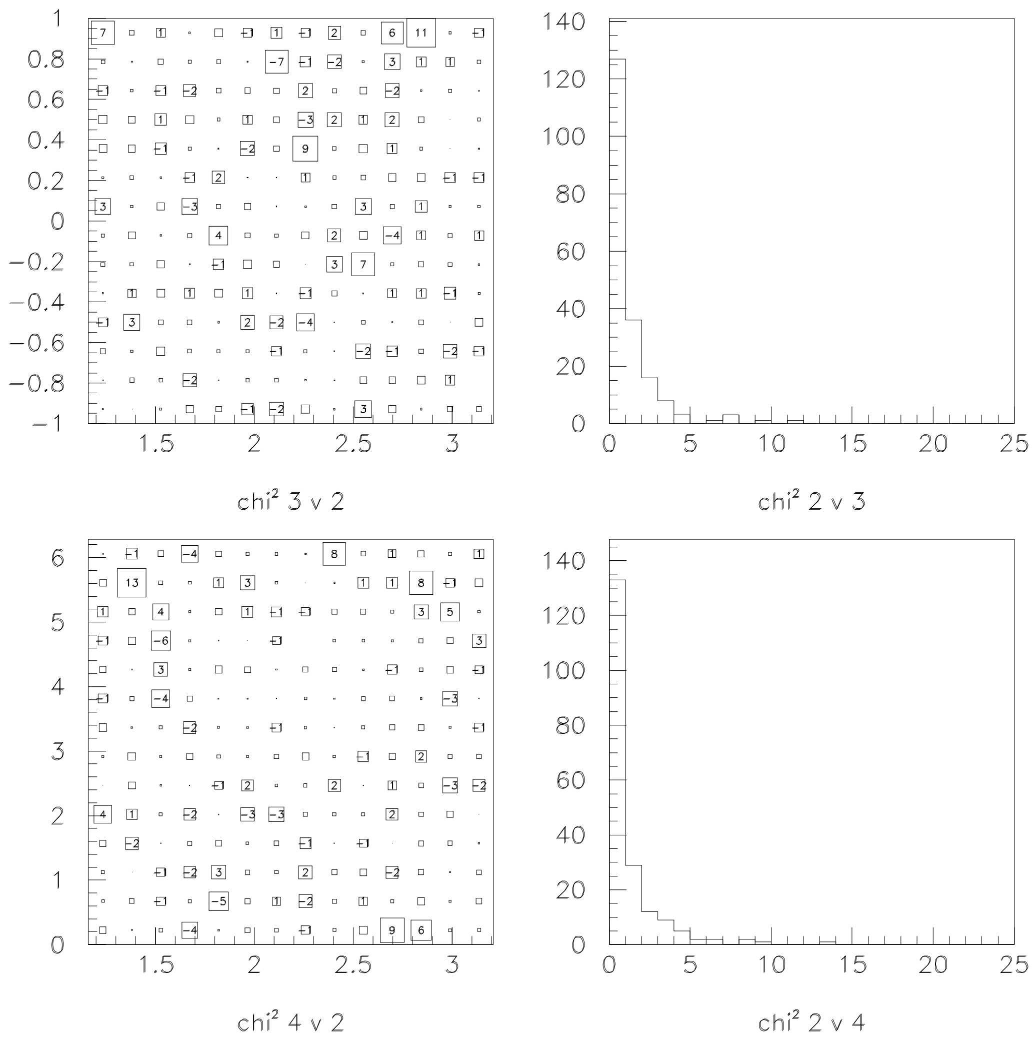

Figure H.14: Signal region of the Real data set vs. Fit 3 Model as seen by χ^2 representation. The minus sign means that there were more points in the model than the actual distribution.

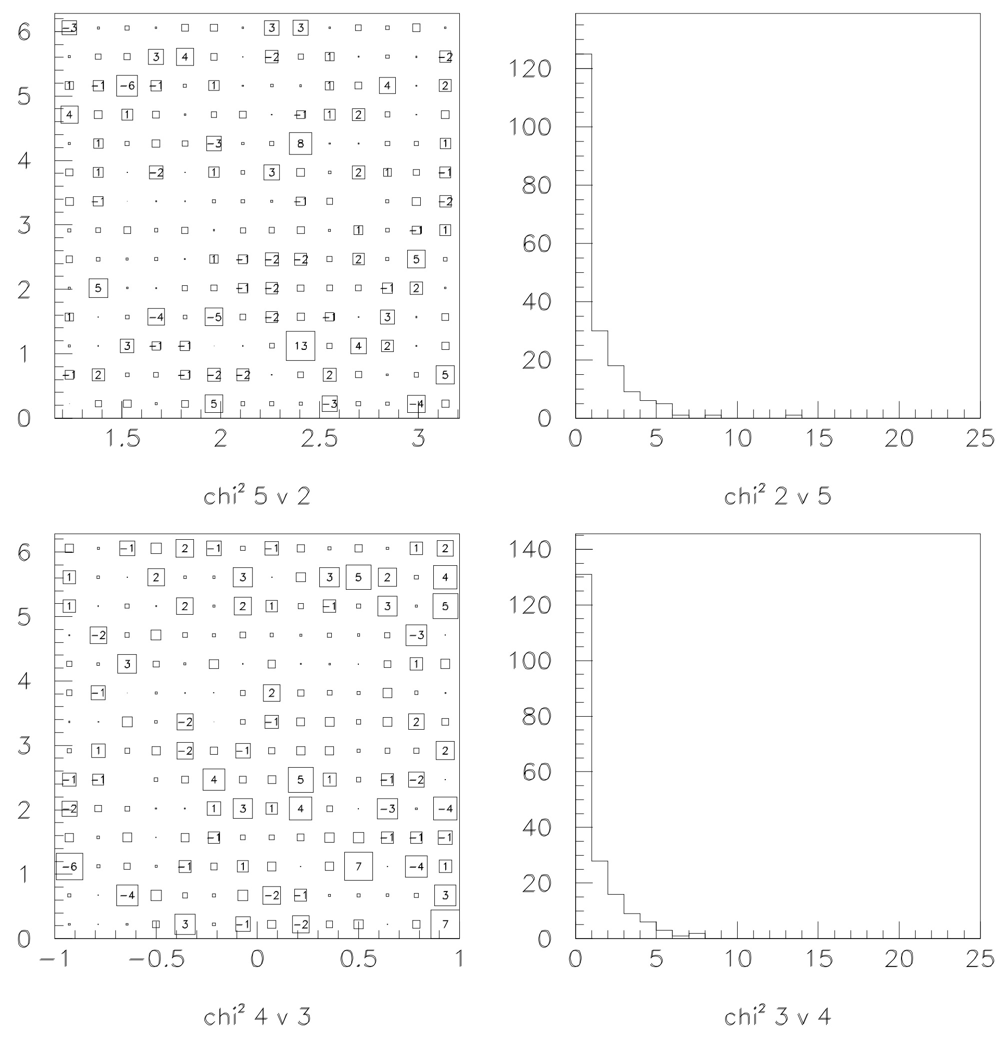

Figure H.15: Signal region of the Real data set vs. Fit 3 Model as seen by χ^2 representation. The minus sign means that there were more points in the model than the actual distribution.

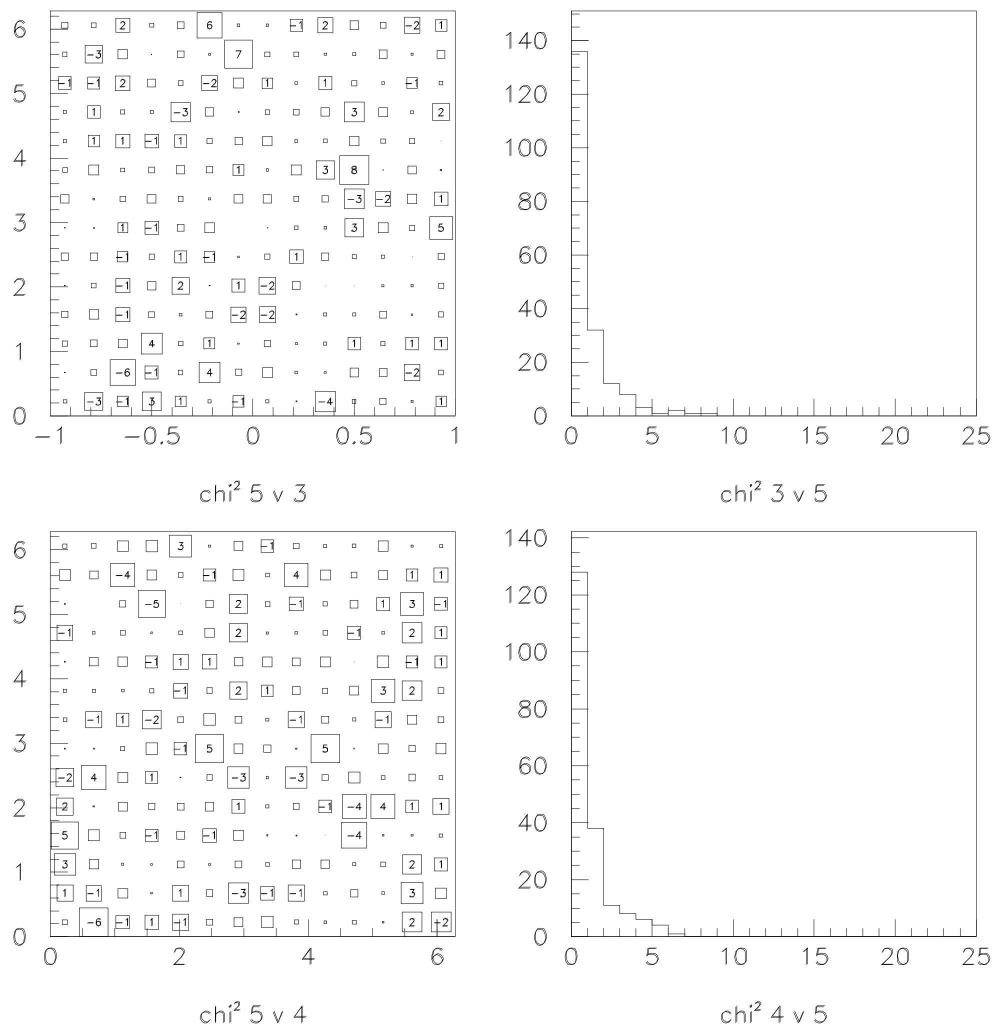

Figure H.16: Signal region of the Real data set vs. Fit 3 Model as seen by χ^2 representation. The minus sign means that there were more points in the model than the actual distribution.

Appendix I

Simple Fits of the Data

I.1 Simple Search for Resonances

I.1.1 Fit 1: Nonresonant, $\overline{\mathrm{K}}^{*0}$, and Δ^{++}

In my search for resonances, we opted to start with resonances which we felt sure were there. As can be inferred from the section title, we searched for the Nonresonant, $\overline{\mathrm{K}}^{*0}$ resonant, and Δ^{++} resonant modes. The comparison of the model to the data in one dimensional projections can be seen in figure I.1. The comparison in two dimensional projections can be seen in figure I.2. Judging from the projections of the real data in figure I.1, one can clearly see the $\overline{\mathrm{K}}^{*0}$ resonance which is spiked and the Δ^{++} resonances which is seen as a bump. The general fit is also evident figure I.2, where the $\overline{\mathrm{K}}^{*0}$ band is seen in the first eight plots, and the hole in "4 v 3" is in both the model and actual. The breakdown of the contribution from each of these modes in the model can be seen in figure I.3. In order to determine if there is a missing resonance in this fit, we subtracted the model from the real data projections and looked at the difference divided by phase space. See figures I.4 and I.5 for the projections of the differences. There initially appears to be a resonance in the pK projection. Note that the Breit-Wigner formula that we used was $\frac{-m\Gamma_0}{s-m^2+im\Gamma}$, implying that we did not take the centrifugal barrier into account.

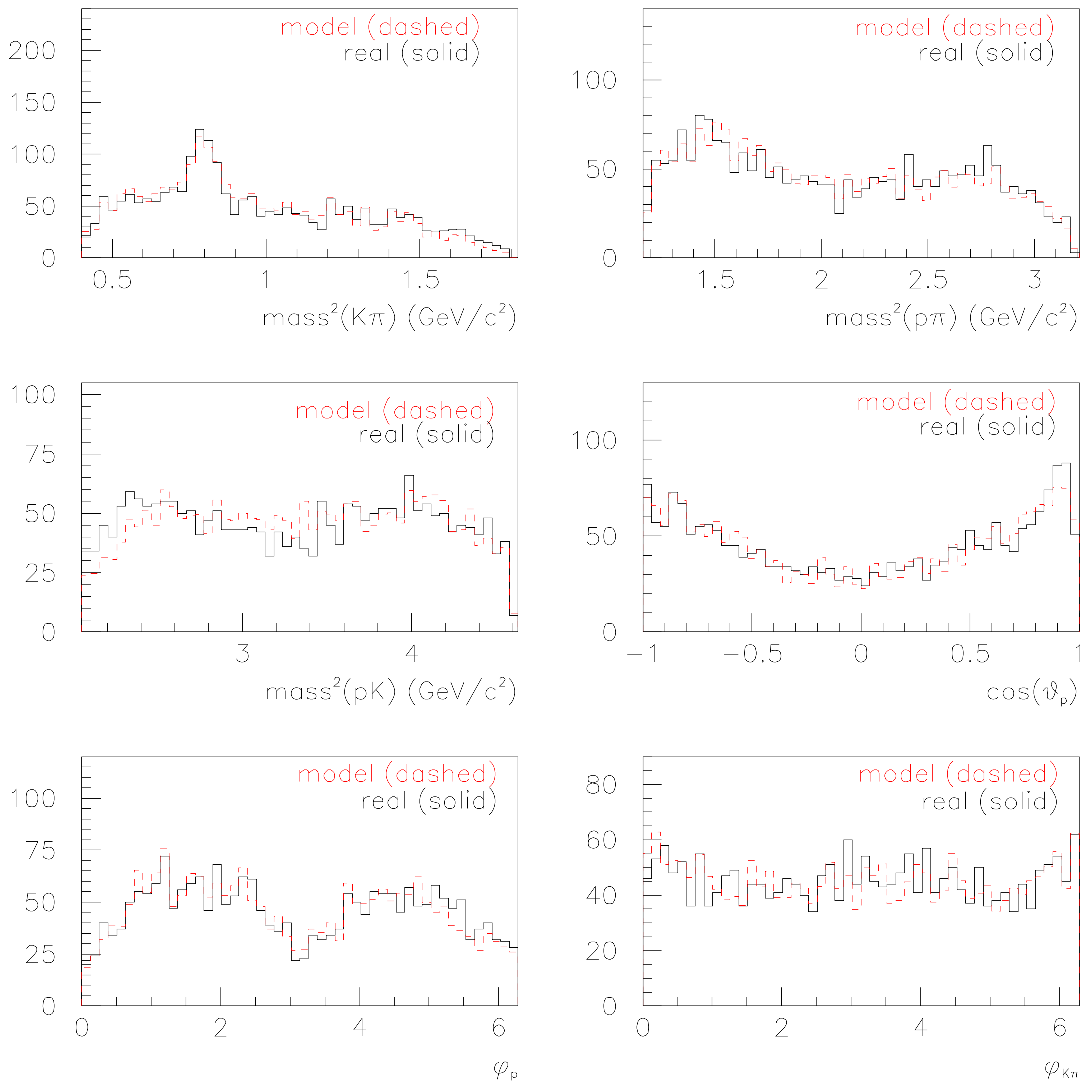

Figure I.1: Projections of the real data and Fit 1 superimposed for comparison purposes.

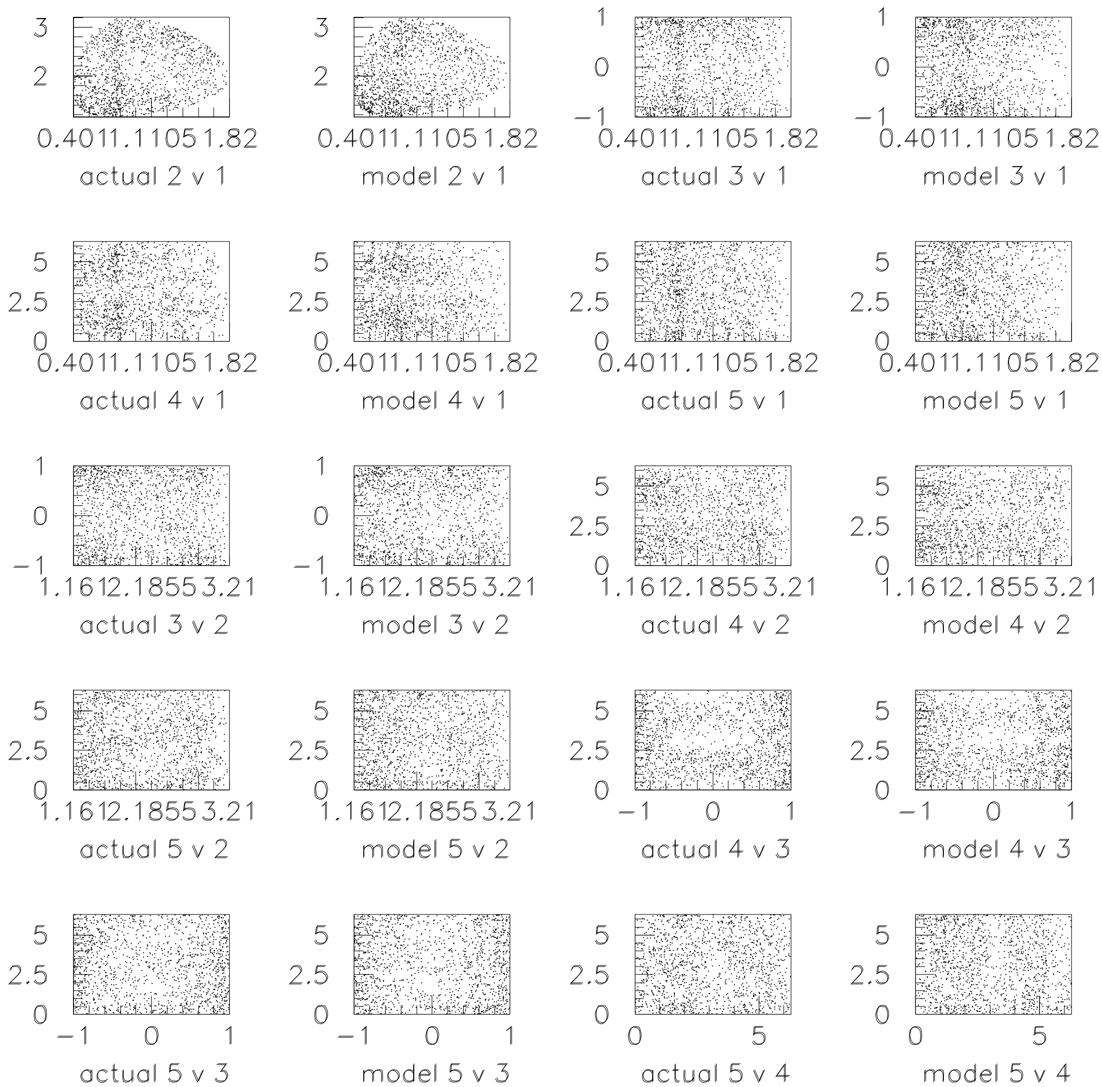

Figure I.2: The two dimensional projections of Fit 1 and real data, where the numbers 1 - 5 represent the dimensions outline in the beginning of the previous section. Note the $\overline{\mathrm{K}}^{*0}$ band in the first eight plots, and the hole in "4 v 3" is in both the model and actual.

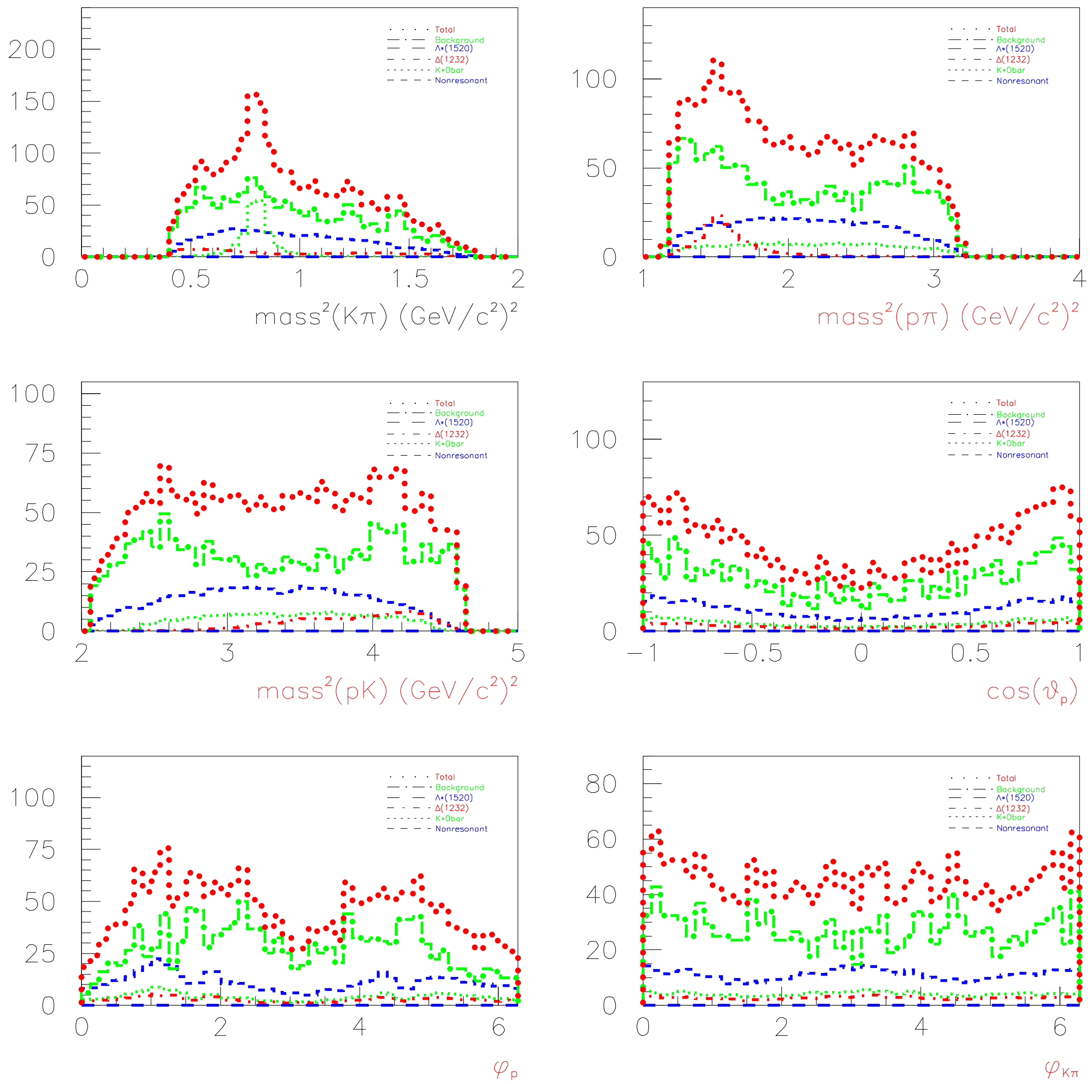

Figure I.3: Projections of the model broken down by resonance mode for Fit 1. The need for the angular dimensions is subtly apparent by the slight dip of the Δ^{++} projection in the middle of the $\phi_{K\pi}$ plot while the nonresonant distribution peaks.

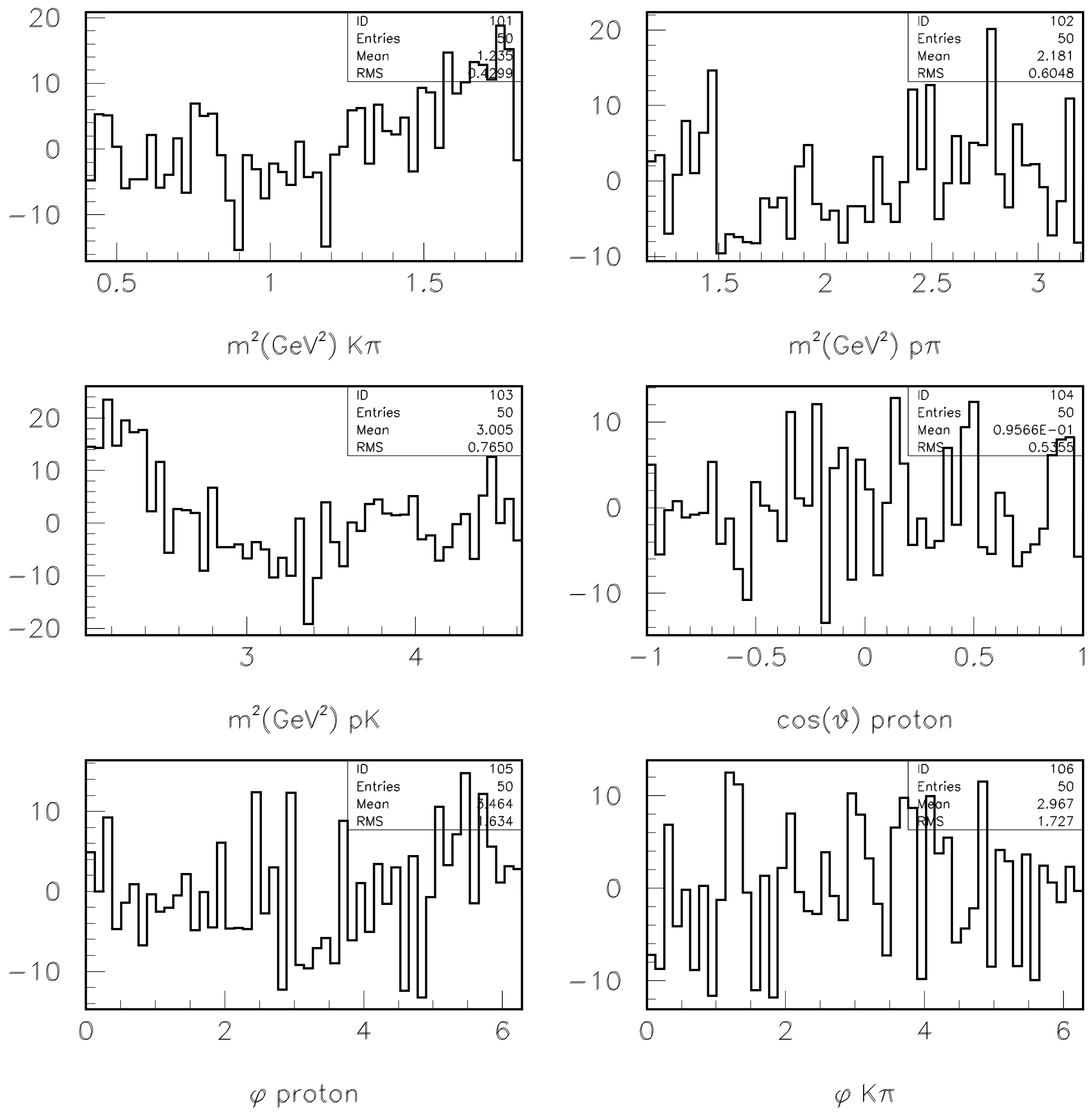

Figure I.4: Projections of the real data minus Fit 1 and divided by phase space. From the m^2_{pK} plot there seems to be a missing resonance in the lower m_{pK} phase space.

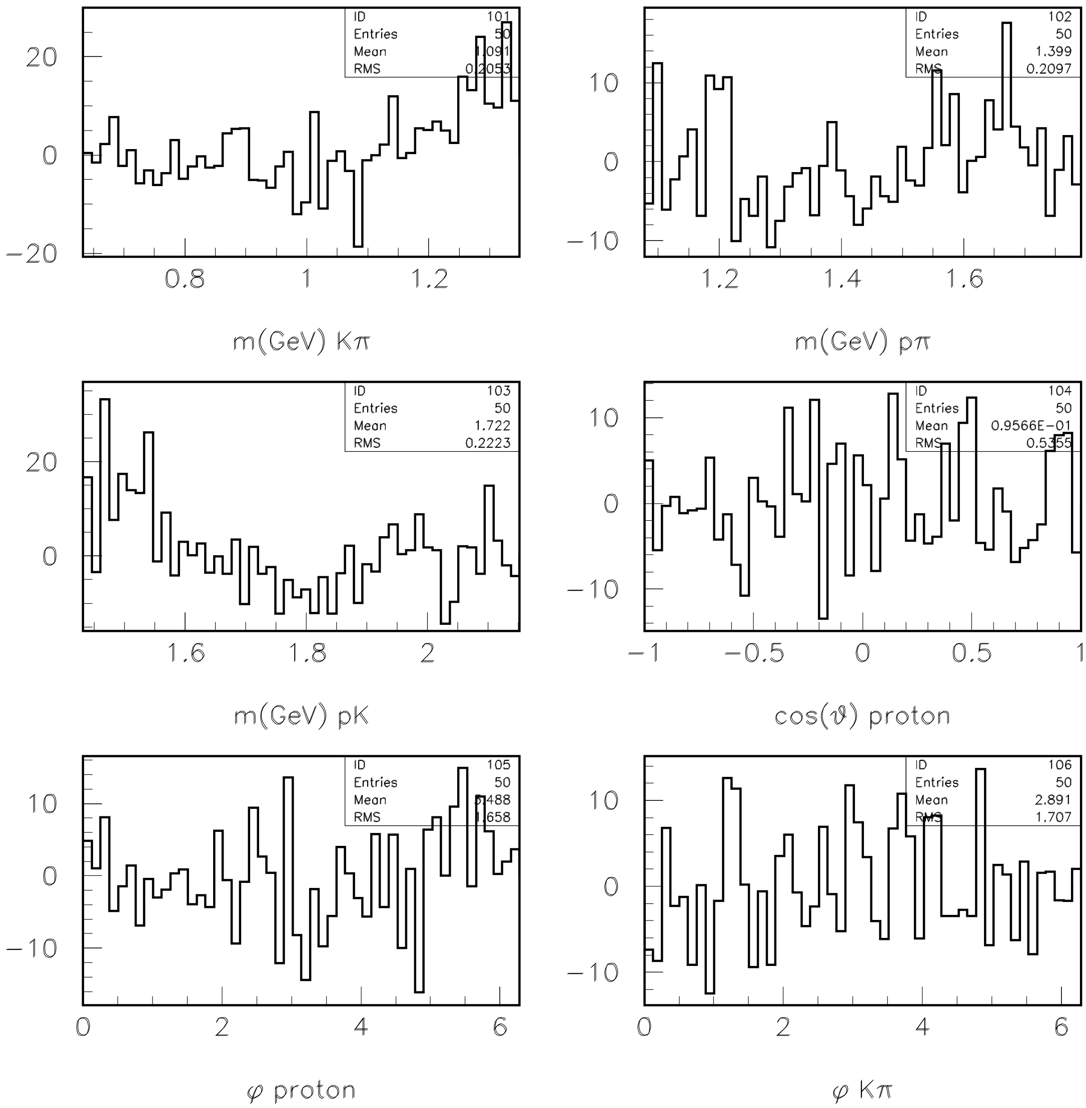

Figure I.5: Projections of the real data minus Fit 1 and divided by phase space. Note that the first 3 histograms are mass and not mass^2. From the m_{pK} plot there seems to be a missing resonance in the lower m_{pK} phase space.

I.1.2 Fit 2: Nonresonant, $\overline{\mathrm{K}}^{*0}$, Δ^{++}, and $\Lambda(1520)$

With the hint of a pK resonance from the last fit, the question arises of what resonance should be included in a subsequent fit. we opted to add the $\Lambda(1520)$ resonance. Although a narrow resonance, it has been seen in a previous analysis[Boz 93], so it seemed a logical choice. Other potential resonances are explored in section 9.5.

For a one dimensional projection comparison of the model and data, see figure I.6. For a two dimensional comparison, see figure I.7. Again, one can see the $\overline{\mathrm{K}}^{*0}$ and the Δ^{++} resonances. The $\Lambda(1520)$ resonance seems to be there, but its presence is not as obvious. The breakdown of the contribution from each of these modes in the model can be seen in figure I.8. Again, we subtracted the one dimensional projections of the model from the real data projections and we divided these by phase space. The results of this subtraction can be seen in figures I.9 and I.10. Note that the Breit-Wigner formula that we used was $\frac{-m\Gamma_0}{s-m^2+im\Gamma}$, implying that we did not take the centrifugal barrier into account.

Also note that fit 2a and 2b produced the same projections, so we presented fit 2b in this section.

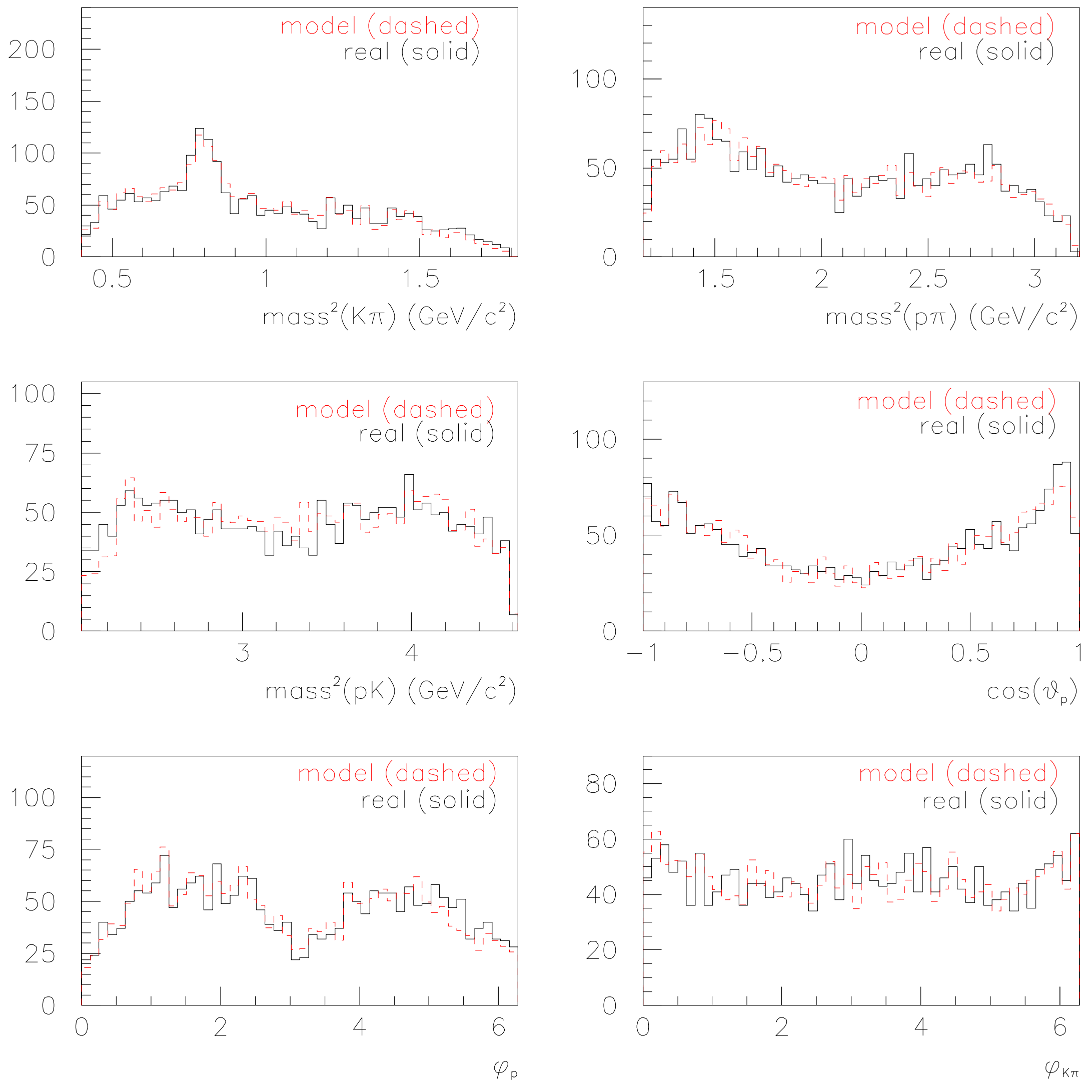

Figure I.6: Projections of the real data and Fit 2b superimposed for comparison purposes.

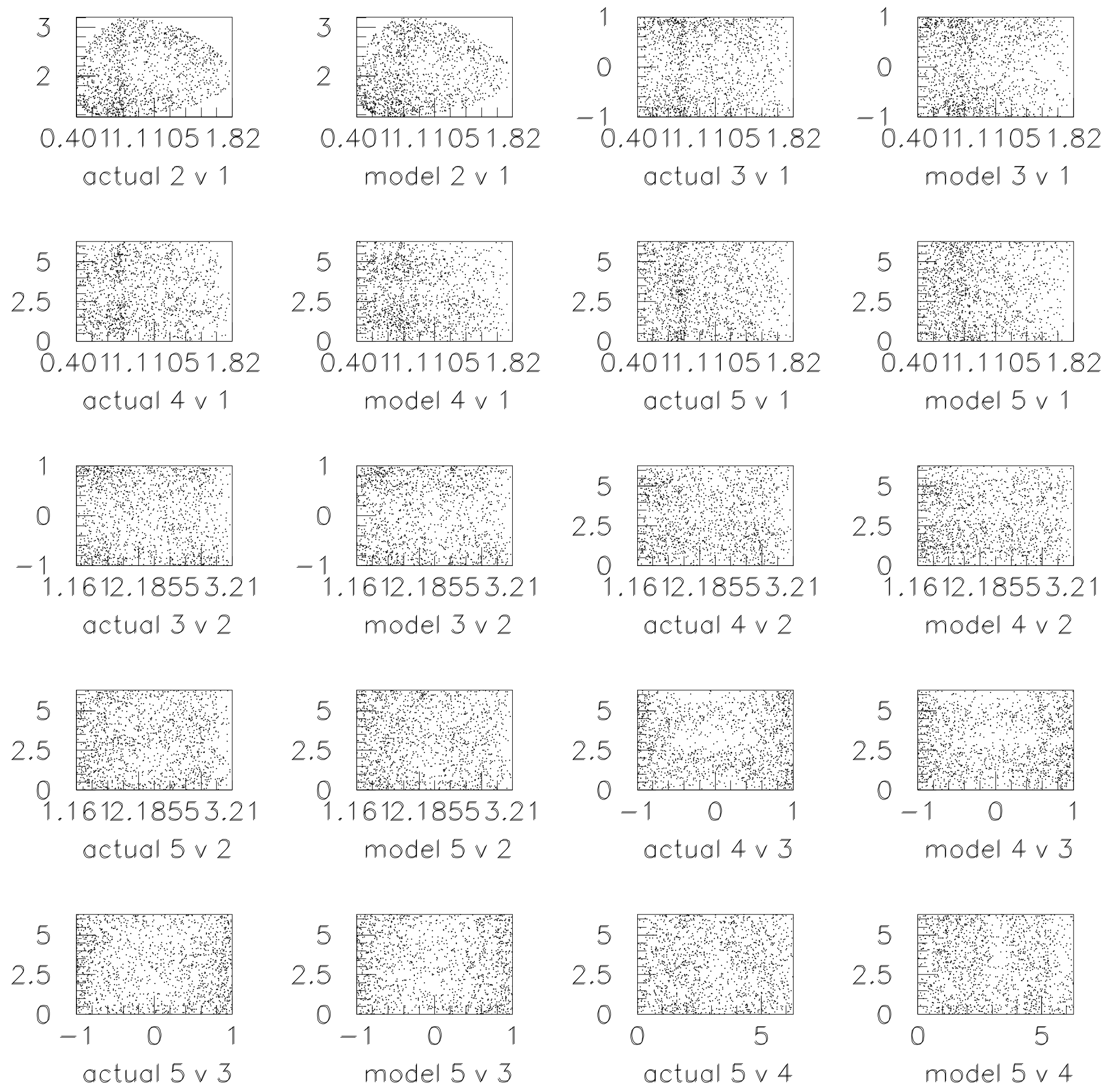

Figure I.7: The two dimensional projections of Fit 2b and real data, where the numbers 1 - 5 represent the dimensions outline in the beginning of the previous section. Note the $\overline{\mathrm{K}}^{*0}$ band in the first eight plots, and the hole in "4 v 3" is in both the model and actual.

Figure I.8: Projections of the model broken down by resonance mode for Fit 2b.

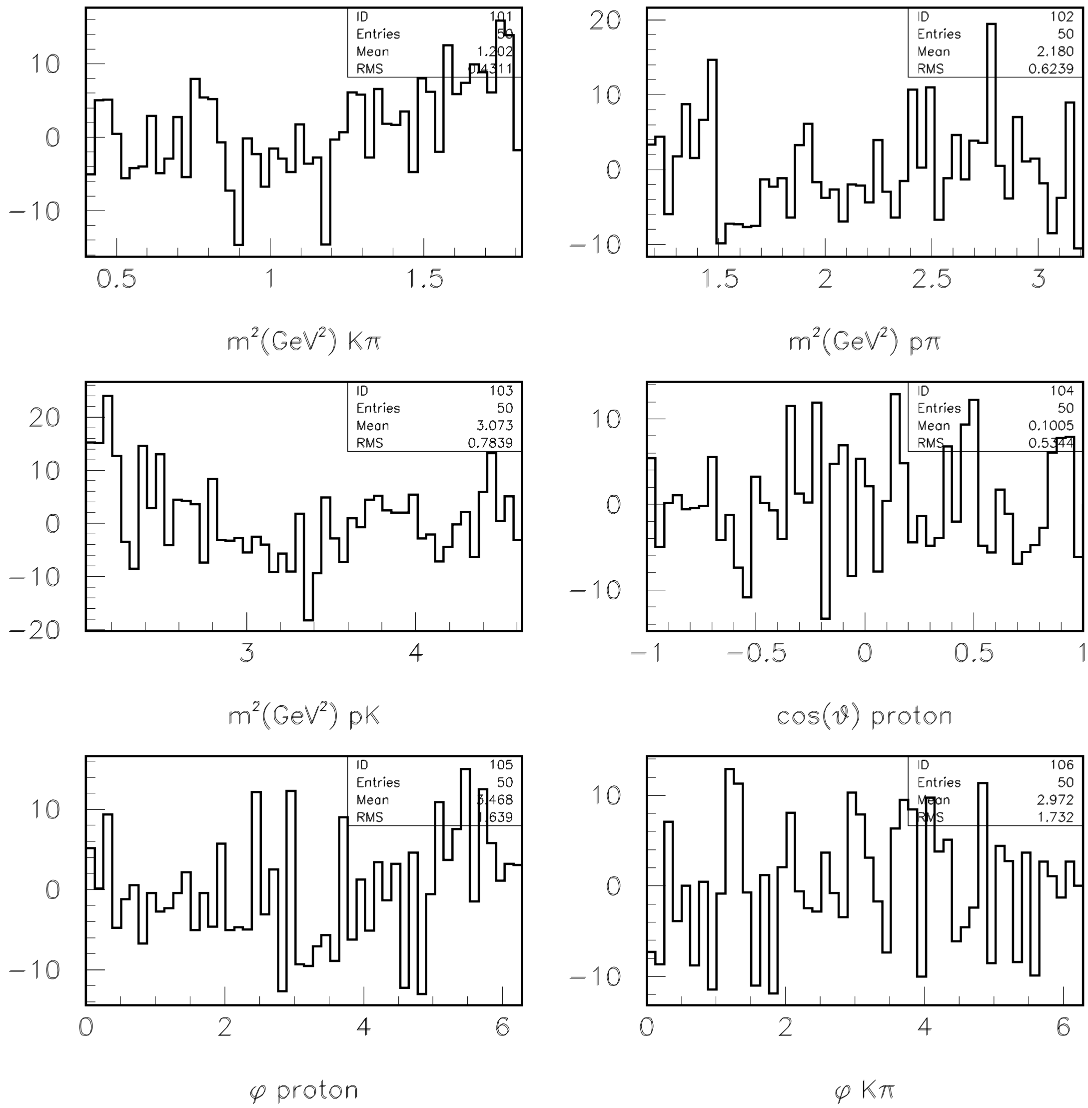

Figure I.9: Projections of the real data minus Fit 2b and divided by phase space. The addition of the $\Lambda(1520)$ accounted for some the discrepancies in the low pK mass range.

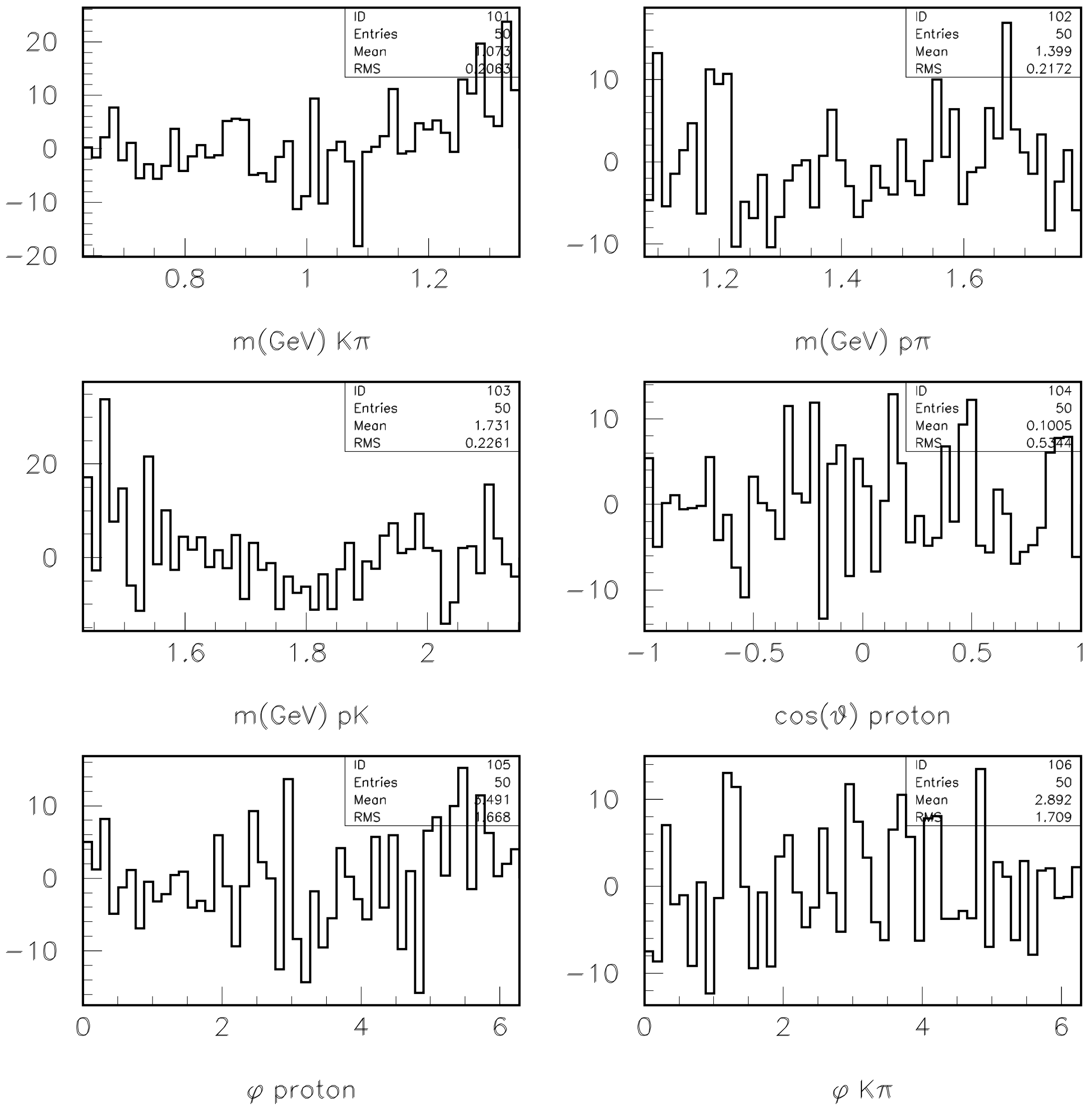

Figure I.10: Projections of the real data minus Fit 2b and divided by phase space. Note that the first 3 histograms are mass and not mass^2. The addition of the $\Lambda(1520)$ accounted for some the discrepancies in the low pK mass range.

I.1.3 Fit 3: Nonresonant, $\overline{K}^{*0}$, Δ^{++}, Λ(1520), plus the mass plot fit parameters

The previous fits were good for getting a feel for what which modes were present. However, the proper fit should include some other factors. One of these factors is that the errors in the mass plot fit needed to be propagated throughout the fit, so the mass plot fit was incorporated into the process. Also, it had been noticed within the Collaboration that the width of the Λ_c depended on x_F. This, too, was incorporated. Thus, fit three is most accurate of these fits.

For a one dimensional projection comparison of the model and data, see figure I.11. For a two dimensional comparison, see figure I.12. Again, one can see the $\overline{K}^{*0}$ and the Δ^{++} resonances. The Λ(1520) resonance seems to be there, but its presence is still not as obvious from the plot. The breakdown of the contribution from each of these modes in the model can be seen in figure I.13. Again, we subtracted the one dimensional projections of the model from the real data projections and We divided these by phase space. The results of this subtraction can be seen in figures I.14 and I.15.

The Breit-Wigner resonance formula we used is the corrected formula as is seen in equations 2.28 and 2.29

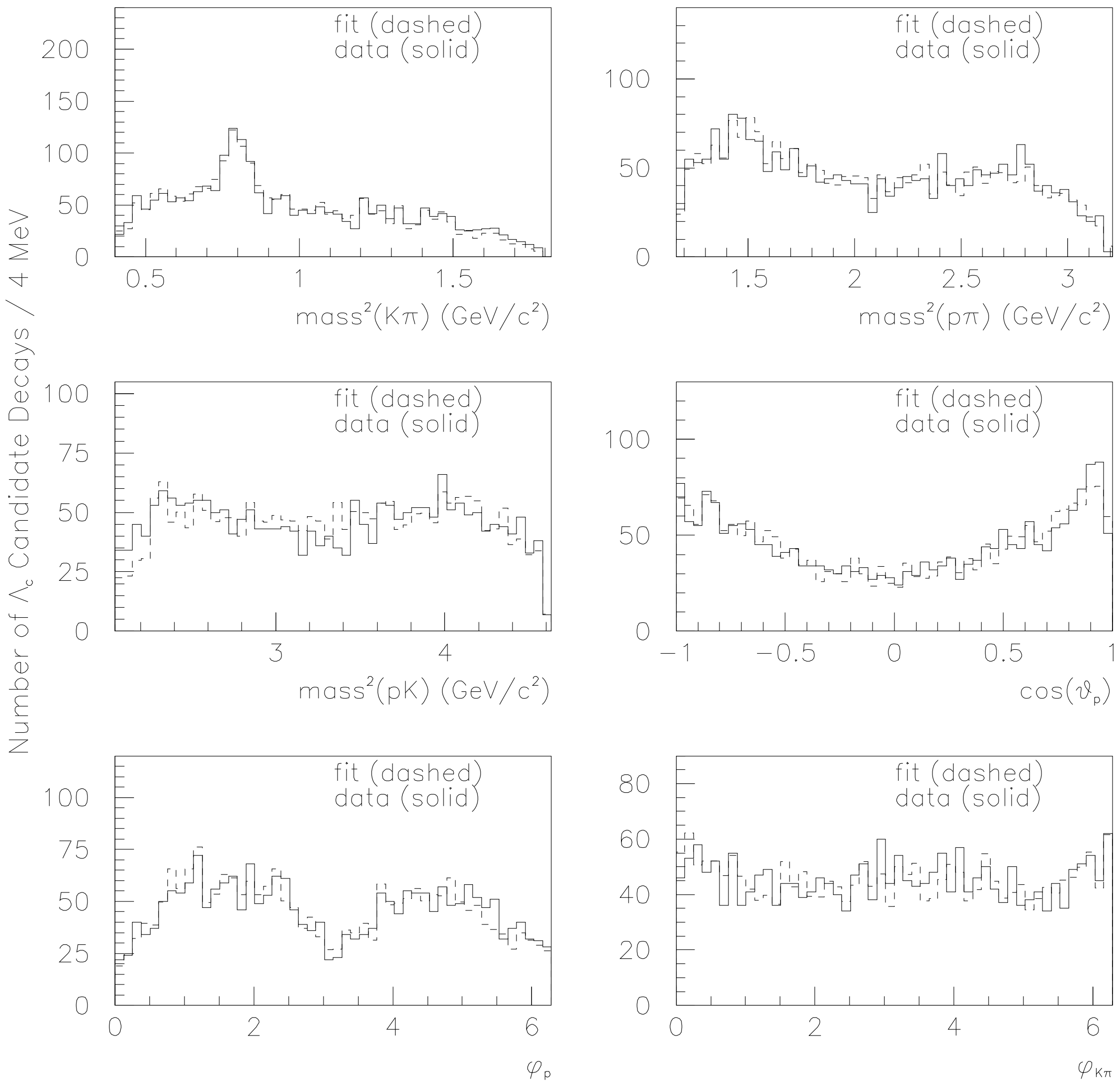

Figure I.11: Projections of the real data and Fit 3 superimposed for comparison purposes.

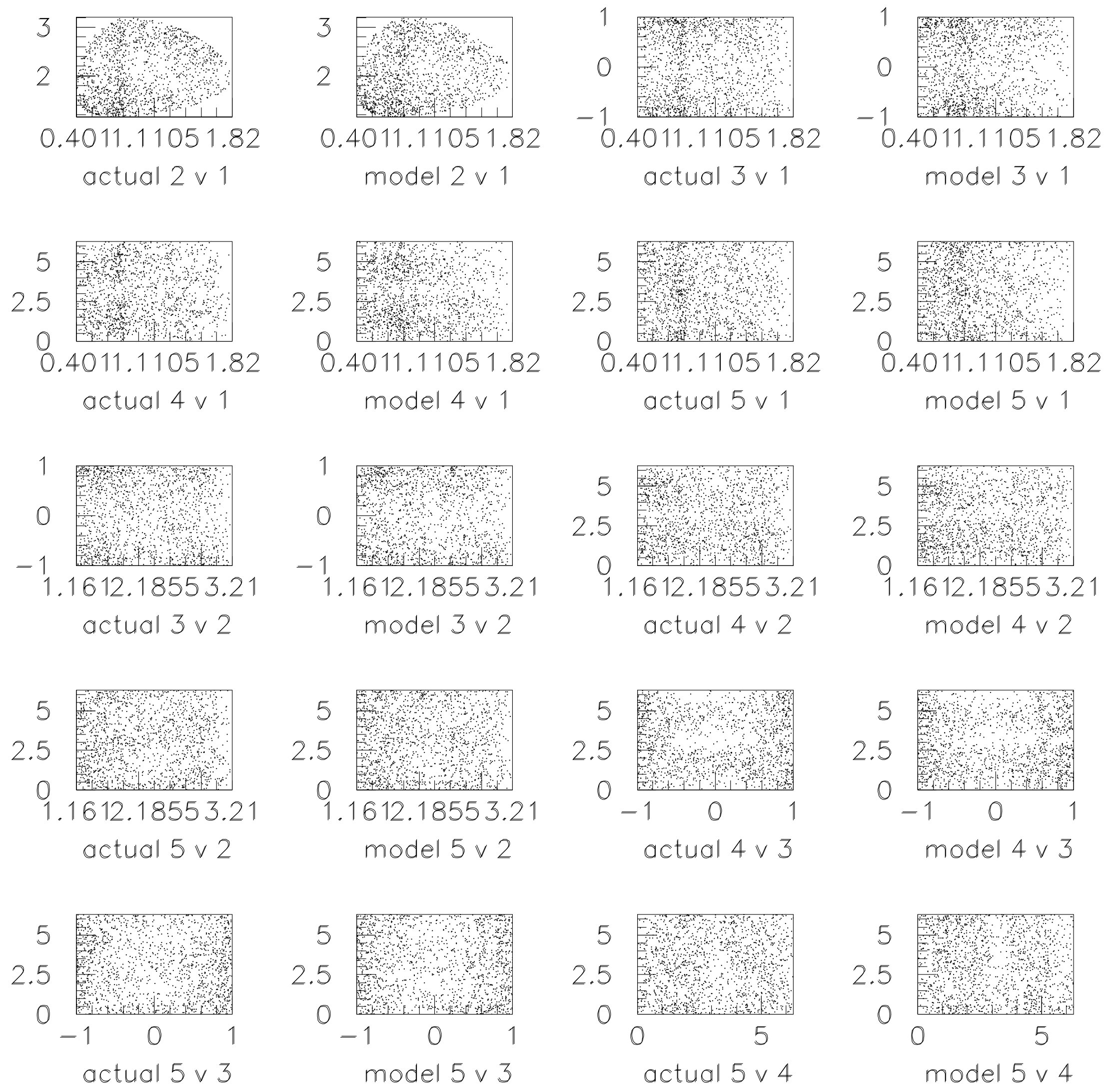

Figure I.12: The two dimensional projections of Fit 3 and real data, where the numbers 1 - 5 represent the dimensions outline in the beginning of the previous section. Note the $\overline{\mathrm{K}}^{*0}$ band in the first eight plots, and the hole in "4 v 3" is in both the model and actual.

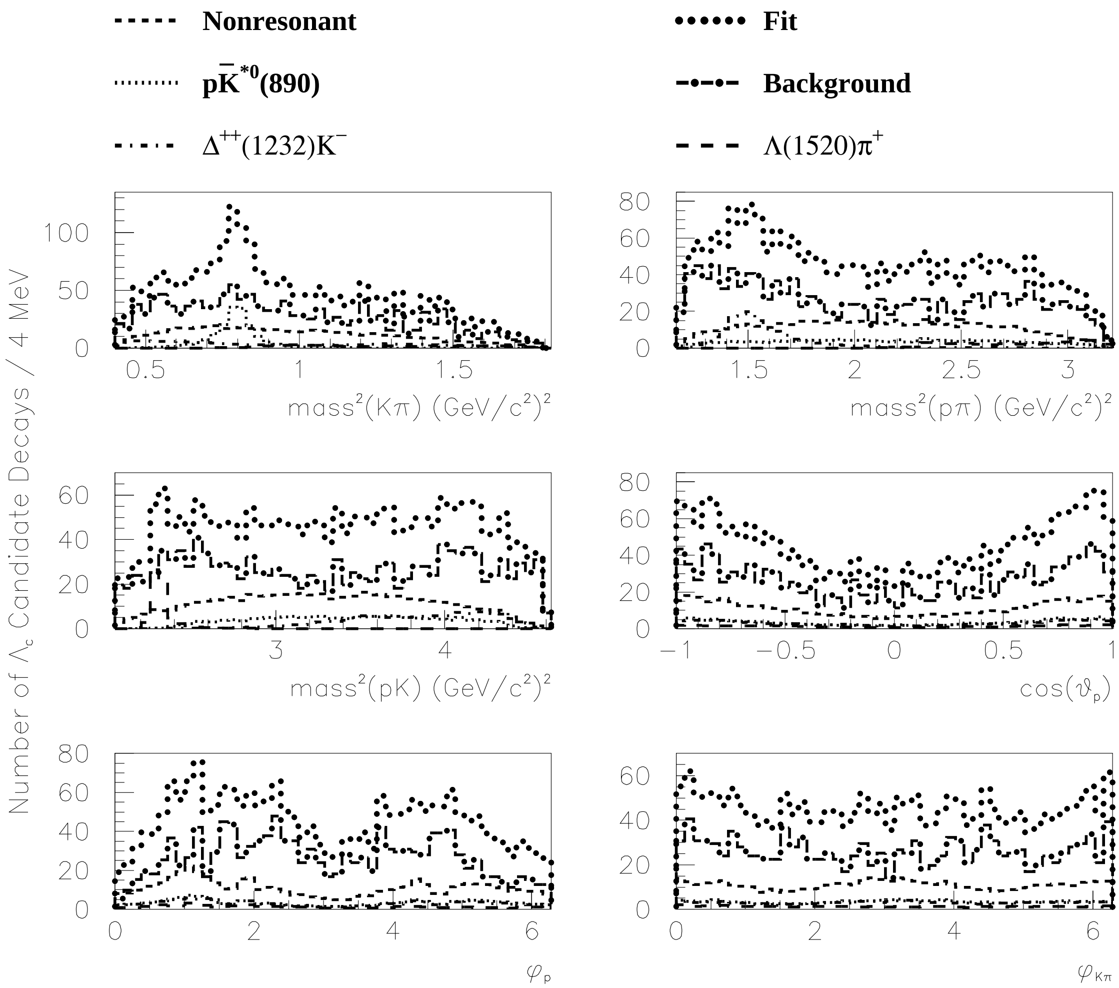

Figure I.13: Projections of the model broken down by resonance mode for Fit 3.

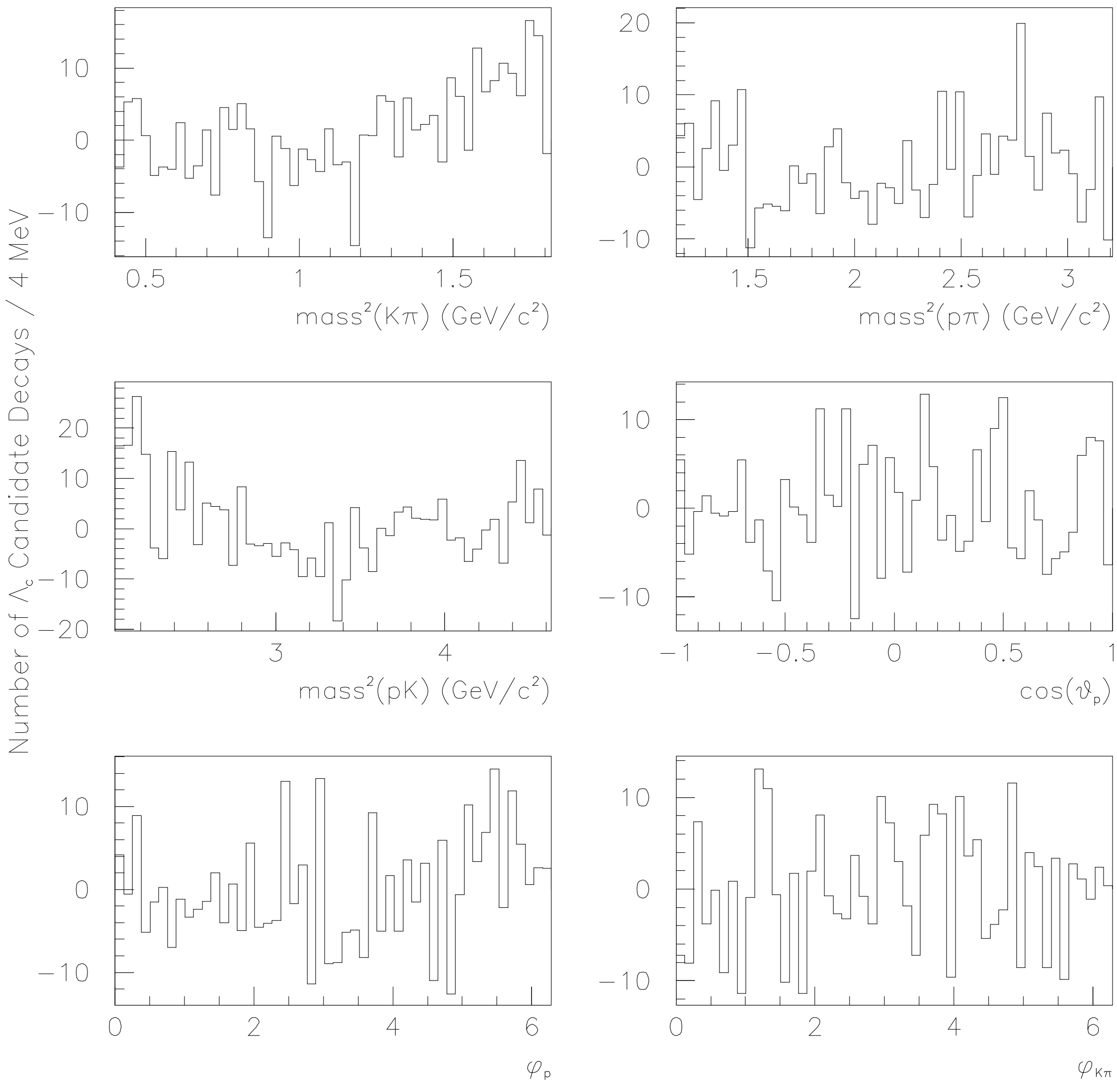

Figure I.14: Projections of the real data minus Fit 3 and divided by phase space.

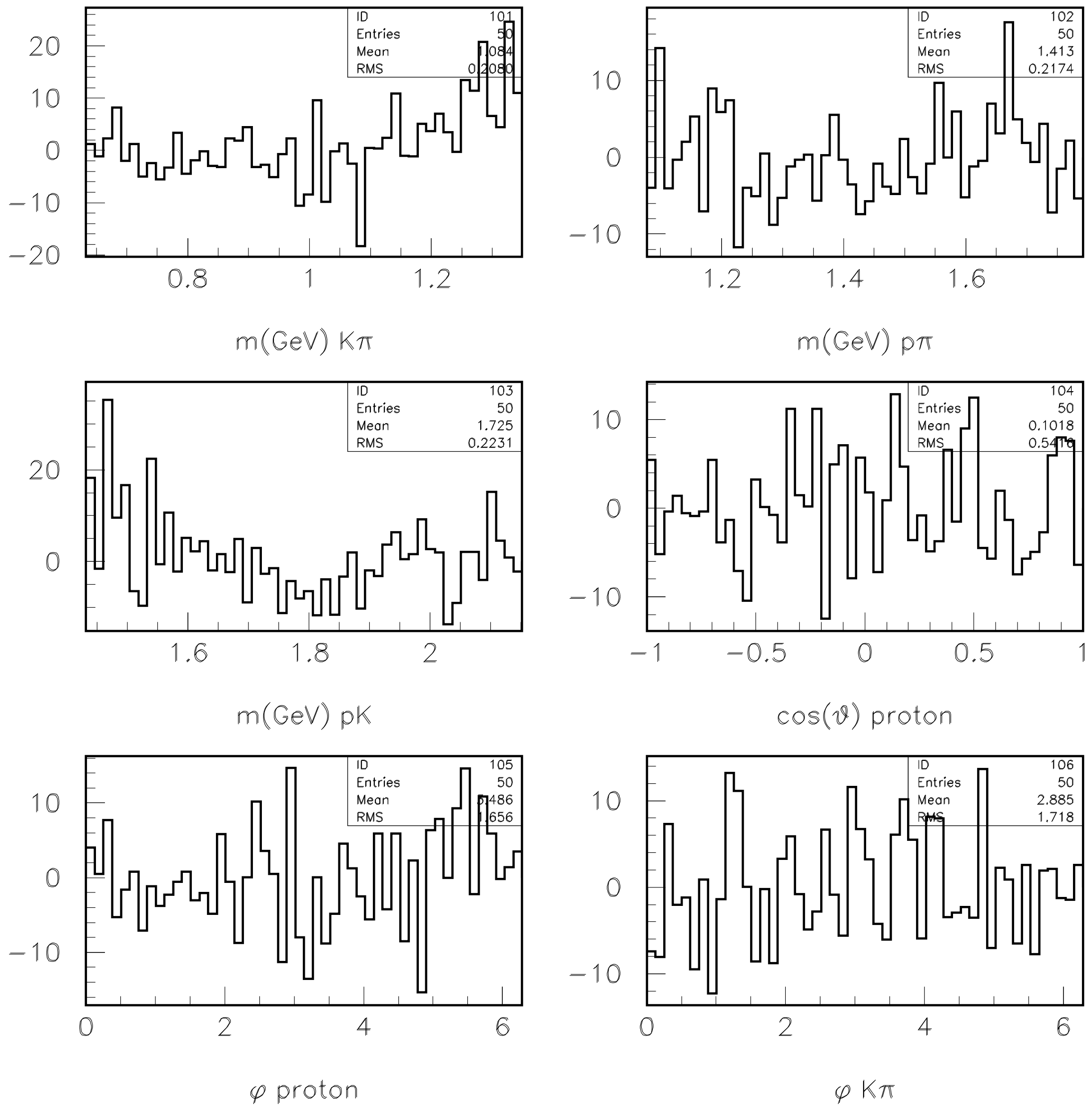

Figure I.15: Projections of the real data minus Fit 3 and divided by phase space. Note that the first 3 histograms are mass and not mass^2.

I.2 Statistical Results

In the tables below, the variable ϕ represents the phase of the decay with respect to one of the $\overline{\mathrm{K}}^{*0}$ amplitudes (for Fits 1 and 2a) or with respect to one of the nonresonant amplitudes (for Fits 2b and 3) which was assumed to have $\phi = 0.0$ and a magnitude of 1.0.

In table I.2, FCN refers to the function value found by MINUIT. It has only a relative meaning, in that it is the value that MINUIT is minimizing. It is presented for those who want to draw a conclusion. χ^2 refers to the χ^2 fit found for each of the dimensions used in the fit, as defined in chapter 8.

Mode	Vrbl	Fit 1	Fit 2a	Fit 2b	Fit 3
$p\overline{K}^{*0}$	E_1	1.00	1.00	0.37± 0.05	0.34± 0.04
	ϕ_{E_1}	0.00	0.00	3.55± 0.83	0.45± 0.80
	E_2	0.31± 0.26	0.43± 0.17	0.16± 0.07	0.14± 0.06
	ϕ_{E_2}	1.79± 1.21	2.23± 1.17	5.77± 0.68	2.79± 0.68
	E_3	0.53± 0.16	0.37± 0.17	0.14± 0.06	0.14± 0.06
	ϕ_{E_3}	1.88± 0.86	2.53± 1.04	6.08± 0.56	2.85± 0.53
	E_4	0.06± 0.14	0.05± 0.14	0.02± 0.05	0.04± 0.05
	ϕ_{E_4}	3.19± 2.33	3.89± 4.54	1.16± 2.59	4.57± 1.41
$\Delta^{++}K^-$	F_1	0.52± 0.15	0.61± 0.13	0.23± 0.06	0.19± 0.05
	ϕ_{F_1}	3.92± 0.75	4.44± 0.98	1.71± 0.29	4.97± 0.30
	F_2	0.56± 0.13	0.50± 0.13	0.18± 0.05	0.18± 0.04
	ϕ_{F_2}	5.46± 0.66	5.55± 0.72	2.82± 0.35	6.23± 0.38
$\Lambda(1520)\pi^+$	H_1	0.00	0.14± 0.16	0.05± 0.06	0.05± 0.05
	ϕ_{H_1}	0.00	1.02± 1.57	4.57± 1.12	4.48± 1.04
	H_2	0.00	0.48± 0.08	0.18± 0.04	0.16± 0.03
	ϕ_{H_2}	0.00	3.93± 0.79	1.19± 0.30	1.23± 0.32
Nonresonant	N_{++}	0.08± 0.53	0.36± 0.36	0.13± 0.14	0.10± 0.16
	$\phi_{N_{++}}$	6.22± 4.78	6.21± 1.42	3.48± 0.99	3.96± 1.19
	N_{+-}	2.96± 0.33	2.68± 0.34	1.00	1.00
	$\phi_{N_{+-}}$	2.37± 0.68	2.74± 0.82	0.00	0.00
	N_{-+}	0.15± 0.53	0.16± 0.36	0.06± 0.14	0.01± 0.57
	$\phi_{N_{-+}}$	1.84± 2.47	3.05± 2.44	6.60± 2.14	1.31± 3.32
	N_{--}	0.17± 0.58	0.54± 0.49	0.20± 0.21	0.11± 0.21
	$\phi_{N_{--}}$	6.18± 5.18	4.98± 0.94	2.25± 1.06	2.46± 1.85
Polarization	$\mathbf{P}_{\Lambda_c}$	0.03± 0.16	-0.08± 0.14	-0.08± 0.14	-0.09± 0.14
# Signal Evnts	n_s	886.40	886.40	886.40	950.71± 38.35
# Bgrnd Evnts	n_b	1384.10	1384.10	1384.10	1319.79± 42.87
Bgrnd Quad Term	b_q	-12.67	-12.67	-12.67	-0.10± 10.60
Bgrnd Linear Term	b_l	1.32	1.32	1.32	1.33± 0.48
Mass$_{\Lambda_c}$ (GeV/c^2)	m_0	2.29	2.29	2.29	2.29± 0.00
Width$_{\Lambda_c}$ (MeV/c^2)	σ_l	0.00	0.00	0.00	20.27± 4.88
Width$_{\Lambda_c}$ (MeV/c^2)	σ_c	9.89	9.89	9.89	9.33± 0.56

Table I.1: The result of the MINUIT fits. Note that Fit 2a is the same as Fit 2b except for the fixed variable. The mass and width of the resonances used in the fits were those given by the PDG. In Fit 3, the width of the Λ_c peak $= \sigma = \sigma_l x_F + \sigma_c$.

	Fit 1	Fit 2a	Fit 2b	Fit 3
FCN_1	21086.43	21042.35	21042.35	
FCN_2	-8515.95	-8515.95	-8515.95	
$\mathrm{FCN}_{\mathrm{total}}$	12571.61	12526.40	12526.40	12494.78
$\chi^2 : m^2_{\mathrm{K}\pi}$	49.8	36.7	36.7	35.9
$\chi^2 : m^2_{\mathrm{p}\pi}$	47.1	42.8	42.8	40.9
$\chi^2 : m^2_{\mathrm{pK}}$	64.2	53.3	53.3	59.0
$\chi^2 : cos(\theta_{\mathrm{p}}]$	37.2	37.4	37.4	36.6
$\chi^2 : \phi_{\mathrm{p}}$	41.8	43.2	43.2	40.1
$\chi^2 : \phi_{\mathrm{K}\pi}$	47.2	46.9	46.9	45.4
χ^2: sum_1	233.5	216.0	216.0	212.6
DOF_1	231	227	227	
$\chi^2 : m(\mathrm{pK}\pi)$	58.9	58.9	58.9	64.5
$\chi^2 : sum_{\mathrm{total}}$	292.4	274.9	274.9	277.1
$\mathrm{DOF}_{\mathrm{total}}$	275	271	271	270

Table I.2: The result of the MINUIT fit. χ^2 sum_1 was found by taking $\frac{2}{3}$ the sum of the first 3 values plus the sum the of the next 3. Each of the first 6 χ^2's was found by comparing the model and real histograms spread out over 50 bins. FCN_1 and DOF_1 are the MINUIT FCN value and the degrees of freedom, respectively, for the fit without the mass plot fit. FCN_2 is the MINUIT FCN value for the mass plot separately. Fit 3 incorporated the mass plot fit and the Λ_c width dependence on x_F into the total fit, therefore there is no FCN_1, FCN_2, or DOF_1.

The values which are displayed in table I.1 along with the covariant matrix generated by MINUIT, give us the fit fraction for each decay, as seen in table I.3. The errors on fit fraction k were calculated by $E_k = \sqrt{\sum_{ij} \frac{df_k}{dx_i}\frac{df_k}{dx_j} V_{ij}}$ where f = f($\vec{x}$) = the fit fraction (as described in equation 2.30 on page 13), x_i is the i^{th} element of $\vec{x}$, and V_{ij} is an element from the covariant matrix.

Mode	Fit 1 (%)	Fit 2a (%)	Fit 2b (%)	Fit 3 (%)
$\overline{\mathrm{K}}^{*0}$	19.5±2.6	18.9±2.5	18.9±2.5	17.9±2.5
Δ^{++}	16.4±3.3	17.7±3.1	17.7±3.1	15.9±2.8
$\Lambda(1520)$		7.3±1.7	7.3±1.7	6.7±1.6
Nonresonant	62.4±4.7	54.4±5.0	54.4±5.0	57.6±4.8

Table I.3: The Fit Fraction with statistical errors for the decay $\Lambda_c \to \mathrm{pK}\pi$ from the MINUIT fit.

I.3 Confidence

Subjecting the models to the permutation test used on the acceptance and background, we found the following confidence levels found in table I.4. In this table, "uniform" refers to a comparison of the model to a uniformly distributed set of points; "real" refers to a comparison of the model to the actual distribution of 2,271 points; and "self" refers to a comparison of the half of the model to the other half when split randomly into two equally sized sets.

model vs.	Fit 1 (%)	Fit 2a (%)	Fit 2b (%)	Fit 3 (%)
uniform	10.1±1.8	10.7±1.3	11.1±1.3	10.7±1.6
real	50.5±1.7	50.4±1.3	49.3±1.4	51.1±1.8
self	52.5±2.0	52.1±1.8	52.0±1.4	49.9±2.5

Table I.4: The Confidence of the MINUIT fits using the permutation test described earlier. In this table, “uniform” refers to a comparison of the model to a uniformly distributed set of points; “real” refers to a comparison of the model to the actual distribution of 2,271 points; and “self” refers to a comparison of the half of the model to the other half when split randomly into two equally sized sets.

Appendix J

Two Dimensional Tweaking

J.1 Two Dimensional Tweaking

Tweaking the nearest-neighbor acceptance to match the 2 dimensional distributions yields the results laid out over the next several pages. Note that we broke the plots into a 12 x 12 grid for matching. See figure J.1 for a scatter plot comparison.

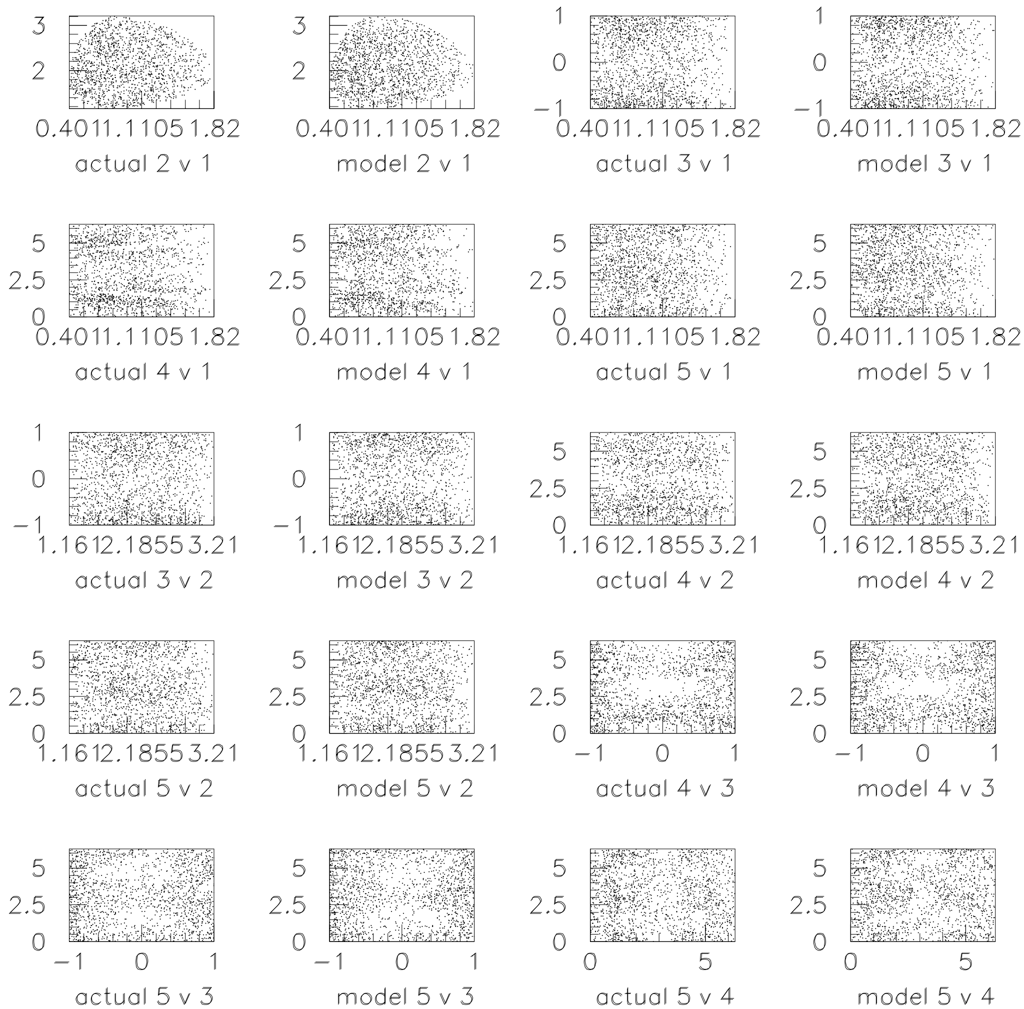

Figure J.1: The two dimensional projections of the Acceptance, where the numbers 1 - 5 represent the dimensions outlined in the beginning of an earlier section. Note that in order to keep the size of this plot reasonable for printing, we projected only around 15% of the real acceptance points to represent the total data set.

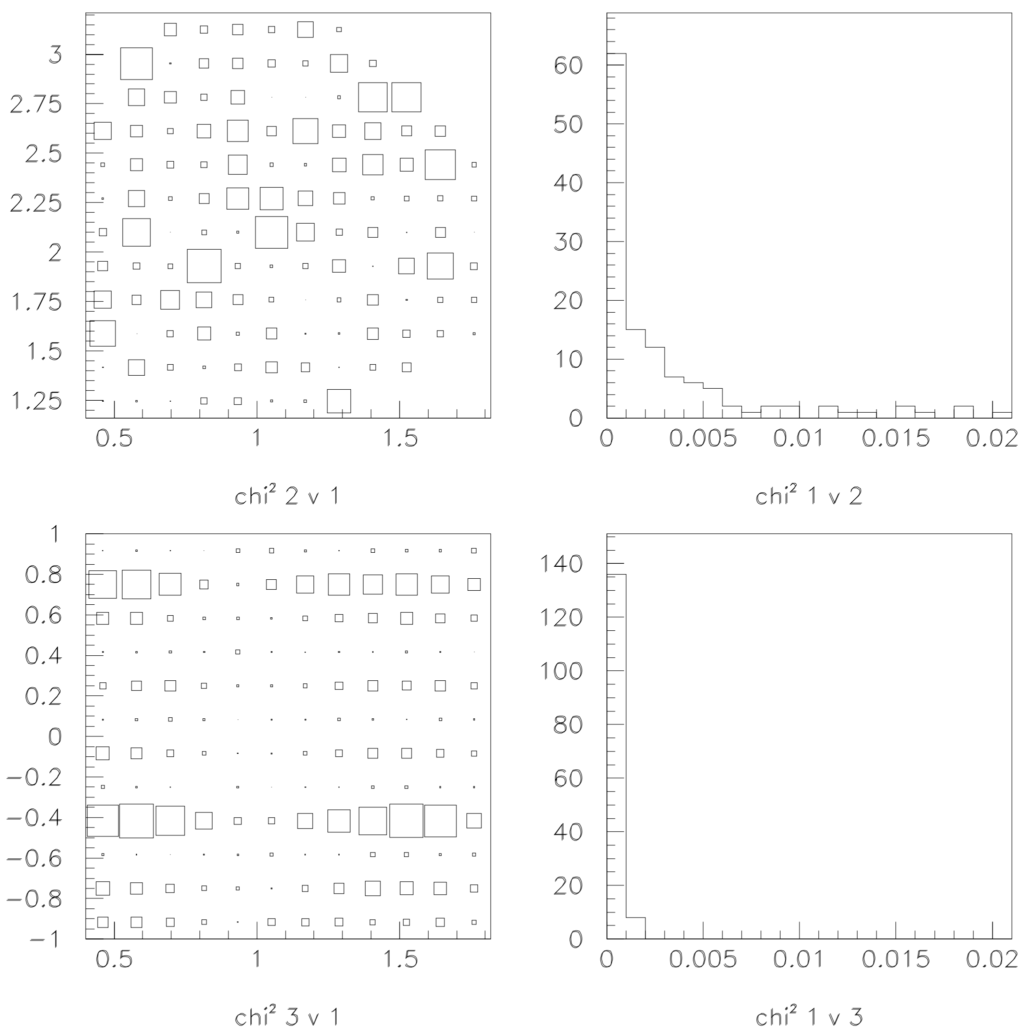

Figure J.2: Two Dimensionally Tweaked Acceptance vs. Model as seen by χ^2 representation.

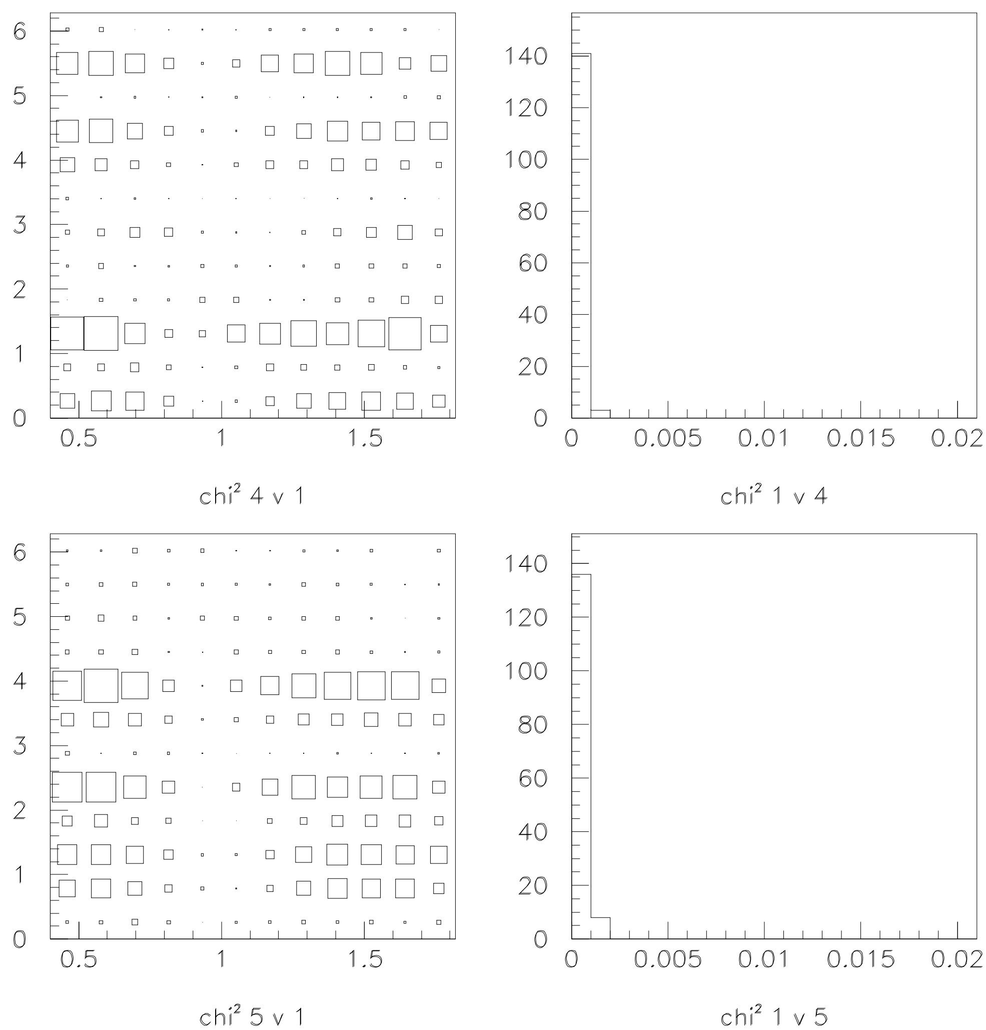

Figure J.3: Two Dimensionally Tweaked Acceptance vs. Model as seen by χ^2 representation.

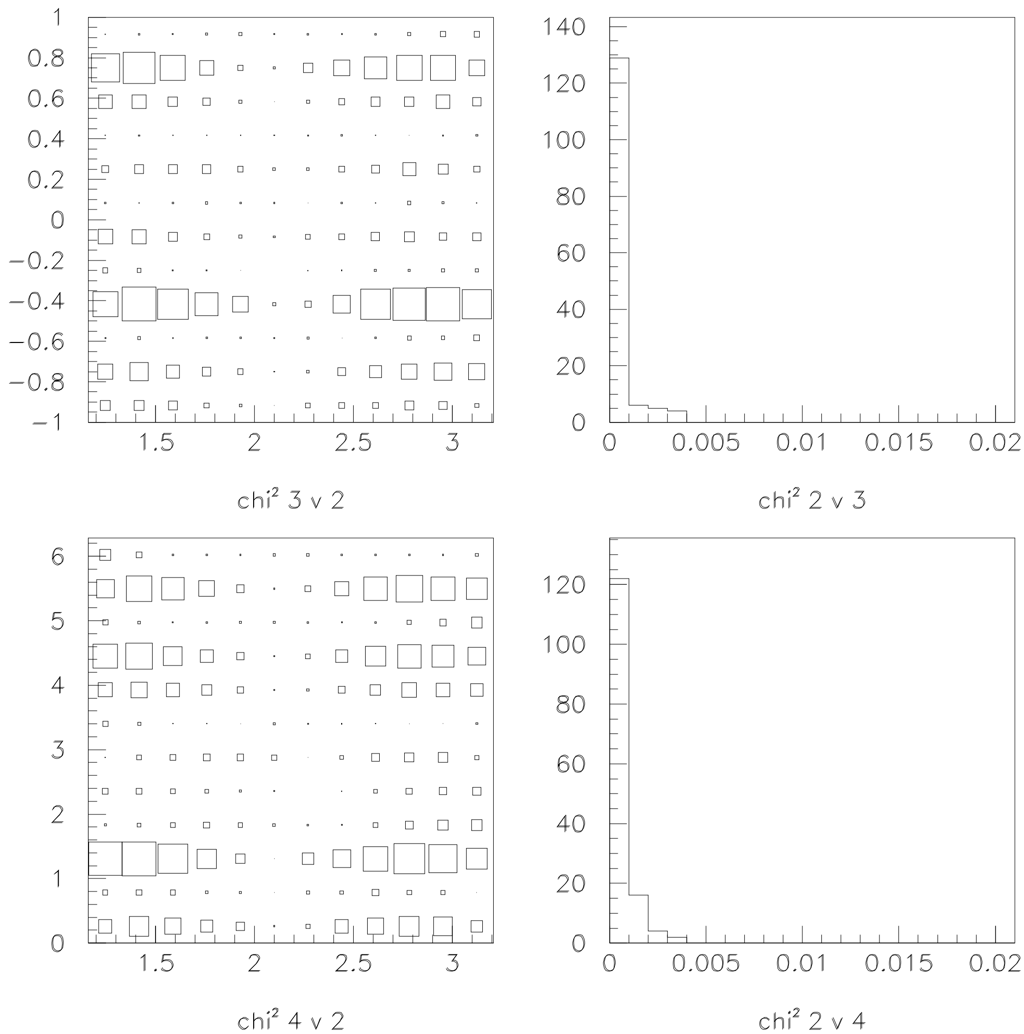

Figure J.4: Two Dimensionally Tweaked Acceptance vs. Model as seen by χ^2 representation.

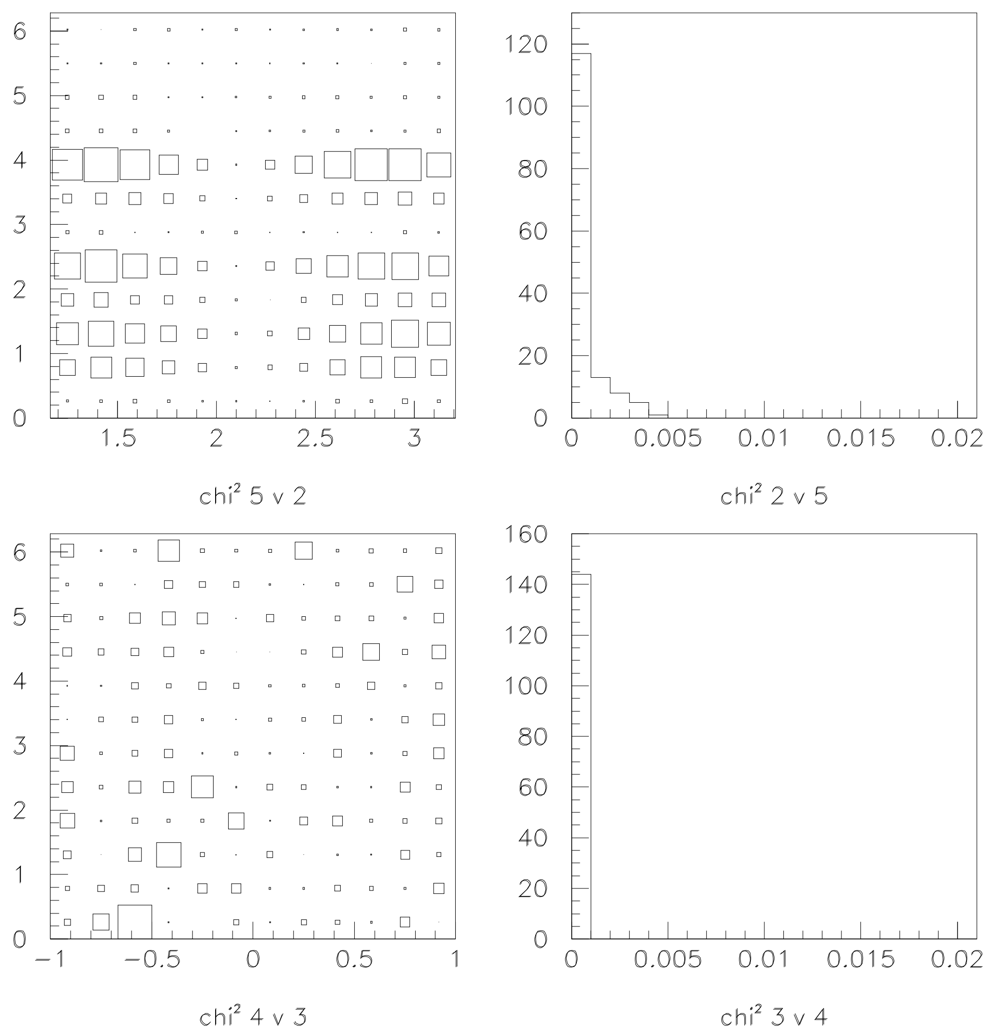

Figure J.5: Two Dimensionally Tweaked Acceptance vs. Model as seen by χ^2 representation.

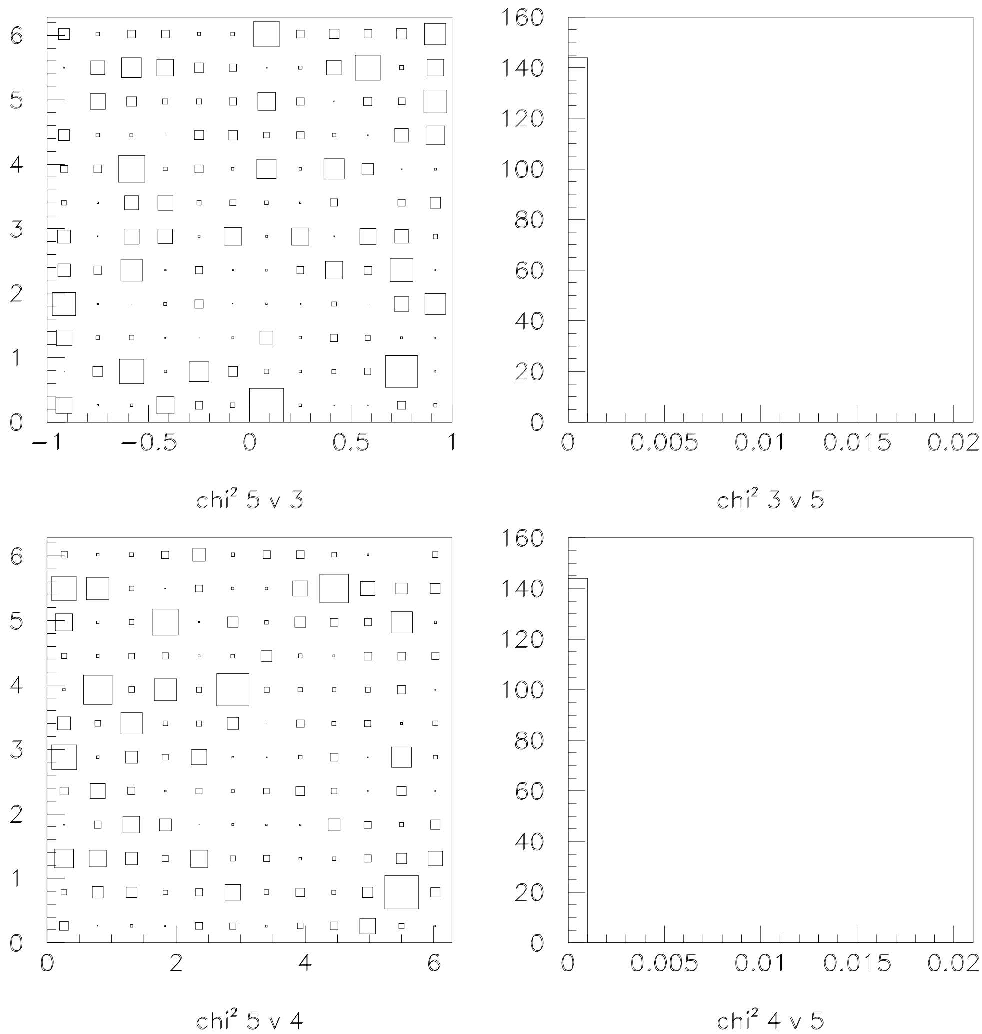

Figure J.6: Two Dimensionally Tweaked Acceptance vs. Model as seen by χ^2 representation.

Appendix K

Spin $\frac{1}{2}^-$

K.1 The Mysterious Spin $\frac{1}{2}^-$ Particle

We fit the data with a nonresonant, $\overline{\mathrm{K}}^{*0}$, Δ^{++}, and a spin $\frac{1}{2}$ particle resonance with a floating mass and width. See tables K.1 and K.2 for the converged mass and width.

$\downarrow L$; spin $\rightarrow$	$\frac{1}{2}^+$	$\frac{1}{2}^-$
0	m = 1.561±0.025 GeV/c^2 Γ = 0.337±0.113 GeV/c^2 FCN = 12418.75	1.565±0.021 GeV/c^2 0.332±0.086 GeV/c^2 12394.03
1	m = 1.540±0.021 GeV/c^2 Γ = 0.305±0.128 GeV/c^2 FCN = 12415.41	1.595±0.016 GeV/c^2 > 0.500 GeV/c^2 12396.25

Table K.1: Mass and width and MINUIT FCN value for the labeled spins and parity in a model of $\Lambda_c \rightarrow \mathrm{pK}\pi$ with $\mathrm{p}\overline{\mathrm{K}}^{*0}$, $\Delta^{++}\mathrm{K}^-$, nonresonant, and a spin $\frac{1}{2}$ particle + π modes of decay.

$\downarrow L$; spin $\rightarrow$	$\frac{1}{2}^+$	$\frac{1}{2}^-$
0	m = 1.522±0.015 GeV/c^2 Γ = 0.210±0.050 GeV/c^2 FCN = 12393.56	1.581±0.028 GeV/c^2 0.460±0.112 GeV/c^2 12380.28
1	m = 1.564±0.015 GeV/c^2 Γ > 0.500 GeV/c^2 FCN = 12403.33	1.589±0.018 GeV/c^2 > 0.500 GeV/c^2 12386.17

Table K.2: Mass and width and MINUIT FCN value for the labeled spins and parity in a model of $\Lambda_c \rightarrow \mathrm{pK}\pi$ with $\mathrm{p}\overline{\mathrm{K}}^{*0}$, $\Delta^{++}\mathrm{K}^-$, $\Lambda(1520)$, nonresonant, and a spin $\frac{1}{2}$ particle + π modes of decay.

For the subsequent displays, we chose to use the fit without the $\Lambda(1520)$ and with the spin $\frac{1}{2}^-$ and $L = 0$.

Mode	Fit 3 (%)	Fit 4 (%)
$\mathrm{p}\overline{\mathrm{K}}^{*0}(890)$	19.5±2.6	19.3±3.0
$\Delta^{++}(1232)\mathrm{K}^-$	18.0±2.9	16.7±3.0
$\Lambda(1520)\pi^+$	7.7±1.8	
spin $\frac{1}{2}^-$		40.1±7.2
Nonresonant	54.8±5.5	65.0±6.9

Table K.3: The decay fractions for $\Lambda_c^+ \to pK^-\pi^+$ with statistical errors from the final fit 3 and 4 (L=0, spin = $\frac{1}{2}^-$).

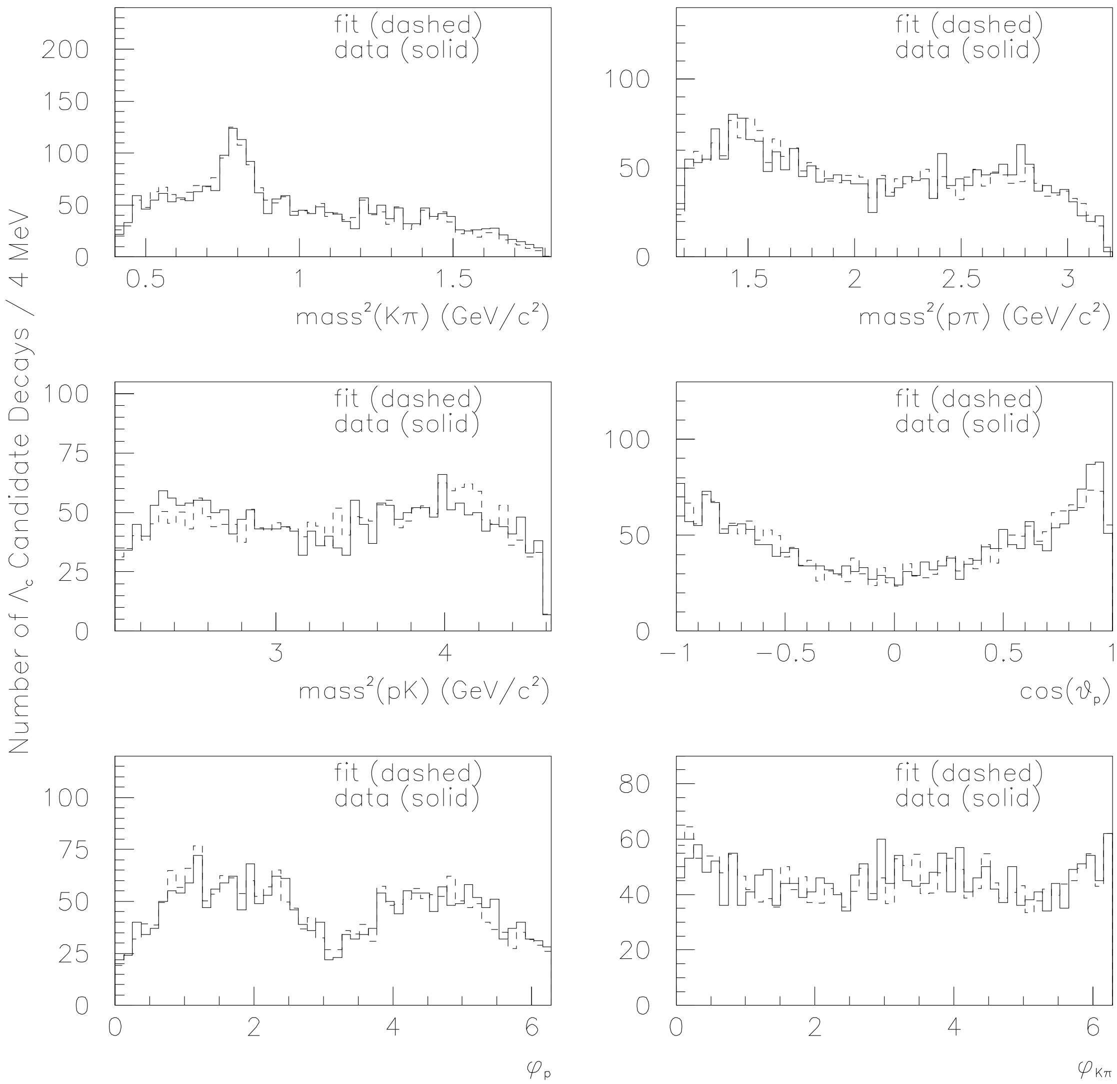

Figure K.1: The one dimensional projections of the new fit and real data.

K.2 $\Lambda(1405)$

There is also some evidence that the excess in the low pK mass range may be due to the upper tail of the $\Lambda(1405)$ resonance. Taking one dimensional projections of the data and subtracting background, correcting for acceptance, and dividing by phase space, we get the plots seen in figures K.2 and K.3. As can be seen in these plots there is an upward trend in the low pK mass range which can not be explained away by statistical fluctuations. Thus, there is some evidence that the upper end of the $\Lambda(1405)$ resonance is contributing to the Λ_c decay.

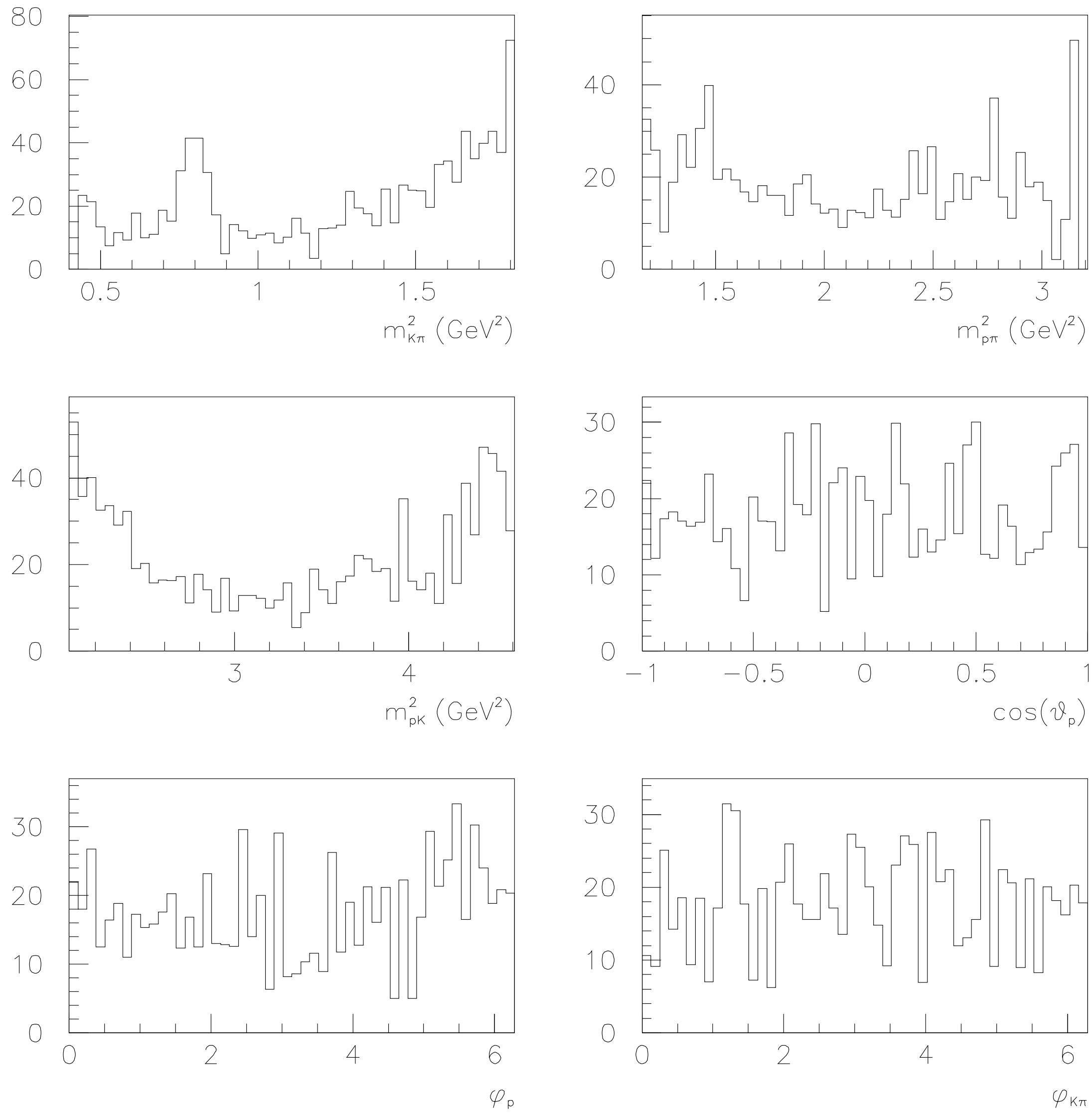

Figure K.2: One dimensional projections of $\Lambda_c \to pK\pi$ data after background subtraction, and acceptance and phase space corrections.

Taking this one step further, we fit the parameters with the $\pi\Lambda(1405)$ resonance mode present, assuming a relativistic Breit-Wigner without centrifugal barrier corrections. As explained in [PDG 98], there is still some debate as to the correct shape to use in describing this resonance, especially above

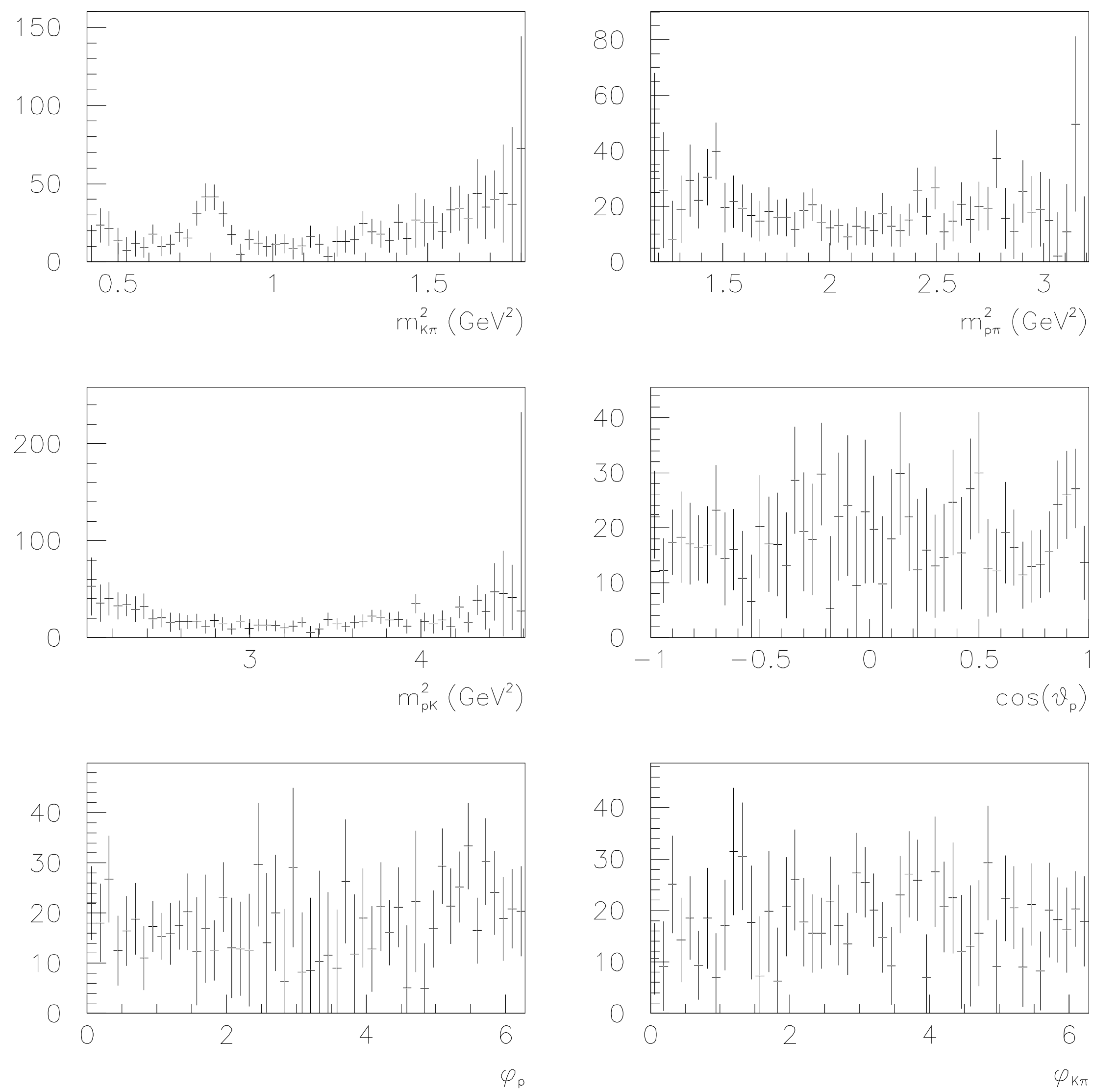

Figure K.3: One dimensional projections of $\Lambda_c \to pK\pi$ data after background subtraction, and acceptance and phase space corrections with error bars.

the pK threshold. See table K.4 for the listing of the parameters, table K.5 for a χ^2 comparison, and table K.6 for the fit fractions with this resonance mode present. For purposes of comparing, all of the models below used the naive relativistic Breit-Wigner.

Mode	Vrbl	Fit 3	Fit 4b	Fit 4c
$p\overline{K}^{*0}$	E_1	0.36± 0.05	0.37± 0.05	0.41± 0.07
	ϕ_{E_1}	3.65± 0.74	3.77± 0.60	4.31± 0.60
	E_2	0.17± 0.07	0.20± 0.05	0.24± 0.05
	ϕ_{E_2}	5.68± 0.67	0.71± 0.46	0.25± 0.56
	E_3	0.13± 0.06	0.01± 0.29	0.08± 0.09
	ϕ_{E_3}	6.09± 0.58	2.70± 3.37	7.11± 0.96
	E_4	0.02± 0.05	0.00± 0.03	0.00± 0.23
	ϕ_{E_4}	1.04± 2.11	5.43± 4.37	5.47± 4.72
$\Delta^{++}K^-$	F_1	0.23± 0.05	0.23± 0.05	0.27± 0.06
	ϕ_{F_1}	1.67± 0.27	1.56± 0.28	1.63± 0.26
	F_2	0.18± 0.05	0.16± 0.04	0.14± 0.05
	ϕ_{F_2}	2.85± 0.32	3.17± 0.34	3.11± 0.34
$\Lambda(1520)\pi^+$	H_1	0.05± 0.06	0.07± 0.05	
	ϕ_{H_1}	4.61± 1.10	3.29± 0.74	
	H_2	0.18± 0.03	0.14± 0.03	
	ϕ_{H_2}	1.20± 0.29	1.33± 0.32	
$\Lambda(1405)\pi^+$	G_1		0.22± 0.04	0.15± 0.09
	ϕ_{G_1}		-0.96± 0.43	5.24± 0.54
	G_2		0.25± 0.05	0.38± 0.07
	ϕ_{G_2}		3.28± 0.32	2.60± 0.33
Nonresonant	N_{++}	0.13± 0.13	0.35± 0.14	0.33± 0.12
	$\phi_{N_{++}}$	3.42± 1.04	-1.67± 0.48	3.93± 0.49
	N_{+-}	1.00	1.00	1.00
	$\phi_{N_{+-}}$	0.00	0.00	0.00
	N_{-+}	0.07± 0.14	0.00± 0.15	0.23± 0.13
	$\phi_{N_{-+}}$	-0.07± 1.74	5.21± 4.91	0.27± 0.66
	N_{--}	0.20± 0.20	0.45± 0.15	0.57± 0.18
	$\phi_{N_{--}}$	2.37± 1.01	3.29± 0.33	2.89± 0.37
Polarization	$\mathbf{P}_{\Lambda_c}$	-0.09± 0.14	-0.33± 0.15	-0.08± 0.14
# Signal Evnts	n_s	951.25± 38.34	966.91± 36.64	960.01± 36.61
# Bgrnd Evnts	n_b	1319.25± 42.86	1303.59± 40.97	1310.49± 41.11
Bgrnd Quad Term	b_q	0.05± 10.62	3.97± 1.40	2.35± 1.40
Bgrnd Linear Term	b_l	1.33± 0.48	1.32± 0.46	1.33± 0.46
Mass_{Λ_c} (GeV/c^2)	m_0	2.29± 0.00	2.29± 0.00	2.29± 0.00
Width_{Λ_c} (MeV/c^2)	σ_l	20.38± 4.87	20.34± 4.81	20.46± 4.78
Width_{Λ_c} (MeV/c^2)	σ_c	9.31± 0.55	9.34± 0.54	9.27± 0.53

Table K.4: The result of the MINUIT fits. The width of the Λ_c peak $= \sigma = \sigma_l x_F + \sigma_c$.

	Fit 3	Fit 4b	Fit 4c
$\mathrm{FCN_{total}}$	12494.74	12429.86	12457.65
$\chi^2 : m^2_{\mathrm{K}\pi}$	35.8	26.9	32.8
$\chi^2 : m^2_{\mathrm{p}\pi}$	43.9	41.5	43.4
$\chi^2 : m^2_{\mathrm{pK}}$	58.1	44.6	51.8
$\chi^2 : cos(\theta_{\mathrm{p}}]$	36.9	37.4	37.7
$\chi^2 : \phi_{\mathrm{p}}$	40.2	39.6	39.5
$\chi^2 : \phi_{\mathrm{K}\pi}$	45.6	42.9	43.3
χ^2: sum_1	214.4	195.2	205.7
$\mathrm{DOF_{total}}$	270	266	270

Table K.5: The result of the MINUIT fit. χ^2 sum_1 was found by taking $\frac{2}{3}$ the sum of the first 3 values plus the sum of the next 3. Each of the first 6 χ^2's was found by comparing the model and real histograms spread out over 50 bins.

Mode	Fit 3 (%)	Fit 4b (%)	Fit 4c (%)
$\overline{\mathrm{K}}^{*0}$	18.5±3.7	17.8±4.1	19.7±4.8
Δ^{++}	17.2±4.1	15.6±4.2	15.9±4.9
$\Lambda(1520)$	7.1±2.1	4.8±1.8	
$\Lambda(1405)$		21.6±6.4	28.0±6.7
Nonresonant	55.4±2.2	65.1±4.7	62.7±6.3

Table K.6: The Fit Fraction with statistical errors for the decay $\Lambda_c \to \mathrm{pK}\pi$ from the MINUIT fit.

Appendix L

Čerenkov Systematic Error Data Tables

L.1 Progress of Kaon Efficiencies

	p_{T} (GeV)		
p (GeV)	0.0-0.4	0.4-0.6	0.6-
6-10	632.00	435.00	253.00
10-15	930.00	719.00	938.00
15-20	810.00	755.00	1263.00
20-25	648.00	698.00	1383.00
25-35	830.00	1104.00	2665.00
35-	866.00	1715.00	7447.00

Table L.1: Kaons from real D$\rightarrow$ K$\pi\pi$ data within the m(K$\pi\pi$) range of 1.84 GeV/c^2 - 1.92 GeV/c^2.

	p_{T} (GeV)		
p (GeV)	0.0-0.4	0.4-0.6	0.6-
6-10	546.00	266.00	71.00
10-15	497.00	366.00	205.00
15-20	352.00	284.00	251.00
20-25	227.00	206.00	235.00
25-35	283.00	286.00	407.00
35-	297.00	526.00	1437.00

Table L.2: Kaons from real D$\rightarrow$ K$\pi\pi$ data outside the m(K$\pi\pi$) range of 1.84 GeV/c^2 - 1.92 GeV/c^2.

	p_{T} (GeV)		
p (GeV)	0.0-0.4	0.4-0.6	0.6-
6-10	268.00	257.67	205.67
10-15	598.67	475.00	801.33
15-20	575.33	565.67	1095.67
20-25	496.67	560.67	1226.33
25-35	641.33	913.33	2393.67
35-	668.00	1364.33	6489.00

Table L.3: Background subtracted Kaons from real D→ K$\pi\pi$ data within the m(K$\pi\pi$) of 1.84 GeV/c^2 - 1.92 GeV/c^2.

	p_{T} (GeV)		
p (GeV)	0.0-0.4	0.4-0.6	0.6-
6-10	210.00	157.00	161.00
10-15	379.00	396.00	569.00
15-20	396.00	424.00	844.00
20-25	379.00	453.00	909.00
25-35	594.00	917.00	1899.00
35-	1154.00	2279.00	7889.00

Table L.4: Kaons from MC D→ K$\pi\pi$ data within the m(K$\pi\pi$) of 1.84 GeV/c^2 - 1.92 GeV/c^2.

	p_{T} (GeV)		
p (GeV)	0.0-0.4	0.4-0.6	0.6-
6-10	36.00	11.00	11.00
10-15	47.00	22.00	16.00
15-20	31.00	29.00	23.00
20-25	24.00	22.00	18.00
25-35	50.00	48.00	51.00
35-	107.00	187.00	534.00

Table L.5: Kaons from MC D→ K$\pi\pi$ data outside the m(K$\pi\pi$) of 1.84 GeV/c^2 - 1.92 GeV/c^2.

	p_{T} (GeV)		
p (GeV)	0.0-0.4	0.4-0.6	0.6-
6-10	186.00	149.67	153.67
10-15	347.67	381.33	558.33
15-20	375.33	404.67	828.67
20-25	363.00	438.33	897.00
25-35	560.67	885.00	1865.00
35-	1082.67	2154.33	7533.00

Table L.6: Background subtracted Kaons from MC D→ K$\pi\pi$ data within the m(K$\pi\pi$) of 1.84 GeV/c^2 - 1.92 GeV/c^2.

	p_{T} (GeV)		
p (GeV)	0.0-0.4	0.4-0.6	0.6-
6-10	118.59	127.94	58.62
10-15	332.66	325.06	391.96
15-20	348.20	361.27	700.08
20-25	223.79	321.08	754.72
25-35	225.32	427.02	1357.59
35-	166.71	418.39	1681.59

Table L.7: Surviving Kaons from real D→ K$\pi\pi$ data within the m(K$\pi\pi$) of 1.84 GeV/c^2 - 1.92 GeV/c^2 after NN cutcuts.

	p_{T} (GeV)		
p (GeV)	0.0-0.4	0.4-0.6	0.6-
6-10	44.48	27.38	8.89
10-15	87.02	72.88	42.45
15-20	67.03	64.32	75.15
20-25	36.61	39.24	73.87
25-35	45.30	51.09	93.25
35-	33.70	74.31	192.88

Table L.8: Surviving Kaons from real D→ K$\pi\pi$ data outside the m(K$\pi\pi$) of 1.84 GeV/c^2 - 1.92 GeV/c^2 after NN cutcuts.

	p_{T} (GeV)		
p (GeV)	0.0-0.4	0.4-0.6	0.6-
6-10	88.93	109.69	52.70
10-15	274.65	276.47	363.65
15-20	303.51	318.39	649.98
20-25	199.38	294.91	705.47
25-35	195.12	392.96	1295.42
35-	144.24	368.85	1553.01

Table L.9: Background subtracted Surviving Kaons from real D→ K$\pi\pi$ data within the m(K$\pi\pi$) of 1.84 GeV/c^2 - 1.92 GeV/c^2 after NN cutcuts.

	p_{T} (GeV)		
p (GeV)	0.0-0.4	0.4-0.6	0.6-
6-10	53.21	55.90	43.87
10-15	146.36	225.08	258.64
15-20	198.18	223.08	500.80
20-25	141.40	222.04	498.52
25-35	169.87	350.32	915.24
35-	152.90	301.30	931.49

Table L.10: Surviving Kaons from MC D→ K$\pi\pi$ data within the m(K$\pi\pi$) of 1.84 GeV/c^2 - 1.92 GeV/c^2 after NN cutcuts.

	p_{T} (GeV)		
p (GeV)	0.0-0.4	0.4-0.6	0.6-
6-10	6.24	3.45	1.81
10-15	16.89	10.41	6.76
15-20	9.96	16.54	13.80
20-25	10.68	10.37	8.73
25-35	12.86	22.40	21.40
35-	10.11	22.11	47.95

Table L.11: Surviving Kaons from MC D→ K$\pi\pi$ data outside the m(K$\pi\pi$) of 1.84 GeV/c^2 - 1.92 GeV/c^2 after NN cutcuts.

	p_{T} (GeV)		
p (GeV)	0.0-0.4	0.4-0.6	0.6-
6-10	49.05	53.60	42.67
10-15	135.10	218.14	254.13
15-20	191.54	212.06	491.60
20-25	134.28	215.13	492.70
25-35	161.30	335.39	900.97
35-	146.16	286.56	899.53

Table L.12: Background subtracted Surviving Kaons from MC D→ K$\pi\pi$ data within the m(K$\pi\pi$) of 1.84 GeV/c^2 - 1.92 GeV/c^2 after NN cutcuts.

L.2 Progress of Proton Efficiencies

	p_{T} (GeV)		
p (GeV)	0.0-0.6	0.6-0.9	0.9-
6-20	55372.00	21692.00	7983.00
20-30	9589.00	7817.00	6149.00
30-40	2868.00	2961.00	3223.00
40-50	811.00	1097.00	1427.00
50-	399.00	782.00	1457.00

Table L.13: The number of protons from Real $\Lambda \rightarrow p\pi$ data within the mass range of 1.1056 GeV/c^2 - 1.1264 GeV/c^2.

	p_{T} (GeV)		
p (GeV)	0.0-0.6	0.6-0.9	0.9-
6-20	11289.00	1676.00	497.00
20-30	1341.00	551.00	353.00
30-40	339.00	216.00	135.00
40-50	121.00	97.00	76.00
50-	73.00	94.00	106.00

Table L.14: The number of Background protons from Real $\Lambda \rightarrow p\pi$ data outside the mass range of 1.1056 GeV/c^2 - 1.1264 GeV/c^2.

	p_{T} (GeV)		
p (GeV)	0.0-0.6	0.6-0.9	0.9-
6-20	51405.59	21103.13	7808.38
20-30	9117.84	7623.41	6024.97
30-40	2748.89	2885.11	3175.57
40-50	768.49	1062.92	1400.30
50-	373.35	748.97	1419.76

Table L.15: The number of Background subtracted protons from Real $\Lambda \rightarrow p\pi$ data within the mass range of 1.1056 GeV/c^2 - 1.1264 GeV/c^2.

	p_{T} (GeV)		
p (GeV)	0.0-0.6	0.6-0.9	0.9-
6-20	21100.00	4849.00	2373.00
20-30	2894.00	1428.00	1642.00
30-40	947.00	536.00	842.00
40-50	277.00	250.00	412.00
50-	98.00	158.00	550.00

Table L.16: The number of protons from MC $\Lambda \rightarrow p\pi$ data within the mass range of 1.1056 GeV/c^2 - 1.1264 GeV/c^2.

	p_{T} (GeV)		
p (GeV)	0.0-0.6	0.6-0.9	0.9-
6-20	7052.00	1022.00	583.00
20-30	1098.00	434.00	470.00
30-40	347.00	169.00	274.00
40-50	102.00	69.00	156.00
50-	53.00	73.00	226.00

Table L.17: The number of Background protons from MC $\Lambda \rightarrow p\pi$ data outside the mass range of 1.1056 GeV/c^2 - 1.1264 GeV/c^2.

	p_{T} (GeV)		
p (GeV)	0.0-0.6	0.6-0.9	0.9-
6-20	18622.27	4489.92	2168.16
20-30	2508.22	1275.51	1476.86
30-40	825.08	476.62	745.73
40-50	241.16	225.76	357.19
50-	79.38	132.35	470.59

Table L.18: The number of Background subtracted protons from MC $\Lambda \rightarrow \mathrm{p}\pi$ data within the mass range of 1.1056 GeV/c^2 - 1.1264 GeV/c^2.

	p_{T} (GeV)		
p (GeV)	0.0-0.6	0.6-0.9	0.9-
6-20	14092.36	9925.62	4729.83
20-30	4677.40	5338.37	4461.11
30-40	1672.82	2180.50	2626.15
40-50	546.66	851.20	1240.01
50-	250.75	576.80	1085.30

Table L.19: The number of Surviving protons from Real $\Lambda \rightarrow \mathrm{p}\pi$ data within the mass range of 1.1056 GeV/c^2 - 1.1264 GeV/c^2 after NN cutcuts.

	p_{T} (GeV)		
p (GeV)	0.0-0.6	0.6-0.9	0.9-
6-20	1062.46	547.56	219.29
20-30	295.32	278.22	200.62
30-40	91.60	101.91	79.76
40-50	30.76	31.21	37.38
50-	10.93	27.56	35.89

Table L.20: The number of Surviving protons from Real $\Lambda \rightarrow \mathrm{p}\pi$ data outside the mass range of 1.1056 GeV/c^2 - 1.1264 GeV/c^2 after the NN cutcuts.

	p_{T} (GeV)		
p (GeV)	0.0-0.6	0.6-0.9	0.9-
6-20	13719.06	9733.23	4652.78
20-30	4573.64	5240.62	4390.62
30-40	1640.63	2144.70	2598.13
40-50	535.85	840.23	1226.87
50-	246.91	567.12	1072.69

Table L.21: The number of Surviving background subtracted protons from Real $\Lambda \rightarrow \mathrm{p}\pi$ data within the mass range of 1.1056 GeV/c^2 - 1.1264 GeV/c^2 after the NN cutcuts.

	p_{T} (GeV)		
p (GeV)	0.0-0.6	0.6-0.9	0.9-
6-20	3372.65	1754.74	1138.46
20-30	1095.33	753.41	956.58
30-40	425.11	281.09	532.11
40-50	130.86	142.62	262.11
50-	33.18	80.07	255.05

Table L.22: The number of Surviving protons from MC $\Lambda \to \mathrm{p}\pi$ data within the mass range of 1.1056 GeV/c^2 - 1.1264 GeV/c^2 after the NN cutcuts.

	p_{T} (GeV)		
p (GeV)	0.0-0.6	0.6-0.9	0.9-
6-20	676.23	254.23	171.86
20-30	329.27	210.71	220.34
30-40	135.23	98.16	151.15
40-50	43.94	35.22	81.82
50-	22.57	30.51	97.90

Table L.23: The number of Surviving background protons from MC $\Lambda \to \mathrm{p}\pi$ data outside the mass range of 1.1056 GeV/c^2 - 1.1264 GeV/c^2 after the NN cutcuts.

	p_{T} (GeV)		
p (GeV)	0.0-0.6	0.6-0.9	0.9-
6-20	3135.06	1665.41	1078.07
20-30	979.64	679.38	879.16
30-40	377.60	246.60	479.01
40-50	115.43	130.25	233.37
50-	25.25	69.35	220.65

Table L.24: The number of Surviving Background subtracted protons from MC $\Lambda \to \mathrm{p}\pi$ data within the mass range of 1.1056 GeV/c^2 - 1.1264 GeV/c^2 after the NN cutcuts.

Appendix M

Further Study

The amount of physics which can come from this research is not limited to the bulk of this dissertation. Other area of exploration include looking for other baryon decays, exploring the relationship between polarization of transverse momentum, or looking for CP violation.

M.1 Looking for $\Xi_c \to pK\pi$

Once the cuts were established, we looked for $\Xi_c \to pK\pi$, in order to determine the decay fraction for the two decays. See figure M.1.

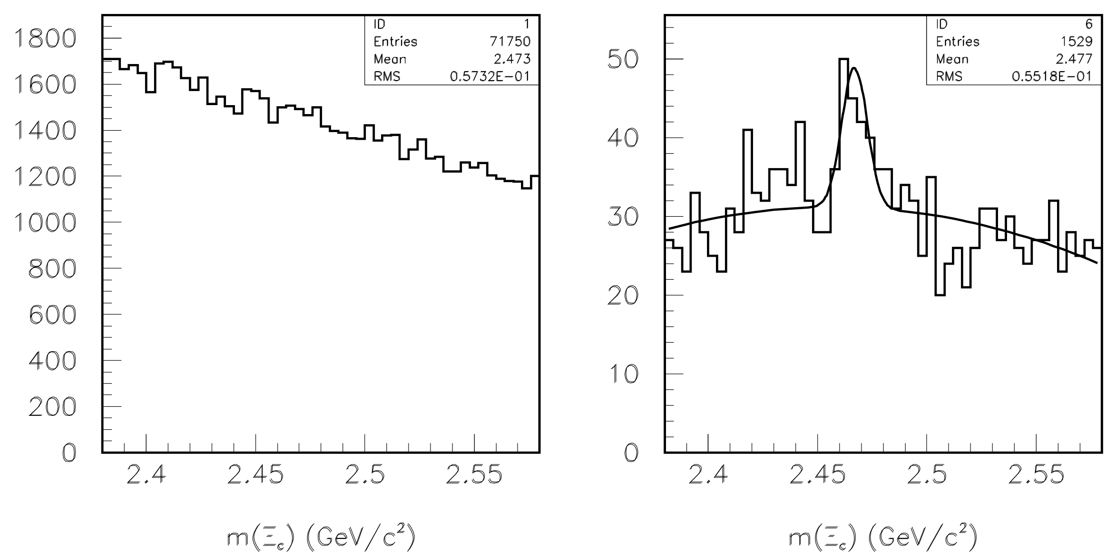

Figure M.1: (left) Mass($pK\pi$) of the Real data set before Neural Net cuts and (right) after. It has a significance of 3.07σ. There are 64 ± 21 signal events and 1464 background events assuming that the peak is Gaussian and the background is quadratic.

M.2 The Effect of Transverse Momentum and Feynman-x on Polarization

In order to determine if there is a relationship between the polarization of the Λ_c and the transverse momentum, p_T, of the Λ_c, we broke the data set into three divisions of p_T so that roughly the same number of events were in each division. These results can be seen in chapter 9. If we broke the p_T distribution into 4 bins with the boundaries seen in table M.1, we get the polarizations seen in figure M.2.

bin	1	2	3	4
p_T range (GeV/c^2)	0.00 - 0.60	0.60 - 0.95	0.95 - 1.43	1.43 - 5.20
$\overline{p}_T$ (GeV/c^2)	0.38	0.77	1.17	1.95
Number of events	568	568	568	567

Table M.1: Information on the bins of p_T.

Breaking the data set into bins of p_T and x_F (as seen in table M.2.

$\downarrow x_F/p_T \rightarrow$ $\overline{p}_T =$	0.00 - 0.71 0.45	0.71 - 1.24 0.96	1.24 - 5.21 1.80
-0.12 - 0.06 ($\overline{x}_F = 0.01$)	-0.03±0.41 249	-0.30±0.49 255	-0.87± 0.18 254
0.06 - 0.12 ($\overline{x}_F = 0.09$)	0.45±0.62 258	-0.77±0.45 246	-0.56±0.29 253
0.12 - 0.59 ($\overline{x}_F = 0.19$)	0.04±0.38 251	-0.01±0.44 256	-0.44±0.42 249

Table M.2: Polarization in the 9 bins of x_F and p_T. The number under the polarization is the number of events in that particular bin.

M.3 CP violation

In theory, CP violation can be checked using this helicity technique, however statistics prevents any meaningful contribution. By dividing the data sample into Λ_c and $\overline{\Lambda}_c$, one can look for patterns. See table M.3 for a listing of the parameters. Note that the FCN value as found by MINUIT are similar for each of the similarly polarized data sets. Although the lower FCN value, for example, for the Λ_c fit indicates the better fit, those FCN values are close enough to make me wonder if there is even a better fit. (The Breit-Wigner amplitude used is the uncorrected relativistic formula seen in equation 2.28.)

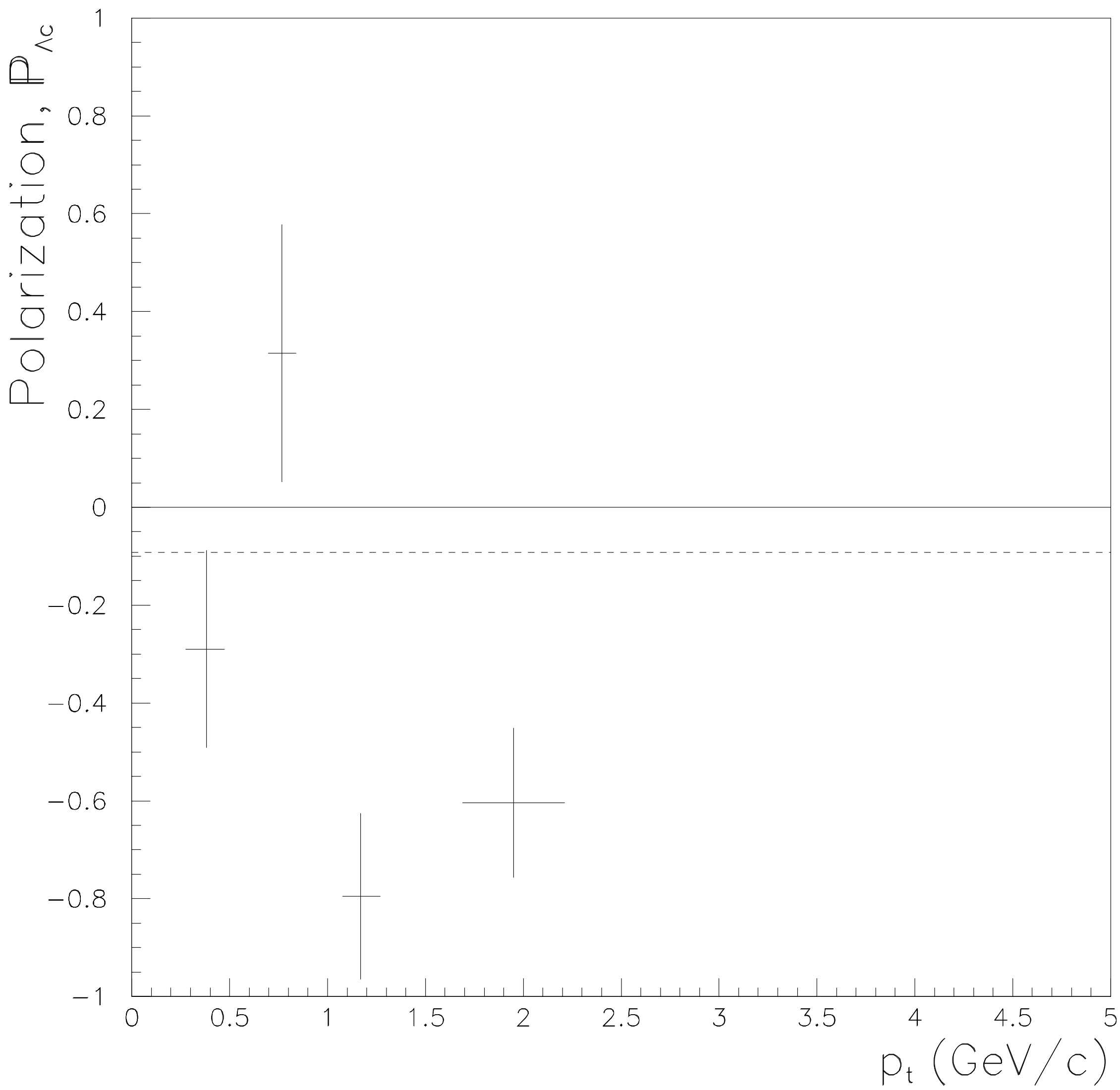

Figure M.2: The polarization of the Λ_c as a function of the Λ_c's transverse momentum. The vertical bars represent the error as found by MINUIT. They are placed at the average p_T value for that region. The horizontal bars represent the standard deviation of p_T from the mean for each particular bin. The dotted line represents the value of the polarization when it was assumed constant for all data events.

	Λ_c	Λ_c	$\overline{\Lambda}_c$	$\overline{\Lambda}_c$
FCN	6130.550	6130.956	6402.190	6404.198
E_1	0.18± 0.10	0.47± 0.09	0.51± 0.28	0.15± 0.11
ϕ_{E_1}	2.68± 0.81	0.14± 0.55	1.21± 0.86	2.94± 0.73
E_2	0.11± 0.07	0.16± 0.10	0.00± 0.36	0.22± 0.10
ϕ_{E_2}	0.00± 0.72	5.78± 0.91	4.74± 4.69	6.25± 0.55
E_3	0.08± 0.06	0.22± 0.08	0.43± 0.21	0.12± 0.14
ϕ_{E_3}	6.94± 0.92	-0.95± 0.42	6.08± 0.57	3.54± 1.12
E_4	0.15± 0.07	0.09± 0.07	0.43± 0.22	0.45± 0.15
ϕ_{E_4}	1.71± 0.56	0.87± 0.71	2.40± 0.70	4.45± 0.59
F_1	0.14± 0.08	0.27± 0.08	0.00± 0.24	0.30± 0.09
ϕ_{F_1}	1.94± 0.44	1.97± 0.27	0.83± 4.69	5.21± 0.50
F_2	0.13± 0.06	0.23± 0.09	0.55± 0.27	0.25± 0.13
ϕ_{F_2}	2.19± 0.77	3.39± 0.42	0.71± 0.76	2.66± 0.43
H_1	0.02± 0.04	0.16± 0.07	0.27± 0.17	0.24± 0.09
ϕ_{H_1}	4.75± 1.98	3.84± 0.64	5.27± 0.71	1.02± 0.47
H_2	0.10± 0.05	0.12± 0.06	0.29± 0.15	0.15± 0.10
ϕ_{H_2}	0.71± 0.66	1.53± 0.48	0.10± 0.78	2.28± 0.74
N_{++}	0.36± 0.35	0.08± 0.13	0.96± 0.59	0.53± 0.31
$\phi_{N_{++}}$	4.16± 1.03	3.12± 1.47	2.31± 0.83	4.42± 0.49
N_{+-}	1.00	1.00	1.00	0.14± 0.18
$\phi_{N_{+-}}$	0.00	0.00	0.00	3.31± 1.13
N_{-+}	0.17± 0.13	0.00± 1.34	0.32± 0.28	1.00
$\phi_{N_{-+}}$	1.66± 0.64	2.80± 5.07	4.61± 0.82	0.00
N_{--}	0.12± 0.12	0.74± 0.54	0.97± 0.53	0.54± 0.33
$\phi_{N_{--}}$	1.65± 0.76	4.00± 0.65	0.69± 0.61	2.91± 0.59
$\mathbf{P}_{\Lambda_c}$	-0.73± 0.23	0.50± 0.22	-0.53± 0.16	0.24± 0.23
n_s	488.14± 26.91	487.20± 25.76	422.68± 25.33	427.64± 26.94
n_b	638.36± 29.57	639.30± 28.55	720.82± 30.65	715.86± 31.84
b_q	-6.01± 14.01	-6.03± 1.41	-10.61± 1.41	-8.79± 13.48
b_l	1.83± 0.68	1.83± 0.60	0.96± 0.56	0.94± 0.63
m_0	2.29± 0.00	2.29± 0.00	2.29± 0.00	2.29± 0.00
σ_l	11.72± 6.62	11.38± 6.50	21.89± 6.62	21.86± 6.59
σ_c	9.05± 0.77	9.02± 0.75	8.98± 0.77	9.12± 0.80

Table M.3: Parameter values for Λ_c and $\overline{\Lambda}_c$.

Bibliography

[Ait 98] E. M. Aitala, et al. *A Search for D^0-$\overline{D}^0$ Mixing and Doubly-Cabibbo-Suppressed Decays of the D^0 in Hadronic Final States*. **Physical Review D** 57, 13 (1998).

This outlined the basics of the detector of E791.

[Ait 97] E. M. Aitala, et al. *The Doubly Cabibbo-Suppressed Decay* $D^+ \rightarrow K^+\pi^-\pi^+$. **Physical Letters B** 404, 187-193 (1997).

A Dalitz plot analysis.

[Alc 93] Vicens Gaitan Alcalde. *Neural Networks in high Energy Physics: From Pattern Recognition to Exploratory Data Analysis*. Doctoral Dissertation. November 1993.

This dissertation does more exploration of Neural Networks. It also goes into more detail of using Neural Networks for probability density estimation.

[Ama 93] S. Amato, et al. *The E791 Parallel Architecture Data Acquisition System*. **Nuclear Instruments and Methods in Physics Research** A324, 535-542 (1993).

This gave the gory details of how the information from the detector was processed. It also sketched out how the detector was set up.

[Anj 93] J.C.Anjos, et al. *Dalitz plot analysis of D→* $K\pi\pi$ *decays*. **Physical Review D** 48, 1 (1 July 1993).

This sketches out the basic technique of Dalitz plot analyses.

[Anj 90] J.C.Anjos, et al. *Study of decays of the* Λ_c^+. **Physical Review D** 41, 3 (1 February 1990).

This provided me with some historical background into other studies that have been done on the Λ_c^+.

[App 92] J.A.Appel. *Hadroproduction of Charm Particles*. **Annual Review of Nuclear and Particle Science** 42, 367-399 (1992).

This is a good overview of the previous 18 years of charm physics research. It's nice as a comparison of the experiments.

[App 86] J.A.Appel, P.M.Mantsch, M.M.Streetman, and R.M.Robertson. *Hadron Calorimetry at the Fermilab Tagged Photon Spectrometer Facility*. **Nuclear Instruments and Methods in Physics Research A** 243, 361-373 (1986).

A detailed explanation of the Calorimeters used in the experiment.

[Ast 88] D. Aston, et al. *A Study of* $\mathrm{K}^{-}\pi^{+}$ *Scattering in the Reaction* $\mathrm{K}^{-}\mathrm{p} \rightarrow \mathrm{K}^{-}\pi^{+}\mathrm{N}$ *at 11 GeV/c* **Nuclear Physics B** 296, 493 (1988).

I got the r_0 for $\overline{\mathrm{K}}^{*0}$ from this.

[Bar 87] D. Bartlet, et al. *Performance of the Cherenkov Counters in the Fermilab Tagged Photon Spectrometer Facility.* **Nuclear Instruments and Methods in Physics Research A** 260, 55-75 (1987).

This article explained how the Cerenkov detectors worked.

[Bas 81] M. Basile, et al. *A Measurement of Two Resonant Contributions in the* Λ_c^+ *Branching Ratios.* **Nuovo Cimento** 62A, 14 (1981).

An early work in the study of the $\Lambda_c^+ \rightarrow \mathrm{pK}^{-}\pi^{+}$ resonant substructures. It is hard to believe any conclusions were made with the poor data that this group had. It was superseded by [Boz 93].

[Bea 91] R. Beale and T. Jackson. **Neural Computing: An Introduction**. Adam Hilger, Bristol, 1991.

This book, in conjunction with [Bis 95, Smi 93], was invaluable in my understanding of Neural Networks. Of the three books, this one gives the most fundamental foundation on the subject.

[Bis 95] Christopher M. Bishop. **Neural Networks for Pattern Recognition**. Clarendon Press, Oxford, 1995.

This book, with [Bea 91, Smi 93], was very helpful in understanding neural nets. Of the books cited, it was the most thorough treatment of the subject.

[Bjo 89] James D. Bjorken. *Spin-dependent Decays of the* Λ_c. **Physical Review D** 40, 5 (1 September 1989).

A background paper for [Pur 96].

[Boz 93] A. Bozek, et al. *A Study of* Λ_c^+ *decays into* $\mathrm{pK}^{-}\pi^{+}$, $\mathrm{pK}^{-}\pi^{+}\pi^{0}$, *and* $\mathrm{pK}^{-}\pi^{+}\pi^{0}\pi^{0}$. **Physics Letters B** 312, 247-252 (1993).

This was the definitive paper up to now on the branching fractions of $\Lambda_c^+ \rightarrow \mathrm{pK}^{-}\pi^{+}$.

[Bra 96] Steve Bracker, et al. *A Simple Multiprocessor Management System for Event-Parallel Computing.* **IEEE Transactions in Nuclear Science** NS-43, 2457 (1996).

The definitive reference for the E791 data acquisition system.

[Bue 90] David J. Buerger. **Latex for Engineers and Scientists**. McGraw-Hill Publishing Company, New York, 1990.

This book, with [Lam 94, Shu 94], was invaluable in my writing this dissertation.

[Cha 84] G. Charpak and F. Sauli. *High-Resolution Electronic Particle Detectors.* **Annual Review of Nuclear Science**, Volume 34, 1984 in [Fer 91]

This gave the background of how SMD's work.

[Cor 75] M. J. Corden, et al. *An Analysis of the Λ(1520) Observed in a K^- Neutron Production Experiment*. **Nuclear Physics B** 84, 306 (1975).

This paper gave one of the forms of the corrected width in the Breit-Wigner amplitudes.

[Cus 84] Priscilla B. Cushman. *Electromagnetic and Hadronic Calorimeters* in [Sau 92].

This tells how the calorimeters work.

[Dha 96] W.G.D.Dharmaratna and Gary R. Golstein. *Single Quark Polarization in Quantum Chromodynamics Subprocesses*. **Physical Review D** 53, 1073 (1 February 1996).

This paper develops the polarization dependence on transverse momentum and the Feynman x.

[Dun 98] Isard Dunietz. *Heavy Baryon Production and Decay.* **Physical Review D** 58, 094010 (22 September 1998).

A theoretical paper.

[E791] E791 Collaboration. *Study of Production and Decay of Charmed Particles Produced Using a 500 GeV Pi Minus Beam at the Fermilab Tagged Particle Spectrometer* **http://fnphyx-www.fnal.gov/experiments/e791/welcome.html**, 1998.

This is the official website for E791 from where I got figure of the detector

[Fer 91] T. Ferbel, ed. **Experimental Techniques in High Energy Nuclear and Particle Physics** World Scientific, Singapore, 1991.

This book gave detail on many current detectors. It was quite valuable in writing the chapter on the E791 detector.

[Fra 94] E687 Collaboration, P. L. Frabetti *et al.*, Phys. Lett. **B331**, 217 (1994).

This paper outlined the corrected Breit-Wigner formula which we used.

[Fre 68] A.P.French. **Special Relativity**. W.W.Norton & Company, New York, 1968.

An excellent reference on special relativity. Most is understandable to anyone with a good precalculus background, though calculus would help in a few places. Also note that A.P.French once taught a University of South Carolina, Columbia.

[Fro 79] A. G. Frodesen, O.Skjeggestad, H. Tofte. **Probability and Statistics in Particle Physics**. Universitetsforlaget, Bergen, 1979.

This is the most useful book I used. I had it with me for most of the dissertation.

[Gla 91] Sheldon Glashow. **The Charm of Physics**. AIP, New York, N.Y., 1991.

This gave a overview of the theory underlying QED and QCD. Although I found the section on elementary particles good for the layman, I found the section on grand unification to be quite over the layman's head. If you make it through his introduction in this section, the subsequent subsections do clarify some of the points, but it would help to have an elementary physics understanding of QED and QCD.

[Hab 94] Howard E. Haber. *Spin Formalism and Applications to New Physics Searches.* **HEP-PH-9405376** (April 1994).

This paper gives another look at the helicity formalism.

[Hei 96] Jaret Heise. *Studies of Helium-Based Gas Mixtures Using a Small Cell Drift Chamber.* **http://www.physics.ubc.ca/~jaret/Thesis/Thesis.html**, 1996.

This is an excerpt from his Masters Thesis. It is a clearly written piece on Drift Chambers.

[Iva 98] M.A.Ivanov, J.G.Körner, V.E.Lyubovitskij, and A.G.Rusetsky. *Exclusive Nonleptonic Decays of Bottom and Charm Baryons in a Relativistic Three-Quark Model: Evaluation of Non-factorizing Diagrams.* **Physical Review D** 57, 5632 (1 May 1998).

A theoretical paper.

[Jac 59] M. Jacob and G. C. Wick. *On the General Theory of Collisions for Particles with Spin.* **Annals of Physics** 7, 404-428 (1959).

This is good for background on [Pur 96].

[Jam 81] F. James. *Determining The Statistical Significance of Experimental Results.* Lectures presented at 1980 CERN School of Computing. (13 February 1981).

This text discusses the comparison of multidimensional distributions.

[Kal 64] Gunnar Källén. **Elementary Particle Physics**. Addison-Wesley Publishing Company, Inc. Reading, Massachusetts. 1964.

This gives more detail than [Per 87] on Dalitz plot analyses.

[Koc 80] R. Koch and E. Pietarinen. *Low Energy πN Partial Wave Analysis.* **Nuclear Physics A** 336, 331 (1980).

I got the r_0 for Δ^{++} from this.

[Kor 94] J.G.Körner, M.Krämer, and D.Pirjol. *Heavy Baryons.* **Progress in Particle and Nuclear Physics** 33, 787 (1994).

A theoretical paper.

[Kor 91] J.G.Körner and H.W.Siebert. *Charm Baryons: Theory and Experiment.* **Annual Review of Particle Science 1991** 41, 511-45 (1991).

More background for [Pur 96].

[Kwa 95] Simon Kwan. *Collaboration Memo offline_doc_196.ps.* 21 November 1994. last revision 13 March 1995.

This memo sketches out the cuts Simon used for his analysis of Λ_c.

[Lam 94] Leslie Lamport. **Latex: A Document Preparation System: User's Guide and Reference Manual**. Addisson-Wesley Publishing Company, Reading, MA, 1994.

This book, with [Bue 90, Shu 94], was invaluable in my writing this dissertation.

[Les 96] Judy Leslie. *Probing Hadroproduction Processes with Charm Meson pairs from 500 GeV π^- Interactions*. Doctoral Dissertation. University of California at Santa Cruz. 1996.

A good source for background on E791.

[Nag 76] M. M. Nagels, et al. *Physics Data*. **Nuclear Physics B** 109, 1-90 (1976).

This source is a "Compilation of Coupling Constants and Low-Energy Parameters". This, in conjunction with [Pil 67, Pil 79], described the corrected Breit-Wigner shape to be used.

[PDG 98] Particle Data Group. *Review of Particle Physics*. **European Physical Journal C** Volume 3, Number 1-4, 1998.

This source is invaluable for the details of current knowledge of each elementary particle and a general overview of detectors, etc.

[Pei 92] Anna Peisert. *Silicon Microstrip Detectors*. in [Sau 92].

This (in conjunction with [Cha 84] have been quite good in detailing how SMD's work. This article, though, more than [Cha 84] gives more math detail on the Physics.

[Per 95] Lalith P. Perera. *An Experimental Study of the Cabibbo Suppressed Decay* $\mathrm{D}^0 \to \mathrm{K}^+\mathrm{K}^-\pi^+\pi^-$. Doctoral Dissertation. University of Cincinnati. November 1995.

A good background source on E791.

[Per 87] Donald H. Perkins. **Introduction to High Energy Physics**. Addison-Wesley Publishing Company, Inc., Menlo Park, California, 1987.

This outlines the basics of meson Dalitz plot analyses.

[Per 74] Martin Perl. **High Energy Hadron Physics**. John Wiley & Sons, Inc., New York, 1974.

Another basic textbook on the title subject.

[Pet 93] Carsten Peterson, Thorsteinn Rögnvaldsson, and Leif Lönnblad. *JETNET 3.0 - A Versatile Artificial Neural Network Package manual*. CERN-TH.7135/94, December 1993.

This is the manual for the Neural Net software package I used. I briefly hits the highlights of the basics for nets, but it does not go into much detail about the how's and why's. [Bea 91, Smi 93, Bis 95] are better references for background (in that order).

[Pil 79] Harmut Pilkuhn. **Relativistic Particle Physics**. Springer-Verlag, New York, 1979.

A good source, in conjunction with [Nag 76, Pil 67], on the corrected the Breit-Wigner shape.

[Pil 67] Harmut Pilkuhn. **The Interactions of Hadrons**. John Wiley & Sons, Inc., New York, 1967.

A more thorough treatment of the subject than [Per 74]

[Pur 96] Milind V. Purohit. *Collaboration Memo offline_doc_269.ps. Angular Dependence in Weak Decays of Charm Baryons*. memo to E791 collaboration. 5 January 1996.

This memo starts the detail of the calculations that are needed to be incorporated into the analysis of charm baryon decay.

[Row 66] Penelope A. Rowlatt. **Group Theory and Elementary Particles**. Longmans, Green, and Co., Ltd. London, 1966.

This has been quite good, so far, in explaining the connection of group theory and Physics. I would recommend it as a starting point for any graduate student in Physics.

[Sau 92] Fabio Sauli, ed. **Instrumentation in High Energy Physics**. World Scientific, Singapore, 1992.

This book, along with [Fer 91], has been instrumental in understanding how each part of the detector works.

[Shu 94] J. Kenneth Shultis. **Latex Notes: Practical Tips for Preparing Technical Documents**. P T R Prentice Hall, Englewood Cliffs, NJ, 1994.

This book, with [Bue 90, Lam 94], was invaluable in my writing this dissertation.

[Smi 93] Murray Smith. **Neural Networks for Statistical Modeling**. Van Nostrand Reinhold, New York, 1993.

This book, in conjunction with [Bea 91, Bis 95], was invaluable in my understanding of Neural Networks. This book was one step up in difficulty from [Bea 91].

[Tri 93] Arun Tripathi. *Collaboration Memo offline_doc_115.txt*. memo to E791 collaboration. 17 August 1993.

This memo provides the description of the stripping process.

[Upp 94] Taruni Uppal, R.C.Verma, and M.P.Khanna. *Constituent Quark Model Analysis of Weak Mesonic Decays of Charm Baryons* **Physical Review D** 49, 3417 (1 April 1994).

A theoretical paper.

[Wat 63] M. B. Watson, M Ferro-Luzzi, R. D. Tripp. *Analysis of* Υ_0^**(1520) and Determination of the* Σ *Parity*. **Physical Review** 131, 2248 (1963).

I got the r_0 for $\Lambda(1520)$ from this.

[Yos 96] Shoichi Yoshida. *Minutes of E791 Collaboration Meeting*. July 1996.

These notes discuss the questionable area involved in the experimental data.

Glossary

Acceptance	This is the phase space which is allowed by the physics and the detector. It is simulated by the surviving reconstructed Monte Carlo.
Anode	This is a positively charged wire. It is used in detectors to attract drifting electrons. See section 4.4.2 on page 29 for a more specific application.
Background	This is anything that is not what I want to study. It is the weeds of physics. It is simulated in this paper by data that is not under the signal region. See figure 6.6 on page 46 for the part of the data used for background.
Baryon	An elementary particle that is comprised of three quarks or three antiquarks. It, therefore, has a half-integral spin. For example, Λ_c, Δ^{++}. Also, because it has quarks, it will interact with the strong force and thus it is considered a hadron.
Boson	A particle or group of particles with an integral spin. Photons (light) and mesons are bosons.
Charge	A fundamental characteristic of a particle, which causes other charged particles to interact. It is symbolized by a + or -: For example, an electron has a charge of -1, and a proton has a charge of +1. In these units, all particles have integral charges, except for quarks, which have fractional charges.
Dalitz Plot	A display of three body decay used when studying meson decay. It is similar to the 1 vs. 2 plots in my analysis on page 72
E791	The name of the experiment which supplied the data. It was conducted at Fermilab from 1991 - 1992. See appendix A for the list of the members of the Collaboration. See chapter 4 for more detail on the equipment used.

Energy	The property of a system that is the measure of its capacity to do work. It is very important in the study of particles because it is a conserved quantity, i.e. the total energy of a closed system stays the same. It is often used interchangeably with the term "mass" in high energy physics, though this can lead to confusion if uninitiated. In the equation $E=mc^2$, the only difference between mass and energy is a constant. However, that mass, m, is a relativistic mass, which is different from an objects rest mass. In the equation $E^2 = m^2c^4 + p^2c^2$, m is the rest mass, i.e. the mass an object has when at rest relative to the measuring device. The units of energy in this dissertation are electron volts (eV). Because an eV is very small, a more typical unit is a GeV = giga electron volt = 1 billion electron volts.
Fermilab	A research facility in Batavia, Illinois, where the experiment E791 was conducted.
Fermion	A particle or group of particles with a half integral spin. Fro example, leptons and baryons.
Fit Fraction	The percent that a decay goes through a certain resonance. See chapter 11.
Hadrons	A particle which is affected by strong interactions, i.e., a particle made of quarks or gluons (that which binds quarks).
Helicity	The spin projection of a particle relative to the direction of its linear momentum.
Ion	A charged particle or group of particles. The detectors can only directly measure the existence and properties of ions. Neutral particles (as opposed to ions) are only measured by the daughter particles which come from them.
Lepton	An elementary particle with nonintegral spin (a Fermion) and no quarks (doesn't interact with the strong force). Known leptons are electrons (e), muons (μ), tau (τ), their corresponding neutrinos (ν) and antiparticles.
Mass	A property of matter - though there is an effective mass for anything with energy. It is, under certain circumstances, equivalent to energy. Units in this paper for mass are GeV/c^2. If c (the speed of light) is set equal to 1, then the unit is GeV.
Meson	An elementary particle made of a quark and antiquark. For example, $\overline{K}^{*0}$, D. It, like a baryon, is a hadron.
MINUIT	Physics software. Used for minimizing transcendental equations. It can maximize the joint probability of a function, p, by minimizing the -2*ln(p). This is known as a maximum likelihood fit.

Momentum A property of a moving particle. This is another important property because it is conserved in any reaction. From the linear form and the mass of a particle, the energy can be found by $E^2 = m^2c^4 + p^2c^2$. There are two kinds of momentum: linear and angular. Angular momentum at the particle level is usually made up of the orbital momentum and the intrinsic spin.

Monte Carlo Monte Carlo (MC), in general, refers to any randomizing program. In high energy physics, it refers to the creation of ideal data randomly chosen, in order to simulate a physical process. For example, the MC created for this dissertation, was the ideal case of Λ_c^+ decaying into $pK^-\pi^+$. This ideal data was then sent through a simulated detector in order for me to know like what the real Λ_c's look.

Particle An object too small to see.

Phase Space A multidimensional space in which the coordinates are defined by the important parameters of the problem. It is the regions where physics can happen.

Polarization The property of a particle which signifies how the particle's spin is oriented relative to a common reference frame.

QCD Quantum Chromodynamics. The theoretical basis for predicting any reaction which involves quarks.

Quark A fundamental particle. The building blocks of hadrons (mesons and baryons). It is an essential ingredient in all strong interactions. There are currently six known quarks: u (up), d (down), s (strange), c (charm), b (bottom or beauty), and t (top or truth).

Resonance An extremely short lived ($\sim 10^{-23}$s) elementary particle which appears in some particle decay. Looking for these is part of the dissertation.

Spin An intrinsic property of a particle. If the particle has an integral spin (0,1,2,3,...) the particle is a boson. If it has a half integral spin ($\frac{1}{2}$, $\frac{3}{2}$, ...) it is a fermion.

Tevatron The facility at Fermilab used for accelerating protons.

Vertex The point at which new particles are formed, either by decay or by collision. In this dissertation, there are primary vertices - the point at which the pion beam hit the target nucleon creating a shower of particles - and secondary vertices - the point at which one of the products from the primary vertex decays, for example $\Lambda_c \rightarrow pK\pi$.

Index